

Electron microscopy study of pure and Sr-substituted LaCoO_3

Zur Erlangung des akademischen Grades eines
DOKTORS DER NATURWISSENSCHAFTEN
von der Fakultät für Physik
des Karlsruher Institutes für Technologie (KIT)

genehmigte Dissertation

von

Dipl.-Phys. Levin Dieterle
aus Offenburg

Tag der mündlichen Prüfung: 27.01.2012
Referent: Prof. Dr. D. Gerthsen
Korreferent: Prof. Dr.-Ing. E. Ivers-Tiffée

angefertigt am
Laboratorium für Elektronenmikroskopie
Karlsruher Institut für Technologie (KIT)

Parts and excerpts of this thesis have already been published as journal articles:

Copyright 2011 by Elsevier.

Reprinted from L. Dieterle, B. Butz, and E. Müller. Optimized Ar⁺-ion milling procedure for TEM cross-section sample preparation. *Ultramicroscopy*, 111(11):1636–1644, 2011.

Copyright 2011 by John Wiley & Sons, Inc.

Reprinted from L. Dieterle, P. Bockstaller, D. Gerthsen, J. Hayd, E. Ivers-Tiffée, and U. Guntow. Microstructure of nanoscaled La_{0.6}Sr_{0.4}CoO_{3-δ} cathodes for intermediate-temperature solid oxide fuel cells. *Advanced Energy Materials*, 1(2):249–258, 2011.

Copyright 2009 by the American Physical Society.

Reprinted from D. Fuchs, L. Dieterle, E. Arac, R. Eder, P. Adelman, V. Eyert, T. Kopp, R. Schneider, D. Gerthsen, and H. v. Löhneysen. Suppression of the ferromagnetic state in LaCoO₃ films by rhombohedral distortion. *Physical Review B*, 79:024424/1-9, 2009.

Contents

Preface	1
1. Fundamentals	3
1.1. Properties of pure and Sr-substituted LaCoO_3	3
1.1.1. Perovskite structure	3
1.1.2. Phase equilibria and phase stability	10
1.1.3. Defect model	11
1.1.4. Electronic and ionic conductivity	12
1.1.5. Thermal expansion	13
1.1.6. Crystal field theory and spin states	15
1.2. Experimental techniques	18
1.2.1. Equipment	18
1.2.2. Electron tomography	18
1.2.3. Analytical transmission electron microscopy	21
2. Optimization of Ar^+-ion milling procedure for TEM cross-section sample preparation	27
2.1. Introduction	27
2.2. Experimental results	29
2.2.1. Geometrical setup	29
2.2.2. Monte-Carlo simulation of the sputtering process	30
2.2.3. Preparation and ion milling of Si cross-section samples	39
2.2.4. Single-sector milling of other materials	43
2.3. Discussion	46
2.3.1. Double-sector versus single-sector ion milling	46
2.3.2. Discrepancies between simulations and experiments	48
2.3.3. Influence of the epoxy width	51

3. Nanocrystalline $\text{La}_{0.6}\text{Sr}_{0.4}\text{CoO}_{3-\delta}$ thin-film cathodes	53
3.1. Introduction	53
3.2. Sample fabrication	57
3.2.1. $\text{Ce}_{0.9}\text{Gd}_{0.1}\text{O}_{1.95}$ electrolyte substrates	57
3.2.2. $\text{La}_{0.6}\text{Sr}_{0.4}\text{CoO}_{3-\delta}$ thin-film cathodes	57
3.2.3. Reference materials for quantitative X-ray spectroscopy	59
3.2.4. Sample preparation for transmission electron microscopy	60
3.3. Experimental results	61
3.3.1. Isothermal grain growth and grain-size distribution	61
3.3.2. Porosity and three-dimensional microstructure	67
3.3.3. Crystalline phases	72
3.3.4. Qualitative X-ray analyses	76
3.3.5. Quantitative X-ray analyses	78
3.4. Discussion	84
3.4.1. Microstructure	84
3.4.2. Correlation of microstructure with electrochemical cathode performance	88
4. Microstructure of epitaxial LaCoO_3 thin films	91
4.1. Introduction	91
4.2. Sample preparation	93
4.3. Experimental results	96
4.3.1. Geometric relation between deposited film and substrate	96
4.3.2. Microstructural characterization by electron microscopy	97
4.3.3. Microstructural characterization by X-ray diffractometry	102
4.4. Discussion	107
4.4.1. Microstructure	107
4.4.2. Correlation with magnetic properties	109
5. Summary	113
Appendix A. MATLAB source code	119
Bibliography	125

Acronyms

3D	three dimensional
APU	auxiliary power unit
BF	bright field
CF	crystal field
CGO	general: gadolinia-substituted ceria, here: $\text{Ce}_{0.9}\text{Gd}_{0.1}\text{O}_{1.95}$
DF	dark field
EDXS	energy-dispersive X-ray spectroscopy
EELS	electron energy-loss spectroscopy
EIS	electrochemical impedance spectroscopy
FC	field-cooled
FIB	focused ion beam
FM	ferromagnetic
FWHM	full width at half maximum
GGA+U	generalized gradient-corrected density-functional calculation
HAADF	high-angle annular dark-field
HRTEM	high-resolution transmission electron microscopy
HS	high spin
ICP-AES	inductively coupled plasma-atomic emission spectroscopy
IS	intermediate spin
IT-SOFC	intermediate-temperature solid oxide fuel cell
LCO	lanthanum cobalt oxide LaCoO_3
LS	low spin

LSAT	lanthanum strontium aluminum tantalum oxide (LaAlO ₃) _{0.3} (SrAl _{0.5} Ta _{0.5} O ₃) _{0.7}
LSC	general: lanthanum strontium cobalt oxide (La,Sr)CoO _{3-δ} , here: La _{0.6} Sr _{0.4} CoO _{3-δ}
LSCF	lanthanum strontium cobalt iron oxide (La,Sr)(Co,Fe)O _{3-δ}
LSM	lanthanum strontium cobalt oxide (La,Sr)MnO _{3-δ}
MC	Monte-Carlo
MIEC	mixed ionic and electronic conducting
PIPS	precision ion polishing system
PLD	pulsed laser deposition
PM	pseudomorphic
RBS	Rutherford backscattering spectroscopy
ROI	region of interest
SAED	selected-area electron diffraction
SEM	scanning electron microscopy
SIRT	simultaneous iterative reconstruction technique
SOFC	solid oxide fuel cell
SQUID	superconducting quantum interference device
STEM	scanning transmission electron microscopy
TEC	thermal expansion coefficient
TEM	transmission electron microscopy
TM	transition metal
ToF-SIMS	time-of-flight secondary ion mass spectroscopy
TPB	triple-phase boundary
TW	twinned
WBP	weighted back-projection
XRD	X-ray diffraction
YSZ	yttria-substituted zirconia

Symbols

a, b, c	fitting parameter
a_f	in-plane lattice parameter
α_{imp}	ion impact angle, i.e. the angle between the surface and incident ion beam
$\Delta\alpha_{\text{imp}}$	relative change of ion impact angle α_{imp} with increasing sector deflection
α_i, α	(local) surface inclination angle
α_{max}	maximum sample tilt angle for tomography
$\Delta\alpha$	tilt angle increment during tilt series acquisition
α_{pc}	pseudocubic lattice angle
α_{rh}	angle between rhombohedral basis vectors
a_{pc}	pseudocubic lattice parameter
A_{proj}	projected grain area
a_{rh}	rhombohedral lattice parameter
α_{sputt}	ion incident angle which is directly accessible for most ion mills
ASR	area specific resistance
a_{sub}	lattice parameter of substrate
β	wedge angle
c_A, c_B	atomic fractions of element A and B, respectively
c_f	out-of-plane lattice parameter
D	modulation length
d	average grain diameter
Δ_{cf}	crystal-field splitting
δ	oxygen non-stoichiometry
Δ_{ex}	intra-atomic exchange interaction
Δq_x	spacing of satellite reflections
e	elongation factor
ϵ	lattice mismatch
η	kinematic velocity
η	sol viscosity
F	Faraday constant
f	parameter of sputtering yield
\mathbf{g}	lattice vector
γ_{semi}	semi-sector angle
γ_{lv}	liquid-vapour surface tension

g	gravitational acceleration
h_i	local height
i	index variable
I_0	initial intensity
I	intensity
I_A, I_B	integrated characteristic X-ray intensities of element A or B, respectively
j_{load}	load current density
k	proportionality factor
k_{AB}	Cliff-Lorimer k -factor
k_B	Boltzmann constant
λ	wavelength
l_i	projected coordinates, seen from the ion source, measured with respect to h_1
l_{max}	maximum projected coordinate
m	correction factor for the epoxy sputtering yield
m_s	saturated magnetic moment
N	total number of voxels
n_{Co}	number of Co atoms
n_{pores}	number of voxels segmented as pores
n_{ls}	number of laser ablation shots
ω_0	central peak position
$\Delta\omega_0, \Delta\omega$	mosaik spread
P	pressure
P_{O_2}	oxygen partial pressure
ϕ	porosity
π	mathematical constant
p	position
R	gas constant
r_A, r_B, r_O	ionic radii of A or B cation or O anion, respectively
ρ	density
$r_{1..4}, r_i, r_j,$	different structural variants of the rhombohedral lattice regarding the substrate orientation
R	displacement
S	spin
σ_{el}	electronic conductivity
σ_{ion}	ionic conductivity
Σ	parameter of sputtering yield
T	temperature
t	sample thickness or time, respectively
t_{an}	annealing time
t_{crit}	critical sample thickness for which both sample surfaces are exposed to the ion beam
t_{film}	film thickness

t_{hold}	holding time during dip-coating
T_{max}	annealing temperature
ΔT_{\downarrow}	cooling rate
ΔT_{\uparrow}	heating rate
T_{sub}	substrate temperature
T_{C}	Curie temperature
t_{tol}	perovskite structure tolerance factor
θ	incident angle
U_{load}	cell voltage upon load
U_{N}	Nernst voltage
V	volume
v_{in}	inserting velocity
v_{out}	withdraw velocity
v_{th}	treshold value
V_{tot}	total volume
V_{void}	void volume
w	thickness of epoxy layer
ξ	extinction length
x, y, z	spatial coordinates
$Y(\theta)$	sputtering yield
Z	atomic number

Preface

In our technology-driven society there is a constant need for functional materials with new or improved properties. Most of the relevant physical properties of these materials are determined significantly by their microstructure. Understanding the relationship between the microstructure and physical properties lead to fundamental physical insights. Furthermore, the knowledge of the microstructure as well as the local chemical composition is absolutely essential if materials with new or enhanced properties have to be tailored for a special application. For this purpose, electron microscopy is a powerful tool to characterize these materials, because it facilitates the correlation of microstructural information and chemical composition down to the atomic level. Among functional materials, those with perovskite structure are characterized by a variety of interesting physical and chemical properties. Due to the flexibility of the perovskite structure regarding chemical composition, the arising properties can be tuned in a broad range. Among these are for example mixed ionic and electronic conductivity, high-temperature superconductivity, magnetoresistance, ferroelectricity, dielectricity, piezoelectricity and catalytic properties. These properties make them suitable for wide range of applications like gas-diffusion membranes, magnetic sensors, read heads for hard-disk drives or as non-volatile computer memories.

Furthermore, perovskite-type materials are a popular cathode material for solid oxide fuel cells (SOFCs). The actual challenge in SOFC research is the reduction of the operating temperature from 700–900 °C to 500–700 °C. Especially for mobile applications, such as auxiliary power units (APUs), reduced operating temperatures are advantageous, because this facilitates faster start-up times, simplifies thermal management, minimizes thermal degradation of cell and stack components and, thus, enhances system reliability and longevity. However, an operating temperature in the range of 500–700 °C decreases electrolyte conductivity and electrode kinetics significantly. New cell materials and designs are needed to overcome this drawback. Although thin-film electrolytes in anode supported cells are capable to reduce the portion of ohmic losses significantly, reduction of cathodic polarization losses is still a subject matter of research. Nanoscaled Sr-substituted LaCoO_3 is a capable cathode material for the intended temperature regime. Compared to state-of-the-art cathode materials like $(\text{La,Sr})(\text{Co,Fe})\text{O}_{3-\delta}$, it exhibits better mixed ionic and electronic conduction and better electro-catalytic activity.

Within this work the microstructure and local chemical composition of nanoscaled $\text{La}_{0.6}\text{Sr}_{0.4}\text{CoO}_{3-\delta}$ thin-film cathodes were investigated by electron microscopic techniques to attain deeper physical insights into the correlation between microstructure and electrochemical properties.

Furthermore, LaCoO_3 has recently attracted much attention due to its unusual electronic and magnetic properties at ambient pressure and the observation of ferromagnetism in epitaxially strained thin films. While bulk LaCoO_3 exhibits a non-magnetic ground state, ferromagnetic order is observed in strained, epitaxial films below a Curie temperature of $T_C \approx 85$ K. Understanding the microstructural origin of the ferromagnetic order will lead to deeper physical insights, which may stimulate the development of future sensor applications on the basis of LaCoO_3 .

The present work is composed of four parts; each of them focuses on a different aspect of material properties, preparation of samples for transmission electron microscopy (TEM) and the microstructural and local chemical characterization of LaCoO_3 and Sr-substituted LaCoO_3 .

Chapter 1 gives an overview on the material properties (e.g. structural, electrochemical and magnetic properties) of pure and Sr-substituted LaCoO_3 , with focus on the properties covered in this work. The second part of the work (**Chapter 2**) deals with the optimization of Ar-ion milling for TEM sample preparation. As for all microscopic techniques an optimal sample preparation is essential for outstanding results. Without the findings gained in this part most of the results in the following chapters would not have been possible. Major parts of this chapter were published in *Ultramicroscopy* [1]. In the third part (**Chapter 3**) nanostructured $\text{La}_{0.6}\text{Sr}_{0.4}\text{CoO}_{3-\delta}$ SOFC cathodes are characterized. Electron diffraction, electron tomography and extensive chemical analysis were performed and correlated with electrochemical properties. The presented results were published in *Advanced Energy Materials* [2].

The last part (**Chapter 4**) addresses the microstructural origin of ferromagnetism in strained epitaxial LaCoO_3 layers and the suppression of the ferromagnetic state in case of rhombohedral distortion. Parts and excerpts of this chapter were published in *Physical Review B* [3].

1. Fundamentals

1.1. Properties of pure and Sr-substituted LaCoO_3

1.1.1. Perovskite structure

Sr-substituted LaCoO_3 is one member of the large group of materials adopting perovskite structure. The perovskite prototype structure is derived from the mineral perovskite (CaTiO_3), which was first discovered in the Ural Mountains of Russia by Rose (1798–1873) in 1839 and named after the Russian mineralogist Perovski (1792–1856). **Figure 1.1** shows two examples of naturally-occurring perovskites of two different localities.

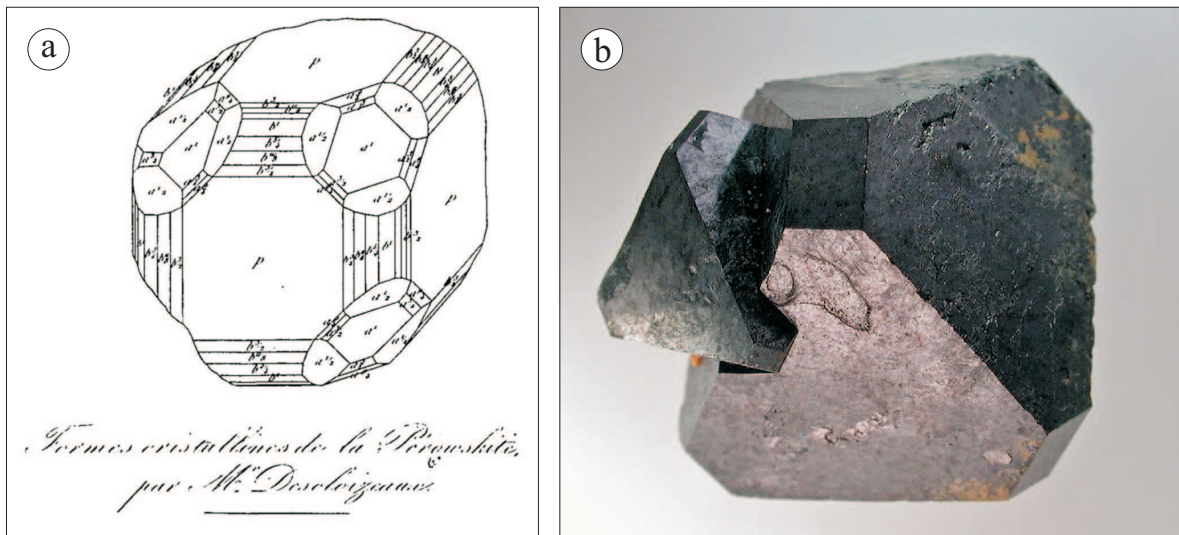


Figure 1.1.: a) Perovskite crystal. The complex faces result from a combination of pseudo-cubic, pseudo-octahedral and various pseudo-dodecahedral faces. Type locality[†]: Akhmatovskaya Kop' (Achmatovsk Mine), Nazyamskie Mts, Zlatoust, Chelyabinsk Oblast', Southern Urals, Russia. Ink drawing by M. Descloizeaux [4]. b) Dysanalite (niobium-rich perovskite variety) intergrowth of two truncated octahedra (1.6 cm × 1.5 cm × 1.4 cm). Locality: Perovskite Hill, Magnet Cove, Hot Spring County, Arkansas, USA. Photo and collection Kelly Nash [5].

[†] the locality where a particular mineral species was first identified.

Many fascinating properties are observed in the family of materials with perovskite structure making them interesting for theoretical and application-oriented point of view. Interesting physical properties of perovskites range from colossal magnetoresistance, ferroelectricity, superconductivity, charge ordering to complex interaction between structural, magnetic and transport properties.

The general chemical formula for a perovskite-type compound is ABX_3 , where A and B are cations of different sizes and X is an anion that bonds to both. The A-ions are larger than the B-ions. In the ideal structure with cubic symmetry, the B-cation is in 6-fold coordination, surrounded by an octahedron of anions. The A-cation has a 12-fold cuboctahedral coordination. Axes formed by B-X bonds of the octahedra coincide with the crystallographic axes in cubic symmetry. Several viewpoints can be used to describe the structure. The most common description is the corner-sharing octahedron. It is the most intuitive depiction if distortions from ideal symmetry are considered. Beside the lattice parameter no further degree of freedom is available in case of ideal cubic symmetry to modify the perovskite structure.

Despite the simplicity of the original perovskite crystal structure, this family of compounds shows an enormous variety of structural modifications and variants. Hence, Goldschmidt [6] proposed an empirical tolerance factor t_{tol} to specify the degree of distortion from the ideal cubic structure. For vanishing distortion from the ideal cubic structure, the tolerance factor approaches the value of one. The tolerance factor can be calculated by using the ionic radius of oxygen r_{O} and the radii r_{A} and r_{B} of the cations A and B:

$$t_{\text{tol}} = \frac{r_{\text{O}} + r_{\text{A}}}{\sqrt{2}(r_{\text{O}} + r_{\text{B}})}$$

Up to now, all known, stable perovskite structures have t_{tol} -values in the range of $0.78 < t < 1.05$. Perovskites with tolerance factors $t_{\text{tol}} > 1$ are typically tetragonal, while materials with lower tolerance factors exhibit rhombohedral, orthorhombic or monoclinic symmetry.

For LaCoO_3 , t_{tol} lies between 0.92 and 0.96, depending on the spin configuration of the Co-ion. The ionic radius of the Co-ion in low-spin configuration (LS) corresponds to a value of $r_{\text{Co}_{\text{LS}}^{3+}} = 0.525 \text{ \AA}$ and in high-spin configuration (HS) to $r_{\text{Co}_{\text{HS}}^{3+}} = 0.61 \text{ \AA}$ [9]. At ambient temperature, bulk LaCoO_3 exhibits a rhombohedral distorted perovskite crystal structure (space group $R\bar{3}c$) with a lattice parameter $a_{\text{rh}} = 5.3788 \text{ \AA}$ and angle $\alpha_{\text{rh}} = 60.798^\circ$ between the basis vectors, independent of the spin configuration [7, 10–15]. In this structure the La-ion occupies Wyckoff position 2a, the Co-ion position 2b and the O-ion 6e [7]. The structural parameters are summarized for the rhombohedral structure in **Table 1.1** and for the cubic in **Table 1.2**. Three-dimensional representations of the rhombohedral and cubic unit cells are depicted in **Figure 1.2a** and **Figure 1.2d**, respectively.

site	element	Wyckoff position	coordinates
A cation	La	2a	$(1/4, 1/4, 1/4)$
B cation	Co	2b	$(0, 0, 0)$
X anion	O	6e	$(0.2003(1), 0.2972(1), 0.75)$

Table 1.1.: Atomic sites in the rhombohedral perovskite structure (space group $R\bar{3}c$, $a_{\text{rh}} = 5.3788 \text{ \AA}$ and $\alpha_{\text{rh}} = 60.798^\circ$) [7].

site	element	Wyckoff position	coordinates
A cation	La/Sr	1b	$(1/2, 1/2, 1/2)$
B cation	Co	1a	$(0, 0, 0)$
X anion	O	3d	$(1/2, 0, 0)$

Table 1.2.: Atomic sites in the cubic perovskite structure (space group $Pm\bar{3}m$, $a_{\text{cub}} = 3.84 \text{ \AA}$) [8].

For better comparability with cubic symmetry it is convenient to describe the rhombohedral perovskite structure in a pseudo-cubic representation. The axes of the pseudo-cubic LCO unit cell correspond to those of the aristotype[‡] perovskite, with lattice parameter a_{pc} and angle α_{pc} . They can be calculated with the general dot product for affine (non-rectangular) coordinate systems:

$$\alpha_{\text{pc}} = \arccos \frac{1 - 2 \cos \alpha_{\text{rh}}}{2 \cos \alpha_{\text{rh}}} = 90.685^\circ$$

$$a_{\text{pc}} = \frac{1}{2} \sqrt{a_{\text{rh}}^2 (3 - 2 \cos \alpha_{\text{rh}})} = 3.826 \text{ \AA}$$

In order to avoid confusions, the use of the pseudo-cubic representation is marked with the index pc in the following.

The view along the pseudo-cubic $[100]_{\text{pc}}$ (see **Figure 1.2b**) and $[110]_{\text{pc}}$ zone axis (see **Figure 1.2c**) in the rhombohedral perovskite structure reveals the alternate rotation and tilting of the O-ion octahedra, which are twisted around the $[111]_{\text{pc}}$ direction.

Substitution of La^{3+} by the roughly two times larger Sr^{2+} increases the pseudo-cubic lattice parameter a_{pc} almost linearly. **Figure 1.3a** shows the pseudo-cubic lattice parameter a_{pc} as a function of the Sr-content [14]. In addition to the increase of a_{pc} due to the Sr^{2+} -substitution, t_{tol} also increases, resulting in a decrease of the rhombohedral distortion of the unit cell (see **Figure 1.3b**), until a transition to the cubic perovskite structure occurs.

[‡] a high-symmetric structure, which can be viewed as an idealized version of a structure with lower symmetry. It was introduced by Megaw and Darlington [16] in relation to perovskites, where it is still mostly used. The cubic perovskite structure (adopted at most by half a dozen compounds) is regarded as the aristotype for the vast number of perovskites with lower symmetry, which are denoted as hettotype structures.

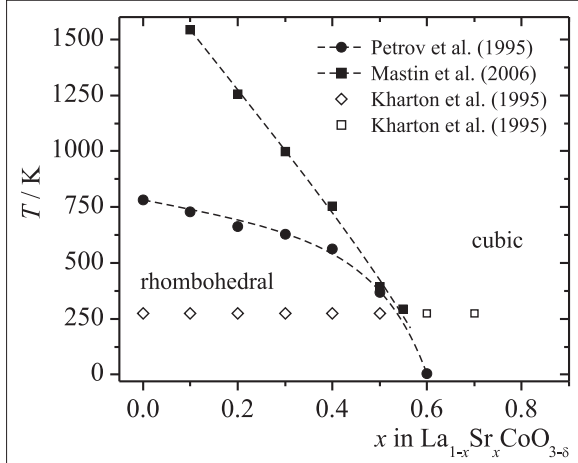


Figure 1.4.: $\text{La}_{1-x}\text{Sr}_x\text{CoO}_{3-\delta}$ phase transition temperature from rhombohedral to cubic structure.

the cubic ABX_3 perovskite structure (symmetry $Pm\bar{3}m$), the La^{3+} and Sr^{2+} -cations statistically occupy Wyckoff position 1b (0,0,0), the Co-ion Wyckoff position 1a ($1/2, 1/2, 1/2$) and O-anions Wyckoff position 3d ($1/2, 0, 0$) (see **Table 1.2**) [8]. A three-dimensional representation of the cubic unit cell is depicted in **Figure 1.2d**. The view along the $[100]$ and $[110]$ zone axes is shown in **Figure 1.2e** and **Figure 1.2f**, respectively. In contrast to the rhombohedral structure, the edges of the oxygen octahedra are orientated along the $\langle 110 \rangle$ directions.

This transition, which is a function of temperature and degree of substitution, is given for example by Petrov et al. [14] or Mastin et al. [17] (see **Figure 1.4**). Despite the large discrepancy at low Sr-substitutions, both data sets converge with increasing Sr-content. Kharton et al. [18] analyzed the occurring phases at room temperature as a function of Sr-substitution. They restricted the phase transition range to $0.5 < x < 0.6$ in accordance to van Doorn and Burggraaf [19]. Other groups determined the transition from rhombohedral to cubic symmetry of $\text{La}_{1-x}\text{Sr}_x\text{CoO}_{3-\delta}$ at ambient temperature at a substitution level of $x = 0.5$ [14, 19–21]. A further increase of the Sr-content lowers the temperature for phase transition. In

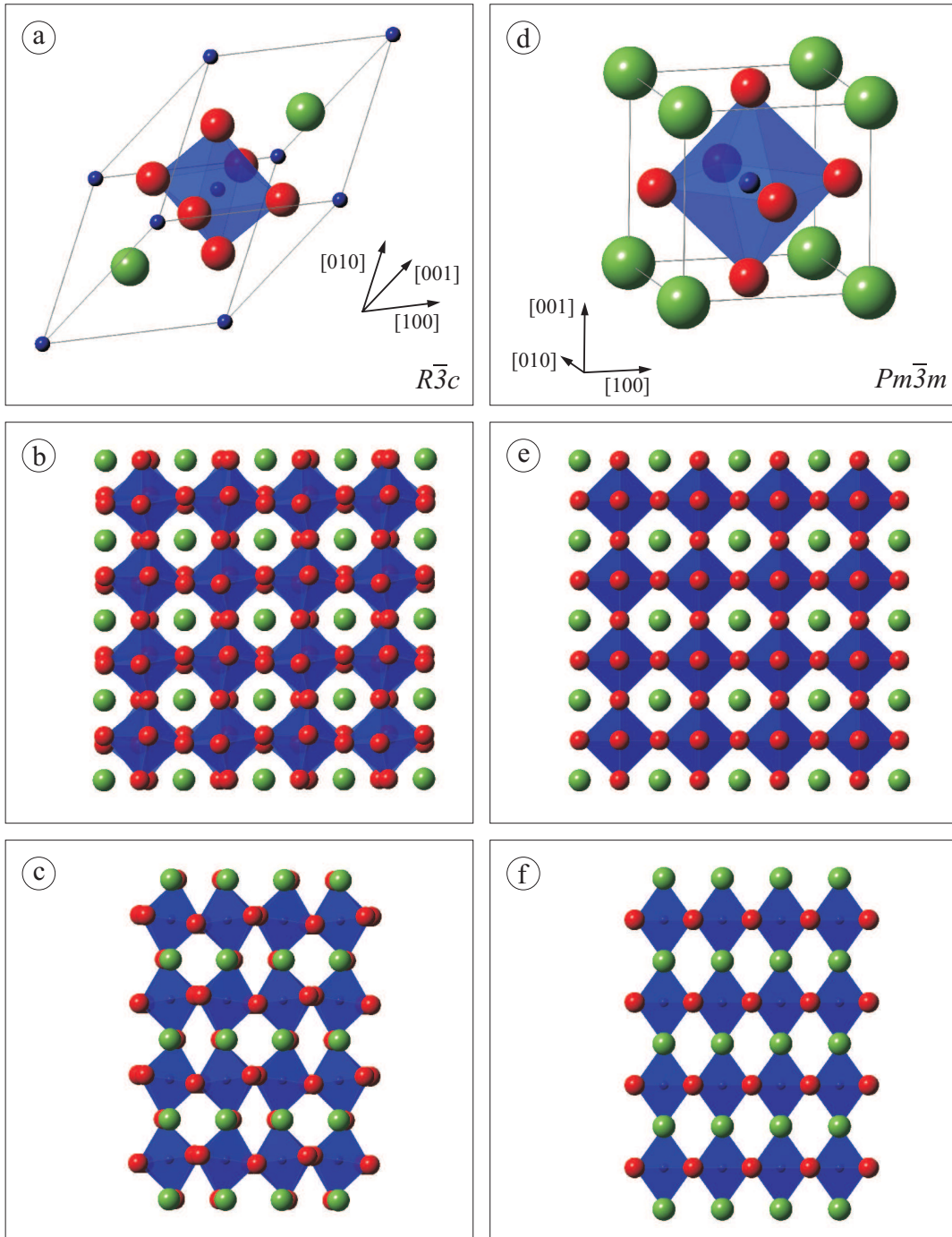


Figure 1.2.: Model of the perovskite structure. Green spheres represent the A-cations, blue spheres the B-cations and red spheres the oxygen anions forming an octahedron. a) Rhombohedral cell with rotated oxygen octahedron (space group $R\bar{3}c$), with b) view along $[100]_{pc}$ and c) along $[111]_{pc}$ and d) ideal cubic cell (space group $Pm\bar{3}m$), with e) view along $[100]$ and f) along $[111]$.

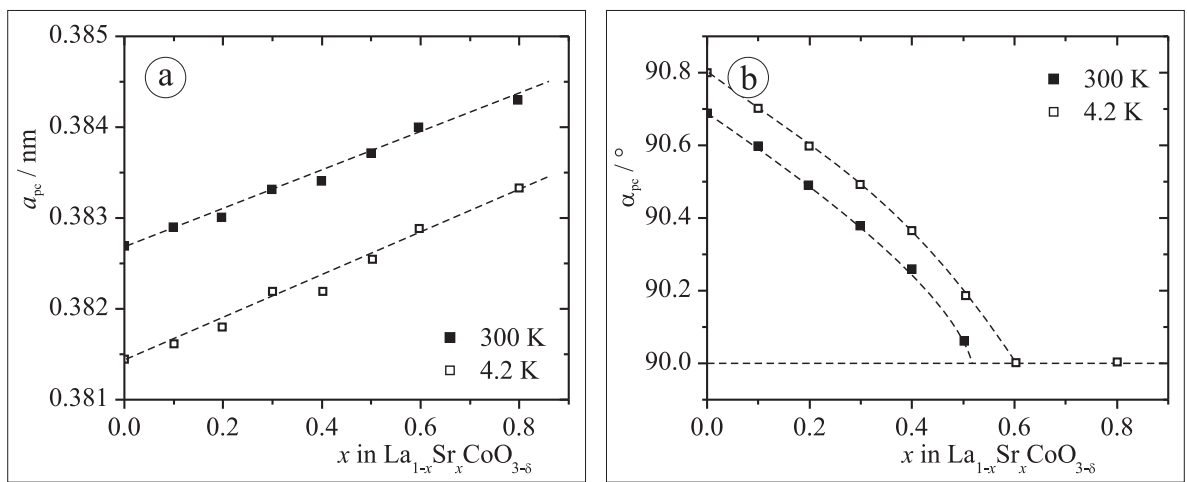


Figure 1.3.: a) Pseudo-cubic lattice parameter a_{pc} and b) cell angle α_{pc} between $[100]$ and $[010]$ for in pseudo-cubic representation.

Ordered phases

Besides simple cubic and rhombohedral structures, several quite complex ordered perovskite-related structures are known. Especially oxygen vacancy ordered structures are common in oxygen-deficient perovskites [22]. In the La-Co-O system two homologous structure series are known, which are obtained by reduction of LaCoO_3 .

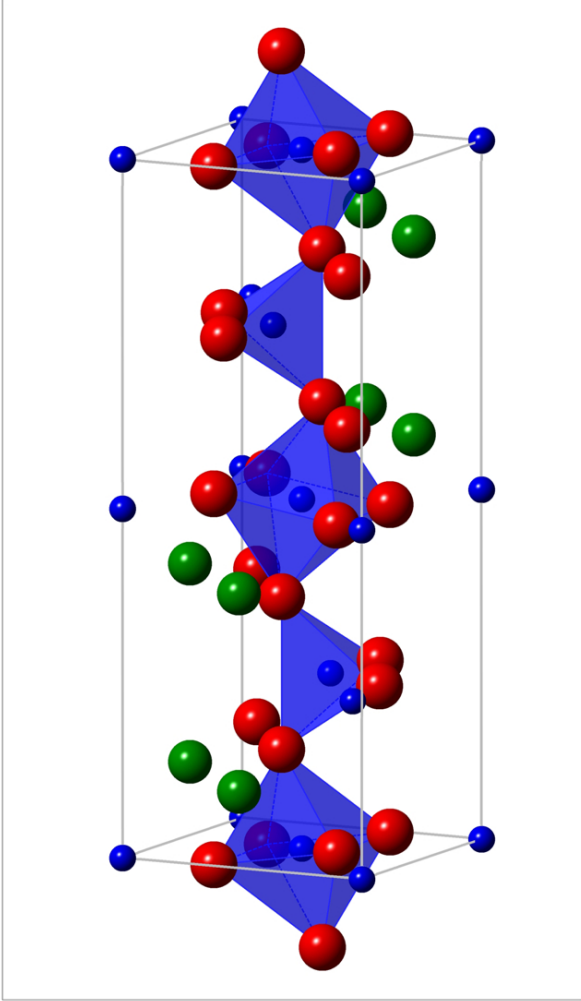


Figure 1.5.: Representation of the brownmillerite structure. Color assignment analog to **Figure 1.2**.

The homologous Ruddlesden-Popper series $\text{La}_{m+1}\text{Co}_m\text{O}_{3m+1}$ is received by reduction at high temperature ($T > 900\text{ K}$) until complete reduction into Co and La_2O_3 occurs [23, 23]. Upon reduction at lower temperature, the homologous series $\text{La}_n\text{Co}_n\text{O}_{3n-1}$ is known [24, 25]. For $n = 2$ the well-known brownmillerite prototype structure is adopted, which is shown in **Figure 1.5**. It is derived from the perovskite structure by introducing oxygen vacancies in every second CoO plane parallel to the c -direction. The vacancies are arranged in strings along the $[110]$ direction in the CoO planes. Klie and co-workers [26] observed a brownmillerite-like structure for $\text{La}_x\text{Sr}_{1-x}\text{Fe}_y\text{Cr}_{1-y}\text{O}_{3-\delta}$. Stemmer et al. [27] found perpendicular brownmillerite nano-domains in epitaxial $\text{La}_{0.5}\text{Sr}_{0.5}\text{CoO}_{3-\delta}$ thin films on (001) -orientated LaAlO_3 as well as in $\text{SrCoO}_{3-\delta}$ bulk material [28]. Furthermore, this structure was found in other perovskite-type material systems like $\text{La}_{1-x}\text{Ca}_x\text{FeO}_{3-y}$ [29] or $\text{SrFe}_{1-x}\text{V}_x\text{O}_{2.5+x}$ [30]. The structure formed for $n = 3$ ($\text{La}_3\text{Co}_3\text{O}_8$) can be considered as an intergrowth between the brownmillerite and the perovskite prototype structure [24]. For $n = \infty$ the rhombohedral perovskite structure LaCoO_3 is adopted. Gspan and co-workers [31] found a brownmillerite-related structure

for $\text{La}_{0.4}\text{Sr}_{0.6}\text{CoO}_{2.71}$, with oxygen vacancies arranged along the $[100]$ direction. For $\text{La}_{0.3}\text{Sr}_{0.7}\text{CoO}_{3-\delta}$ van Doorn and Burggraaf [19] proposed a oxygen-vacancy superstructure comparable to the structure of $(\text{La,Sr,Ba})(\text{Co,Cu})\text{O}_{3-\delta}$ [32] and $\text{YBaCo}_{2-x}\text{Cu}_x\text{O}_{3-\delta}$ [33].

1.1.2. Phase equilibria and phase stability

Investigations of the phase equilibria in the system La–Sr–Co–O are very sparse. Aksenova et al. [34] investigated the phase equilibria and crystal structures of solid solutions in the system $\text{LaCoO}_{3-\delta}$ – $\text{SrCoO}_{2.5\pm\delta}$ – $\text{SrFeO}_{3-\delta}$ – $\text{LaFeO}_{3-\delta}$ (cf. **Figure 1.6a**). Cherepanov et al. [35] investigated the phase equilibria of La–Sr–Co–O at 1100 °C in air (see **Figure 1.6b** and **1.7**). Slight deviation from the $\text{La}_{1-x}\text{Sr}_x\text{CoO}_{3-\delta}$ solid solution results either in the precipitation of CoO in the case of Co-excess or $\text{La}_{1-y}\text{Sr}_y\text{CoO}_4$ for Co-depletion. This was confirmed by Morin et al. [36], who stated that the stability regime of $\text{La}_{0.5}\text{Sr}_{0.5}\text{CoO}_{3-\delta}$ is very narrow. Even deviations of only 0.3% from the nominal A/B-cation ratio of the perovskite, i.d. $0.997 < A/B < 1.003$, results in formation of a secondary phase as mentioned above.

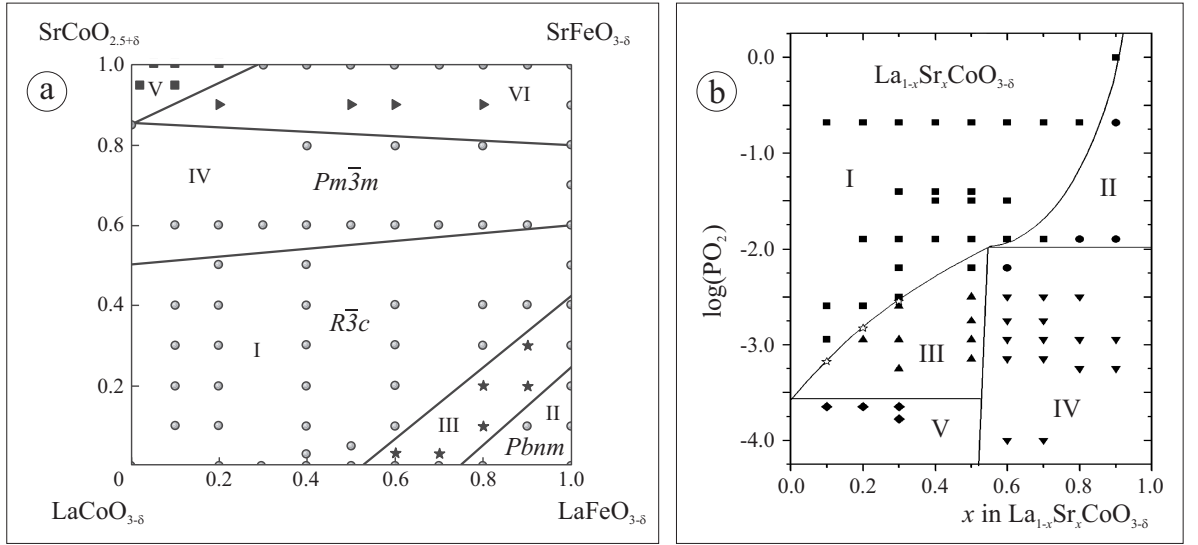


Figure 1.6.: a) Phase equilibria and crystal structures of solid solutions in the $\text{LaCoO}_{3-\delta}$ – $\text{SrCoO}_{2.5\pm\delta}$ – $\text{SrFeO}_{3-\delta}$ – $\text{LaFeO}_{3-\delta}$ system at 1100 °C in air: I) $\text{La}_{1-x}\text{Sr}_x\text{Co}_{1-y}\text{Fe}_y\text{O}_{3-\delta}$ solid solutions (space group $R\bar{3}c$), II) $\text{La}_{1-x}\text{Sr}_x\text{Co}_{1-y}\text{Fe}_y\text{O}_{3-\delta}$ solid solutions (space group $Pbnm$), III) mixture of $R\bar{3}c$ and $Pbnm$ solid solutions, IV) $\text{La}_{1-x}\text{Sr}_x\text{Co}_{1-y}\text{Fe}_y\text{O}_{3-\delta}$ solid solutions (space group $Pm\bar{3}m$), V) $\text{SrCoO}_{2.5\pm\delta} + \text{SrFe}_{0.3}\text{Co}_{0.7}\text{O}_{3-\delta} + \text{La}_{0.15}\text{Sr}_{0.85}\text{CoO}_{3-\delta}$ and VI) $\text{SrFe}_{1-z}\text{Co}_z\text{O}_{3-\delta} + \text{La}_{1-x}\text{Sr}_x\text{Co}_{1-y}\text{Fe}_y\text{O}_{3-\delta}$ [34].
b) Cross-sections of the La–Sr–Co–O phase diagram along $\text{La}_{1-x}\text{Sr}_x\text{CoO}_{3-\delta}$ with I) $\text{La}_{1-x}\text{Sr}_x\text{CoO}_{3-\delta}$, II) $\text{La}_{1-x'}\text{Sr}_{x'}\text{CoO}_{3-\delta} + \text{SrCoO}_x$, III) $\text{La}_{1-x'}\text{Sr}_{x'}\text{CoO}_{3-\delta} + (\text{La}_{1-y'}\text{Sr}_{y'})_2\text{CoO}_4$, IV) $(\text{La}_{1-y'}\text{Sr}_{y'})_2\text{CoO}_4 + \text{SrCoO}_x$ and V) $\text{La}_4\text{Co}_3\text{O}_{10} + (\text{La}_{1-y'}\text{Sr}_{y'})_2\text{CoO}_4$ [35].

Ovenstone and co-workers [37] analyzed the phase transitions and phase decomposition of $\text{La}_{1-x}\text{Sr}_x\text{CoO}_{3-\delta}$ at low oxygen partial pressures and reducing atmospheres, respectively. $\text{La}_{0.6}\text{Sr}_{0.4}\text{CoO}_{3-\delta}$ was found to be stable up to 1000 °C at oxygen partial pressure of 10^{-4} atm, whereas Morin et al. [36] stated 1254 °C as phase transition temperature for

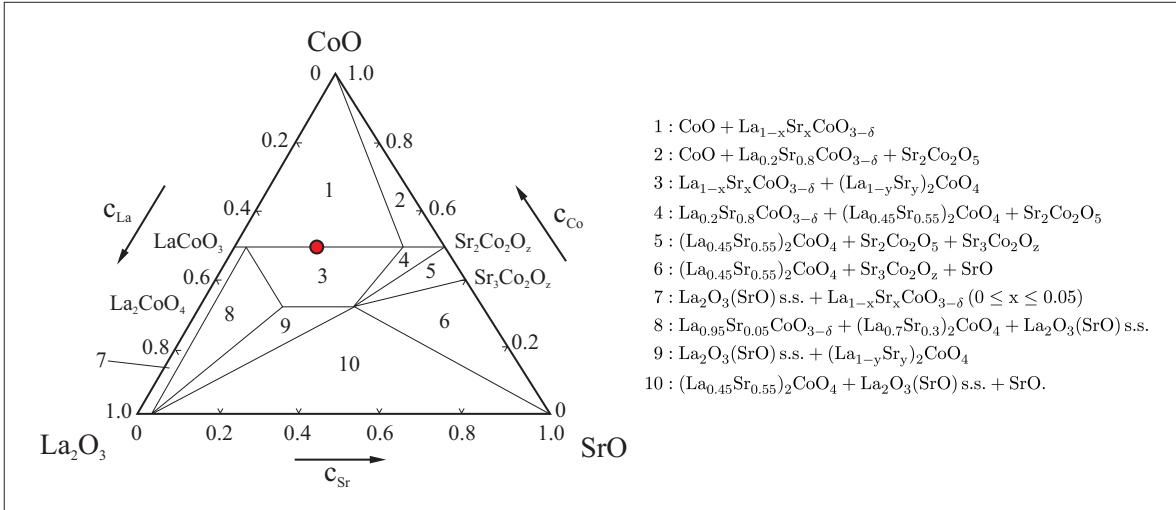


Figure 1.7.: Phase diagram of the La-Sr-Co-O system at 1100 °C in air [35].

$\text{La}_{0.5}\text{Sr}_{0.5}\text{CoO}_{3-\delta}$. At higher temperature $\text{La}_{0.6}\text{Sr}_{0.4}\text{CoO}_{3-\delta}$ decomposes irreversibly to $(\text{La},\text{Sr})\text{CoO}_4$ and CoO . Formation of a brownmillerite phase was not observed down to an oxygen partial pressure of 10^{-5} atm.

In reducing atmosphere (4% H_2) a brownmillerite phase is formed at 250 °C, which decomposes at 375 °C and LaSrCoO_4 begins to form. The decomposition into La_2O_3 , SrO and metallic Co starts above 400 °C until it is completed at about 600 °C [37].

1.1.3. Defect model

According to current knowledge, transport properties, like electronic and ionic conductivity, but also oxygen-reduction characteristics depend significantly on the defects at the anionic sublattice in $\text{La}_{1-x}\text{Sr}_x\text{CoO}_{3-\delta}$ [14]. In general, it is assumed that the valence states of the lanthanum (La^{3+}), strontium (Sr^{2+}) and oxygen (O^{2-}) ions are fixed, while the transition metal cobalt can adopt a valence state between Co^{2+} and Co^{4+} [38]. Hence, in order to ensure electro-neutrality, substitution of a trivalent A-site cation (La^{3+}) by a divalent acceptor (e.g. Sr^{2+}) requires the compensation of the effective negative charge. This is achieved either by increasing the valence state of the B-site cation (electronic compensation) and/or the formation of oxygen vacancies (ionic compensation). Using the common Kröger-Vink notation [39] this can be expressed by:



The brackets therein refer to the concentration of the enclosed species in mole fraction, the prime symbol represents one unit of negative charge with respect to the site in the host lattice which is indicated by the index. The superscript bullet represents one unit of positive charge. V_{O} refers to a vacancy in the oxygen lattice and $[V_{\text{O}}^{\bullet\bullet}]$ corresponds the oxygen non-stoichiometry δ .

In general, ionic and electronic compensation mechanisms compete with each other, depending on composition, oxygen partial pressure and temperature. Oxygen non-stoichiometry increases with increasing temperature, increasing Sr-content and decreasing oxygen partial pressure. **Figure 1.8a** shows the relationship between oxygen non-stoichiometry and mean Co-valence for different Sr-substitution levels and oxygen partial pressures at 800 °C [38]. Here the mean valence state n_{Co} of the Co-ion is calculated under consideration of electro-neutrality to $n_{\text{Co}} = 3 + x - 2\delta$. For low Sr-substitutions ($x < 0.2$), an increase in x mainly results in an increase in mean Co-valence, while for $0.2 \leq x \leq 0.5$ the ionic compensation is the dominating process and δ increases. For larger $x \geq 0.5$ electronic compensation prevails again. A comparable behavior is also observed for other temperatures [38]. The oxygen non-stoichiometry δ as a function of the oxygen partial pressure $p\text{O}_2$ is plotted in **Figure 1.8b**. According to Mizusaki et al. [38], $\log \delta$ is almost proportional to $\log p\text{O}_2^{-1/2}$ for $\delta < 0.01$. For $\delta > 0.01$ the $p\text{O}_2$ dependence becomes weaker with increasing δ .

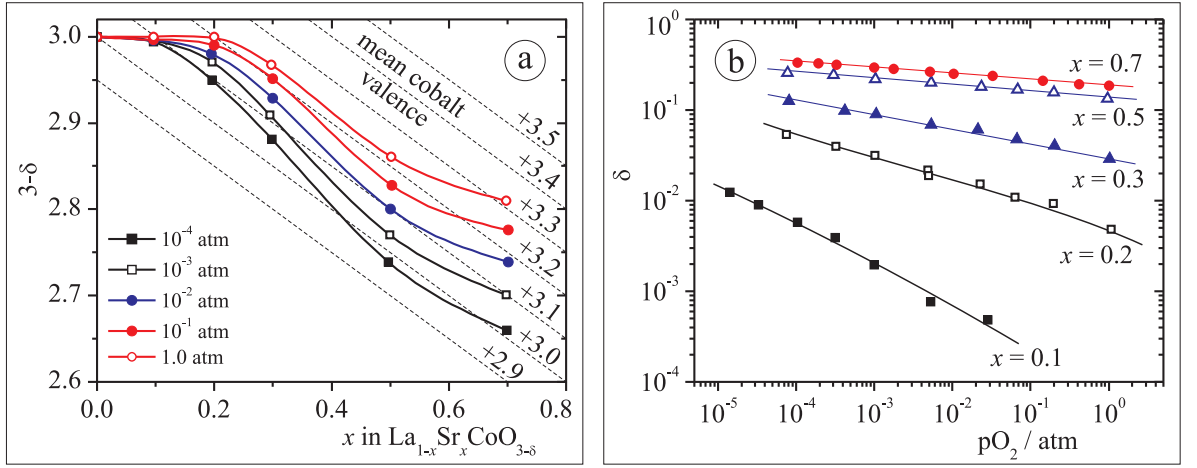


Figure 1.8.: a) Change in oxygen stoichiometry and mean cobalt valence and b) non-stoichiometry δ vs. oxygen partial pressure of $\text{La}_{1-x}\text{Sr}_x\text{CoO}_{3-\delta}$ with different Sr-content at 800 °C [38].

1.1.4. Electronic and ionic conductivity

Compared to other perovskite-type materials for SOFC cathode applications, the electronic and ionic conductivity is exceptionally large in $\text{La}_{1-x}\text{Sr}_x\text{CoO}_{3-\delta}$. Hence, LSC is classified as a mixed ionic and electronic conducting (MIEC) material. For $\text{La}_{0.5}\text{Sr}_{0.5}\text{CoO}_{3-\delta}$ Ullmann et al. [42] reported an electrical conductivity σ_{el} of 1349 S/cm measured at 800 °C in air. For $\text{La}_{0.6}\text{Sr}_{0.4}\text{CoO}_{3-\delta}$ they determined a value of $\sigma_{\text{el}} = 1585$ S/cm, while Petrov et al. [14] and Petric et al. [40] found slightly higher values of $\sigma_{\text{el}} = 1820$ S/cm and $\sigma_{\text{el}} = 1595$ S/cm, respectively. **Figure 1.9a** shows Arrhenius plots of the electrical conductivity for different Sr-substitutions [14, 40]. As it can be seen, the maximum in electrical conductivity is reached for the stoichiometry $\text{La}_{0.6}\text{Sr}_{0.4}\text{CoO}_{3-\delta}$. The observed

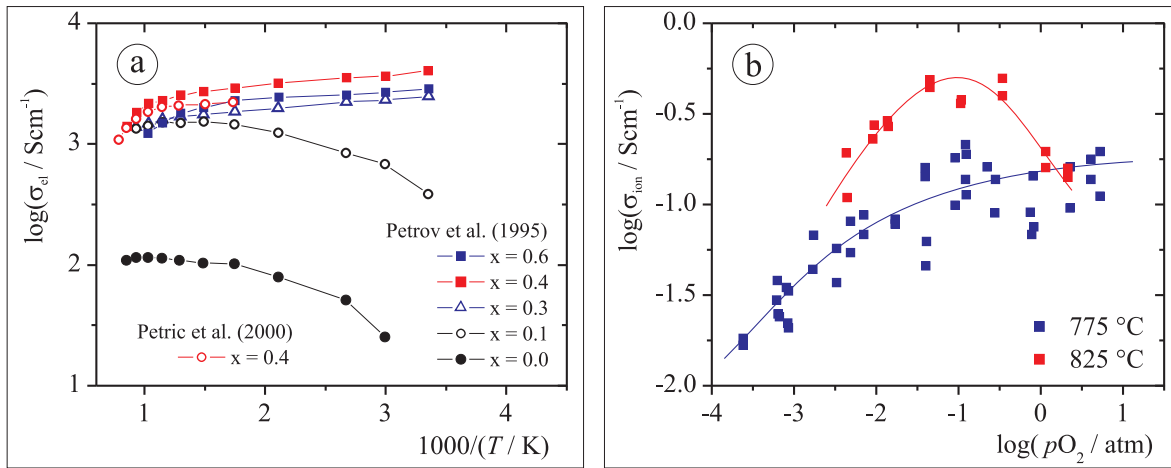


Figure 1.9.: a) Arrhenius plot of electrical conductivity σ_{el} at 680 °C $\text{La}_{1-x}\text{Sr}_x\text{CoO}_{3-\delta}$ for different Sr-substitutions [14, 40] and b) ionic conductivity as a function of oxygen partial pressure [41].

values for σ_{el} are three order of magnitude higher than the values observed for the ionic conductivity. Teraoka et al. [43] determined the ionic conductivity to $\sigma_{ion} = 0.22 \text{ S/cm}$ at 800 °C in air. Ullmann et al. [42] reported values between $\sigma_{ion} = 0.09 \text{ S/cm}$ and 0.8 S/cm at 800 °C for $\text{La}_{0.5}\text{Sr}_{0.5}\text{CoO}_{3-\delta}$ and $\text{La}_{0.3}\text{Sr}_{0.7}\text{CoO}_{3-\delta}$, respectively. As σ_{ion} depends on the O^{2-} -vacancy concentration, it should increase with decreasing $p\text{O}_2$. However, Bucher et al. [41, 44] found for $p\text{O}_2 < 1 \text{ atm}$, which corresponds to $3 - \delta < 2.93$, no region of increasing σ_{ion} with increasing oxygen vacancy concentration at 775 °C (cf. **Figure 1.9b**). This indicates an immobilization of ionic charge carriers due to formation of vacancy-ordered structures even at relatively low oxygen non-stoichiometries of $\delta > 0.07$. At 825 °C, the ionic conductivity increases with increasing oxygen non-stoichiometry up to $p\text{O}_2 = 0.1 \text{ atm}$ ($\delta = 0.1$) until it drops. Bucher et al. concluded that vacancy ordered structures are less easily formed at higher temperatures and low oxygen non-stoichiometry.

1.1.5. Thermal expansion

Thermal expansion of solid materials is classically described in terms of a thermal expansion coefficient (TEC) α . Ohno, Nagata and Sato [45] determined the thermal expansion coefficient for $\text{La}_{0.6}\text{Sr}_{0.4}\text{CoO}_{3-\delta}$ to be $\alpha = 20.5 \times 10^{-6} \text{ 1/K}$ for ($400 \text{ °C} \leq T \leq 700 \text{ °C}$) and $16.4 \times 10^{-6} \text{ 1/K}$ for ($20 \text{ °C} \leq T \leq 400 \text{ °C}$). This value coincides in the high-temperature regime with the findings of Petric and co-workers, who determined the thermal expansion coefficient in the temperature range $30 \text{ °C} \leq T \leq 1000 \text{ °C}$ [40]. Furthermore, the thermal expansion coefficient increases with Sr-content. It increases from $18.5 \times 10^{-6} \text{ 1/K}$ for $x = 0.2$ to $26.0 \times 10^{-6} \text{ 1/K}$ for $x = 0.9$.

However, the classical description is not quite adequate for MIEC oxides, because lattice volume is a function of both, temperature and oxygen-vacancy concentration. As shown

by Adler [46] thermal expansion can be described more adequately by using a volumetric chemical expansivity (β_{chem}) in addition to the traditionally defined volumetric thermal expansivity (β_T).

$$\beta_T = \left(\frac{\partial \ln V}{\partial T} \right)_{x_V, P} \quad \beta_{\text{chem}} = \left(\frac{\partial \ln V}{\partial x_V} \right)_{T, P}$$

Where V is the specific volume, T the temperature, P the total pressure and x_V is the O-vacancy mole fraction, defined as $x_V = \delta/3$. Chen et al. [47] determined the equilibrium thermal expansivity (β_T) and O-vacancy chemical expansivity (β_{chem}) for $\text{La}_{1-x}\text{Sr}_x\text{CoO}_{3-\delta}$ ($x = 0.2, 0.4$ and 0.7) at different $p\text{O}_2$ -values. Equilibrium thermal expansion was found to depend only moderately on temperature, whereas the chemical expansivity increases with O-vacancy concentration. They explained this behavior by lattice-strain relaxation due to increased introduction of O-vacancies into the lattice. For $\text{La}_{0.6}\text{Sr}_{0.4}\text{CoO}_{3-\delta}$ the chemical expansivity was found to be $\frac{1}{3}\beta_{\text{chem}}(x_V) = (0.055 + 0.811x_V) \times 10^{-6}$, whereas the mean equilibrium thermal expansion coefficient was determined to $\frac{1}{3}\beta_T = (14.2 + 4.84 \times 10^{-3}(T - 25^\circ\text{C})) \times 10^{-6}$.

Compared to state-of-the-art electrolytes like Y-substituted zirconia with a thermal expansion coefficient of $\alpha \approx 10.0 \times 10^{-6} \text{ 1/K}$ at 600°C [48] or Gd-substituted ceria (CGO) with $\alpha \approx 12.5 \times 10^{-6} \text{ 1/K}$ at 600°C [49], $\text{La}_{0.6}\text{Sr}_{0.4}\text{CoO}_{3-\delta}$ has a much higher thermal expansion. This mismatch results in mechanical stress upon heating and cooling of SOFCs during thermo cycles and ultimately may leads to cracking and breakdown of the SOFC system. However, the application of porous LSC thin-film cathodes can outflank this mismatch in thermal expansion coefficients between cathode and substrate as shown by Peters [50].

1.1.6. Crystal field theory and spin states

Magnetic properties are determined essentially by the electronic configuration of the material. For a free atom or ion, the valence electrons are distributed in the available orbitals according to Hund's rules:

1. The total spin S is maximized without violating the Pauli principle to minimize the Coulomb energy.
2. The angular momentum L is maximized regarding rule 1.
3. The total angular momentum is $J = |L \pm S|$; (+) if the shell is more than half full, else (-).

In the case of the transition-metal (TM) ion Co^{3+} the valence electrons occupy the $3d$ -orbitals which are five-fold degenerated in energy per spin. The atomic orbitals, with exception of the s -orbital, show no spherical symmetry. The angular dependency of the electron density of the different $3d$ orbitals is shown in **Figure 1.10**.

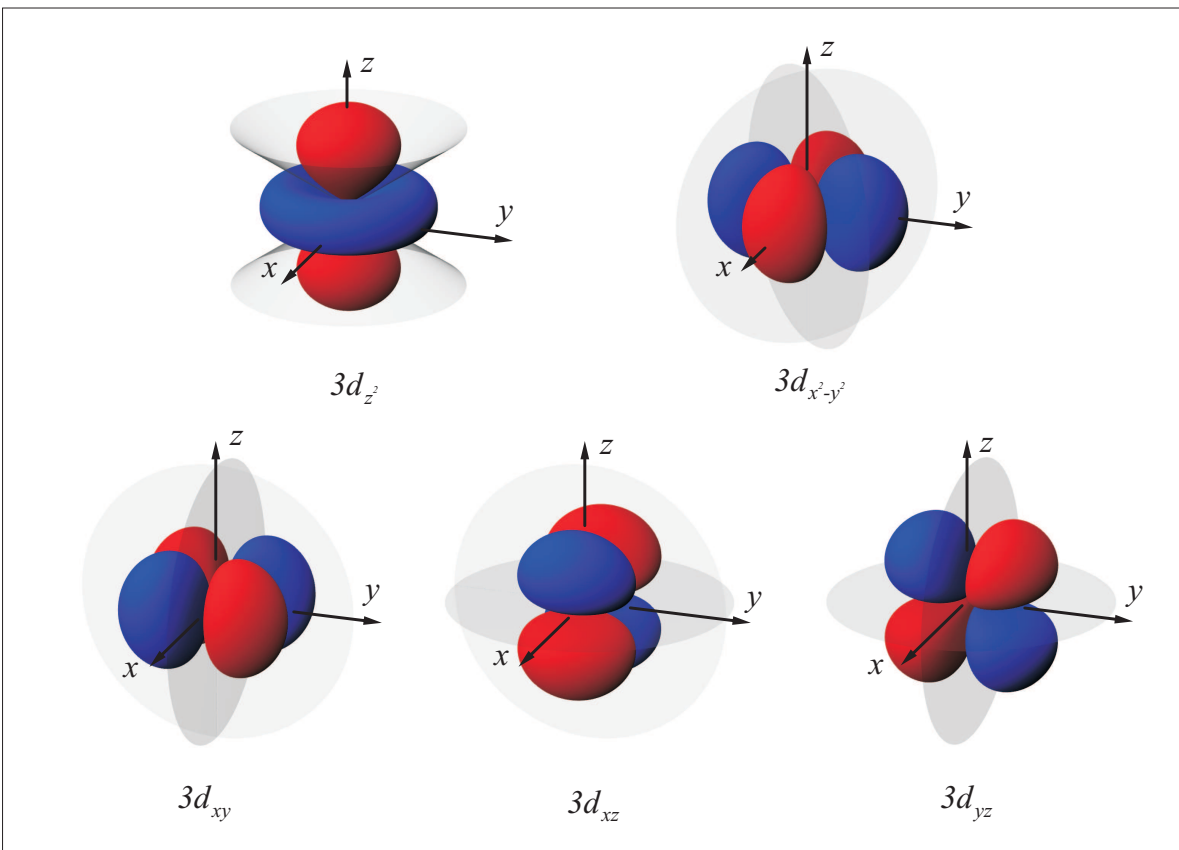


Figure 1.10.: Angular dependence of the electron distribution in the six $3d$ orbitals. Positive phase is displayed in blue and negative phase in red [51].

Within the perovskite lattice, the arms of the d_{z^2} and $d_{x^2-y^2}$ orbitals lie along the x , y or z -axis, respectively, where the octahedrally arranged negative charged ligands are located. Those two $3d$ -orbitals will experience a repulsive force from the ligands, resulting in a higher energy, while the three orbitals lying between the ligands (d_{xy} , d_{yz} , d_{xz}) will have lower energy. Hence, the energetic degeneracy of the $3d$ -orbitals is partly resolved under the influence of the anisotropic crystal field (CF) caused by the six surrounding O^{2-} -ions in the perovskite lattice. The influence of the O^{2-} -ions (the so called ligands) surrounding the Co-ion on its $3d$ -states is described by the ligand-field theory (LFT). The m_L -levels split into the t_{2g} ground level (three-fold degenerated per spin) and the e_g upper level (two times degenerated per spin) due to the octahedral environment of the perovskite structure (see **Figure 1.11**). The energy difference between the t_{2g} and e_g -states that arises from the interaction of the orbitals with the electric field of the ligands is usually expressed as $\Delta_{cf} = 10 Dq$, the crystal field splitting.

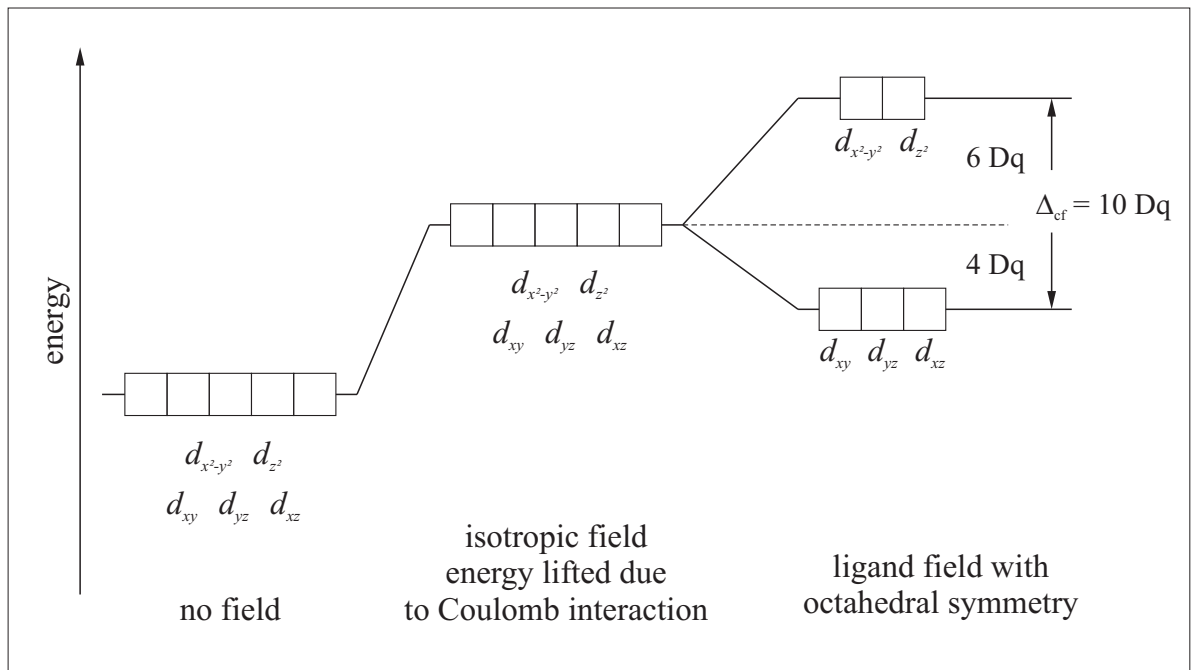


Figure 1.11.: Energy levels of $3d$ orbitals within isotropic and octahedral environment.

The electrons can be distributed in three different ways into the orbitals, depending on the strength of the crystal field splitting Δ_{cf} compared to the strength of the Hund's coupling J_{H} :

- If $\Delta_{\text{cf}} > 3J_{\text{H}}$, all six electrons occupy the t_{2g} -states. The energy J_{H} is necessary to place an electron in a paired state. This state ($t_{2g}^6 e_g^0$, total spin $S = 0$) (1. Hund's rule is broken) is denoted as low-spin (LS) state.
- For $2J_{\text{H}} < \Delta_{\text{cf}} < 3J_{\text{H}}$ all spin-up states of the t_{2g} -orbital are filled with one electron. Then two spin-down electrons are placed into the t_{2g} states and an additional spin-up electron occupies the e_g -state. This state ($t_{2g}^5 e_g^1$, total spin $S = 1$) is denoted as intermediate-spin (IS) state.
- When $J_{\text{H}} < \Delta_{\text{cf}} < 2J_{\text{H}}$ all spin-up states are occupied and the last spin-down electron is placed in t_{2g} orbital. Hence, the so called high-spin (HS) state ($t_{2g}^4 e_g^2$) has a total spin $S = 2$. This state corresponds to the electronic configuration of a free ion, according to the Hund's rules.

The octahedron can be distorted spontaneously because the distortion lowers the overall energy of the complex. This distortion removes the energetic degeneration in case of asymmetric filled orbitals and is known as Jahn-Teller effect.

1.2. Experimental techniques

The goal of this work was the microstructural and chemical characterization of perovskite-based materials by means of scanning and transmission electron microscopy. As numerous characterization techniques were used, the following section only gives a brief overview with emphasis on the most important aspects of the methods applied.

1.2.1. Equipment

The microstructural characterization was carried out using a 200 kV Philips CM200 FEG/ST transmission electron microscope equipped with a field-emission electron gun. For imaging, a $2k \times 2k$ CCD as well as a $4k \times 4k$ TemCam-F416 CMOS camera from TVIPS (Tietz Video and Imaging Processing Systems GmbH, Munich, Germany) was used. Selected-area electron diffraction (SAED) patterns for characterization of the crystalline phases were recorded on imaging plates from DITABIS (Digital Biomedical Imaging Systems AG, Pforzheim, Germany), which provide a linear contrast transfer. Digitization of the diffraction patterns was achieved by a 16-bit scanner (DITABIS AG, Pforzheim, Germany), providing an excellent dynamic range. In addition, the $4k \times 4k$ TemCam-F416 CMOS camera provides a capable alternative as recording device for electron diffraction patterns. The open-source curve-fitting and data analysis software FITYK [52] was used for empirical background subtraction of radially integrated SAED patterns. In addition to the CM200 FEG/ST, an aberration-corrected FEI Titan³ 80-300 operating at 300 kV equipped with an image C_s-corrector was used for investigations of the two and three-dimensional microstructure on the nanoscale. This microscope is equipped with an EDAX X-ray detector operating at a dispersion of 20 eV/channel as well as a post-column energy filter (Gatan imaging filter, GIF) from Gatan, Inc. (USA). Image simulations (kinematic diffraction patterns and high-resolution TEM (HRTEM) images) were performed with the software package JEMS by P. Stadelmann [53].

1.2.2. Electron tomography

The efficiency of SOFC cathodes depend significantly on their microstructure. Complex morphologies like rough surfaces, pores and gas channels increase the electrochemically active surface area of the cathode. The nanocrystalline and porous nature of $\text{La}_{1-x}\text{Sr}_x\text{CoO}_{3-\delta}$ fabricated by metal-organic deposition (see in detail in **Chapter 3.3**) leads to an overlap of a wealth of features when viewed in projection by TEM. This complicates conclusions on the three-dimensional structure or makes porosity evaluation due to an unknown sample thickness impossible. Electron tomography facilitates the investigation of the three-dimensional microstructure, which is reconstructed on the basis of two-dimensional projections of the sample acquired in different directions of view. Although several techniques like μ -tomography [54], focused ion beam tomography [55–57], transmission X-ray microscope based X-ray tomography [58, 59], mercury intrusion [54, 60], nitrogen adsorption [61] or the Archimedes method [54, 62] are known, they fail either with respect to spatial resolution for pores in the 10 to 40 nm range or

are averaging techniques, hence lacking essential information about the spatial distribution of pores. Therefore, electron tomography is the only experimental method which combines both, imaging of nanometer-sized pores, gas channels and their spatial distribution and quantitative measurement of the volume fraction of porosity. Porosity data for nanoscaled $\text{La}_{0.6}\text{Sr}_{0.4}\text{CoO}_{3-\delta}$ -based materials were not reported in literature before. However, knowledge of the actual porosity and correlation with the electrochemical performance is essential, if finite element methods shall be used to model, optimize and tailor the microstructure.

The projection requirement

A transmission electron microscope is commonly equipped with several image acquisition devices like CCD cameras or different types of scanning transmission electron microscopy (STEM) detectors (c.f. **Figure 1.12a**), more or less suitable for electron tomography. To be suitable for a tomographic reconstruction, an image signal must meet several prerequisites. The most crucial is, that the acquired signal is the sum of intensity $I(x, y)$ of the transmitted object perpendicular to the image plane. This is true for the ideal case. In two dimensions this is expressed by

$$P(r, \theta) = \int I(x, y) ds$$

as schematically sketched in **Figure 1.12b**. However, a strictly monotonically varying function is commonly sufficient to fulfill the projection requirements.

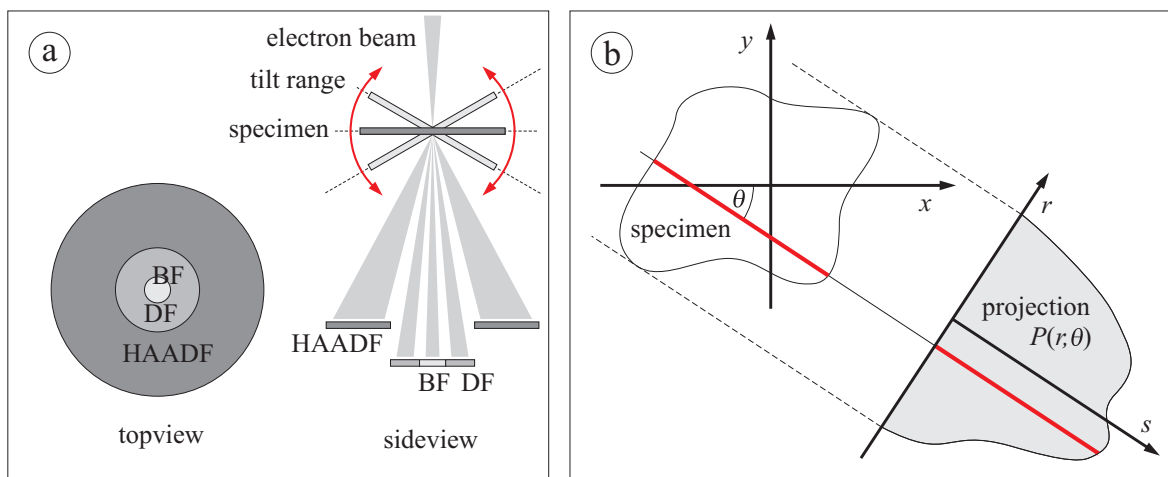


Figure 1.12.: a) Projection process in two dimensions and b) Schematic diagram of the detector layout in a scanning transmission electron microscope showing the relative positions of the brightfield (BF), dark-field (DF) and high-angle annular dark-field (HAADF) detectors.

In TEM, there are several competing contrast mechanisms. However, only some obey the projection requirement. For amorphous materials, contrast in conventional TEM bright-field (BF) images is mainly determined by mass-thickness contrast. It arises from changes in sample density and thickness. Hence, images underlying mass-thickness contrast are suitable for tomographic reconstruction. In contrast to amorphous materials, dynamical interactions between electron beam and the crystal potential result in complex image contrasts (e.g. thickness and bending contours or diffraction contrast) within crystalline materials.

BF contrast depends almost entirely on the diffraction conditions of the investigated crystallites, resulting in a non-monotonic relationship between contrast and sample thickness. Hence BF TEM images cannot be used for electron tomography of crystalline samples [63].

To overcome this limitation, STEM can be used. Images in STEM-mode are formed by scanning a small focused electron probe (typically in the order of 1 Å) over the sample. At each point either the transmitted electrons (STEM BF image) or scattered electrons (dark-field (DF) image) or both are detected. The different possible detector setups are schematically shown in **Figure 1.12a**. However, images formed by unscattered or electrons scattered into low angles ($\alpha_{\text{scatt}} < 10 \text{ mrad}$) still exhibit diffraction contrast. Only the signal of electrons scattered into angles beyond Bragg-reflections ($\alpha_{\text{scatt}} \gg 10 \text{ mrad}$) obey the projection requirement, because they are predominantly incoherent. Hence, they do not show contrast changes associated with coherent scattering. These electrons are detected by the so called high-angle annular dark-field (HAADF) detector. Moreover, these electrons are scattered close to the nucleus of the atom. Hence, the cross-section for HAADF scattering approaches the unscreened Rutherford scattering cross-section, which is strongly dependent on the atomic number Z , resulting in an image intensity, which is proportional to Z^ν . The exponent ν is smaller than 2 because the Coulomb potential of the bare nucleus is screened by the atomic electron cloud. It ranges from $1.6 < \nu < 1.9$ depending on the used inner and outer collection angle of the detector [64].

Volume reconstruction

The goal of volume reconstruction is the recovery of missing z -information of an object point (x, y, z) in 3D space that is lost during the imaging process. The reconstruction of a three-dimensional object from a set of two-dimensional projections is based on the *central slice theorem*, stating that the Fourier transform of an object's projection is a central plane in the Fourier transform of the object [65].

The standard method of tomographic reconstruction is the weighted back-projection (WBP). Unfortunately, this method is not stable against formation of artifacts. These filtering artifacts occur predominantly around edges and may lead to information loss. An alternative and often used method for reconstruction is the simultaneous iterative reconstruction technique (SIRT) [66]. The iterative procedure is repeated until the increase in image information stagnates, typically after at least 15 iterations. Due to the lack of a good termination criterion to determine whether the number of iterations is sufficient or not [67], this point remains always somewhat subjective. At present,

SIRT gains increasing popularity due to the increase in computing power. Furthermore, this algorithm increases the signal-to-noise ratio by averaging the noise out. Since the reconstructed volume contains all frequency information and is only negligibly affected by edge artifacts, SIRT instead of WBP is used for volume reconstruction in this work.

1.2.3. Analytical transmission electron microscopy

If a beam of fast electrons interacts with a sample, numerous signals are generated. Typical electron energies in TEM are in the range of 60 to 300 keV. The occurring interactions range from elastically and inelastically scattered electrons, Auger electrons and in certain materials, visible light. Furthermore, continuum radiation (called *Bremsstrahlung*) and element characteristic X-rays are generated. In conventional TEM only the elastically scattered and transmitted (unscattered) electrons are used for imaging (bright- or dark-field imaging or diffraction patterns). However, it is possible to collect X-rays with an appropriate detector for qualitative and quantitative chemical analyses [68]. The power of analytical TEM lies in the fact that the compositional information can be correlated with the microstructure of the sample on the nanometer scale.

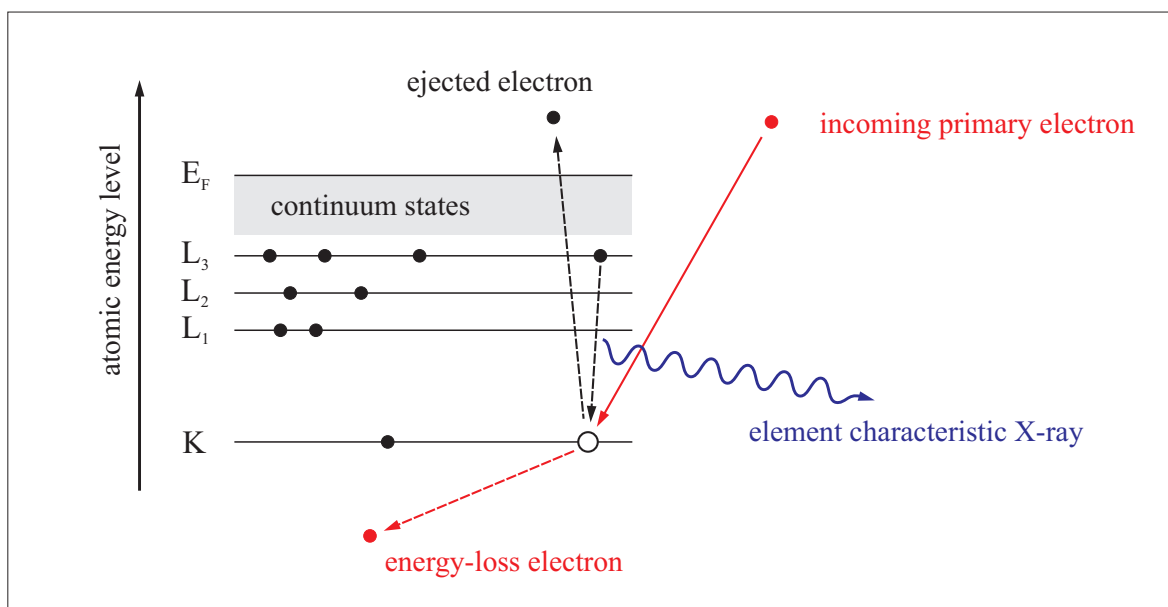


Figure 1.13.: Generation of element characteristic X-radiation

A high-energy electron can transfer energy to an inner-shell electron of an atom in the sample. If the transferred energy exceeds the binding energy, the inner-shell electron is excited in the conduction band, leaving a hole in the inner-shell behind. The excited (ionized) atom will approach its lowest energy (ground state) by filling the hole with an electron from an outer shell. This transition is accompanied by the emission of either an X-ray or an Auger electron. The energy of the emitted X-ray quantum corresponds to the energy difference between initial and final state of the emitting electron. If, for

example, an inner K-shell electron is ejected from an atom of the sample, the hole in the K-shell can be filled by an electron from the L-shell by emission of an element-characteristic $K\alpha$ quantum. This process is shown schematically in **Figure 1.13**.

The International Union of Pure and Applied Chemistry (IUPAC) recommendations are to refer to X-ray lines by writing the initial and final levels separated by a hyphen [69], e.g. Co K-L₃ and to abandon the Siegbahn notation, e.g. Co K α ₁, which is based on the relative intensities of the lines. The nomenclature and the correspondence between the two notations is given in **Table 1.3**. Since the substitution has not yet become common in the community, the Siegbahn notation is used for this work.

Siegbahn labeled the element characteristic X-ray emission lines after following scheme:

1. element (La, Sr Co, etc.)
2. electron shell that was ionized and subsequently filled (K, L, M...).
3. energetic "distance" of the shell providing the neutralizing electron (marked by a Greek letter; α indicates the next upper shell, β the shell after next, ...).
4. sublimes are identified by numerical subscripts.

source shell	shell filled									
	K		L _I		L _{II}		L _{III}		L _{IV}	
	SN	IUPAC	SN	IUPAC	SN	IUPAC	SN	IUPAC	SN	IUPAC
L _I	—	—	—	—	—	—	—	—	—	—
L _{II}	K α_2	K-L _{II}	—	—	—	—	—	—	—	—
L _{III}	K α_1	K-L _{III}	—	—	—	—	—	—	—	—
M _I	—	—	—	—	L η	L _{II} -M _I	Ll	L _{III} -M _I	Ll	L _{III} -M _I
M _{II}	K β_3	K-M _{II}	L β_4	L _I -M _{II}	—	—	Lt	—	Lt	L _{III} -M _{II}
M _{III}	K β_1	K-M _{III}	L β_3	L _I -M _{III}	L β_{17}	L _{II} -M _{III}	Ls	L _{II} -M _{III}	Ls	L _{III} -M _{III}
M _{IV}	K $\beta_{5'}$	K-M _{IV}	L β_{10}	L _I -M _{IV}	L β_1	L _{II} -M _{IV}	L α_2	L _{II} -M _{IV}	L α_2	L _{III} -M _{IV}
M _V	K $\beta_{5''}$	K-M _V	L β_9	L _I -M _V	—	—	L α_1	—	L α_1	L _{III} -M _V

Table 1.3.: Nomenclature for the element characteristic X-ray lines in Siegbahn notation (SN) and corresponding IUPAC nomenclature [69].

Quantitative energy-dispersive X-ray analyses

Quantitative energy-dispersive X-ray spectroscopy (EDXS) was performed using the standard-based Cliff-Lorimer method [70]. This technique is preferred to quantification with the database of the EDXS system software because it yields higher accuracy data if standard samples with well known and similar composition compared to the investigated sample are available for calibration. The method converts the observed integrated intensity ratio of the elements A and B into the atomic fraction ratio by the equation:

$$\frac{c_A}{c_B} = k_{AB} \frac{I_A}{I_B}$$

where k_{AB} is the so called Cliff-Lorimer k -factor, c_A and c_B the atomic fractions and I_A and I_B the measured integrated characteristic X-ray intensities of the elements A and B within the analyzed volume. Atomic fractions of cations in a ternary system (like the investigated La–Sr–Co system) are converted to absolute concentrations using the relation $c_{\text{La}} + c_{\text{Sr}} + c_{\text{Co}} = 1$. The original work of Cliff and Lorimer neglects the influence of absorption and secondary fluorescence within in the thin-foil approximation. However, if the generated X-ray intensity is appreciably absorbed in the TEM sample it should be corrected, using *Beer-Lambert's law*,

$$I = I_0 \exp \left(- \left(\frac{\mu}{\rho} \right)_{\chi}^{\eta} \rho x \right)$$

where I is the transmitted X-ray intensity, I_0 the initial intensity and $\left(\frac{\mu}{\rho} \right)_{\chi}^{\eta}$ the mass-absorption coefficient (in cm^2/g) for X-radiation at a given energy η in matter with composition χ and density ρ along a path of the length x . Mass-absorption coefficients for compound materials are calculated by averaging the values for the constituent elements according to their respective mass concentrations. In **Table 1.4** mass-absorption coefficients [71] which are relevant for this work are given.

compound	$\left(\frac{\mu}{\rho} \right)_{\text{comp}}^{\text{La-L}\alpha_1}$ [cm^2/g]	$\left(\frac{\mu}{\rho} \right)_{\text{comp}}^{\text{Sr-K}\alpha_1}$ [cm^2/g]	$\left(\frac{\mu}{\rho} \right)_{\text{comp}}^{\text{Co-K}\alpha_1}$ [cm^2/g]
LaCoO ₃	219	-	303
LaSrGaO ₄	291	42	-
LaSrAlO ₄	293	55	-
La _{0.6} Sr _{0.4} CoO _{3-δ}	240	52	233

Table 1.4.: Mass-absorption coefficients [cm^2/g] of La-L α_1 , Sr-K α_1 and Co-K α_1 radiation in LaCoO₃, LaSrGaO₄, LaSrAlO₄ and La_{0.6}Sr_{0.4}CoO_{3- δ} , respectively [71].

Using *Beer-Lambert's law* the intensity ratio $\frac{I_B}{I_A}$ can now be described as [72]:

$$\frac{I_B}{I_A} = \left(\frac{I_B}{I_A}\right)_0 \frac{\left(\frac{\mu}{\rho}\right)^A \left[1 - \exp\left[-\left(\frac{\mu}{\rho}\right)^B \rho t \csc \alpha\right]\right]}{\left(\frac{\mu}{\rho}\right)^B \left[1 - \exp\left[-\left(\frac{\mu}{\rho}\right)^A \rho t \csc \alpha\right]\right]}$$

where $\left(\frac{I_B}{I_A}\right)_0$ is the absorption-corrected intensity ratio, t the foil thickness, α the take-off angle of the X-ray detector ($\alpha = 14.9^\circ$ in case of the FEI Titan³ 80-300 microscope), $\left(\frac{\mu}{\rho}\right)^A$ and $\left(\frac{\mu}{\rho}\right)^B$ the mass-absorption coefficients of the characteristic X-ray radiation of element A and B in the analyzed sample volume, respectively.

If it is assumed that the X-ray intensity is completely generated at one half of the sample thickness, the equation can be simplified to:

$$\frac{I_B}{I_A} = \left(\frac{I_B}{I_A}\right)_0 \exp\left(-\left[\left(\frac{\mu}{\rho}\right)^B - \left(\frac{\mu}{\rho}\right)^A\right] \rho \frac{t}{2} \csc \alpha\right)$$

This equation can be rewritten as

$$\ln \frac{I_B}{I_A} = \ln \left(\frac{I_B}{I_A}\right)_0 + \Delta_{AB} t$$

where Δ_{AB} describes the thickness dependence. Using this equation, the measured intensity ratio $\frac{I_B}{I_A}$ can be used for the linear extrapolation to $t = 0$ to get the absorption-free intensity ratio $\left(\frac{I_B}{I_A}\right)_0$ and the absorption-free Cliff-Lorimer $(k_{A,B})_0$ -factor. This factor can be used to calculate the atomic fractions of elements A and B in the investigated samples.

2. Optimization of Ar⁺-ion milling procedure for TEM cross-section sample preparation

2.1. Introduction

Samples of high quality are indispensable for every kind of transmission electron microscopy (TEM) investigation. In this context, high quality means TEM samples with large electron-transparent regions of interest (ROI). Furthermore, it means constant sample thickness in the order of only a few ten nanometers within such ROI. This is advantageous for most TEM techniques, in particular for quantitative analyses by energy-dispersive X-ray spectroscopy (EDXS) or electron energy-loss spectroscopy (EELS). However, the preparation of cross-section samples of thin films or layered structures especially on substrates with different sputtering yields may be difficult. Ayache et al. [73,74] published a comprehensive and authoritative guide for (ROI) sample preparation that presents all common techniques. Preparation techniques like cleaving [75,76], micro-cleaving [77], ion digging [78] or tripod polishing [79,80] usually do not reach the specification of plane parallelism described above.

The well-established procedure by grinding, foil- or felt-polishing and Ar⁺-ion milling may fail as well, due to inappropriately chosen milling parameters. Various detailed solutions for the mechanical thinning procedure are described in the literature [74,81–83]. Nevertheless, applicable information on parameters for the Ar⁺-ion milling is sparse, although Ar⁺-ion milling as the final preparation step is the most critical step in achieving the demand of plane parallelism of the electron transparent regions. Depending on primary ion energy and geometrical (e.g., sputtering angle) as well as device-specific parameters (e.g., selection of azimuthal sectors for anisotropic ion milling during rotation of the sample in the ion mill) a large variety of inappropriately etched TEM samples can be obtained. Hence, much time is often wasted for preparation of cross-section samples with large wedge angles or even cross-section samples, where the ROI is preferentially etched or, in worst case, completely removed during ion milling [84,85]. Solely Barna [86] recommended single-sector ion milling as adequate technique to prepare plane parallel sample regions. He presented a phenomenological model that qualitatively explains the evolution during ion milling.

Goals and outline

In the following, the Ar⁺-ion milling process of TEM cross-section samples is investigated more quantitatively to improve reliability and reproducibility of this preparation step. Therefore, systematic ion-milling experiments of Si cross-section samples were performed using a commercial Gatan precision ion polishing system (PIPS) [87, 88]. The obtained cross-sectional profiles were evaluated after focused ion beam (FIB) sectioning these final samples. Furthermore, topographical evolution of the TEM sample profile is modeled by Monte-Carlo (MC) methods with main emphasis on understanding the strong discrepancies between single-sector (milling only one half of the cross-section sample) and double-sector (simultaneous milling of both halves of a cross-section sample) ion milling.

2.2. Experimental results

This part of the work comprises Monte-Carlo simulations of profile evolution of TEM cross-section samples during Ar^+ -ion milling (**Section 2.2.2**) as well as the experimental evaluation (**Section 2.2.3**).

2.2.1. Geometrical setup

Figure 2.1 shows the schematic arrangement of the ion guns and their covered solid angles, i.e. active sectors, in side and top view for clarification of the nomenclature, used in the following. Furthermore, a TEM cross-section sample and the central epoxy line is depicted with respect to the orientation of the ion guns. The graphics applies to both, the simulations as well as the presented ion-milling experiments. It is essential for application of the proposed ion-milling procedure that the ion guns (from both sides of the TEM sample, top and bottom) are only active in specific sectors perpendicular to the central epoxy line, as indicated in **Figure 2.1** (top view).

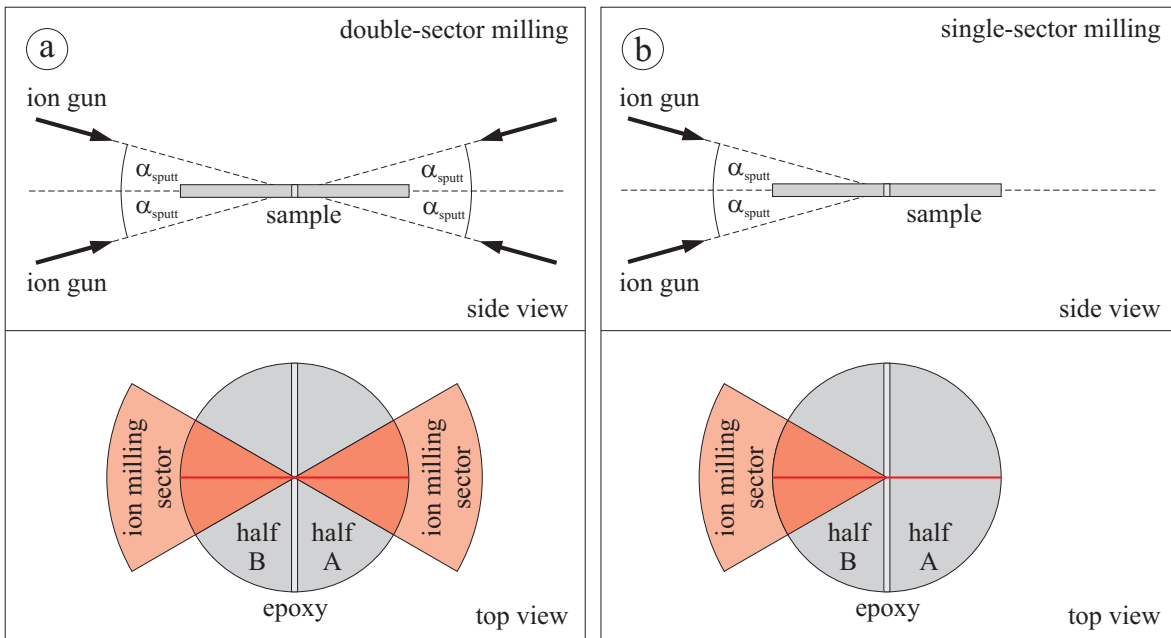


Figure 2.1.: Geometrical setup for a) double-sector ion-milling and b) single-sector ion-milling in side- and top-view.

Two ion-milling modes are distinguished in the following:

- dual-sector milling: top and bottom ion guns are activated in specific sectors while half A or B is opposed during sample rotation (c.f. **Figure 2.1a**).
- single-sector milling: top and bottom ion guns are activated in a specific sector while half A is opposed during sample rotation (c.f. **Figure 2.1b**).

For many commercial ion mills this is realized either by an oscillating/rocking sample holder (e.g., Fishione, Baltec, Linda Technoorg) or the modulation of the incident ion beam, i.e. switching the ion beam sector-wise on/off (e.g., Gatan PIPS [87, 88]) during sample rotation. The sputtering angle α_{sputt} denotes the incident angle which is directly accessible for most ion mills.

2.2.2. Monte-Carlo simulation of the sputtering process

To understand the strong difference in the cross-sectional profiles that evolve during single- and double-sector Ar^+ -ion milling of TEM cross-section samples, a qualitative two-dimensional MC simulation was implemented in the software package MATLAB [89] (source code is presented in **Appendix A**). The simulation is based on the assumption that the local removal of material during ion milling is, apart from shadowing, independent of sputtering at neighboring regions. Hence, it only depends on the sputtering speed determined by the local surface inclination and composition (i.e. by the local binding, which is not considered in this study). Thus, the sample topography is modified at the impact position (sampling point of the surface) of the Ar^+ -ion projectiles. However, the simulation does not model the atomistic processes in detail. The program code relies on the parameterized dependency of normalized sputtering yield $Y(\theta)$ on the impact angle θ , i.e. the angle between direction of the incident beam and the surface normal of the sample (see inset in **Figure 2.2**). Since Si cross-section samples are easily prepared and its Ar^+ -ion sputtering yield is well known, silicon was chosen as appropriate model system. The experimental results of the systematic ion milling are presented in **Section 2.2.3**.

Sputtering yield

Figure 2.2 shows a compilation of available experimental data [86,90–96] on the sputtering yield of silicon (Ar^+ -ion impact) versus incident angle θ . For better comparability (experimental data obtained at various primary energies) all datasets were normalized with respect to the sputtering yield at vertical impact ($Y(0^\circ)$). Despite the large amount of data sets close to normal (0°) and at intermediate incident angles, studies at oblique incident angles beyond the maximum of the sputtering yield are sparse.

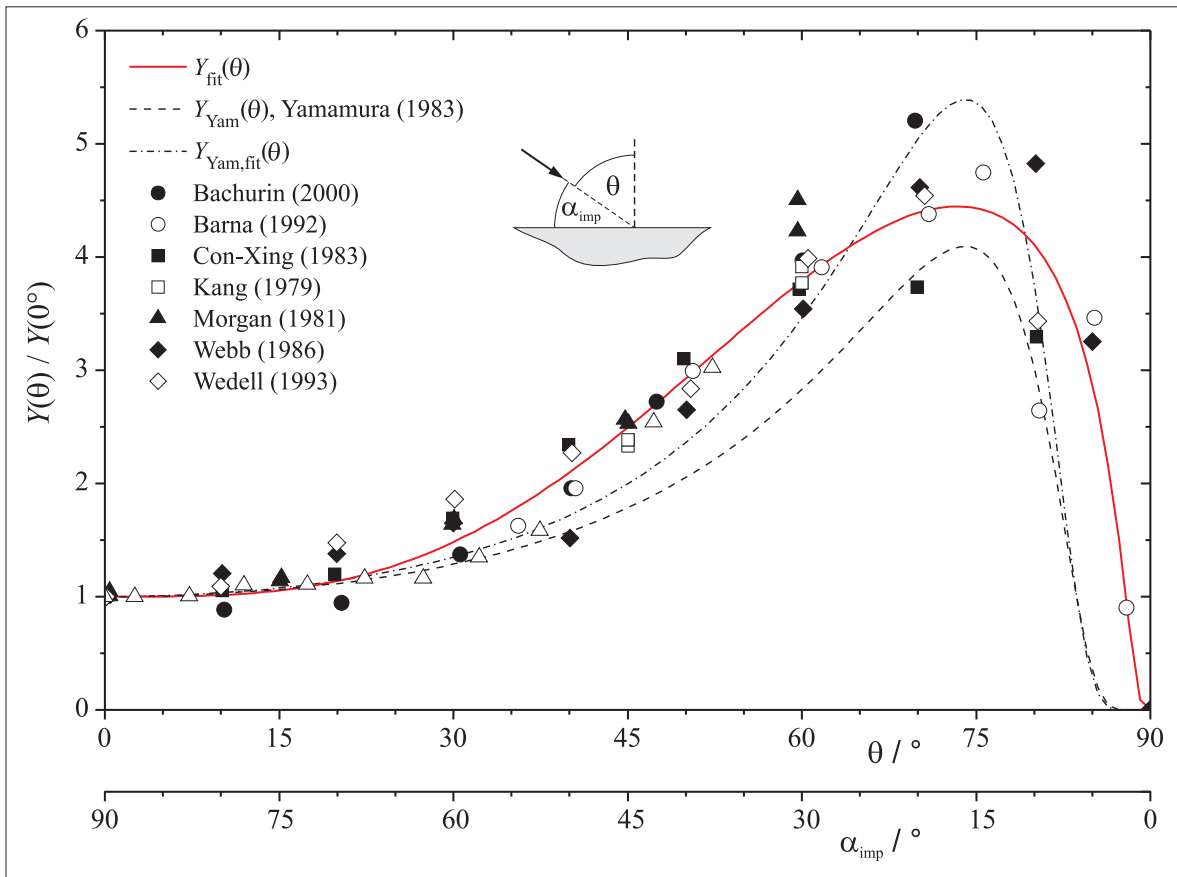


Figure 2.2.: Compilation of experimental data [86,90–96] of the Si sputtering yield $Y(\theta)$ (Ar^+ -ion impact), normalized to $Y(0^\circ)$, as a function of the incident angle θ (angle between impacting ions and surface normal) and $\alpha_{\text{imp}} = 90^\circ - \theta$.

As can be seen in **Figure 2.2**, the sputtering yield increases continuously up to a maximum at about $\theta = 73^\circ$, which is followed by a strong decrease. Finally, the sputtering yield levels off to zero at glancing incident (90°). Furthermore, two curves (dashed lines) are displayed, matching the data only to a limited extent. Both are based on Yama-

mura's empirical description [97] of the angular dependency of the normalized sputtering yield:

$$Y_{\text{Yam}}(\theta) = \frac{1}{\cos(\theta)^f} \exp(-\Sigma(\frac{1}{\cos \theta} - 1)) \quad (2.1)$$

Two sets of parameters were used to calculate the curves:

- $f = 2.485$, $\Sigma = 0.682$ were proposed by Yamamura and co-workers for 3 keV Ar⁺-ion impact on Si [97]. Both values were derived from extrapolation (in comparison to other materials) and are not directly based on Ar⁺-ion sputtering experiments on Si.
- fit of **Equation 2.1** to the summarized literature data (see **Figure 2.2**) results in $f_{\text{fit}} = 2.97 \pm 0.17$, $\Sigma_{\text{fit}} = 0.81 \pm 0.06$ ($\chi_{\text{red}}^2 = 0.45$).

To minimize the discrepancies between model and experiment, a modified analytical expression for the normalized sputtering yield

$$Y_{\text{fit}}(\theta) = (1 + a \sin^b \theta) \exp\left(-c \cdot \left(\frac{1}{\cos \theta} - 1\right)\right) \quad (2.2)$$

was used for the MC simulations in this work. A better fit of the experimental data with $a = 4.92 \pm 0.24$, $b = 3.30 \pm 0.20$, and $c = 0.068 \pm 0.008$ can be obtained with **Equation 2.2** ($\chi_{\text{red}}^2 = 0.11$). The result is plotted as red solid line.

In this study the angle $\alpha_{\text{imp}} = 90^\circ - \theta$, i.e. the angle between the surface and incident ion beam, is used (see inset in **Figure 2.2**). For a completely flat sample surface, α_{imp} equals α_{sputt} , which is adjusted at the ion-milling device.

For realistic modeling of the ion-milling behavior of Si cross-section samples, the properties of the epoxy layer have to be considered besides the bulk properties of the silicon halves. Unfortunately, no data for the angular dependency of the Ar⁺-ion sputtering yield on the epoxy used, or comparable hydrocarbons are available in literature. From experimental experience - epoxy is often completely removed when the final sample thickness is reached (despite the fact, that hydrocarbons may form a graphitic protection layer during ion milling, because it tends to coke) - a higher sputtering yield is assumed. This is implemented in the simulation by a sputtering yield which is $m = 1.5$ times higher than that of Si (same angular dependency). The influence of this arbitrary factor m on the final simulated cross-section profiles as well as the explanation for the chosen value is discussed in detail in **Section 2.3**. It is noted that a variation of the factor does not have a drastic influence on the cross-section profiles as long as it is not set to 1 (equal sputtering yield of the epoxy and the Si).

Simulation of cross-section sample profiles

In commercial ion mills usually two ion guns for simultaneous thinning of top and bottom sample side are used. In contrast to this arrangement, only impacting ions from one ion source are modeled in the MC simulations. This ion source is situated above one of the two halves (half B) of the cross-section sample (sputtering angle α_{sputt}). Thus, the evolution of only one of the two sample surfaces (top) is simulated. The final sample profiles presented in the following are obtained by mirroring the simulated topography (sample surface) on the horizontal center line. This simplification is only valid for negligibly small holes at the final stage of ion milling, as long as impacting ions do not hit the thinnest regions of the opposed half directly. Double-sector milling (milling of both halves simultaneously) is achieved by mirroring the simulated topography vertically after 300000 ion-collision events, whereas sample orientation was kept static relative to the impacting projectiles for single-sector milling.

For both cases a two-dimensional model was generated that represents a cut through the cross-section sample perpendicular to the epoxy as indicated by a red line in **Figure 2.1**. It consists of an epoxy layer in between two Si halves named A and B. Starting point for each simulation was a completely flat surface. Factors like crystalline orientation, ion reflection, redeposition of sputtered material, density variations of sample and epoxy, variations of incident beam angle due to sector rotation, and surface amorphization of the sample during ion milling were not taken into account in the simulation. From the physical point of view one would try to model the lateral expansion of a sampling point of the surface as small as the original interaction area of a single impacting ion. Since this area is only of the order of a few nanometer the whole model would consist of orders of magnitude more sampling points than used in the simulations. This would increase the computing time immensely. Consequently, only a limited number of $n = 400$ sampling points was chosen; each sampling point represents a finite area of the sample surface. The local properties of the sample surface are given in a matrix. Each sampling point i at the position x_i stores parameters like local height h_i , projected coordinate l_i (seen from the ion source, measured with respect to h_1), and surface inclination angle α_i (see **Figure 2.3**). All local angles are measured with respect to the original surface. Positive values indicate an ascending surface, while negative values denote a descending surface. For each collision event several calculation steps were performed to simulate the change in local height of the respective sampling point (cf. **Figure 2.3a**). First, a projectile (ion) is generated at a random position p between 0 and the maximum projected coordinate l_{max} . The probability for the generation at position p is uniformly distributed corresponding to an assumed constant ion-current density. This can be expected in the center of a TEM sample due to the small sputtering angle and, thus, wide spread ion beam on the surface. Its impact position, i.e. sampling point on the surface, is determined as the smallest index i where $l_i > p$. The height h_i of the corresponding sampling point is reduced proportionally to the sputtering yield according to the local impact angle $\alpha_{i,\text{imp}} = \alpha_{\text{sputt}} + \alpha_i$. To adjust the local removal of matter (sputtering yield) to the initially chosen sample height of 100 ul (unit of length) a proportionality factor $k = 0.00001$ is introduced.

The shape of the obtained cross-sectional profiles, either wedge-shaped or plane parallel, is independent of that proportionality factor in a large range. However, the roughness of the modeled surfaces depends slightly on it. The chosen value is a compromise between calculation time (number of events necessary for a sufficient removal of material) and surface roughness. Since the local roughness of common Ar⁺-ion milled TEM samples is small in comparison to their coarse cross-sectional profile, the value $k = 0.00001$ is justified. Only large values (> 0.1) lead to implausible steps and thus to an extreme local surface roughness which have never been observed in ion-milling experiments. As mentioned before, the roughness on the atomic scale is not investigated here.

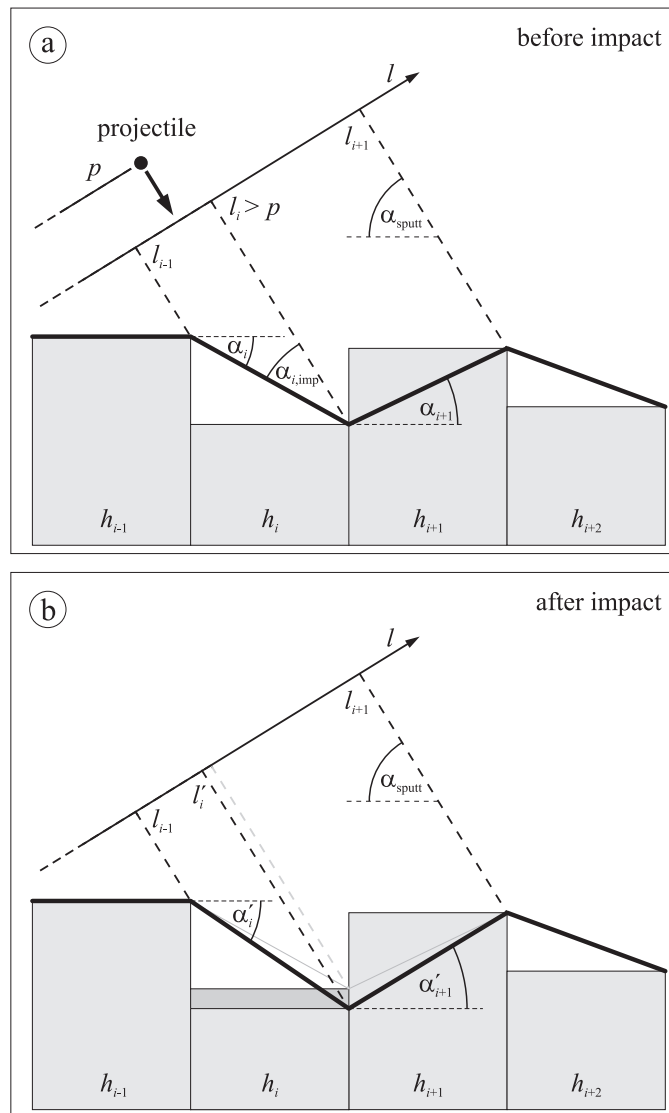


Figure 2.3.: Schematic illustration of the geometry (sampling point properties) used in the MC simulation a) before and b) after the impact of a projectile.

Finally, the surface inclination angles α'_i , α'_{i+1} , and the new projected coordinate l'_i are recalculated for the next iteration step (see **Figure 2.3b**). The coordinate l_{i+1} is not affected by this step because h_{i+1} is not changed. To simulate the topographical evolution of a sample profile (see below) during Ar^+ -ion milling several millions of such collision events were performed.

Three different setups for ion milling of TEM cross-section samples are discussed in the following, double-sector milling at the sputtering angles α_{sputt} of 4° and 10° , and single-sector milling at $\alpha_{\text{sputt}} = 4^\circ$. **Figure 2.4** and **Figure 2.5** show the simulated sample profiles (gray) in units of length (ul) as well as the temporal evolution of the top surface (faint lines) in equidistant time intervals (in each subfigure from top to bottom). Each interval corresponds to 7.2×10^5 projectiles. The direction of the incident Ar^+ -ion beam is marked in the subfigures by red and blue arrows. According to **Figure 2.4**, both double-sector milling simulations start with the formation of a small trench at the sample interface due to the higher sputtering yield of the epoxy. The impact angle and, thus, the sputtering rate (cf. **Figure 2.2**) is much higher at the uncovered edges of the silicon halves than at the flat surfaces of the sample. This leads to a broadening of the trench and thus to the formation of plane sidewalls with opposed but constant slopes, i.e. a wedge-shaped profile (wedge angle β). Depending on the sputtering angle the resulting wedge angles are $\beta_{\text{DS10,sim}} = 22.3^\circ$ ($\alpha_{\text{sputt}} = 10^\circ$, **Figure 2.4a**) and $\beta_{\text{DS4,sim}} = 7.1^\circ$ ($\alpha_{\text{sputt}} = 4^\circ$, **Figure 2.4b**), respectively. With increasing number of collision events, the width of the trench is broadened continuously whereas the slopes of the sidewalls of the Si halves remain constant. The broadening of the trench is enhanced with decreasing sputtering angle. In contrast to the double-sector milling simulations, the simulation of the single-sector ion milling shows a completely different behavior (cf. **Figure 2.5**). Again, milling of the epoxy proceeds faster than that of the silicon. However, only the edge of the ion-beam-facing side is exposed to the ion beam. This is side A in the first part, and side B in the second part of the simulation. In the first part of the simulation, the epoxy remains in the shadow of Si half B with a constantly inclined surface (**Figure 2.5**, dashed line, $-10 \text{ ul} < x < 10 \text{ ul}$). Since the removal of material at the uncovered edge of side A is much higher compared to the bulk of side B (angular dependency of sputtering yield) the edge is smoothed and repelled into the material on the surface of Si half A, leaving an almost plane surface behind. This is associated with formation of a topographic step between sample halves A and B as indicated by a dashed black line in **Figure 2.5**. The height of this step remains constant in time, due to the similar inclination of the surfaces of A and B next to the epoxy. It only depends on the width of the epoxy between the sample halves A and B as well as on the sputtering angle of the incident beam. Since the milling rate of the plane surfaces is limited by the small sputtering angle, the sample topography is horizontally mirrored (on the epoxy plane) after 10 time steps (B facing active ion gun) corresponding to an azimuthal rotation of the sample by 180° in the ion mill. As it is recognizable in the second part of the simulation (**Figure 2.5**, part below the dashed line), strongly enhanced sputtering immediately starts at side B. This again leads to the formation of a plane plateau on the formerly thicker sample half B, which lies below the previous

plateau of half A. This procedure - milling the two sample halves alternately - turned out to preserve plane parallel surfaces even if the sample is flipped as it is visualized in **Figure 2.5**. However, the overall removal of material and, thus, the thinning rate are smaller compared to double-sector thinning as indicated by the thickness evolution in the simulations (cf. **Figure 2.4b** and **Figure 2.5**).

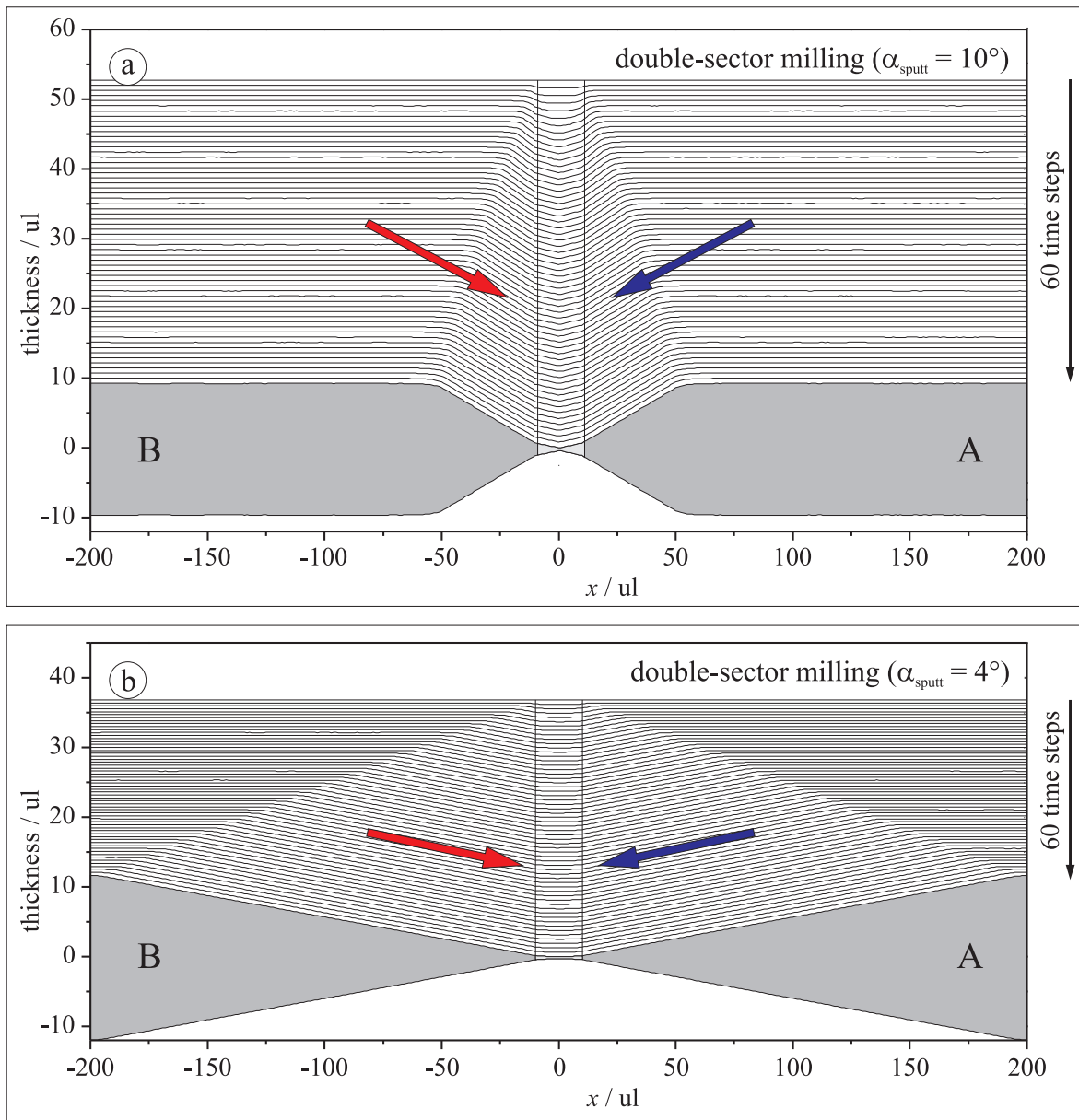


Figure 2.4.: Monte-Carlo simulations of cross-section sample profiles in units of length (ul) during Ar^+ -ion milling in the double-sector mode at a) 10° and b) 4° . The Si halves (A, B) are dark gray, the epoxy is light gray.

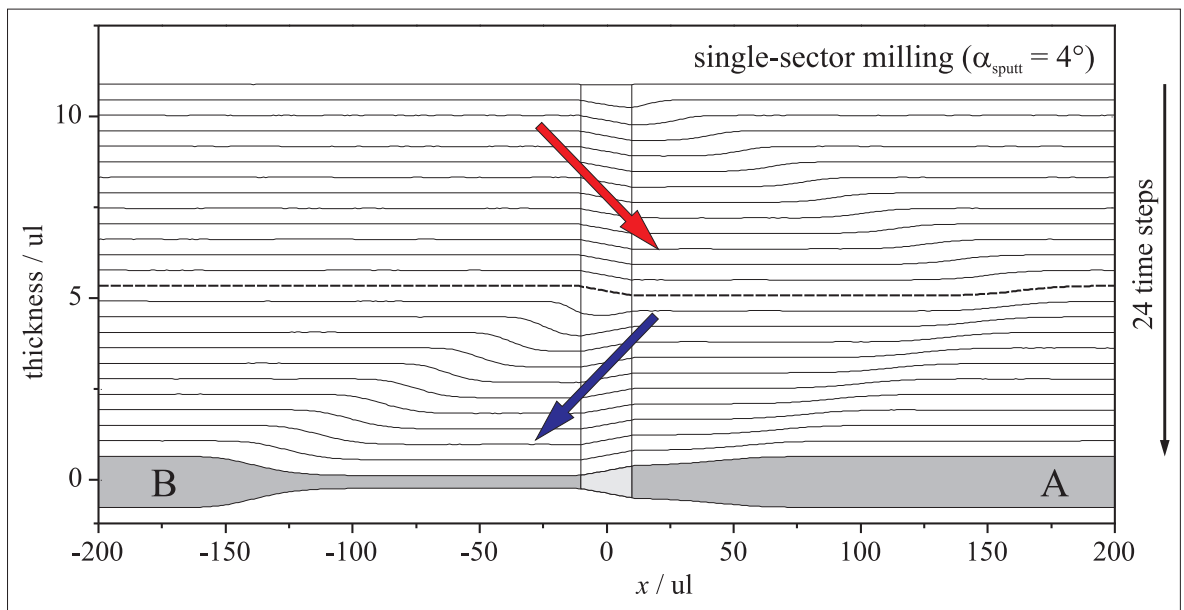


Figure 2.5.: MC simulations of cross-section sample profile in units of length (ul) during single-sector Ar^+ -milling at $\alpha_{\text{sputt}} = 4^\circ$. The Si halves (A, B) are dark gray, the epoxy is light gray. The dashed line indicates the change of the impact direction of the Ar-ions on the surface, corresponding to a azimuthal rotation by 180° of the sample.

2.2.3. Preparation and ion milling of Si cross-section samples

Standard (100) Si wafers were used to prepare cross-section samples to verify the simulated profiles by experiments. Final samples were orientated along the $[1\ 1\ 0]$ -zone axis. For this purpose, a stack of four Si pieces were glued together using Gatan G-1 epoxy (curing on a hot plate at $T = 100\text{ }^\circ\text{C}$ until the epoxy changed its color). The obtained sandwich was cut into slices (thickness $300\ \mu\text{m}$) using a precision diamond-wire saw (Well Drahtsägen, Mannheim, Germany). Discs were cut using an ultrasonic disk cutter (Gatan, Model 601). The discs were mechanically ground to a final thickness of about $80\ \mu\text{m}$. Both sample sides were then dimple ground with a $15\ \text{mm}$ brass wheel with $3\ \mu\text{m}$ diamond paste. Each side was consecutively felt-polished using 3 , 1 and $0.25\ \mu\text{m}$ diamond paste, until a final thickness of $4\ \mu\text{m}$ to $5\ \mu\text{m}$ was reached in the center of the TEM cross-section sample. In this stage, the silicon appears reddish-orange translucent under back-illumination [98]. After the mechanical thinning, the samples were ion milled using a commercial Gatan PIPS. This milling system consists of two rare-earth Penning-type ions guns (PIGs). The maximal sputtering angle for both ion guns is $+10^\circ$ (top) and -10° (bottom). Electronic ion-beam modulation facilitates automated deactivation of the ion guns each time the ion beam leaves the fixed sector of $\pm 10^\circ$ perpendicular to the epoxy of the cross-section sample. The acceleration energy of both ion guns was set to $3\ \text{keV}$. The gas flow was used to regulate the beam current per ion source to 90% of its maximum resulting in a beam current of about $25\ \mu\text{A}$.

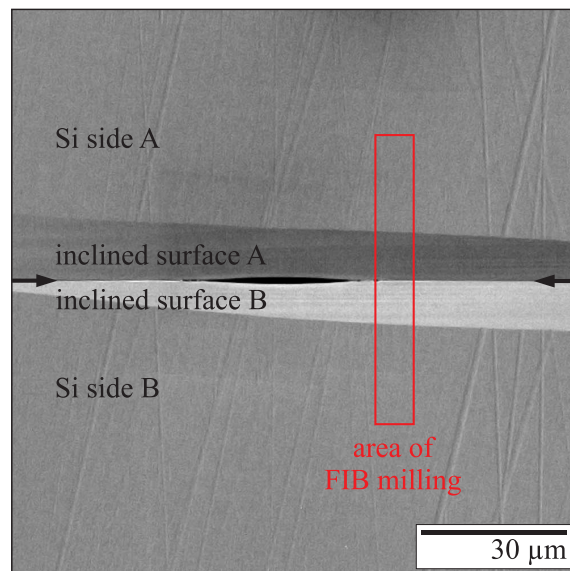


Figure 2.6.: SEM image (secondary-electron imaging) of the TEM silicon cross-section sample milled in double-sector mode at 4° (DS4). The arrows mark the central epoxy line. The red rectangle indicates the region close to the hole where the FIB-cutting was performed to evaluate the final cross-sectional profile.

sample	DS10	DS4	SS4
sector selection	double-sector	double-sector	single-sector
sputtering angle α_{sputt}	$\pm 10^\circ$	$\pm 4^\circ$	$\pm 4^\circ$
Ar ⁺ -ion energy	3 keV	3 keV	3 keV
rotation speed in the milling sector	2.5 rpm	2.5 rpm	2.5 rpm
MC simulated			
wedge-angle β_{sim}	22.3°	7.1°	0°
experimental			
wedge-angle $\beta_{\text{exp,FIB}}$	17.7°	11.9°	$\approx 0^\circ$
wedge-angle $\beta_{\text{exp,TEM}}$	19.2°	11.8°	$\approx 0^\circ$ (not measurable)

Table 2.1.: Ion-milling parameters, MC-simulated and experimental determined wedge-angles of Si cross-section samples.

To compare the sample profiles after Ar⁺-ion milling with the simulations (**Figure 2.4** and **Figure 2.5**), the same sputtering angles and selection of active sectors (single-sector/double-sector milling) as in the simulations were applied. The milling parameters and sample labels are summarized in **Table 2.1**.

Figure 2.6 shows a scanning electron microscopy (SEM) image of DS4 after ion milling (secondary electron (SE) imaging). The epoxy line between both Si halves (marked by black arrows in **Figure 2.6**) is oriented horizontally in the center of the picture. Next to the small lenticular hole, which extends about 30 μm along the interface, the thinned (wedge-shaped) regions along the epoxy line are visible by showing bright and dark gray contrast. This contrast results from the wedge shape of the cross-sectional profile and is due to the inclination of the surfaces with respect to the Everhart-Thornley detector used for SE imaging. Due to that topographical contrast, opposing inclined Si surfaces show darker and brighter contrast, respectively. Scratches originating from mechanical polishing were broadened during ion milling. Due to the higher sputtering yield of the epoxy compared to the silicon, both edges of the silicon sandwich were exposed to the ion beam instantaneously during double-sector ion milling. This fact led to a locally increased impact angle and, thus, to an increase of the sputtering rate (cf. **Figure 2.2**) along the edges. As predicted by the simulations (**Figure 2.4b**), a wedge-shaped sample profile with constant slope is formed. Increasing the sputtering angle to 10° (DS10) decreases the width of the central thinned area with wedge shape, as predicted by the simulation. As will be shown later, this is explained by a significantly larger wedge angle. Altering the milling conditions from double-sector to single-sector milling drastically changes the milling behavior and, thus, the final topography. This is also in good consistence with the simulations. In contrast to DS4 and DS10, SS4 did not show the formation of a trench with symmetric side walls. The ion-gun-facing side of the sample

is preferentially etched as suggested by the simulations. With increasing milling time the topographical step was driven into the bulk (away from the epoxy interface), leaving a thinner and almost flat region behind. The surfaces of this region are parallel to the initial sample surfaces. Hence, the ROI of this sample half was protected from ion milling by shadowing (cf. **Figure 2.5**). The small inclination angles of the surfaces were too small to utilize any topographical contrast for SEM imaging. The sputtering on the plane sample surfaces close to the epoxy line is strongly limited by the small sputtering angle $\alpha_{\text{sputt}} = 4^\circ$ (cf. **Figure 2.2**). It is therefore necessary to flip the sample by 180° after the edge is driven away several μm from the epoxy line. As a result, the opposite sample side is thinned by driving a new step back from the epoxy. Depending on the initial sample thickness, this procedure of flipping the sample may become necessary several times. For the initial sample thickness and parameters used it was sufficient to flip the sample once (one time milling each half of the sample).

To confirm the simulated wedge angles and thickness profiles, two different methods were applied to evaluate the prepared samples:

- analyzing thickness contours at defined imaging conditions (known imaging vector)
- direct imaging of the profile by FIB cutting.

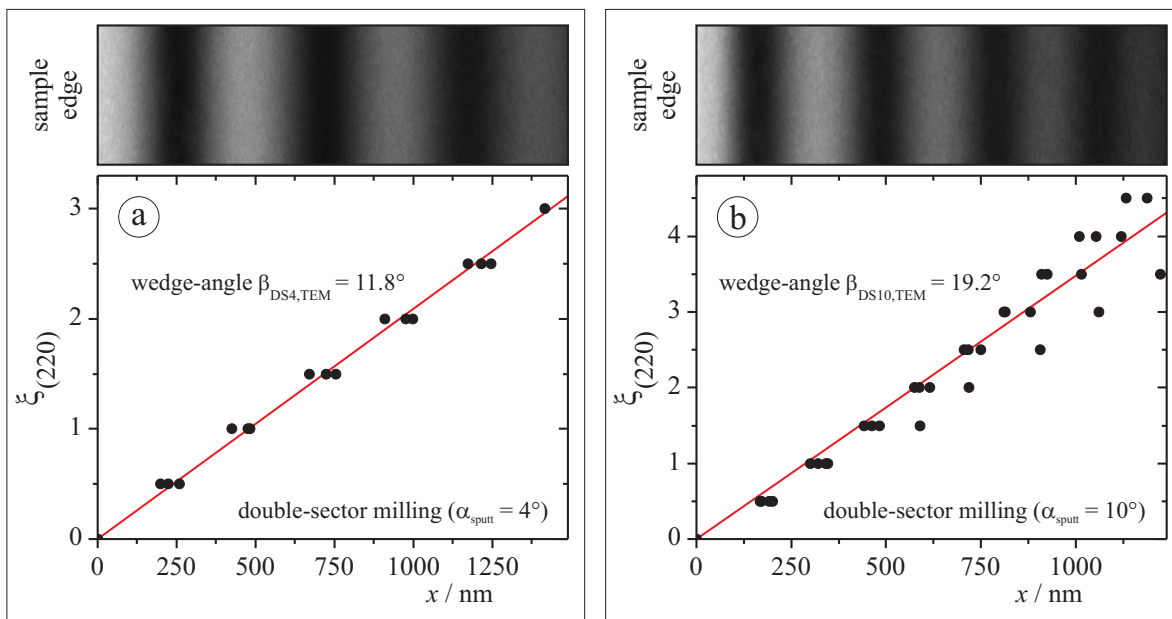


Figure 2.7.: Bright-field images using $\mathbf{g}_{(220)}$ as imaging vector and evaluated thickness profile of silicon cross-section samples of a) DS4 and b) DS10. Graph and micrographs are scaled equally.

Figure 2.7 shows TEM bright-field micrographs of the Si cross-section samples DS4 (see **Figure 2.7a**) and DS10 (see **Figure 2.7b**) acquired in $\mathbf{g}_{(220)}$ two-beam condition.

The equidistant thickness contours indicate a linearly increasing thickness with increasing distance to the sample edge. The imaging condition corresponds to an extinction length of $\xi_{(220)} = 99 \text{ nm}$ [99]. Evaluation of the thickness contours at several positions along the sample yields wedge angles of $\beta_{\text{DS4,TEM}} = 11.8^\circ$ for DS4 and $\beta_{\text{DS10,TEM}} = 19.2^\circ$ for DS10. The wedge angle for the sample SS4 was not measurable, because thickness contours were not visible within the homogeneously thinned area.

To confirm the TEM-evaluated wedge angles, cuts perpendicular to the epoxy line were prepared in the vicinity of the hole by means of focused ion beam (FIB) milling using a FEI Strata 400S. A representative region for DS4 is marked by a rectangle in **Figure 2.6**. Prior to FIB milling, the samples were covered by a layer of platinum to avoid surface damage induced by the Ga^+ -ion beam. Additionally, the mechanical stability of the electron transparent region especially of SS4 was enhanced by this procedure.

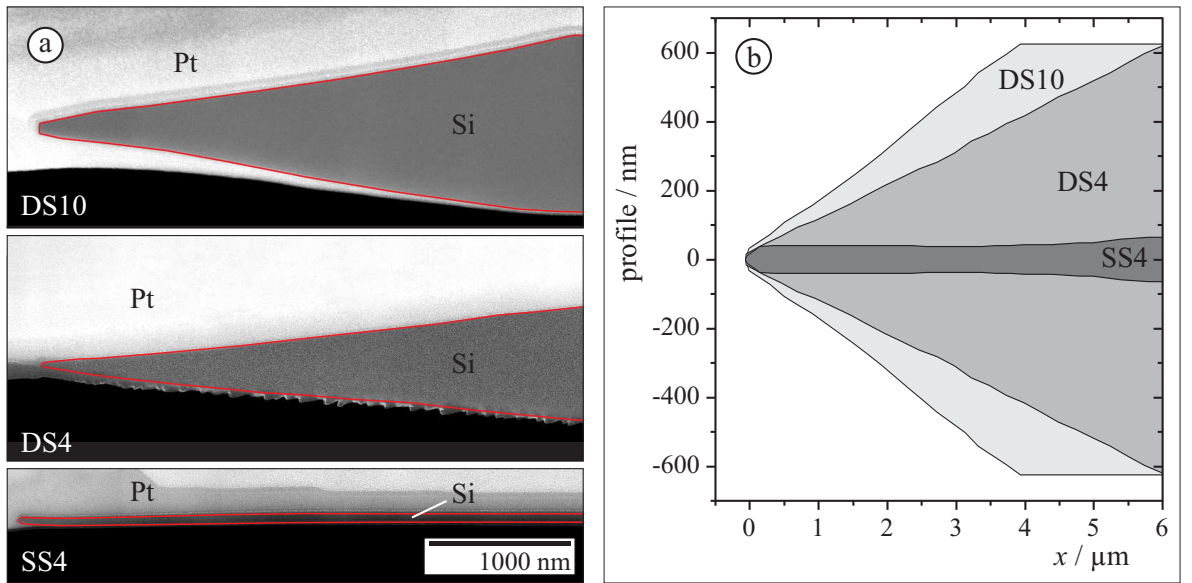


Figure 2.8.: a) SEM images of FIB cuts of Si cross-section samples (DS10, DS4, and SS4) and b) measured thickness profiles (ordinate inflated) of DS10 (light gray), DS4 (middle gray) and SS4 (dark gray).

Figure 2.8a shows SEM micrographs of cross-sectional profiles of DS10, DS4 and SS4. The deposited platinum exhibits two different intensities, which depends on the deposition technique. Electron-beam deposited platinum appears darker, whereas the use of the Ga^+ -ion beam for deposition led to a Pt layer with brighter contrast in the SEM images due to its higher density and thus higher SE yield. The determined sample profiles are summarized in **Figure 2.8b**.

The thickness for the two double-sector milled samples increases almost linearly with distance to the epoxy (left to right) and levels off in a flat plateau after $4 \mu\text{m}$ (DS10) and $10.5 \mu\text{m}$ (DS4), respectively. In contrast, SS4 shows almost constant thickness until it increases slightly in a distance of $4 \mu\text{m}$ from the interface. Behind this homo-

geneously thinned area the overall sample thickness increases negligibly with a wedge angle of $\beta_{\text{SS4}} = 1.3^\circ$, whereas DS4 and DS10 show wedge angles of $\beta_{\text{DS4,FIB}} = 11.9^\circ$ and $\beta_{\text{DS10,FIB}} = 17.7^\circ$, respectively.

2.2.4. Single-sector milling of other materials

The knowledge obtained by the combination of simulation and experimental evaluation was transferred to other materials to verify the capability of the single-sector ion-milling procedure. **Figure 2.9a** shows a TEM bright-field micrograph of an epitaxial EuTiO_3 thin film deposited on a single-crystalline SrTiO_3 substrate by pulsed laser deposition. After grinding and polishing (thickness $1\ \mu\text{m}$ to $2\ \mu\text{m}$, measured in the center) this sample was ion milled at 4° and $3.3\ \text{keV}$ Ar^+ -ion energy using the single-sector mode (sample turned two times by 180° during the complete milling procedure). The whole electron-transparent area extends a few $10\ \mu\text{m}$ along the EuTiO_3 thin film. The (002) two-beam imaging conditions correspond to a calculated extinction length of $\xi_{(002)} = 52\ \text{nm}$ [99]. From the observed contrast sequence of the thickness contours (white arrow in **Figure 2.9a** marks a hole in the SrTiO_3 substrate) it is concluded that a $1.2\ \mu\text{m}$ -broad region with a thickness of 0.5 to $1.5\ \xi_{(002)}$ along the epoxy has formed. Contrast variations within this region are attributed to local bending. Beyond this area the thickness rises rapidly (narrow, parallel thickness contours in **Figure 2.9a**).

A second example is presented in **Figure 2.9b**. The bright-field image shows a $130\ \text{nm}$ thick Sm_2O_3 thin film on polycrystalline CeO_2 , which contains a grain boundary within the substrate on the right-hand side of the image. The sample was milled at 4° ($3.7\ \text{keV}$ Ar^+ -ion energy) in the single-sector mode (sample turned two times by 180° during the complete milling procedure). The contrast is homogeneous apart from some bend contours, indicating that thickness variations are small within the depicted field of view. **Figure 2.10** illustrates the time evolution of the step position of this sample during single-sector ion milling in equidistant time steps ($\Delta t = 2\ \text{min}$). The sample is imaged in reflected light applying polarized-light microscopy in crossed polarization. For better visualization, micrographs are contrast inverted, thus pores appear as dark/black dots within the light gray CeO_2 substrate. The schematic geometry of the sample is given at the top of the diagram to clarify the geometry used. Furthermore, the actual sputtering direction as well as the step position is marked by a red arrow and red line, respectively. After $8\ \text{min}$ the sputtering direction is changed by 180° and the sputtering angle is slightly reduced to about 3.5° . Henceforth, the height of the step on sample side A decreases, as illustrated by the vanishing contrast of the step in the micrographs.

These two material-science examples underline the outstanding potential of the procedure of alternating single-sector Ar^+ -ion milling to prepare homogeneously thick TEM samples.

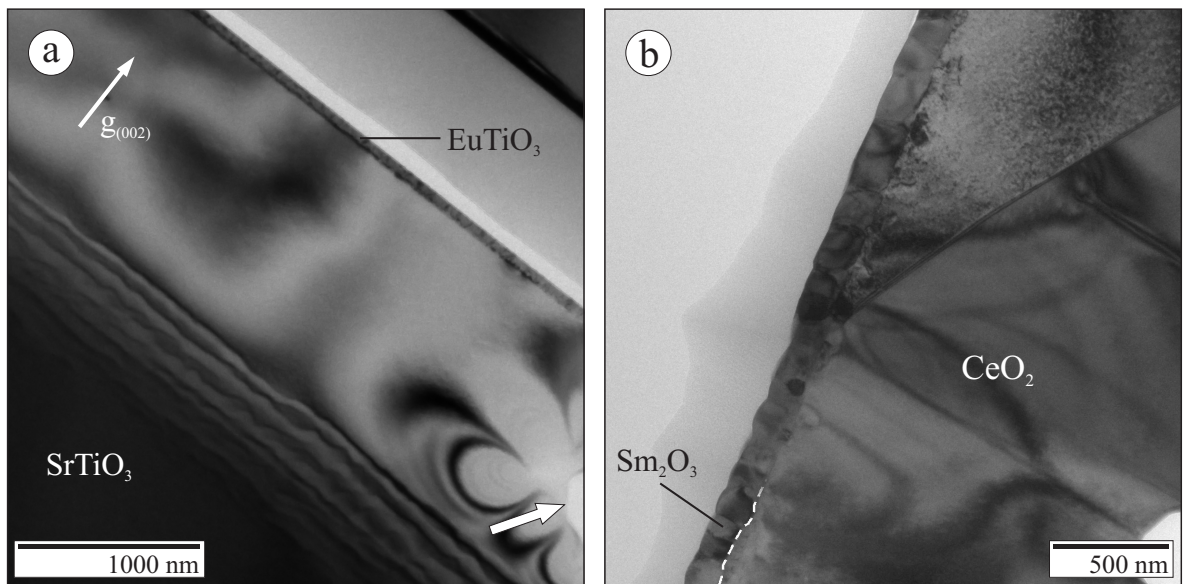


Figure 2.9.: TEM bright-field image of a) an epitaxial EuTiO_3 thin-film (50 nm) on single crystalline SrTiO_3 substrate recorded in (002) two-beam condition, b) TEM bright-field image of a Sm_2O_3 thin-film on poly-crystalline CeO_2 . Both samples were milled by alternating single-sector milling the two samples halves using an angle of 4° .

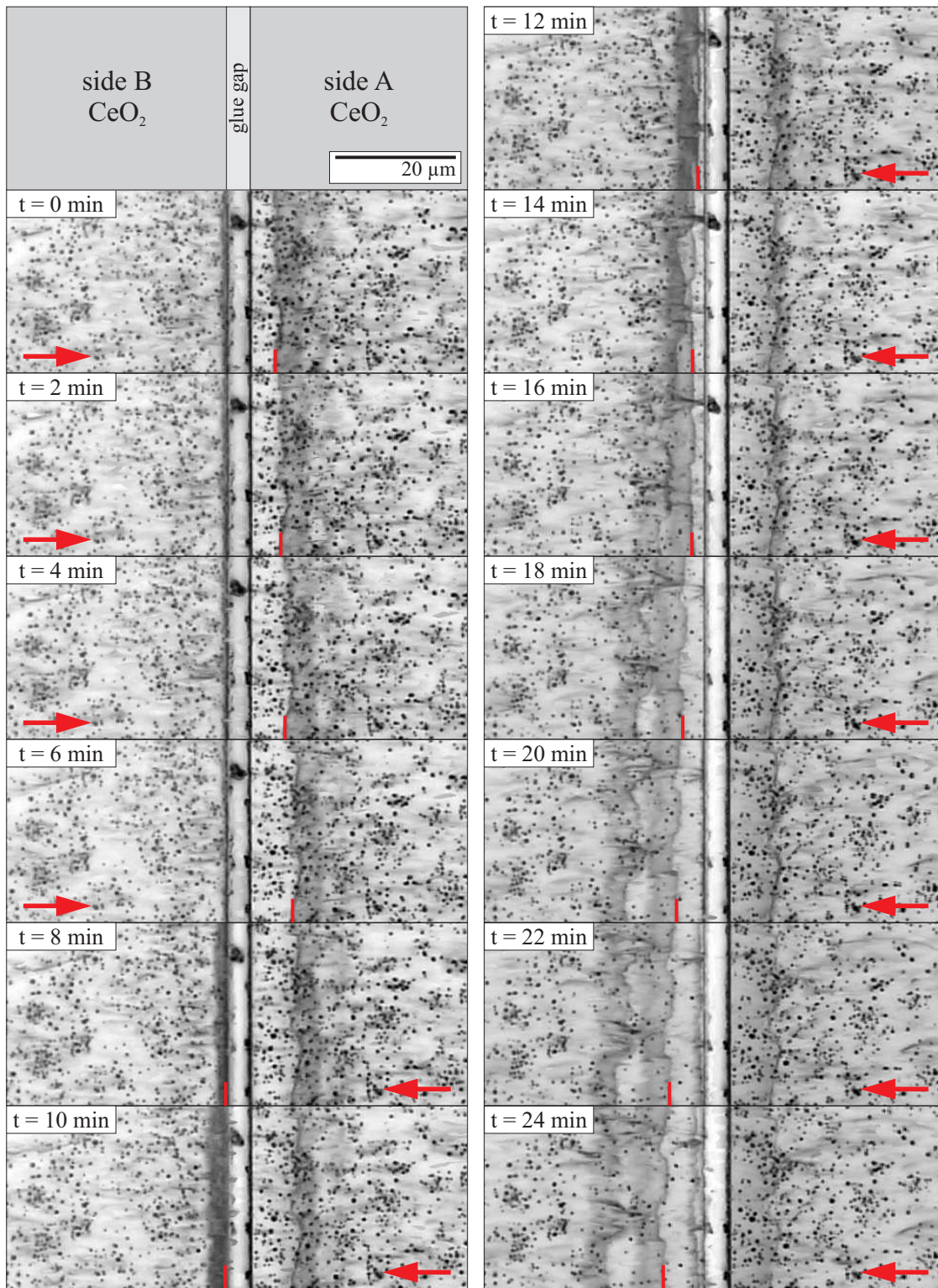


Figure 2.10.: Movement of formed step during single-sector ion milling of Sm₂O₃ thin-film on CeO₂ in equidistant time steps of 2 min. Sputtering direction is marked by a red arrow.

2.3. Discussion

2.3.1. Double-sector versus single-sector ion milling

Despite the simplicity of the model used for the MC simulations, the calculated sample profiles (see **Figure 2.4** and **2.5**) are qualitatively in good agreement with the experimentally determined ones (see **Figure 2.8**). The formation of wedge-shaped cross-sectional profiles during double-sector milling can be understood by the lack of shadowing of the sample edges of that sample half which faces the ion guns during ion milling. The trend of decreasing wedge angle with decreasing sputtering angle (**Figure 2.8**) is qualitatively explained by the increase of the impact angle of the incident ion beam on the ion-gun-facing surface of the opposing sample half. As a rough guide one can say that the resulting wedge angle is about twice the sputtering angle.

$$\beta \approx 2\alpha_{\text{sputt}}$$

Hence, this strategy of double-sector ion milling will fail in preparing large plane parallel, electron-transparent regions along the epoxy line of cross-section TEM samples. In contrast, simulations as well as ion-milling experiments clearly demonstrate that the suggested procedure of alternate milling the halves of a cross-section TEM sample (single-sector mode) enables the preparation of the required plane parallel regions. During single-sector milling, the sample half, which faces the active ion gun, is always protected (shadowed) by the sample half below the active gun. The simulations (**Figure 2.5**) corroborate this explanation by the reproduction of the formation of a topographical step between both sample halves during single-sector milling. These qualitative findings coincide with the conclusions drawn by Barna [86].

The suggested milling procedure for TEM cross-section samples exhibiting large, plane parallel regions of interest can be summarized as:

1. **Mechanical sample preparation** including sectioning, sandwich gluing (ceramic or brass cylinder), cutting as well as dimple grinding and polishing from both sides
2. **Single-sector Ar⁺-ion milling** until
 - a) ion-gun opposed sample side is near electron transparency
⇒ proceed with point 3
or
 - b) formed topography step is repelled several micrometer into material. Change the sputtering direction (azimuthal rotation by 180°) and return to point 2
3. **Final ion polishing**
 - a) flip sample by 180°
 - b) reduce ion energy and sputtering angle
 - c) start Ar⁺-ion polishing (ROI is always shadowed and protected by the substrate)

For better visualization, **Figure 2.11** shows a detailed flow chart of the suggested single-sector milling. For final ion polishing of the sample half of interest, it is recommended to mill that respective half downwards (self-shadowing). Using the example of **Figure 2.5** (final thinning of side B), downwards means that the ion guns are positioned above and below side B, facing side A. A small sputtering angle (1.5 to 3°), depending on the milling device used) assures slow and, thus, secure but homogeneous thinning of the thin ROI until the desired thickness is reached. A larger sputtering angle may be chosen to homogeneously thin the plane surfaces at higher rate. It is clear that the thin regions of side A (directly facing the ion guns) may be completely removed due to lack of shadowing by side B (dependent on sputtering angle and milling time).

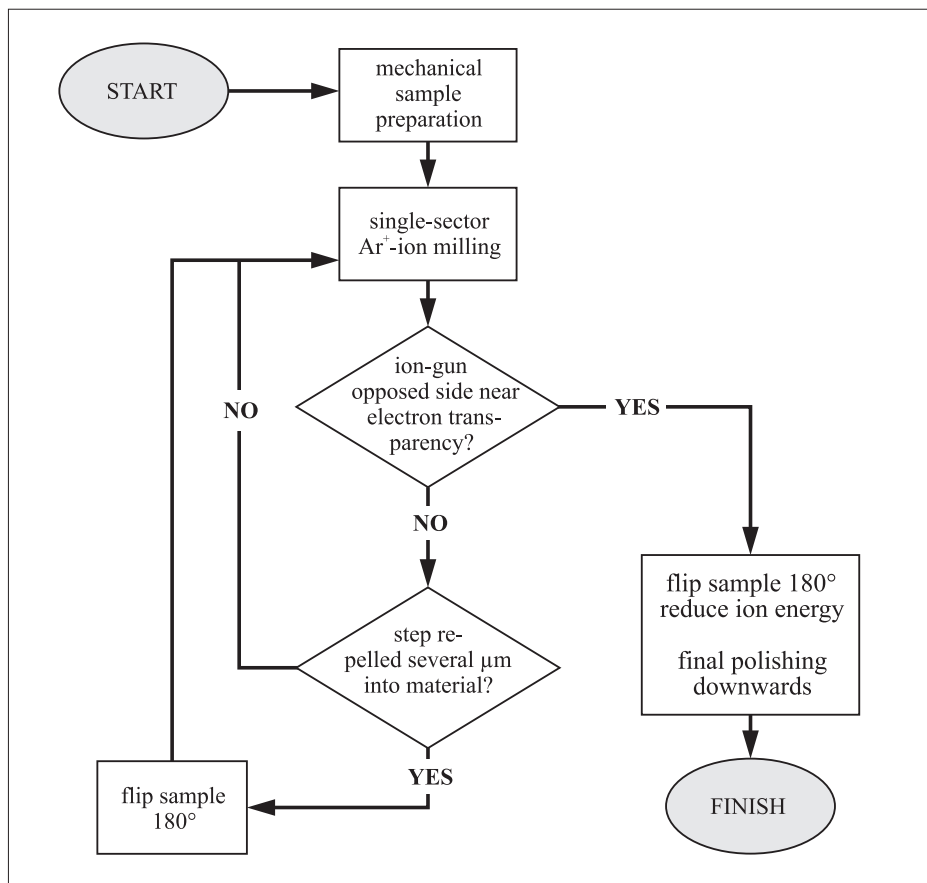


Figure 2.11.: Flow chart of suggested single-sector ion milling procedure.

2.3.2. Discrepancies between simulations and experiments

The deviations between simulated and experimentally obtained wedge angles (compare **Table 2.1**) are attributed to various reasons. Different aspects contributing to these deviations are discussed in the following.

As most important contribution, the imprecise description of the **angular dependency of the sputtering yield** at low sputtering angles was identified. Slight variations of that dependency especially at small sputtering angles $\alpha_{\text{sputt}} (< 10^\circ)$ at glancing incidence have a significant impact on the cross-sectional profiles obtained by simulations. In this angular range (important for ion milling) the experimental data are sparse and the theoretical predictions of the sputtering yield (**Figure 2.2**) differ most significantly. This particularly explains the strong deviation of the simulated and experimental wedge angle of DS4, while the experimental wedge angle of DS10 deviates less from the simulation. Due to the large variety of target-projectile combinations and target-atom binding energies, no universal description of the angular dependency of the sputtering yield is available. Seah et al. [100] concluded that Yamamura et al.'s [97] approach for the angular dependence of the sputtering yield is more accurate than the SRIM-derived (SRIM-The Stopping and Range of Ions in Matter; software package) dependence, which results in severe artifacts. Yamamura and coworkers provide a complete table set of Σ and f -values for a large variety of target-projectile combinations. A part of these parameters is obtained by fitting available experimental data on polycrystalline materials. Others, including the values for Si, are derived from extrapolation. However, **Figure 2.2** clearly demonstrates that Yamamura et al.'s approach does not describe the sputtering yield for Ar^+ -ions on silicon at glancing incidence satisfyingly. The experimental determination of $Y(\theta)$ requires flat surfaces and low doses, because surface roughness averages the angular dependence due to a distribution of microscopic incidence angles. Silicon and also other materials are known to form ripples which increase the surface roughness significantly at larger doses and/or longer sputtering time, respectively [101]. For small incidence angles α_{sputt} most published measurements of sputtering yields are affected by this problem.

Missing experimental data on the **sputtering yield of the epoxy used** is a drawback for the simulations. This value strongly influences the step height between sample halves A and B in the case of single-sector milling and the final wedge angle evolving during double-sector milling. From daily experience it is known, that the sputtering rate of pure epoxy at common ion energies is higher than for most non-organic materials (as considered in our simulations).

Figure 2.12 shows the dependency of the resulting wedge angle (double-sector milling) for $\alpha_{\text{sputt}} = 4^\circ$ and $\alpha_{\text{sputt}} = 10^\circ$ on the factor m between sputtering yield of Si and that of the epoxy (cf. **Section 2.2.2**). The values were obtained by repeating the simulations by varying the value m in the range of $1 \leq m \leq 2$ as well as one simulation without epoxy in between both halves. The extreme case of $m = 1$, where the sputtering yield of the epoxy equals that of Si, leads to a wedge angle of 0° (homogeneous thinning all over the surface). This is obvious as it represents the case of homogeneous Si with

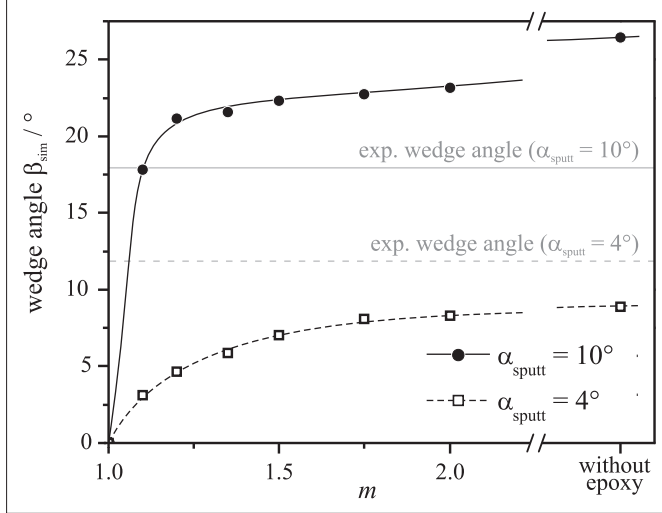


Figure 2.12.: MC-simulated wedge angles of double-sector ion-milled TEM samples in dependence of the scaling factor m .

flat surface. In general, any increase of this value leads to the formation of a wedge-shaped profile. Since a factor of $m = 1.5$ represents the experimental results in good approximation, it was chosen for the simulations. However, the resulting simulated wedge angle slightly underestimates ($\alpha_{\text{sputt}} = 4^\circ$) or overestimates ($\alpha_{\text{sputt}} = 10^\circ$) the experimental results, due to the mentioned reasons above. In order to tune (minimize) the final wedge angle (cf. **Figure 2.12**) of double-sector milled samples one may think about the possibility to reduce the sputtering yield of the epoxy by adding a specific amount of more resistant material, e.g. inorganic nanoparticles. However, the average sputter yield of the envisaged compound should be slightly higher than that of the surrounding material of interest to facilitate trench formation.

Furthermore, **geometrical aspects** contribute to the observed discrepancies. Ion channeling [22] along low-indexed crystallite directions may influence the sputtering yield for a specific incident sputtering angle on single crystals. To minimize this influence, the ion guns are commonly active while the sample is rotated/rocked azimuthally in a finite sector (for the Gatan PIPS this sector covers $\pm 30^\circ$) perpendicular to the epoxy (cf. **Figure 2.1**). In addition, it is well-known that rotating/rocking of inhomogeneous samples (e.g., with holes, or a mixture of different phases) during ion-milling at small sputtering angles minimizes anisotropic thinning and, thus, the formation of localized thickness variations due to inhomogeneous shadowing. These facts associated with sample rotation/rocking are not taken into account in the simulations. Rotating/rocking the sample leads on the one hand to an increasing projected distance between both sample halves (width of the epoxy) along the incident ion beam. Hence, it has a direct influence on the step height evolving between the two sides during single-sector milling. On the other hand, the absolute impact angle α_{imp} on inclined surfaces decreases with increasing semi-sector angle. **Figure 2.13a** depicts the dependence of impact angle α_{imp} in the center of the sputtering-sector ($\gamma_{\text{semi}} = 0^\circ$) and at maximum deflection of the semi-sector

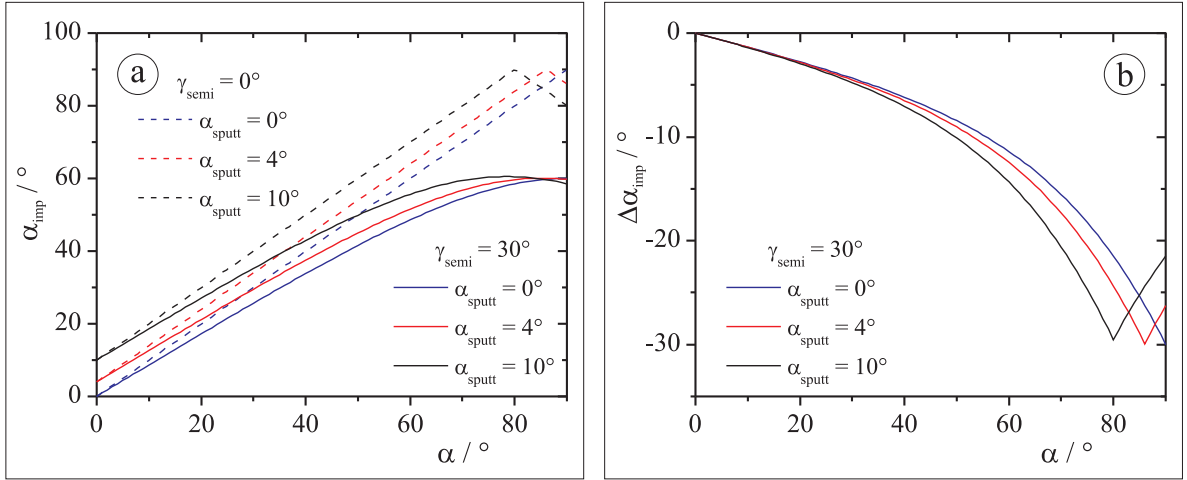


Figure 2.13.: a) Absolute projectile impact angle α_{imp} in the center of the sputtering-sector and at maximum semi-sector angle of $\gamma_{\text{semi}} = 30^\circ$ and b) relative change in the impact angle at maximum semi-sector angle ($\gamma_{\text{semi}} = 30^\circ$) and sputtering-angles of $\alpha_{\text{sputt}} = 0^\circ, 4^\circ$ and 10° as a function of the surface inclination α .

angle ($\gamma_{\text{semi}} = 30^\circ$) on the surface inclination α . The relative change of the impact angle $\Delta\alpha_{\text{imp}}$ at maximum sector elongation is shown in **Figure 2.13b**. This geometric effect leads, especially at strongly inclined surfaces and high sputtering angles, to a decrease of the absolute impact angle and, therewith, to a shift to higher sputtering rates. As a result, the sputtering yield of strongly inclined surfaces increases, resulting in a decreased sample wedge angle for larger sputtering angles, if sample rotation/rocking is not taken into account. This correlates with the two-dimensional simulations, for which too large wedge angles are observed at higher sputtering angles. **Energetic aspects** may contribute to the deviations as well. The installed ion guns in the PIPS are not mono-energetic as assumed in the simulations. In fact, there is a distinct maximum around the adjusted acceleration energy with moderate contributions to lower energies [102]. This fraction consists of non-ionized atoms accelerated by collision interactions within the beam. In addition, the direction of the incident Ar^+ -ions is not as precisely defined as assumed in the simulations (average sputtering angle α_{sputt}). Furthermore, **ion reflection** at the sample surface has not been considered in the simulations, which increases with decreasing sputtering angle (glancing incidence) and leads to a higher sputtering yield at protruding topography features.

Despite of all these shortcomings, the formation of homogeneously thinned areas during single-sector milling is well reproduced by the simulations.

2.3.3. Influence of the epoxy width

Milling Si cross-section samples with central epoxy layers of various thicknesses showed that the initial width of the epoxy plays an important role for the quality of the final TEM sample. Zinkle et al. [85] described this phenomenon geometrically. For a critical sample thickness of $t_{\text{crit}} = 2w \tan \alpha_{\text{sputt}}$ (w is the thickness of the epoxy layer between both sample halves) both sample surfaces are exposed to the ion beam after removing the epoxy completely. In other words, the width of the epoxy determines the removal of matter and, thus, the final thickness of the shadowed half of the TEM sample. Furthermore, Zinkle et al. [85] assumed that the inclination of the surface of the adhesive runs parallel to the incident ion beam whereas the MC simulations in this study showed that the inclination of that surface depends on the sputtering yield of the epoxy. It is obvious that, if the gap between both sample halves is too wide, a significant portion of the region of interest is sputtered away before the sample thickness reaches electron transparency. As a consequence, sandwiches with thin glue gaps ($< 1 \mu\text{m}$) are essential to preserve the interesting surface regions along the adhesive during double-sector ion milling. To overcome the disadvantage of thicker epoxy layers ($> 2 \mu\text{m}$), e.g., in the case of rough or structured sample surfaces, single-sector milling at low incident sputtering angles (1.5 to 3°) may be helpful. Milling at such small angles is also recommended by Helmersson and Sundgren [83] for preparation of samples consisting of materials with strongly differing sputtering yields. Hence, the problem of preferential thinning can be reduced.

3. Nanocrystalline $\text{La}_{0.6}\text{Sr}_{0.4}\text{CoO}_{3-\delta}$ thin-film cathodes

3.1. Introduction

Rising raw oil prices, increasing environmental pollution and ever-expanding energy needs lead to a change of thinking in our society. Environmental protection and sustainable utilization of energy sources gain more and more attention. Therefore, governmental and non-governmental organizations seek for a solution for present and future energy problems on an international level. Furthermore, increasing energy prices will push technology development in the sector of renewable energy sources as well as sustainable energy usage. As energy-conversion device, fuel cells with high efficiency and low or zero emissions have received significant attention in the past 20 years. They are a promising approach to replace combustion-based mobile and stationary electrical generators at all sizes and can contribute to reduce carbon dioxide emission.

Working principle of a solid-oxide fuel cell

A ceramic solid oxide fuel cell (SOFC) is an all solid-state energy conversion device that produces electricity by electrochemical combination of fuel and oxidant gases across an ionic conducting electrolyte. The working principle can be described as a galvanic cell, in which reagents and products of the redox reaction are continuously supplied and removed [103,104]. A simplified functional principle of an SOFC is schematically shown in **Figure 3.1**.

The chemical energy is provided in the form of fuel (hydrogen or hydrocarbons) on the anode side and oxidization gas (oxygen or air) on the cathode side. To prevent a direct combustion of the reactants, fuel and oxidant-gas compartments are separated by an oxygen-ion (O^{2-}) conducting, electrically insulating and gas-tight ceramic electrolyte membrane, consisting of Y-substituted zirconia (YSZ) or Gd-substituted ceria (CGO) [104,106,107]. The operation mechanism of the SOFC is based on the presence of a chemical potential gradient across the electrolyte due to the difference in oxygen partial pressures between cathode and anode. This chemical potential gradient is the driving force for oxygen-ion diffusion from the cathode through the solid electrolyte to the anode. Constant oxygen-ion diffusion is maintained by a continuous supply and removal of reagents and products.

Before oxygen ions are incorporated into the electrolyte material, a variety of reactions take place at the cathode side, including adsorption and dissociation of oxygen molecules into atoms and ionization of the oxygen atoms by collecting two electrons. In the case of

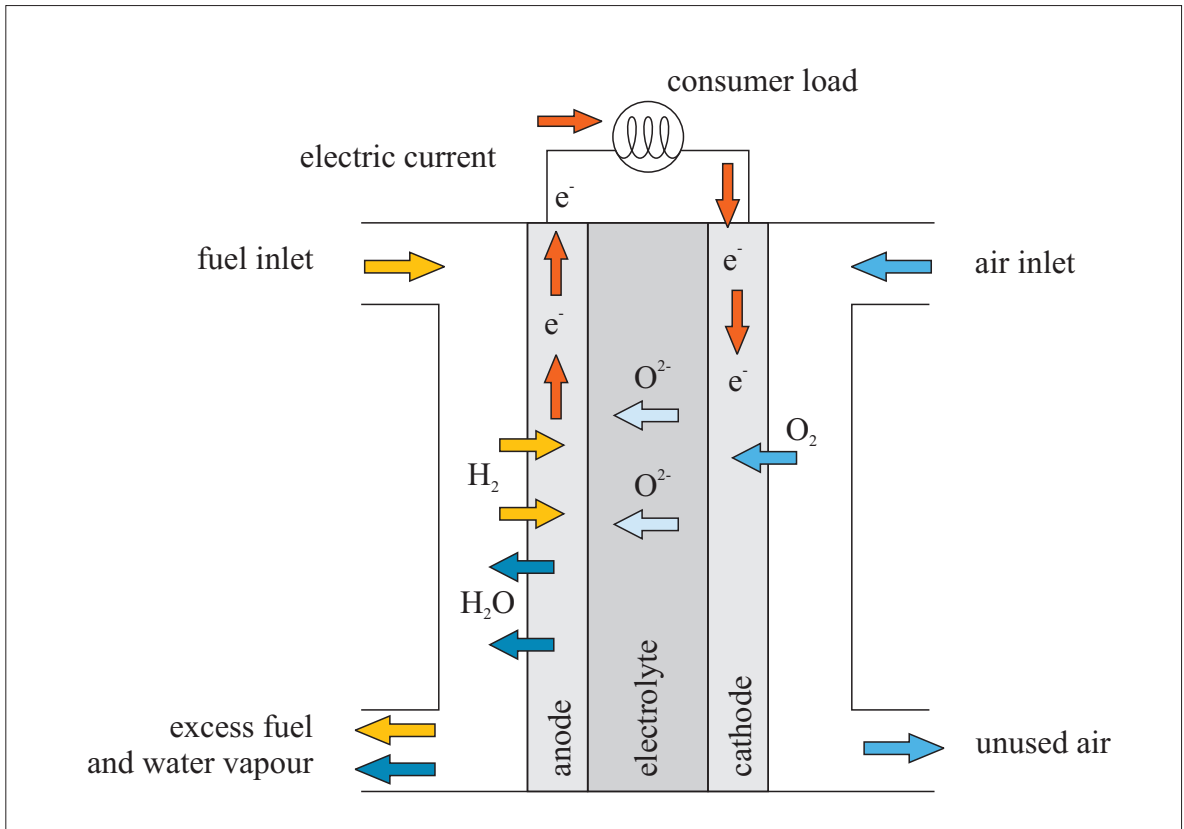
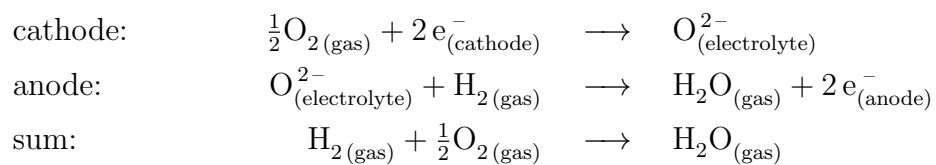


Figure 3.1.: Schematic function principle of an SOFC [105] (slightly modified).

materials with negligible ionic conductivity like $(\text{La},\text{Sr})\text{MnO}_{3-\delta}$ (LSM) this mechanism is restricted to the cathode-electrolyte-gas triple-phase boundaries (TPB). In contrast, this reduction takes place on the whole cathode surface for materials with mixed-ionic and electronic conducting (MIEC) properties like $(\text{La},\text{Sr})\text{CoO}_{3-\delta}$ (LSC) or $(\text{La},\text{Sr})(\text{Co},\text{Fe})\text{O}_{3-\delta}$ (LSCF). After migration through the electrolyte, the oxygen ions react with the fuel gas to water vapor (in case of hydrogen fuel) and/or carbon oxides (in case of hydrocarbon fuels) on the anode side.

If, for example, hydrogen is used as fuel gas, the electrochemical reactions at the cathode and anode can be summarized as follows:



The oxygen-ion transport results in electron depletion at the cathode and electron enrichment at the anode. Consequently, a potential difference between the electrodes is generated, forcing the electrons to flow through the external electric circuit and to perform electrical work.

In case of an open circuit and ideal cell, the Nernst voltage U_N arises between cathode and anode:

$$U_N = \frac{RT}{n_{\text{el}}F} \ln \sqrt{\frac{p_{\text{O}_2(\text{cath})}}{p_{\text{O}_2(\text{an})}}}$$

where R is the gas constant, T the absolute temperature, F the Faraday's constant, $n_{\text{el}} = 2$ the number of released electrons during the ionization process of one utilized fuel molecule and $p_{\text{O}_2(\text{cath})}$ and $p_{\text{O}_2(\text{an})}$ the oxygen partial pressures at cathode and anode, respectively. However, due to several internal irreversible loss mechanisms the cell voltage drops below the thermodynamically predicted Nernst voltage, if the fuel cell is loaded with an electric current.

$$U_{\text{load}} = U_N - j_{\text{load}} \cdot \sum_k ASR_k$$

with j_{load} being the load current density. The respective loss portions k are given by their respective area-specific resistance ASR .

Cathode materials for intermediate-temperature SOFC applications

Conventional SOFCs are commonly operated at 700–1000 °C. However, degradation effects like secondary-phase formation at the cathode-electrolyte interface [108] or cathode poisoning via Cr, which is evaporated from metallic interconnectors used in cell stacks [109], reduce the durability.

Hence, a major target in present SOFC research is the reduction of the operating temperature to an intermediate-temperature range of 500–700 °C, or lower. Especially for mobile applications like auxiliary power units [110, 111] this temperature regime is of great interest. Start up times can be drastically decreased if the operating temperature is lowered. Furthermore, cell degradation is expected to be reduced, thus resulting in an extended lifetime. Moreover, material costs for insulation, housing and interconnects of the fuel cell are reduced because a larger variety of suitable and considerably less expensive materials are available.

However, losses of the electrochemically active electrodes and electrolyte conductivity increase significantly at lower operating temperatures because ionic transport processes in the electrolyte and electrochemical reactions at the electrodes are thermally activated. One approach to face the challenges associated with lower operating temperatures is the application of thin-film electrolytes (thickness < 10 μm) [110, 112] in anode supported cells. They are capable to reduce significantly ohmic losses. The reduction of the polarization losses of the cathode is also still of intense research. Here, reduction of losses can be achieved by the application of materials with high electrochemical activity and optimized microstructure.

Based on the functional principle and requirements for application in an intermediate-temperature SOFC (IT-SOFC), the following properties can be deduced for the cathode material:

- good electronic and ionic conductivity
- large surface area due to a high amount on open porosity
- grain size in the nanometer regime
- stability under working conditions (high temperature and oxidizing atmosphere)
- chemical compatibility with the electrolyte (no interfacial reaction)
- thermal expansion coefficient compatible with that of the solid electrolyte

These requirements for highly sophisticated SOFC cathodes indicate that the cell performance strongly depends on the microstructure of the cathode as well as the cathode-electrolyte interface. Hence, nanoscaled thin-film cathodes with sufficient porosity are of substantial interest for development of intermediate-temperature SOFCs (IT-SOFCs). On the one hand, cathode oxygen reduction is facilitated with increasing porosity, which corresponds to an increased active inner surface. On the other hand, Tuller [113, 114] and Maier [115–121] pointed out that a substantial reduction of the mean grain size of ionic-conducting materials to the nanoscale may lead to an enhanced ionic conductivity due to grain-boundary charging effects. A promising material system for the intended temperature regime is $(\text{La,Sr})\text{CoO}_{3-\delta}$, a perovskite-type material possessing exceptional mixed ionic and electronic conducting properties.

Goal of this work and outline

The goal of the present work was the study of the microstructure (grain-size and porosity) and chemical composition of nanocrystalline $\text{La}_{1-x}\text{Sr}_x\text{CoO}_{3-\delta}$ films (nominal Sr-content of $x = 0.4$) on polycrystalline $\text{Gd}_{0.1}\text{Ce}_{0.9}\text{O}_{1.95}$ (CGO) electrolyte substrates. This electrolyte material exhibits good oxygen-ion conduction and in contrast to YSZ [108] does not react with the cathode material. Furthermore, the microstructural properties were correlated with the SOFC electrochemical performance. Transmission electron microscopy (TEM) combined with selected-area electron diffraction (SAED), energy-dispersive X-ray spectroscopy (EDXS) and scanning transmission electron microscopy (STEM) tomography was applied to study all relevant aspects of the prepared cathode films. The results contribute to the clarification of the origin of the extraordinary good electrochemical performance of nanoscaled $\text{La}_{0.6}\text{Sr}_{0.4}\text{CoO}_{3-\delta}$ thin-film cathodes that were studied by Hayd et al. [122].

3.2. Sample fabrication

The investigated samples were fabricated in cooperation with the *Fraunhofer-Institut für Silicatforschung* (ISC) in Würzburg and the *Institut für Werkstoffe der Elektrotechnik* (IWE) at the Karlsruhe Institute of Technology (KIT). Development and fine tuning of the coating solution for metal organic deposition of $\text{La}_{0.6}\text{Sr}_{0.4}\text{CoO}_{3-\delta}$ thin-films was performed by Dr. Uwe Guntow (ISC). Coating of the electrolyte substrates, pyrolysis and thermal annealing was performed in close collaboration with Jan Hayd (IWE). Comparative chemical analyses of the standard materials for quantitative X-ray spectroscopy were performed by Dr. Dirk Fuchs at the *Institut für Festkörperphysik* (KIT).

3.2.1. $\text{Ce}_{0.9}\text{Gd}_{0.1}\text{O}_{1.95}$ electrolyte substrates

Metal-organic deposition was used for fabrication of nanoscaled $\text{La}_{0.6}\text{Sr}_{0.4}\text{CoO}_{3-\delta}$ thin-film cathodes on Gd-substituted ceria oxide $\text{Ce}_{0.9}\text{Gd}_{0.1}\text{O}_{1.95}$ (CGO) electrolytes (diameter 25 mm, thickness 400 μm to 800 μm). The substrates were produced, ground and polished by Daiichi Kigenso Kagaku Kogyo Co., Ltd (Japan).

However, first results on as-received electrolytes showed formation of a high density of lattice defects within 160 nm beneath the surface due to mechanical stress during polishing. Furthermore, the surface of the CGO substrate contained scratches and pits resulting from single grains, which were pulled out during polishing (see **Figure 3.2a**). To prevent enhanced diffusion along dislocation cores or spurious effects on the electrochemical properties two different annealing setups were tested to heal out defects. Annealing at 900 °C for 24 h resulted in massive recrystallization of the electrolyte surface (compare secondary-electron image or TEM bright-field image in **Figure 3.2b**, recrystallized grain marked by white arrow). Slight contrast variations in near-surface areas indicate an incomplete healing of lattice defects. In contrast, the second tested annealing of an as-received electrolyte at 1300 °C for 3 h resulted in a defect-free surface, accompanied by an increase in surface roughness due to thermal etching of grain boundaries (see **Figure 3.2c**). Based on these preceding experimental results, all CGO electrolytes were subjected to an annealing at 1300 °C for 3 h to anneal surface defects.

3.2.2. $\text{La}_{0.6}\text{Sr}_{0.4}\text{CoO}_{3-\delta}$ thin-film cathodes

For the synthesis of the $\text{La}_{0.6}\text{Sr}_{0.4}\text{CoO}_{3-\delta}$ precursor, solid propionates of La, Sr, and Co were prepared separately. They were obtained by the reaction of $\text{La}_2(\text{CO}_3)_3$, $\text{Co}(\text{OH})_2$, and metallic Sr with propionic acid (in excess) in the presence of propionic acid anhydride. The metal-organic precursors were mixed together at room temperature according to the desired stoichiometry of $\text{La}_{0.6}\text{Sr}_{0.4}\text{CoO}_{3-\delta}$ and dissolved in propionic acid, resulting in a ready-to-use coating solution. The obtained stoichiometry was cross-checked by inductively coupled plasma-atomic emission spectroscopy (ICP-AES).

Top and bottom side of the CGO electrolytes were coated simultaneously by a computer-controlled single dip-coating process (inserting velocity $v_{\text{in}} = 11 \text{ cm min}^{-1}$, immersing time $t_{\text{hold}} = 10 \text{ s}$, withdraw rate of $v_{\text{out}} = 8 \text{ cm min}^{-1}$), followed by drying at room

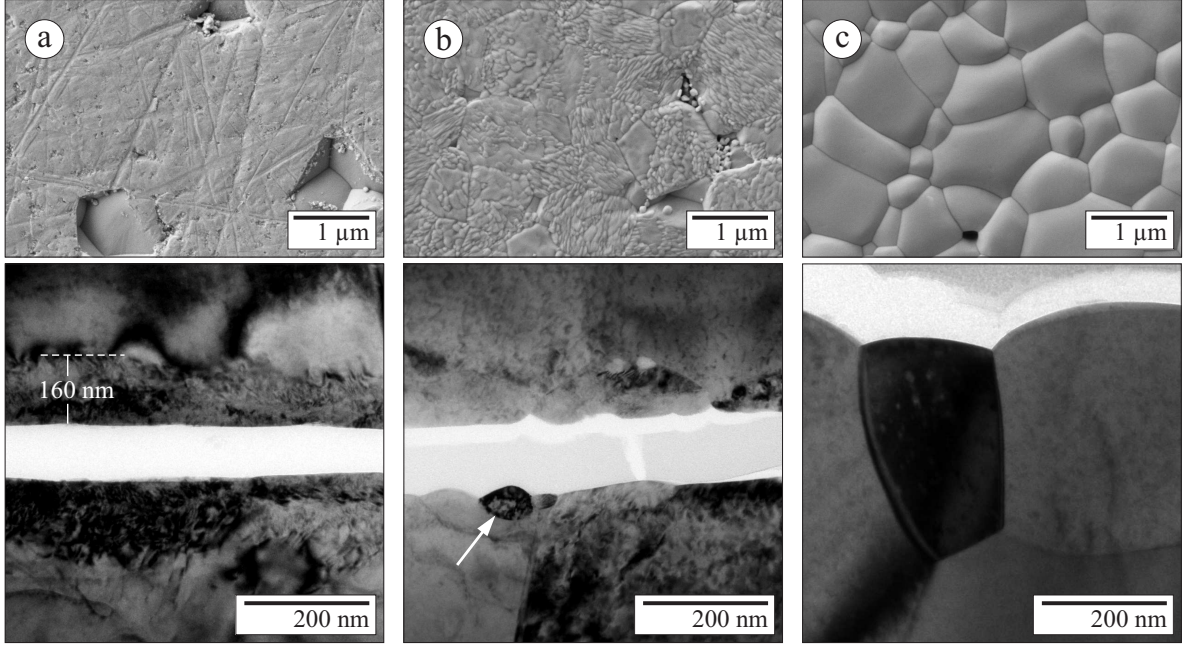


Figure 3.2.: Surface (top, SEM secondary-electron images by Jan Hayd, IWE, KIT) and cross-section (bottom, TEM bright-field images) of the electrolytes. a) as received, b) after annealing at 900 °C for 24 h and c) after annealing at 1300 °C for 3 h.

temperature for 5 min. Best coating results in terms of homogeneity and crack deficiency were obtained with a solution (kinematic viscosity of $\eta = 3.67 \times 10^{-6} \text{ m}^2 \text{ s}^{-1}$ at 20 °C) containing 10 mass % of the resulting oxide. In contrast to other coating techniques like pulsed-laser deposition or physical-vapor deposition, this coating technique is highly suitable for commercially mass production.

The film thickness achieved by dip coating is affected by numerous factors like withdraw rate v_{out} , sol viscosity η , gravitational acceleration g and sol density ρ . The final film thickness for Newtonian liquids [123] is described by

$$l = 0.8 \sqrt{\frac{\eta v_{\text{out}}}{\rho g}}.$$

If withdraw rate and viscosity are low, which is often the case for sol-gel film deposition, this equation is modified by the ratio of viscous drag to liquid-vapor surface tension γ_{lv} according to the relationship derived by Landau and Levich [124].

$$l = 0.94 \frac{(\eta v_{\text{out}})^{\frac{2}{3}}}{\gamma_{\text{lv}}^{\frac{1}{6}} (\rho g)^{\frac{1}{2}}}$$

In a subsequent rapid thermal annealing (RTA) step (heating rate $\Delta T_{\uparrow} > 200 \text{ K min}^{-1}$) at 170 °C for 5 min in a preheated oven all volatile solvents were removed from the

label	ΔT_{\uparrow}	processing parameters			Figure
		T_{\max}	ΔT_{\downarrow}	t_{an} at T_{\max}	
LSC700	3 K min ⁻¹	700 °C	10 K min ⁻¹	0 h	3.3a, b
LSC700-10	3 K min ⁻¹	700 °C	10 K min ⁻¹	10 h	3.3c, d
LSC700-100	3 K min ⁻¹	700 °C	10 K min ⁻¹	100 h	3.3e, f
LSC800	3 K min ⁻¹	800 °C	10 K min ⁻¹	0 h	3.4a, b
LSC800-10	3 K min ⁻¹	800 °C	10 K min ⁻¹	10 h	3.4c, d
LSC800-100	3 K min ⁻¹	800 °C	10 K min ⁻¹	100 h	3.4e, f

Table 3.1.: Sample labeling and processing parameters

coating. For pyrolysis, samples were heated with a heating rate $\Delta T_{\uparrow} = 3 \text{ K min}^{-1}$ to $T_{\max} = 700 \text{ °C}$ or 800 °C , respectively, and immediately cooled down to room temperature with a cooling rate $\Delta T_{\downarrow} = 10 \text{ K min}^{-1}$. During this step the actual perovskite phase is formed. Four samples were additionally subjected to a long-time thermal treatment at $T_{\max} = 700 \text{ °C}$ or 800 °C in air for $t_{\text{an}} = 10 \text{ h}$ or 100 h , respectively, to study the chemical and structural changes of the nanocrystalline LSC and the interface between LSC cathode and CGO electrolyte. Samples labeled as LSC700 and LSC800 in the following were pyrolyzed at 700 °C or 800 °C . LSC700-10, LSC700-100, LSC800-10 and LSC800-100 were additionally subjected to a long-term thermal treatment at 700 °C or 800 °C for 10 h or 100 h in air, respectively. The processing parameters and corresponding sample labeling are summarized in **Table 3.1**.

3.2.3. Reference materials for quantitative X-ray spectroscopy

Three reference materials LaSrAlO_4 , LaSrGaO_4 and LaCoO_3 , were analyzed to obtain k_{AB} -factors for standard-based quantitative EDXS of $\text{La}_{0.6}\text{Sr}_{0.4}\text{CoO}_{3-\delta}$. LaSrAlO_4 and LaSrGaO_4 single crystals ($5 \text{ mm} \times 5 \text{ mm} \times 1 \text{ mm}$ in size) grown by the Czochralski method were purchased from Crystec GmbH Kristalltechnologie (Berlin, Germany). Sintered polycrystalline LaCoO_3 tablets, fabricated by citric acid sol-gel method, were provided by Dr. Dirk Fuchs (*Institut für Festkörperphysik, KIT*). The tablets were sintered at 1250 °C for about 35 h. The expected crystal structure was verified at room temperature by means of X-ray diffraction (Cu source equipped with Ni β -filter). The material was single-phase and XRD-cell refinement confirmed the space group $R\bar{3}c$ with lattice parameter $a = 0.544 \text{ nm}$ and $c = 1.310 \text{ nm}$ according to literature data. The chemical composition of the three standard materials was cross-checked by Rutherford backscattering spectroscopy (RBS). They were found all to be stoichiometric within the experimental limits of $\pm 5 \%$. Hence, the nominal composition was used for the calculation of the absorption free k_{AB} -factors in the following. **Table 3.2** summarizes the quantitative results of the RBS measurements.

sample	experimental cation ratio		nominal cation ratio	
	La/Sr	La/Co	La/Sr	La/Co
LaSrGaO ₄	1.05	—	1.00	—
LaSrAlO ₄	1.00	—	1.00	—
LaCoO ₃	—	1.04	—	1.00

Table 3.2.: Quantitative cation ratios determined by RBS.

3.2.4. Sample preparation for transmission electron microscopy

The type of TEM sample, which needs to be prepared, always depends on the kind of desired characterization. Hence, one should be aware of the type of required analyses prior the preparation process. If structural and chemical variations close to an interface have to be analyzed, a sample, in which the interface is parallel to the incident electron beam, has to be prepared. This necessitates the preparation of TEM cross-section samples. They are prepared conventionally by sandwich gluing, slicing, grinding to a thickness of about 80 μm , dimple grinding and felt polishing as described by Strecker et al. [81]. Afterwards, sample thinning by single-sector Ar⁺-ion milling is performed according to the procedure described in **Section 2.2**. The presented technique enables a reliable and reproducible sample preparation, because the common double-sector ion milling fails by losing the complete LSC thin film in the electron-transparent areas.

For the preparation of plan-view samples, a small piece of sample (about 1.5 mm \times 2.5 mm) is glued on a supporting copper ring. The sample is then dimple ground from the electrolyte side to a minimum thickness of a few microns. This yields short ion-thinning times at sputtering angles of about 15° at an acceleration voltage 4 kV (Gatan Duomill). For the final polishing the acceleration voltage was decreased to about 2.5 kV. The bottom side of the sample holder is sealed with a cover slip glass during Ar⁺-ion sputtering from the top to prevent unwanted redeposition of sputtered material on the LSC thin-film cathode.

Prior to investigation, all TEM samples were coated by a thin carbon layer to reduce charging of the insulating substrate and, thus, sample drift in the microscope. For this purpose the thinned area in the middle of the sample was masked in order to prevent artifacts from the carbon added.

For STEM investigations, the TEM samples were cleaned using a plasma cleaner (Binder Labortechnik, Germany) immediately before the experiment to prevent sample contamination by deposition of cracked hydrocarbons on the sample surface.

3.3. Experimental results

The following subchapter presents the results of the microstructural characterization of nanocrystalline LSC cathodes, including temperature-related microstructural changes, e.g. isothermal grain growth (Section 3.3.1) and decrease of porosity (Section 3.3.2), crystalline phase composition (Section 3.3.3) as well as chemical composition (Sections 3.3.4 and 3.3.5).

3.3.1. Isothermal grain growth and grain-size distribution

The transport properties of MIECs significantly depend on grain size and associated area of intergranular grain boundaries. Hence, the LSC thin-film cathodes were investigated by means of TEM to study the microstructural changes in dependence of annealing parameters.

Figure 3.3 shows TEM bright-field (BF) images of samples pyrolysed and annealed at $T_{\max} = 700\text{ }^{\circ}\text{C}$ after an annealing time t_{an} of 0 h, 10 h or 100 h in plan-view and cross-section perspective, respectively. The corresponding image set for $T_{\max} = 800\text{ }^{\circ}\text{C}$ is displayed in **Figure 3.4**. The cross-section images are orientated in such a way that the LSC thin-film is on top and the CGO electrolyte substrate is on the bottom. The contrast in the cross-section images indicates the absence of interface-reaction phases for all samples, even after the harshest applied thermal treatment ($800\text{ }^{\circ}\text{C}$ for 100 h, c.f. **Figure 3.4f**). The interface between surface of the LSC thin-film cathode and material, which was redeposited during ion milling, is marked by a dashed line for sample LSC800-100.

All samples consist of isotropically orientated grains because the mean grain size is smaller than the thin-film thickness. Furthermore, both, plan-view and cross-section images, respectively, yield an increase of the mean grain size with rising T_{\max} and t_{an} . The mean grain size of the different cathode layers was determined quantitatively from the micrographs in plan-view perspective. The evaluation of the grain size was carried out by estimating the average grain diameter d from a circle being equivalent to the projected grain area A_{proj}

$$d = 2\sqrt{\frac{A_{\text{proj}}}{\pi}}.$$

This procedure is appropriate, as long as the mean grain size is smaller than the film thickness. In case of equal or larger size (brick-like grains) this technique overestimates the mean grain size. This is, to some extent, the case for LSC800-100 (cf. **Figure 3.4f**). For the evaluation, A_{proj} was measured for 100 to 180 grains with distinct Bragg contrast using the public-domain JAVA-based image processing software ImageJ [125]. Since not all grains show homogeneous contrast due to bending or change in thickness, no global threshold value could be applied for grain-size evaluation. Hence, the boundary of the grains was estimated by eye.

sample	grain size d	film thickness l
LSC700	(17 ± 5) nm	(176 ± 15) nm
LSC700-10	(27 ± 7) nm	(167 ± 13) nm
LSC700-100	(28 ± 10) nm	(128 ± 12) nm
LSC800	(29 ± 10) nm	(135 ± 26) nm
LSC800-10	(49 ± 15) nm	(112 ± 13) nm
LSC800-100	(90 ± 33) nm	(131 ± 25) nm

Table 3.3.: Tabulated mean grain size d and thin-film thickness l for all samples.

Figure 3.5 shows the relative frequency of grains as a function of grain size for all samples. For better comparability the distribution was normalized with respect to the total number of evaluated grains. Furthermore, mean grain size (marked by a vertical blue line) and Gaussian fit of the grain-size distribution (red curve) are shown in the figures. All samples exhibit normal grain growth, which can be concluded from the unimodally distributed grain sizes (only one maximum of the grain-size distribution), independent of final annealing temperature. The mean grain size as a function of annealing time t_{an} and temperature T_{max} is displayed in **Figure 3.6a**. It increases from (17 ± 5) nm (LSC700) to (28 ± 10) nm (LSC700-100) applying isothermal annealing at 700°C and from (29 ± 10) nm (LSC800) to (90 ± 33) nm (LSC800-100) at 800°C .

According to the cross-section micrographs, the thickness of the LSC cathode layer decreases with annealing temperature and time. Since the LSC film thickness l varies significantly due to the surface roughness of the CGO substrate, it was measured at about thirty different positions along the film for each sample. It decreases with t_{an} from (176 ± 15) nm to (128 ± 12) nm for $T_{\text{max}} = 700^\circ\text{C}$. In contrast, the film thickness for $T_{\text{max}} = 800^\circ\text{C}$ stays almost constant with t_{an} at about 125 nm. The mean LSC film thickness as function of annealing time is depicted in **Figure 3.6b** and listed in **Table 3.3**.

In addition to the increase of grain size with annealing temperature and time, the amount of porosity decreases upon long-term thermal treatment. Furthermore, larger residual pores are observed in the LSC thin-film at CGO grain boundaries intersecting the electrolyte surface. The substrate surface exhibits a larger curvature in these areas due to thermal etching during annealing of the substrates. These two aspects are presented in **Section 3.3.2** in more detail.

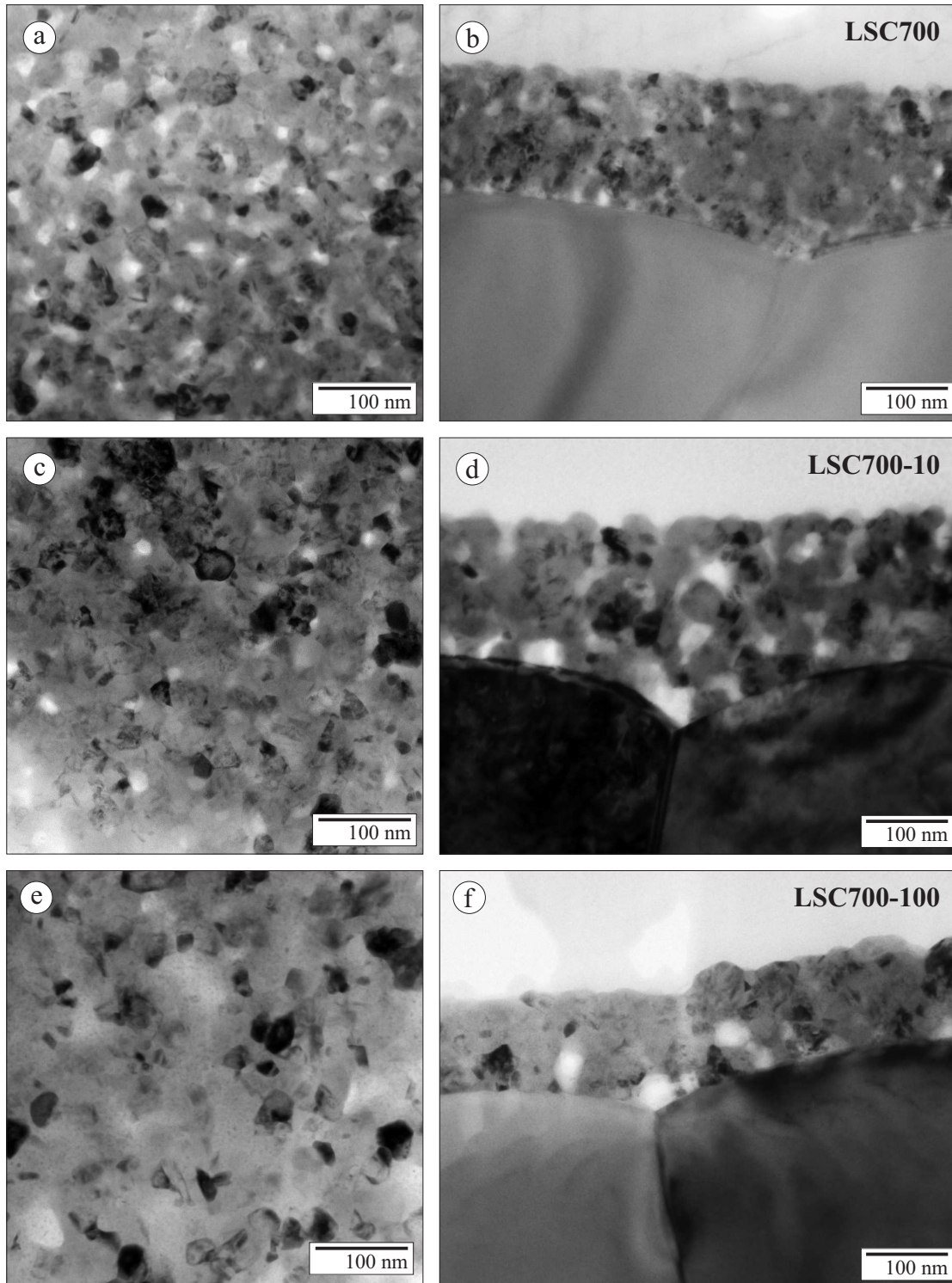


Figure 3.3.: TEM bright-field images of plan-view (left column) and cross-section (right column) samples prepared from (a,b) LSC700, (c,d) LSC700-10, (e,f) LSC700-100.

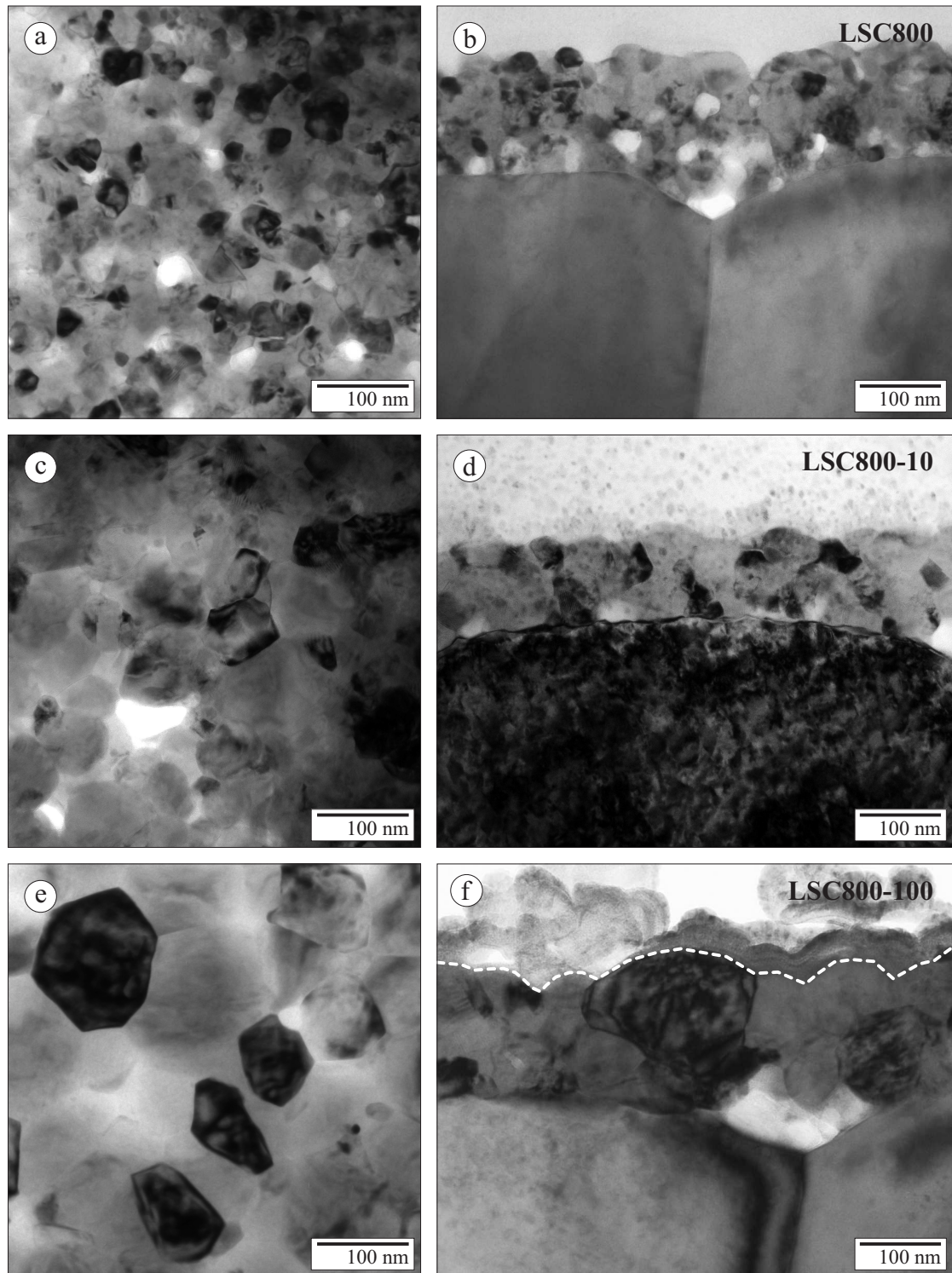


Figure 3.4.: TEM bright-field images of plan-view (left column) and cross-section (right column) samples prepared from (a,b) LSC800, (c,d) LSC800-10, (e,f) LSC800-100.

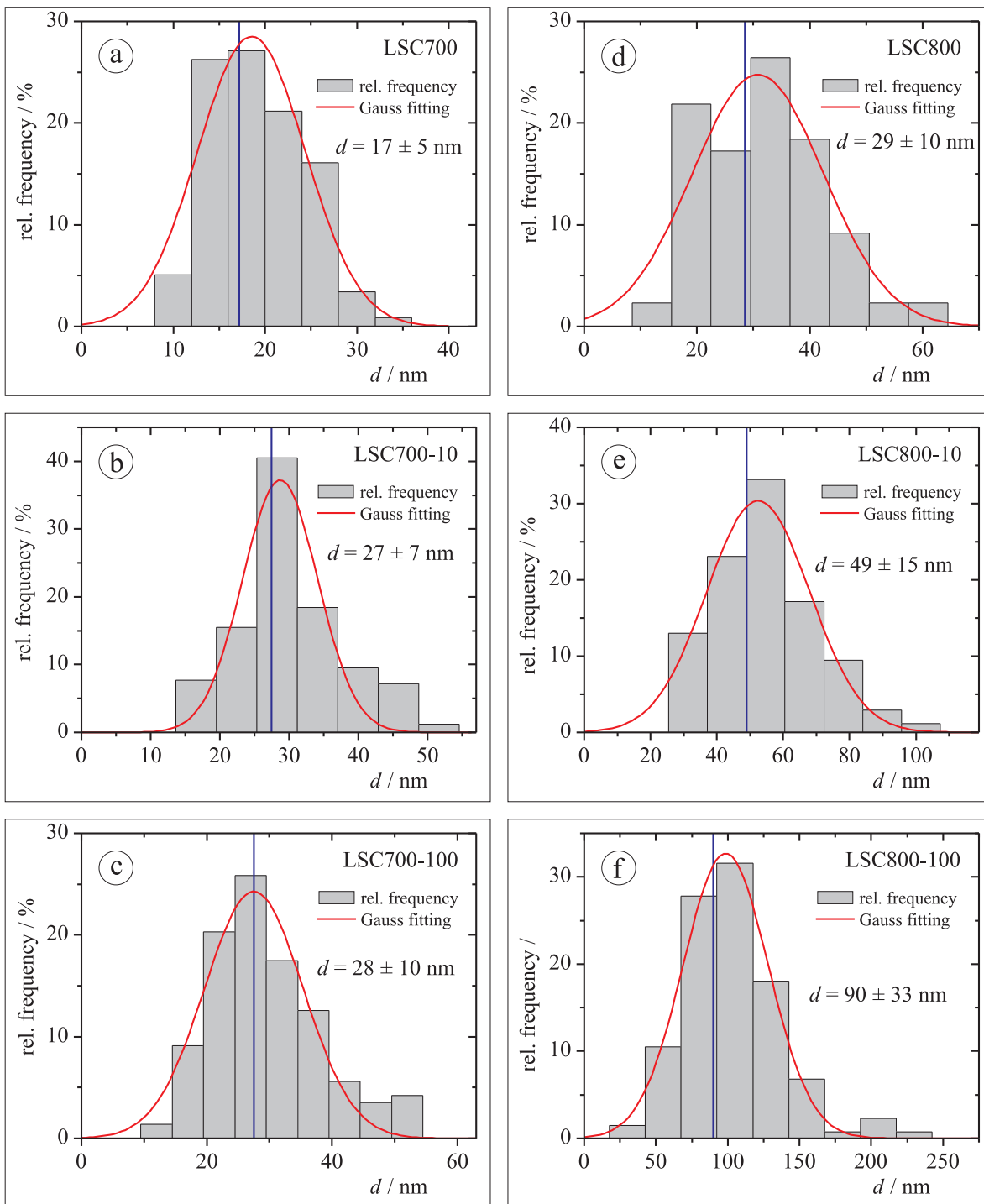


Figure 3.5.: Grain-size distribution of a) LSC700, b) LSC700-10, c) LSC700-100, d) LSC800, e) LSC800-10 and f) LSC800-100 given by the relative frequency as a function grain size.

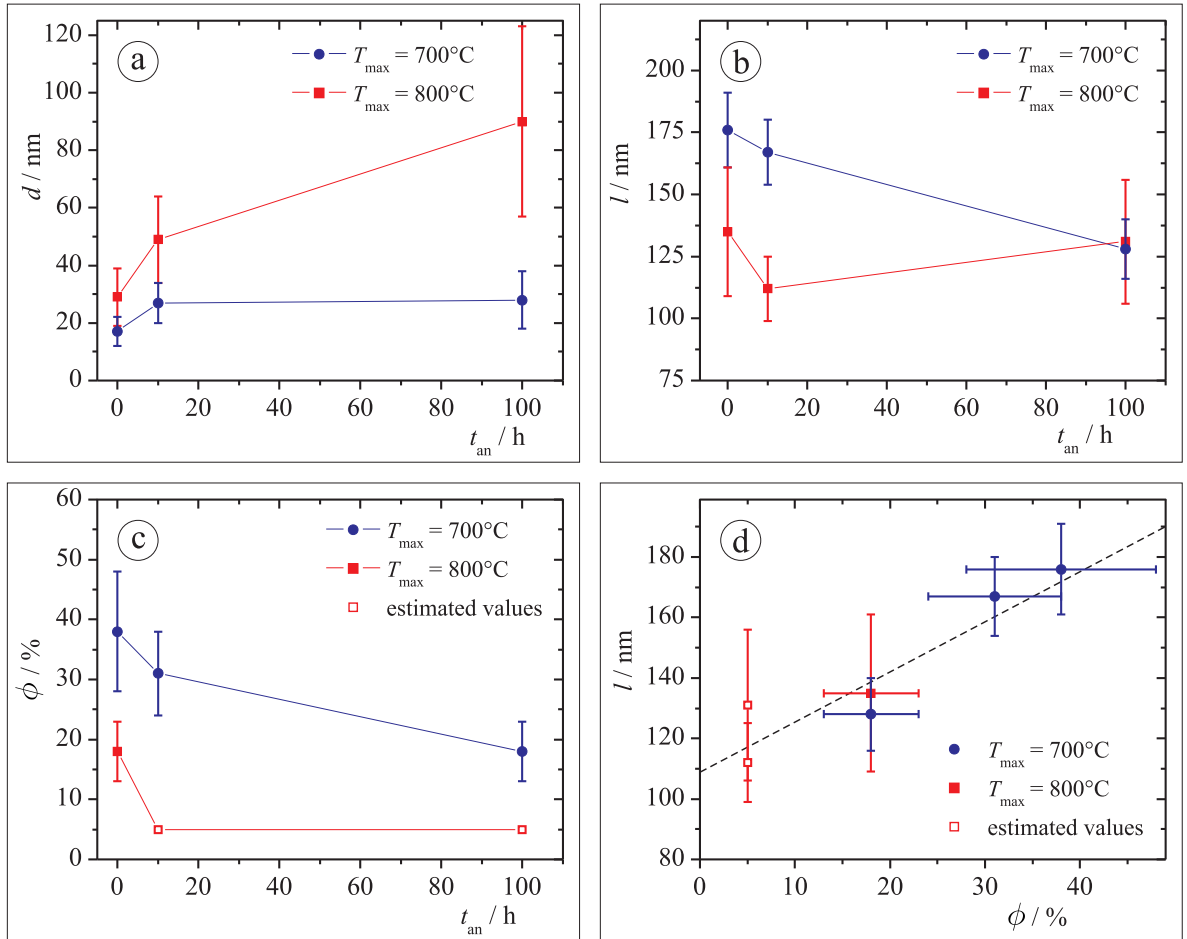


Figure 3.6.: a) Isothermal grain growth, b) LSC cathode layer thickness l and c) porosity ϕ in dependence of the annealing time $t_{\text{an}} = 0$ h, 10 h and 100 h for $T_{\text{max}} = 700^\circ\text{C}$ and 800°C and d) correlation between porosity ϕ and layer thickness l .

3.3.2. Porosity and three-dimensional microstructure

Image acquisition

The amount of porosity significantly controls the air/oxygen flow and oxygen exchange with the LSC cathode layer. Hence, knowledge of the kind (open or closed) and amount of porosity is essential if microstructural and electrochemical properties need to be correlated.

The porosity distribution and three-dimensional microstructure of the LSC cathodes was characterized by STEM tomography in HAADF mode. This imaging mode is advantageous for tomographic experiments because the image contrast is predominantly determined by the average atomic number, sample thickness and density. Compared to TEM bright-field imaging or STEM using a bright-field detector, it is only weakly affected by diffraction contrast. The experiments were performed with a FEI Titan³ 80-300 microscope using a Fischione Instruments Model 2020 Advanced Tomography Holder, enabling sample tilting up to $\pm 80^\circ$. However, during experiments it became apparent, that only a maximum tilt angle of $\alpha_{\max} = \pm 70^\circ$ was applicable, because the region of interest was shadowed by adjacent regions. For acquisition of tilt-image series, an inner detection angle between 84 and 120 mrad was used for the HAADF detector. The sample was mounted into the tomography holder in such a way that the rotation axis during tomographic data acquisition was perpendicular to the LSC/CGO interface. Before starting the experiment, brightness and contrast adjustments were performed at maximum tilt angle to ensure that the HAADF detector covers all image information within the dynamic range during the experiment. The acquisition of the HAADF STEM tilt image series was performed in a area including a section of the LSC film as well as the LSC/CGO interface. A tilt-angle increment $\Delta\alpha = 1.5^\circ$ was used for all experiments, resulting in a stack of 94 images. Throughout the acquisition, the region of interest was recentered after each tilt to adjust the chosen field of view.

Three-dimensional reconstruction and porosity evaluation

Before reconstruction, all projections must be precisely aligned with respect to each other. Since all analyzed samples provided sufficient contrast and image details, alignment of the image stack was performed fiducial-less by cross-correlation. This process defines the rotational axis for the dataset, which runs through the center of the reconstructed volume. The direction of this axis is determined by the tilt axis of the microscope goniometer and the relative sample orientation.

Image reconstruction was performed with the FEI Inspect3D V3.0 software, which applies the simultaneous iterative reconstruction technique (SIRT) algorithm [66]. Between 15 and 25 iterations were used for reconstruction. The reconstructed volume information was stored in a 3D image stack. A representative slice of the LSC cathode of LSC800 is displayed in **Figure 3.7a**. The 3D reconstructions are rescaled in z -direction by the elongation factor $e = 1.10$ (based on the experimental findings of Kawase et al. [126]) to compensate the distortion arising from the inaccessible angle range (missing wedge). This is discussed in detail in **Section 3.4.1**.

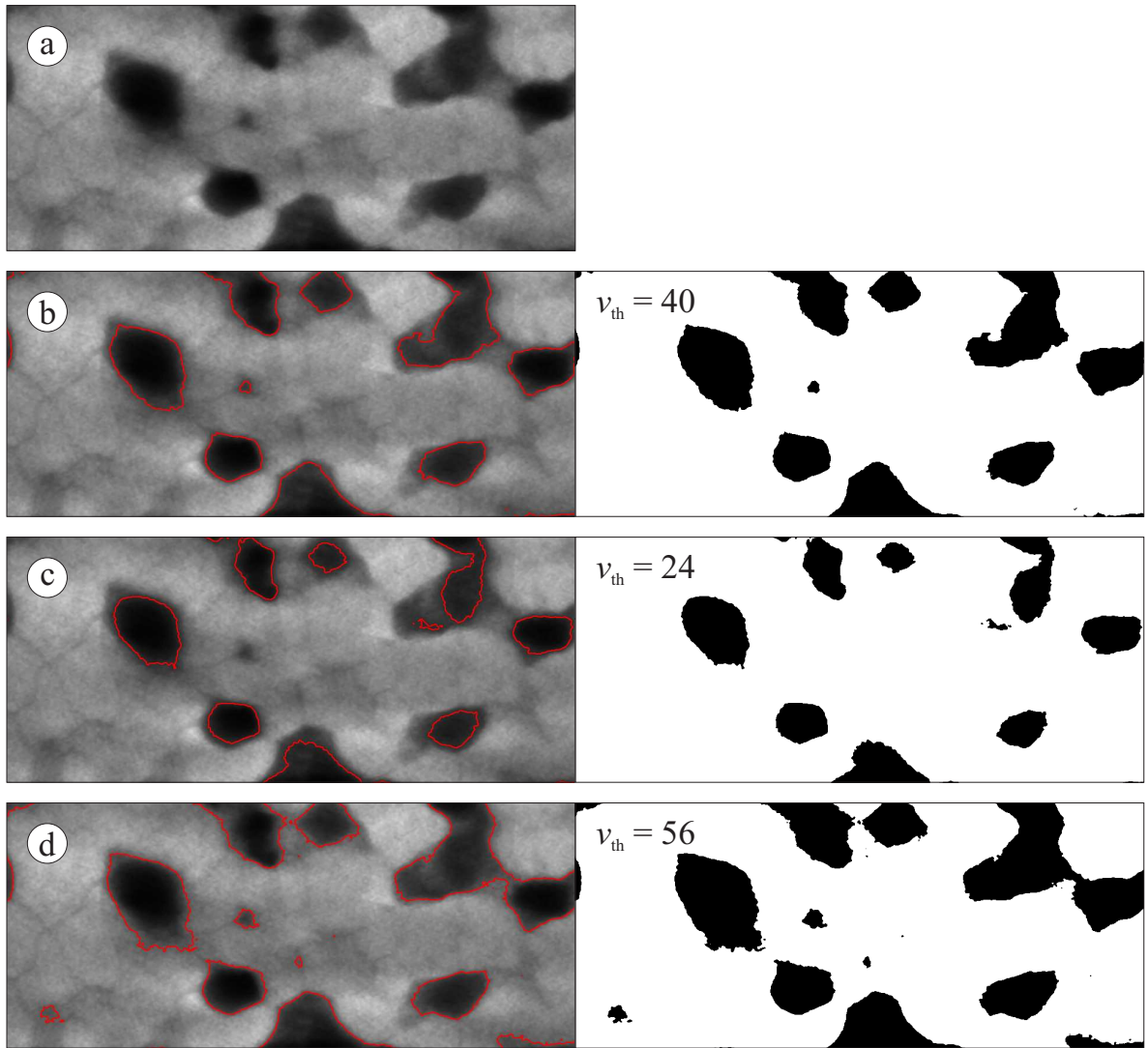


Figure 3.7.: Representative slice of the reconstructed image stack of LSC800 and the corresponding representation after setting a threshold value v_{th} of a) 40, b) 24 and c) 56.

For further quantitative characterization, e.g. porosity evaluation of the three-dimensional (3D) microstructure, this image stack has to be sectioned into the different phases (e.g. pores, cathode and electrolyte material). Segmentation, i.e. the distinction between pores and solid matter, was performed by setting a suitable threshold value v_{th} over the reconstructed volume in each slice of the image stack. This technique was applied, e.g. by Joos et al. [55], for segmentation of focused ion beam-polished microcrystalline (La,Sr)(Co,Fe)O_{3-δ} SOFC cathodes surfaces. All voxels (3D pixels) - resp. pixels of a single slice of the 3D image stack - with a gray scale value below the threshold are partitioned as pores, whereas all others were defined as solid. This threshold value is directly linked to the contrast and brightness settings during image acquisition. Hence, no global value for different samples is applicable. All images in the stack were median filtered after setting v_{th} to decrease the noise. **Figure 3.8a** shows one gray-scale histogram of a reconstructed image stack of cathode layer LSC800. The electrolyte was separated before. Here, the voxel frequency is mapped in dependence of the gray value. Two distinct maxima are observed, which can be ascribed either to pores or to the solid matter of the cathode. The minimum in between (marked by red arrow) can be used as reference point for the determination of the threshold value used for segmentation. Due to the fact that not all reconstructed volumes exhibited such a clear minimum or distinct features in the histogram, the threshold value for segmentation was estimated by eye. **Figure 3.8b** shows the measured porosity of LSC800 as a function of threshold value. As expected, the measured porosity is sensitive to the setting of the threshold value. It increases almost linearly with v_{th} . Therefore it is essential to use a suitable threshold value for calculating the porosity fraction which is shown in **Figure 3.7**.

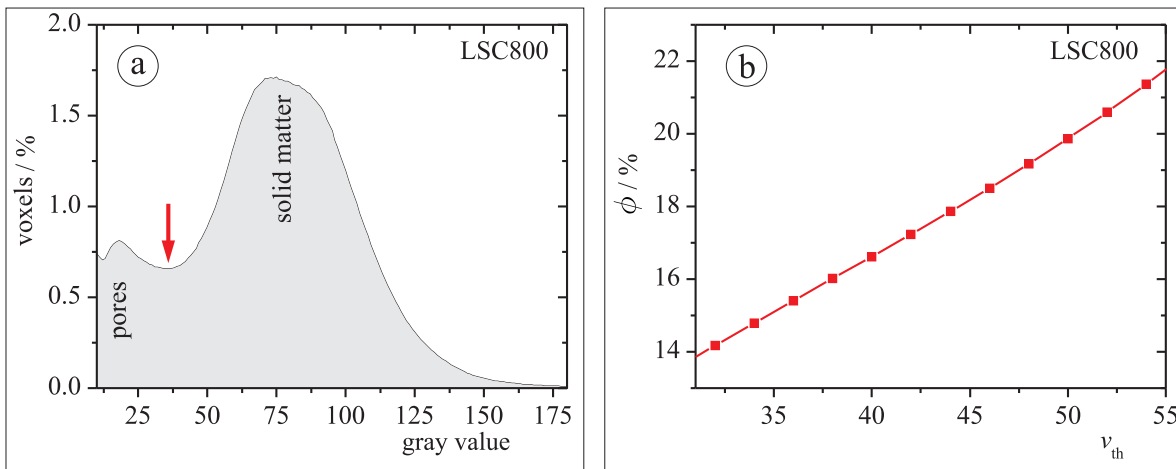


Figure 3.8.: a) Gray scale histogram of the reconstructed image stack of LSC800 and b) porosity in dependence of the threshold value v_{th} .

Figure 3.7a shows a representative slice of the reconstructed image stack of LSC800 and the corresponding representation for three different threshold values (see **Figure 3.7b–d**). Besides the gray-scale image (left column) where the segmentation border is marked by a thin red line, the segmented black and white images are displayed also. Here, pores

are displayed in black and solid matter as white (right column). In the case of LSC800, the threshold value $v_{\text{th}} = 40$ represents the phase boundary between solid matter and pore at best (cf. **Figure 3.7b**). The porosity for each sample is evaluated on the basis of all available segmented black and white image stacks. The porosity or void fraction* ϕ of a material is described by the fraction of volume of voids V_{void} over the total volume V_{tot} , including solid and void components.

$$\phi = \frac{V_{\text{void}}}{V_{\text{tot}}} = \frac{n_{\text{pores}}}{N}.$$

In this case, the porosity was calculated by dividing the number of voxels segmented as pores n_{pores} by the overall number of all voxels N within the reconstructed volume of the cathode layer. The systematic error of the porosity was estimated by increasing/decreasing v_{th} until an obvious under/overestimation of the porosity occurred. For LSC800 a value of $v_{\text{th}} = 24$ underestimates (cf. **Figure 3.7c**) the amount of porosity, whereas for $v_{\text{th}} = 56$ the porosity is overestimated. This correlates to a systematic error of $\Delta\phi = \pm 5\%$. Electrolyte substrate and surface roughness were omitted in this evaluation to ensure straight and comparable results.

sample	no. of experiments	volume V_{tot}	porosity ϕ	
LSC700	2	$7.9 \times 10^{-3} \mu\text{m}^3$	$(38 \pm 10)\%$	Figure 3.9a
LSC700-10	1	$8.1 \times 10^{-3} \mu\text{m}^3$	$(31 \pm 7)\%$	Figure 3.9b
LSC700-100	1	$2.8 \times 10^{-3} \mu\text{m}^3$	$(18 \pm 5)\%$	Figure 3.9c
LSC800	2	$8.5 \times 10^{-3} \mu\text{m}^3$	$(18 \pm 5)\%$	Figure 3.9d
LSC800-10	—	—	5 %*	—
LSC800-100	—	—	5 %*	—

*not measured, estimated value

Table 3.4.: Porosity measured by STEM tomography

The porosity drops from $(38 \pm 10)\%$ for LSC700 to $(18 \pm 5)\%$ for LSC700-100. A significant lower initial porosity of $(18 \pm 5)\%$ is obtained for LSC800 after pyrolysis at 800°C . Since the cathode layer densifies significantly upon heat treatment at 800°C , the remaining amount of porosity within the cathode layers of LSC800-10 and LSC800-100 is negligible. Hence, porosity in these two samples was defined to 5%. Residual pores are only present at the cathode/electrolyte interface and at the intersections between CGO grain boundaries and electrolyte surface (cf. **Figure 3.5e** and **Figure 3.5f**). The results of the porosity determination and the totally evaluated volume V_{tot} are summarized in **Table 3.4** and depicted in **Figure 3.6c**.

* If specified as percentage, the value is multiplied by 100 %

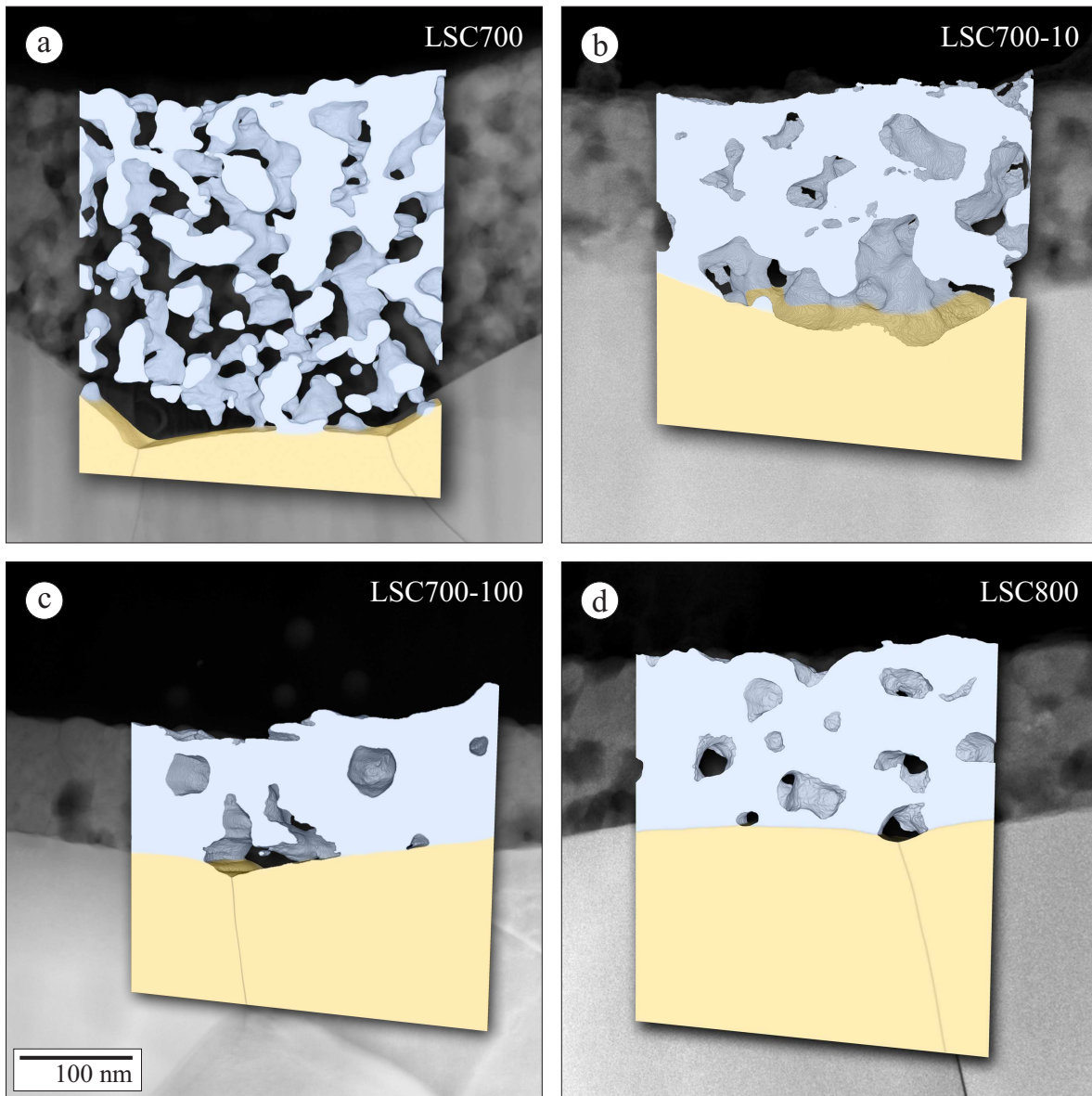


Figure 3.9.: Colored 3D reconstruction of a) LSC700, b) LSC700-10, c) LSC700-100 and d) LSC800. Lateral size of the reconstructed volume is 360 nm. A corresponding HAADF STEM image is presented in the background.

The observed densification is accompanied with reduction of film thickness. As the same amount of LSC is deposited on each sample during the metal organic deposition via dip-coating, porosity is directly correlated with the cathode-layer thickness. In **Figure 3.6d** the average LSC film thickness is plotted over the porosity which shows a linear correlation. The film thickness after complete densification can be calculated by extrapolating the mean film thickness to zero porosity and was found to be $l_{\text{dense}} = (109 \pm 8)$ nm. **Figure 3.9** shows 3D reconstructions of LSC700, LSC700-10, LSC700-100 and LSC800 after threshold segmentation. A corresponding HAADF STEM image of the tilt image series acquired at tilt angle 0° is depicted in the background. The LSC cathode layer is displayed in light blue and the CGO electrolyte substrate in light yellow. Pores are transparent and grain boundaries within the substrate are marked by a thin black line. Material and pores intersecting the edges of the reconstructed volume are clipped. It is noted that the segmentation procedure does not allow a distinction between possible different crystalline phases within the cathode material (see **Section 3.3.3** and **Section 3.3.4**). The 3D reconstruction illustrates that open porosity and gas channels to the surface pervade the complete LSC700 cathode layer (see **Figure 3.9a**) which consists of a porous and fragile framework of nanoscaled LSC grains. This results in a large surface area and makes the complete cathode volume electrochemically active. In contrast to LSC700, a major fraction of the pores appear to be closed porosity in LSC800.

3.3.3. Crystalline phases

The crystal structure of the LSC cathode films was analyzed by electron diffraction using plan-view samples. Due to the small grain sizes, Debye diffraction was employed for structure determination and phase identification. Two different image acquisition devices were used for recording the diffraction pattern: Ditabis imaging plates and a TVIPS TemCam-F416 16 MegaPixel CMOS camera, respectively. Images of the CMOS camera are indicated by the presence of a beam stop in the diffraction pattern. This is necessary to screen the camera chip and scintillator from high intensity irradiation of the directly transmitted electron beam.

In **Figure 3.10a, b, c** and **Figure 3.11a, b, c** contrast-inverted Debye electron-diffraction patterns (left column) of all samples (LSC700, LSC700-10, LSC700-100, LSC800, LSC800-10 and LSC800-100) are presented. Diffraction from such polycrystalline samples (especially for nanoscaled grain sizes) can be viewed in the same way as X-ray diffraction from powders (beside deviating intensities due to differing structure factors). If the reciprocal lattice of a random polycrystal is rotated around all axes it will produce a set of nested concentric spheres. Upon intersection with the Ewald sphere (which approximates in TEM to a slightly curved plane), diffraction patterns composed of concentric rings are produced due to the large number of simultaneously illuminated grains in various orientations.

Prior to radial integration, all evaluated diffraction patterns are distortion corrected by an ImageJ routine to ensure a clear intensity separation of Debye-Scherrer rings. In a first step, an ellipse is fitted to a single Debye ring. Its diameter was chosen as large

as possible to minimize arising errors. The semi-major axis a , semi-minor axis b and rotation ϕ corresponding to the border of the micrograph were used as fitting parameters. The determined parameters were used to rotate the image by ϕ , compress it in the direction of a and stretch it in direction of b , resulting in a undistorted diffraction pattern with perfect circularity. For the CM200 microscope used, the a to b ratio was found to be $a/b = 1.019$ and $\phi = 8^\circ$. The observed distortion originates most likely from the projection system of the microscope. It is not a scanning artifact of the imaging plates during readout, because it is also detected in diffraction patterns recorded with the TVIPS CMOS TemCam-F416 or conventional negatives. Without distortion correction, peaks would be broadened or adjacent rings would smeared up completely during rotational integration. The diffuse background below the reflections was estimated empirically, because a reliable model to simulate background contribution of amorphous material and/or contaminations is not available. Therefore, the free software tool Fitky [52] was applied to model and subtract the diffuse background by fitting user-set sampling points by spline functions.

Background corrected, radial intensity profiles are presented in **Figure 3.10d, e, f** for the LSC700 sample series and **Figure 3.11d, e, f** for the LSC800 series. The radial intensity profile [127] normalizes the integrated intensities around concentric circles with respect to their circumferences as a function of their radii, yielding comparable intensity values. According to the diffraction peaks, several phases within the cathode layer are present. Corresponding kinematical simulations of the diffracted intensities of the phases identified by electron diffraction were performed with the JEMS software [53]. They are displayed in **Figure 3.10** and **3.11** as vertical lines and marked by (\bullet) for $\text{La}_{0.6}\text{Sr}_{0.4}\text{CoO}_{3-\delta}$, (\circ) for the oxygen-vacancy ordered phase, (\blacksquare) for $\text{Ce}_{0.9}\text{Gd}_{0.1}\text{O}_{1.95}$ and (\blacktriangle) for Co_3O_4 .

LSC is identified as rhombohedral perovskite structure with the space group $R\bar{3}c$ (No. 67) as described in **Section 1.1.1**. The diffraction data clearly confirm that LSC with perovskite structure is the major crystalline phase. Nevertheless, additional weaker reflections are present in the diffraction patterns. The intensities at the reciprocal lattice distances of 2.14 , 4.10 and 4.95 nm^{-1} can be clearly assigned to the $\{111\}$, $\{113\}$ and $\{400\}$ reflections of Co_3O_4 . This cobalt oxide crystallizes in cubic spinel structure (space group No. 227, $Fd\bar{3}m$) with the tetragonal 8(a) sites occupied by Co^{2+} , octahedral 16(d) sites ($5/8 \ 5/8 \ 5/8$) occupied by Co^{3+} and 32(e) sites ($0.3881 \ 0.3881 \ 0.3881$) occupied by 32 O^{2-} ions [128]. The $\{220\}$ reflections of Co_3O_4 coincide with reflections of LSC and are only noticeable as small shoulder at 3.5 nm^{-1} in the diffraction pattern of LSC800-100. This can be explained by the decrease in the FWHM of the peaks with increasing grain size. Beside the reflections associated with LSC, CGO and Co_3O_4 , further minor reflections at 1.3 nm^{-1} , 2.9 nm^{-1} , 4.65 nm^{-1} and 5.3 nm^{-1} exist in LSC800 and LSC800-100. These can be clearly identified as oxygen-vacancy ordered tetragonal $\text{La}_{1-y}\text{Sr}_y\text{CoO}_{3-\delta}$. The remaining reflection at 3.2 nm^{-1} is assigned to the $\text{Ce}_{0.9}\text{Gd}_{0.1}\text{O}_{1.95}$ phase with fluorite prototype structure. It originates from remaining parts of CGO crystallites, which were not removed completely during back thinning of the plan-view samples.

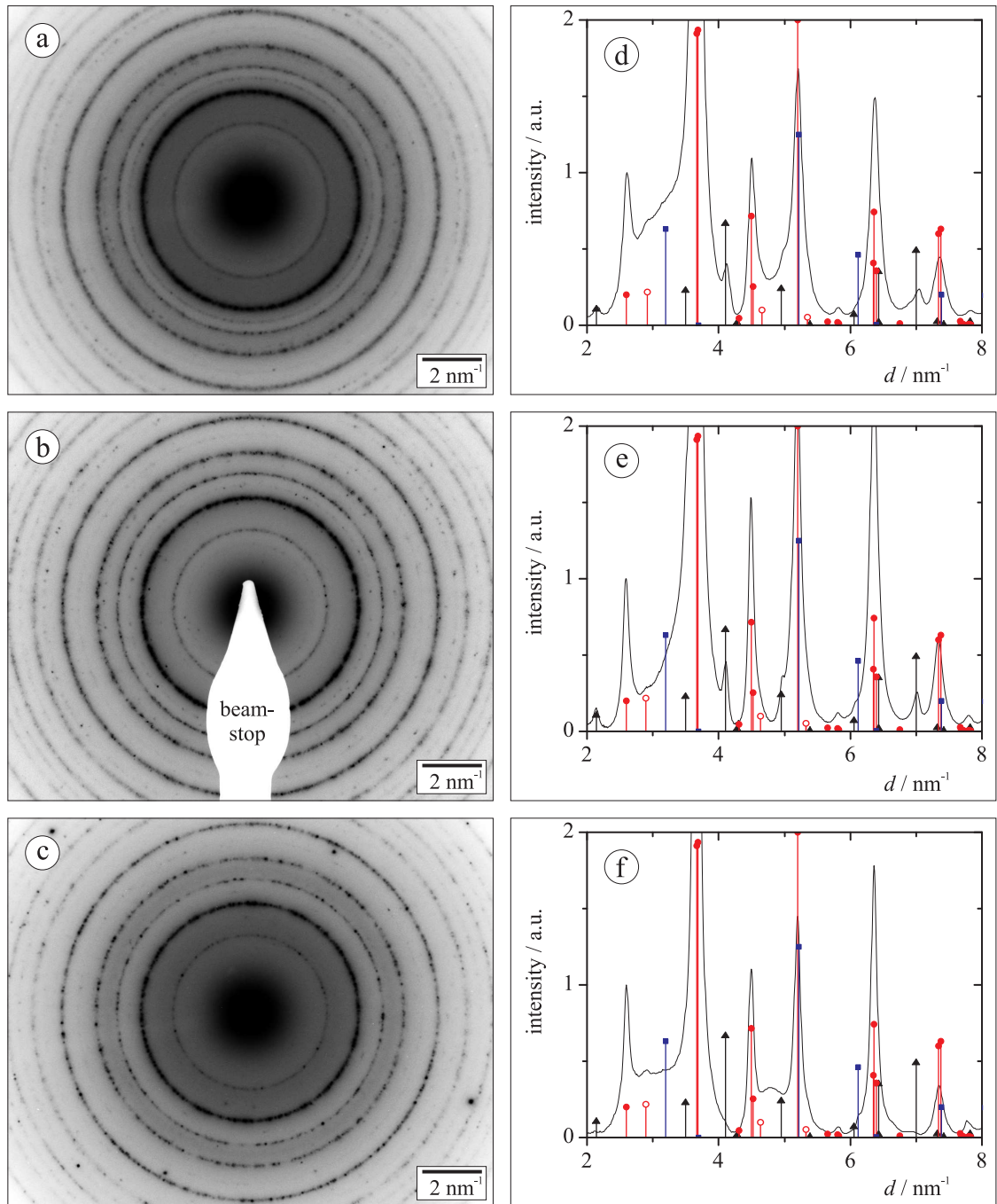


Figure 3.10.: Experimental, contrast-inverted Debye diffraction patterns (left column), radially integrated intensity profiles and simulated Debye diffraction patterns (right column) of (a,d) LSC700, (b,e) LSC700-10 and (c,f) LSC700-100. The individual phases are marked by (●) for $\text{La}_{0.6}\text{Sr}_{0.4}\text{CoO}_{3-\delta}$, (○) for the oxygen-vacancy ordered phase, (■) for $\text{Ce}_{0.9}\text{Gd}_{0.1}\text{O}_{1.95}$ and (▲) for Co_3O_4 .

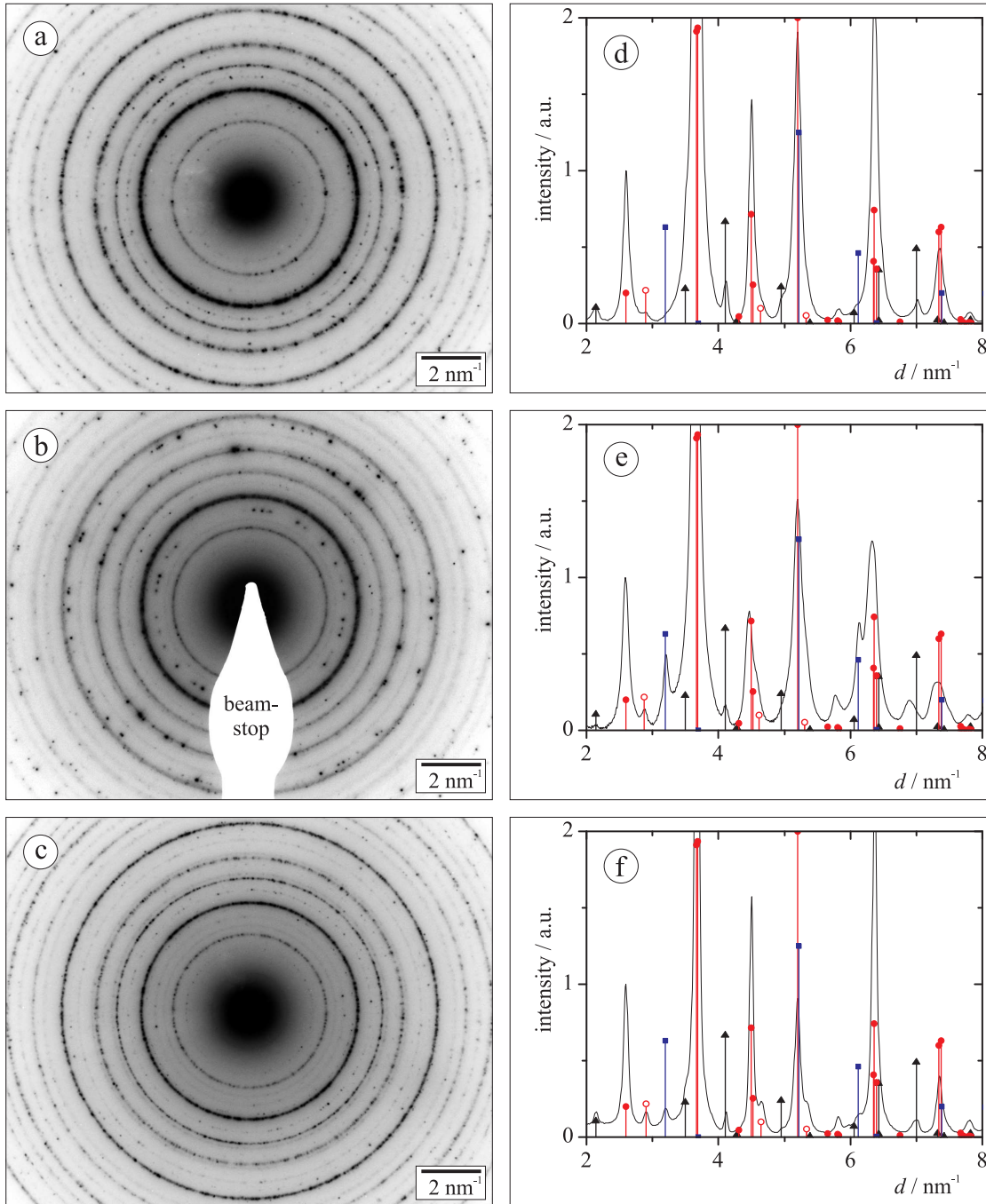


Figure 3.11.: Experimental, contrast-inverted Debye diffraction patterns (left column), radially integrated intensity profiles and simulated Debye diffraction patterns (right column) of (a,d) LSC800, (b,e) LSC800-10 and (c,f) LSC800-100. The individual phases are marked by (●) for $\text{La}_{0.6}\text{Sr}_{0.4}\text{CoO}_{3-\delta}$, (○) for the oxygen-vacancy ordered phase, (■) for $\text{Ce}_{0.9}\text{Gd}_{0.1}\text{O}_{1.95}$ and (▲) for Co_3O_4 .

The discrepancy in relative intensity of measured and simulated reflections is most probably caused by dynamical effects due to varying grain sizes in the different samples. An overall decrease in full width at half maximum (FWHM) of the reflections with increasing annealing temperature and duration from LSC700 to LSC800-100 can be explained by the increasing grain size (see **Figure 3.6a**). Furthermore, diffuse intensity is observed around 3 nm^{-1} , especially in LSC700 and LSC700-100, but it does not occur to such an extent in LSC700-10 and the LSC800 series. However, no clear trend with t_{an} or T_{max} is observed concerning the disappearance of the diffuse intensity in the diffraction patterns. Hence, this effect is assigned to a TEM-sample preparation artifact due to redeposition of material and surface-near amorphization during Ar^+ -ion sputtering.

3.3.4. Qualitative X-ray analyses

The surface exchange coefficient and catalytic properties of a SOFC cathode crucially depends on its chemical composition. Hence, the local chemical composition within the LSC thin-film cathodes was measured with high spatial resolution by EDXS. Drift-corrected EDXS mappings were recorded in STEM mode to obtain an overview of the element distribution in the cathode layers and at the LSC/CGO interface. One second dwell time per pixel for the acquisition of an EDX spectrum resulted in a complete acquisition time of 10–14 h, depending on the resolution used for characterizing the area of interest.

Figure 3.12 shows the distribution of the elements Ce, La, Sr and Co as well as corresponding HAADF STEM images, recorded simultaneously during spectrum acquisition. For elemental mappings of the Ce- and La-distribution the La and Ce K-lines (32.7 and 33.9 keV) were used, because intensities of the L-lines of both elements overlap and cannot be separated properly by a simple energy window, which is a prerequisite for generating element maps. Using K-lines of both elements, a reliable separation of the intensities is assured, however, at the expense of the signal-to-noise ratio. All EDXS maps exhibit a clear separation between cathode and electrolyte material. No intermixing or interfacial reaction phases are observed. Only a slight roughening of the interface is detected in LSC800-100. Furthermore, the mappings clearly demonstrate the existence of grains without La with increasing annealing time (LSC700-100) and pyrolysis temperature (LSC800). They are mainly located in the upper half of the cathode layer. The Sr-distribution was imaged with a combination of Sr-K and Sr-L lines to improve the signal-to-noise ratio. Since both element maps (Sr-K and Sr-L) contain the same information, they were added up. Besides slight fluctuations within the Sr-distribution, especially observed in LSC700-100 and LSC800, there are also grains without Sr in the LSC cathode layers. These crystallites coincide with the La-depleted grains. The Co-map imaged with the Co-K line clearly visualizes that the grains depleted in Sr and La are cobalt oxide precipitates, which were identified as Co_3O_4 by Debye electron diffraction. They are located mainly in the surface region of the cathode. Their number decreases with annealing time, whereas their overall grain diameter increases according to the LSC grain size.

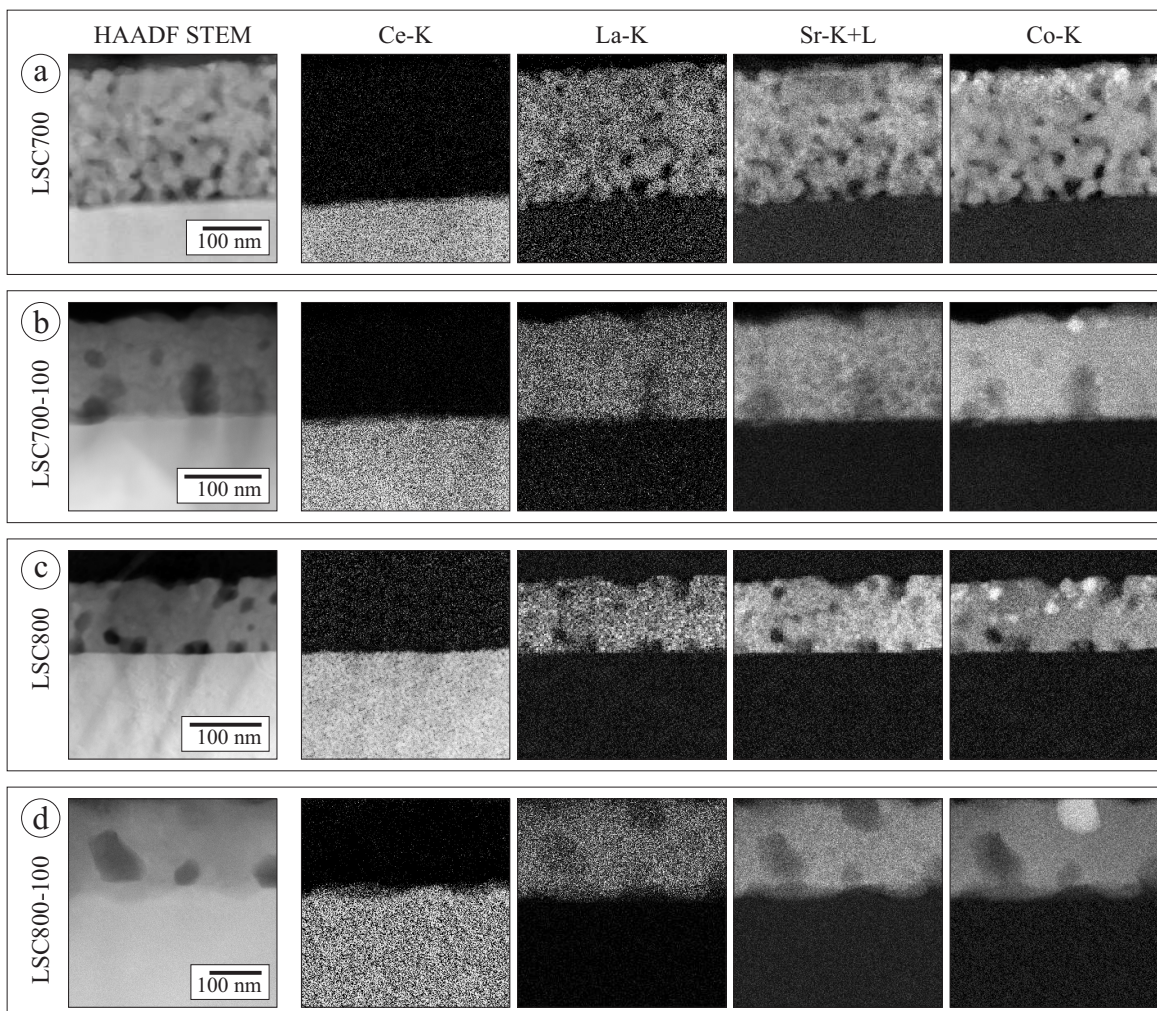


Figure 3.12.: HAADF STEM images and corresponding element distributions of Ce, La, Sr and Co of a) LSC700, b) LSC700-100, c) LSC800 and d) LSC800-100.

3.3.5. Quantitative X-ray analyses

The Cliff-Lorimer method was applied for quantitative analyses of the chemical composition. This method was favored with respect to quantification with the software of the EDXS system because it yields higher accuracy data if standard samples with well known composition (similar to the samples of interest) are available for calibration. For determination of the required absorption-corrected $k_{A,B}$ -factors, sol-gel derived polycrystalline LaCoO_3 as well as LaSrAlO_4 and LaSrGaO_4 single crystals were used as standards. The chemical composition of the three standards was analyzed by RBS using a 2 MeV van-de-Graff $^4\text{He}^{2+}$ linear accelerator. All standard samples are found to be stoichiometric within the experimental-error limits of $\pm 5\%$.

EDX spectra of the standards were recorded at different sample thicknesses using a constant probe current and acquisition time of $t_{ac} = 100$ s to determine the absorption-free Cliff-Lorimer $k_{A,B}$ -factors. **Figure 3.13** and **3.14** show representative EDX spectra of the standard samples LaCoO_3 , LaSrAlO_4 and LaSrGaO_4 as well as the corresponding mass-attenuation coefficient for X-ray absorption of the respective compound [71]. The net counts of the La- $L\alpha_{1,2}$, Sr- $K\alpha_{1,2}$ and Co- $K\alpha_{1,2}$ lines were extracted by subtracting a polynomial background and standardless peak-fitting, allowing variation in energy calibration and resolution (FEI TEM Imaging Analysis software version 3.2 SP6). This method was favored with respect to linear background subtraction determined by two energy windows (positioned at slightly higher and lower energy, relative to the peak position) and peak integration, owing to two reasons:

- Signal overlap with X-ray radiation from spurious electrons and radiation arising from redeposited matter during sample thinning using Ar^+ -ion sputtering.
- Problems in placing appropriate energy windows for background determination between numerous peaks especially in the case of La-L series and Co-K peaks in $\text{La}_{0.6}\text{Sr}_{0.4}\text{CoO}_{3-\delta}$ and the LaCoO_3 standard.

Furthermore, the common Top-Hat filtering could also not be applied because weak peak intensities vanish. All spectra were evaluated by the same procedure to avoid different systematic errors.

For the microanalysis of transition metal elements, K-lines are usually preferred to L-lines to avoid chemical effects (changes in peak shape and position). Furthermore, the K-lines are in general better separated. Nevertheless, the $L\alpha_{1,2}$ -line was used for La-quantification due the unfavorable signal-to-noise ratio of the high-energy La- $K\alpha_2$ line at 33.034 keV. The absorption-free Cliff-Lorimer factors $k_{\text{La,Sr}}$ and $k_{\text{Co,La}}$ are determined by linear extrapolation of the net intensity ratio of

$$\ln\left(\frac{I_{\text{Sr-K}\alpha_{1,2}}}{I_{\text{La-L}\alpha_{1,2}}}\right) \text{ and } \ln\left(\frac{I_{\text{La-L}\alpha_{1,2}}}{I_{\text{Co-K}\alpha_{1,2}}}\right)$$

to zero foil thickness (c.f. **Figure 3.15**).

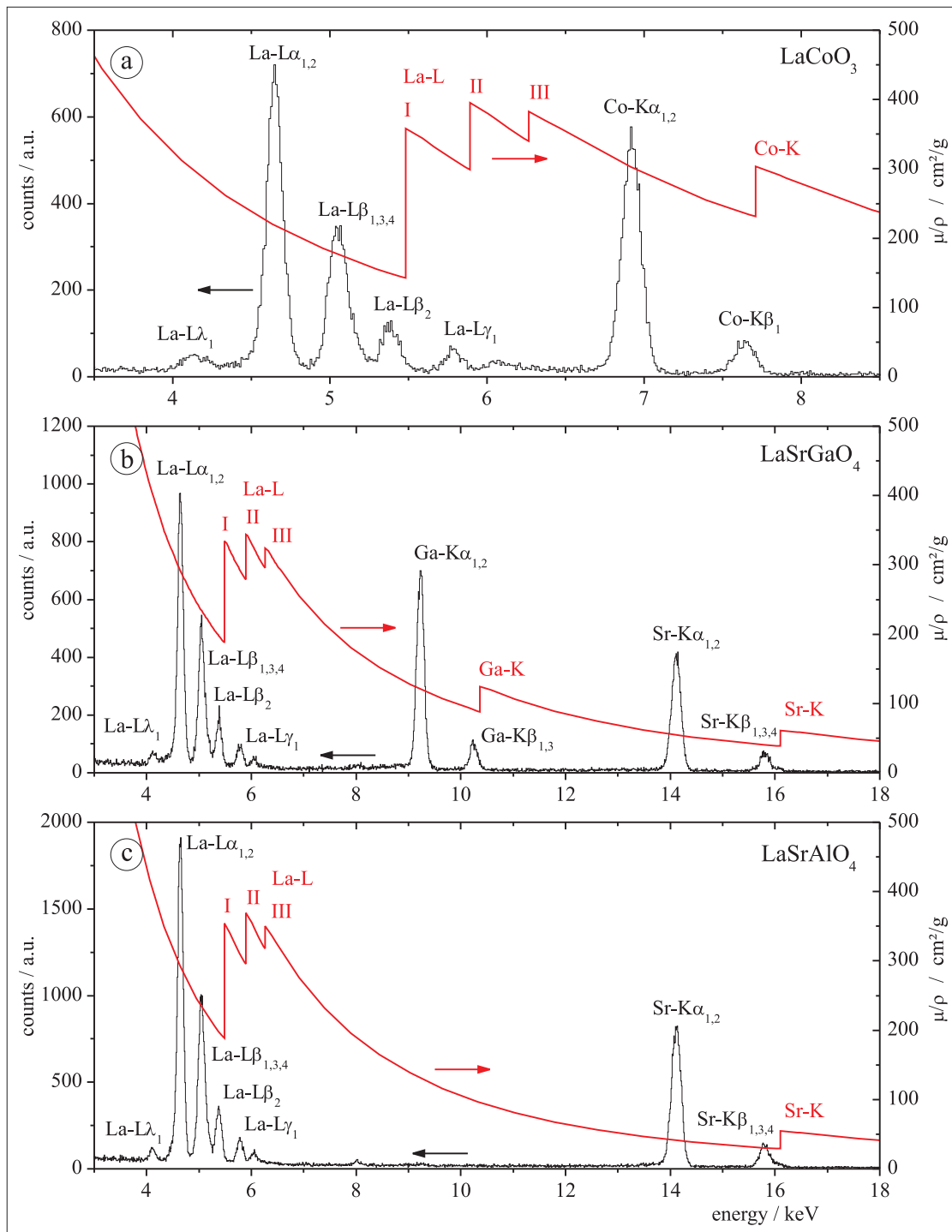


Figure 3.13.: Representative experimental EDX spectra and theoretical mass-attenuation [71] (including element characteristic absorption edges) of a) LaCoO_3 , b) LaSrAlO_4 and c) LaSrGaO_4 as a function of energy.

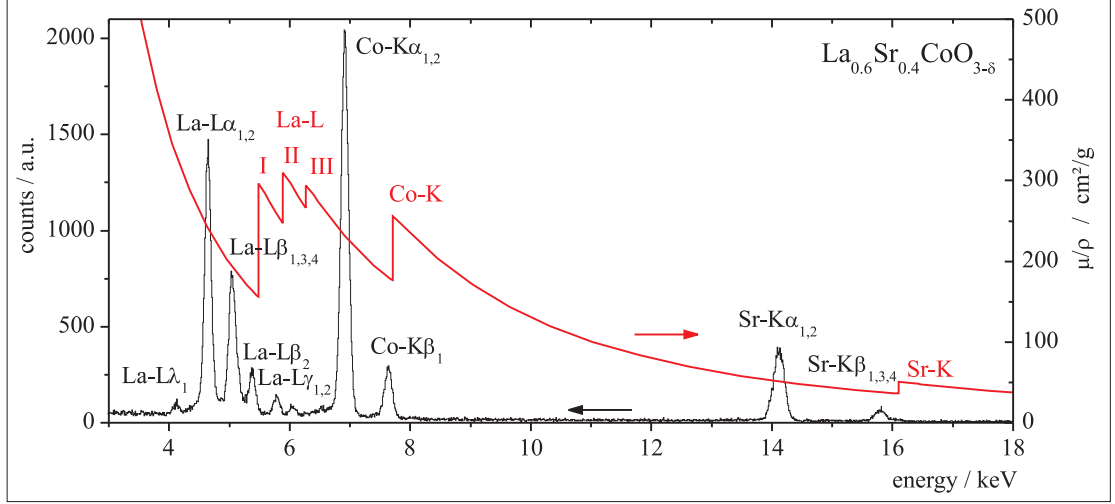


Figure 3.14.: Representative experimental EDX spectrum and theoretical mass-attenuation [71] (including element characteristic absorption edges) of $\text{La}_{0.6}\text{Sr}_{0.4}\text{CoO}_{3-\delta}$ as a function of energy.

The intensity ratios are plotted as a function of the characteristic line with the lowest mass-attenuation coefficient ($\text{Sr-K}\alpha_{1,2}$ intensity in the case of $k_{\text{La,Sr}}$ and the $\text{La-L}\alpha_{1,2}$ intensity for $k_{\text{Co,La}}$), which is, in first approximation, proportional to the sample thickness [129, 130]. The calculated mass-attenuation coefficients of the materials analyzed are summarized in **Table 1.4**. The thickness dependence of the $k_{\text{Co,La}}$ factor is negligible due to similar mass-attenuation coefficients of La and Co.

Allowing a value of 5% as maximum absorbed X-ray intensity, the critical sample thickness can be approximated as

$$t < \frac{0.1}{(\xi_A - \xi_B)\rho}$$

where

$$\xi_{A,B} = \left(\frac{\mu}{\rho}\right)_{A,B} \frac{1}{\sin \alpha}$$

for element A and B respectively [130].

Since the critical thicknesses, calculated on the basis of the attenuation factors given in **Table 1.4**, are 270 nm and higher (see **Table 3.5**), X-ray absorption can be neglected because TEM sample thicknesses were well below these values.

The $k_{\text{Sr,Co}}$ factor was calculated on the basis of the relation

$$k_{\text{Sr,Co}} = \frac{k_{\text{Sr,La}}}{k_{\text{Co,La}}} = \frac{1}{k_{\text{La,Sr}} \cdot k_{\text{Co,La}}}$$

using the experimental values of $k_{\text{La,Sr}}$ and $k_{\text{Co,La}}$ due to the lack of a Sr-Co standard.

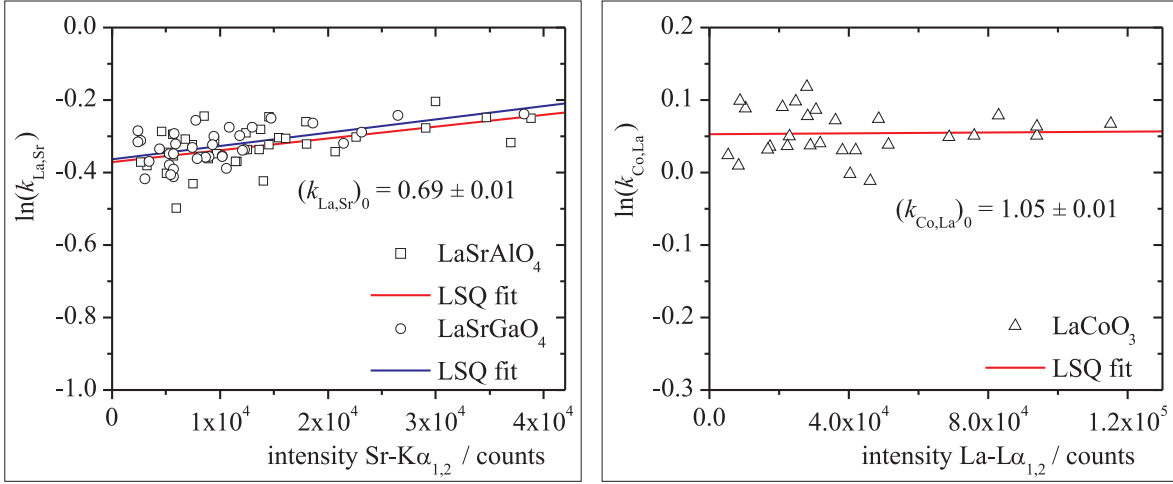


Figure 3.15.: Determination of absorption-free Cliff-Lorimer k -factors.

$k_{A,B}$ -factor	experimental value	TIA database*	t_c [nm]
$k_{La,Sr}$	0.69 ± 0.01	0.74	270
$k_{Co,La}$	1.05 ± 0.01	0.96	6900
$k_{Sr,Co}$	1.38 ± 0.02	1.41	290

*database $k_{A,Si}$ -factor (with reference element Si) used for the evaluation of wt.% concentration ratios, converted for the evaluation of at.% concentration ratios with modified reference.

Table 3.5.: Measured absorption-free Cliff-Lorimer k_{AB} -factors and calculated critical sample thicknesses t_c of the corresponding element combination.

The determined absorption-corrected $k_{A,B}$ -factors for vanishing TEM sample thickness are summarized in **Table 3.5**. For comparison, software-based $k_{A,B}$ -factors (FEI TEM Imaging & Analysis software version 3.2 SP6) are given, too.

The local chemical composition of the LSC thin-films cathode was determined quantitatively using the experimental $k_{A,B}$ -factors. For this purpose element characteristic X-ray intensities were accumulated in four rectangular areas (200 nm x 10 nm in size) at different positions within the cathode layers. They were positioned equidistantly, starting with position 1 close to the LSC/CGO interface and ending with position 4 close to the LSC cathode surface. **Figure 3.16a** depicts the position of the acquisition areas using the example of LSC700. However, absolute distances of the acquisition areas vary slightly due to differing cathode layer thicknesses (compare **Section 3.3.1**).

Figure 3.16 shows the elemental compositions of LSC700 (**Figure 3.16b**), LSC700-100 (**Figure 3.16c**), LSC800 (**Figure 3.16d**) and LSC800-100 (**Figure 3.16e**) as a function of the position. Specified error bars result from statistical errors of the count rates (assuming, that the number of counts obey Poisson statistics, $\sigma_I = \sqrt{I}$) and statistical errors of the experimental determined $k_{A,B}$ -factors. The graphs show that the intended

composition of $\text{La}_{0.6}\text{Sr}_{0.4}\text{CoO}_{3-\delta}$ is achieved close to the LSC/CGO interface. As observed in the EDX mappings before, Co is enriched at the cathode surface due to the precipitation of Co-oxides, though, the gradient decreases with annealing time and temperature. Furthermore, La is slightly depleted at the surface, whereas there is no strong dependency of the Sr-content on the position in the LSC films. The increase in statistical errors in LSC700 (see **Figure 3.16b**) can be explained by decreasing TEM sample thickness towards the surface.

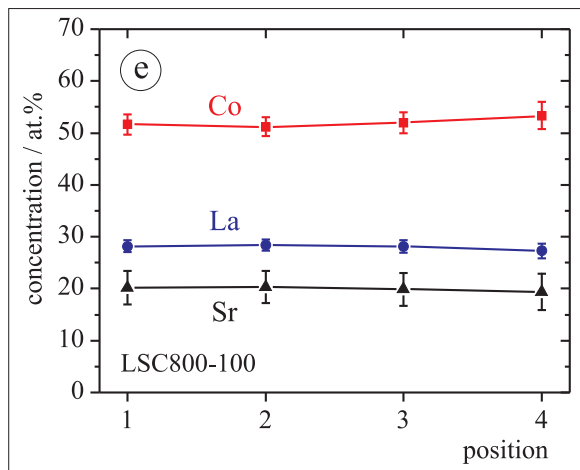
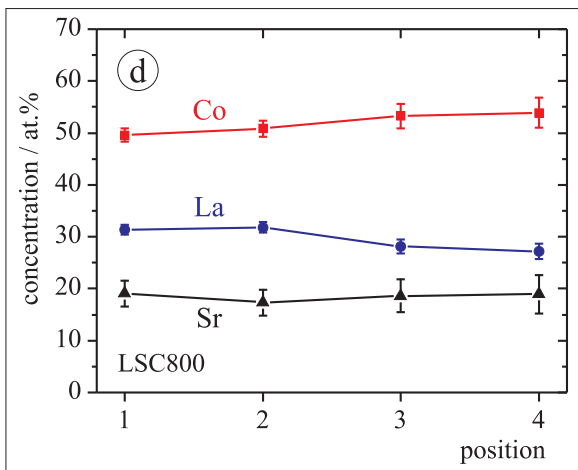
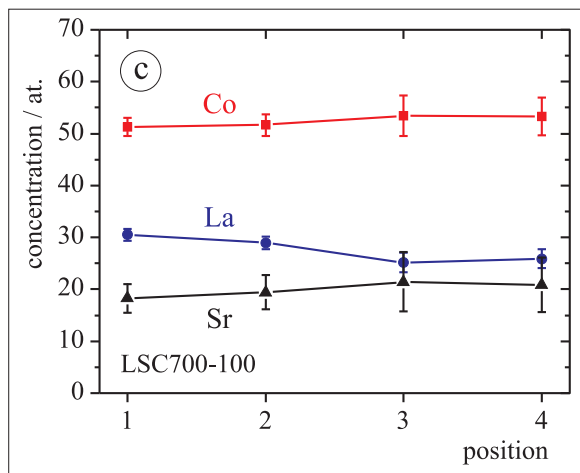
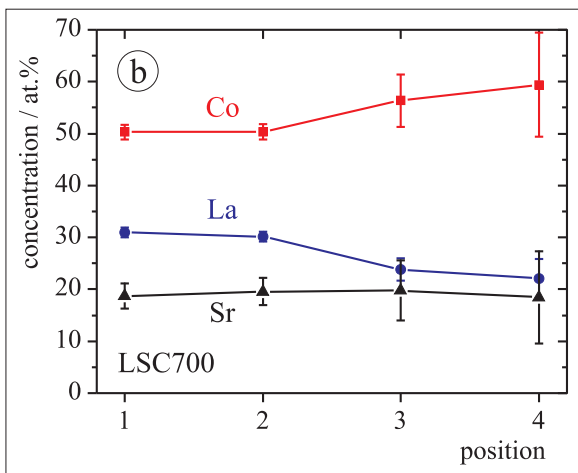
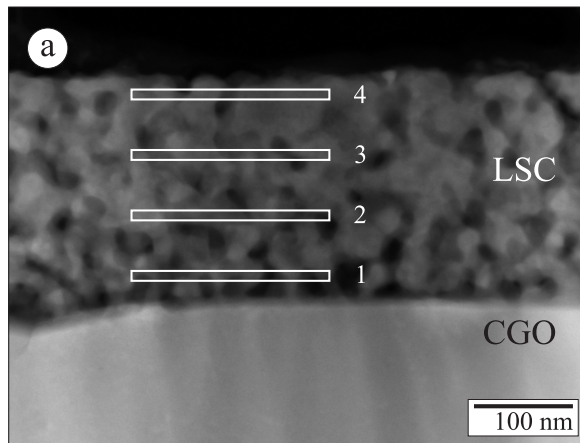


Figure 3.16.: a) Relative positions of acquisition areas within the cathode layer and quantitative La-, Sr- and Co-concentration profiles as a function of the position in the cathode film for b) LSC700, c) LSC700-100, d) LSC800 and e) LSC800-100.

3.4. Discussion

3.4.1. Microstructure

Isothermal grain growth

Isothermal grain growth usually follows a power law. Hence, normal grain growth can be described by

$$d^m - d_0^m = \gamma_0 \exp\left(-\frac{Q}{k_B T}\right) \cdot t$$

for a non-negligible initial grain diameter d_0 . Here, d is the average grain diameter after time t , d_0 is the average initial grain diameter and γ_0 is a weakly temperature-dependent constant. Q represents the activation energy for the predominant transport mechanism for grain boundary motion, k_B the Boltzmann constant and T the temperature, respectively [131]. In this case d_0 corresponds directly to the grain diameter after pyrolysis of the LSC thin-film cathode. The growth exponent m for ceramic materials is generally expected to vary between 2 and 4, depending on the predominant transport mechanism [132]. Unfortunately, none of the parameters could be satisfyingly determined on the basis of the actual number of data points (three different annealing times per temperature). Especially the integration of the d values for LSC700 and LSC800 causes difficulties, because the samples were slowly heated up and immediately cooled down after reaching T_{\max} . Thus, the duration for the heating up and cooling down procedure is a non-negligible factor which contributes to the grain growth.

Nevertheless, it can be concluded that grain growth is subjected to different growth mechanisms for $T_{\max} = 700^\circ\text{C}$ and 800°C because self-limited grain growth is observed for $T_{\max} = 700^\circ\text{C}$ (see **Figure 3.6**). At 700°C , the grain growth stagnates at a grain size of (28 ± 10) nm (LSC700-100), after an initial increase in grain size from (17 ± 5) nm (LSC700) to (27 ± 7) nm (LSC700-10). In contrast, grain sizes for $T_{\max} = 800^\circ\text{C}$ increase rapidly from (29 ± 10) nm (LSC800) to (90 ± 33) nm (LSC800-100) within the first few hours of annealing, accompanied with a nearly complete densification and, thus, destruction of the porous cathode structure. Self-limited grain growth during densification is well known and observed in different material systems. It is discussed in detail for example by Yan [133]. Peters [50] investigated this effect for $\text{La}_{0.5}\text{Sr}_{0.5}\text{CoO}_{3-\delta}$. Despite different growth mechanisms for the two different annealing temperatures, both series exhibit normal grain growth. Normal grain growth is characterized by a steady-state behavior, which means, that the grain-size distribution function is monomodal and has a time invariant shape [134]. Hence, the full width at half maximum (FWHM) scales with the mean grain size. Accordingly, standard deviation of the grain size scales too and was found to be $\sigma_d \sim 1/3d$ for all samples investigated in this work (compare **Table 3.3**).

Zener pinning [135, 136] may also contribute to a limitation of the LSC grain growth. It describes the influence of finely dispersed particles or precipitates on the movement of low- and high-angle grain boundaries through a polycrystalline material. The precipitates prevent motion of grain boundaries by exerting a pinning pressure, which counteracts the driving force of the grain-boundary motion and consequently limits grain

growth. To study this effect, Akashi et al. [137] characterized the grain-growth behavior of LaCoO_3 grains in 15 vol% Co_3O_4 -dispersed LaCoO_3 and 15 vol% La_2O_3 -dispersed LaCoO_3 films. They found, that abnormal grain growth of LaCoO_3 film is inhibited by dispersion of Co_3O_4 and grain growth in La_2O_3 -dispersed LaCoO_3 films is slower compared to pure LaCoO_3 . Sawada and Akashi [138] found no significant influence of the presence of Co_3O_4 on isothermal grain growth of $\text{La}_{0.6}\text{Sr}_{0.4}\text{CoO}_{3-\delta}$. Since the mean grain size of the Co_3O_4 precipitates in the vicinity of the surface correlates with the mean LSC grain size of the thin-film cathodes, Zener pinning is negligible in the actually investigated system. Hence, the predominant contribution to the observed limitation of isothermal grain growth at 700°C is attributed to the densification, as described above.

In previous work [108] $\text{La}_{0.5}\text{Sr}_{0.5}\text{CoO}_{3-\delta}$ thin-film cathodes were deposited on 3.5 mol% yttria-stabilized zirconia (YSZ) electrolytes and subjected to successive RTA steps at 170°C , 700°C and 900°C (15 min each), followed by an additional annealing step at temperatures between 700°C and 1000°C for 8 h. Compared to this work, the average grain size after calcination (LSC700) could be decreased by a factor of three in the present work. This is explained by reduction of the maximum processing temperature from 900°C to 700°C or 800°C , respectively. Westin et al. [139] also reported grain sizes in the range of 20 to 60 nm for $\text{La}_{0.5}\text{Sr}_{0.5}\text{CoO}_{3-\delta}$ after heat treatment at 800°C for 30 min, prepared by an alkoxide route. This is in good accordance with the values determined in this study for this temperature. Bansal and Zhong [140] determined a mean grain size of 15 nm after annealing (700°C for 2 h) of $\text{La}_{0.5}\text{Sr}_{0.5}\text{CoO}_{3-\delta}$ nanopowders prepared by low temperature combustion synthesis (between 300 and 400°C). The results of isothermal grain growth show that the fabrication of nanoscaled LSC cathodes is restricted to temperatures of 700°C (or lower), because fabrication at higher temperature results in a significant increase in grain size. Furthermore, the operation is limited to temperatures below 600°C because the microstructure coarsens within short time periods, as soon as the samples are subjected to temperatures higher than 700°C .

Porosity

The presence of the pores within the nanocrystalline LSC cathode layer can be explained by the metal-organic deposition process. During pyrolysis all organic components of the precursor are burned out. This results on the one hand in volume shrinkage of the film. On the other hand, a stream of gas consisting of carbon oxides and water leaves the cathode. This leads to the formation of a fragile, mechanically interlinked network of LSC grains. Gas channels and high open porosity pervades the whole cathode ($\phi = (38 \pm 10)\%$ for LSC700). In addition, a large surface area is achieved. Upon heat treatment, the LSC layers densifies accompanied by grain growth, resulting in almost dense LSC films after annealing at 800°C for 10 h (c.f. **Figure 3.6c** and **d**). Moreover, residual pores, located at the intersection of CGO grain boundaries with the electrolyte surface (see **Figure 3.3d, f** and **Figure 3.3d, f**), are observed in all samples. They are attributed to a non-optimal wetting of these substrate areas during dip-coating due to the surface tension of the sol.

Distinction between closed and open porosity is not possible due to the small size of the volume analyzed compared to pore and grain size. Furthermore, a significant amount of pores are intersected by the borders of the reconstructed volume. However, a large amount of porosity in LSC700 and partly LSC700-10 seems to be open porosity. However, the fraction of open porosity decreases with annealing time and temperature. Furthermore, the volume fraction of the Co_3O_4 precipitates in the cathode layer could not be determined, on the one hand due to small difference in contrast compared to LSC within the HAADF images, and, on the other hand, due to reconstruction artifacts affecting the local contrast.

Despite the great power of electron tomography for characterization of 3D microstructures, one should keep errors associated with the reconstruction process in mind. According to Radermacher [141, 142], the reconstructed volume significantly suffers elongation caused by the lack of data in the so called *missing wedge*. The elongation of the reconstructed volume takes place in the direction parallel to the electron beam (along the z -axis), which results in a distortion of features in that direction. The x -axis (parallel to the tilt axis) and y -axis (perpendicular to tilt axis and beam direction) remain unaffected. So, distance measurements in z -direction have to be taken with caution. Following expression is derived by Radermacher for the elongation factor e :

$$e = \sqrt{\frac{\alpha_{\max} + \sin \alpha_{\max} \cos \alpha_{\max}}{\alpha_{\max} - \sin \alpha_{\max} \cos \alpha_{\max}}}$$

with α_{\max} as maximum tilt angle. This implies for the maximum experimentally used tilt angle $\alpha_{\max} = \pm 70^\circ$ a theoretical elongation factor of $e = 1.3$. However, van Bavel and Loos [143] stated that experimentally observed elongations in z -direction are considerably smaller than those predicted by Radermacher. Their conclusion is based on experiments performed on spherical gold particles. An elaborate study by Kawase et al. [126] on the impact of the missing wedge for quantitative structural analysis confirm this finding. They carried out experiments on a rod-shaped FIB-cut sample of zirconia fillers in a polymer matrix that could be tilted in the full range of $\pm 90^\circ$. The elongation factor was determined to be 1.10 for $\alpha_{\max} = \pm 70^\circ$ and 1.23 for $\alpha_{\max} = \pm 60^\circ$ tilt. Since, volume ratios, respectively porosities, are invariant against transformation of coordinates, the described elongation has no effect on the porosity evaluation by electron tomography.

Crystalline phases and chemical composition

The experiments confirm LSC perovskite as the main crystalline phase. Nevertheless the formation of Co_3O_4 precipitates in the upper half of the film is detected. They are believed to be an intermediate phase occurring during pyrolysis. This is in accordance with high-temperature XRD analysis of Peters [50] who investigated the phase formation during pyrolysis of the propionic-acid based sol-gel preparation route with slightly differing stoichiometry of $\text{La}_{0.5}\text{Sr}_{0.5}\text{CoO}_{3-\delta}$. He observed that the solid-state reaction of the dried films started with the formation of cobalt oxide (Co_3O_4) during pyrolysis. The first indication for the Co_3O_4 phase is the detection of the most intense (1 1 3) reflection

at 550 °C. For temperatures of 700 °C and above, thermogravimetric analysis showed constant weight indicating the complete removal of the organic compounds and complete crystallization of the perovskite phase besides a minor amount of Co_3O_4 . This corresponds with the findings of Pohl and Westin [144], who investigated $\text{La}_{0.5}\text{Sr}_{0.5}\text{CoO}_{3-\delta}$ prepared by an alkoxide sol-gel route. Cizauskaite and Kareiva [145] investigated LSC samples with different Sr-concentrations, also fabricated by a sol-gel process, by X-ray diffraction. They demonstrated the formation of single-phase perovskite at temperatures between 900 and 1000 °C. During pyrolysis they identified metastable phases like Co_2O_3 , SrCO_3 and SrO up to 700 °C. Depending on the sol-gel chemistry, Co_3O_4 was also found up to 900 °C annealing temperature. Furthermore, Palcut et al. [146] showed that cobalt ions are very mobile. The mobility of the Co^{3+} -cations in LaCoO_3 dominates over the mobility of the La^{3+} -ions for bulk diffusion. Hence, the high mobility may also contribute to the formation of Co_3O_4 .

A formation of the Co_3O_4 phase throughout the TEM sample preparation could be excluded, because the grain size of Co-oxide corresponds to that of LSC and increases with annealing temperature and time. As preparation artifact, grain size of Co_3O_4 precipitates would be independent of the annealing temperature and distributed evenly over the thinned cathode film regions. Furthermore, formation of Co_3O_4 precipitates during pyrolysis of metal-organic deposited LSC significantly contributes to the formation of SrZrO_3 in case of Y_2O_3 -substituted ZrO_2 electrolytes [108]. The formation of Co_3O_4 as intermediate phase leads to an excess on A-site cations, favoring enhanced formation of an insulating SrZrO_3 phase. The formation of Sr- and La-rich phases like $(\text{La,Sr})_2\text{CoO}_4$ is expected in case of an used inert CGO substrate [35,36]. However, this phase could not be detected directly by Debye-electron diffraction, because the angular resolution of electron diffraction is not sufficient to resolve the peaks from those of the dominant perovskite phase. Slight variation of the Sr- and La-content (c.f. **Figure 3.12b** and **3.12c**) indicate the presence of such a phase. Heel et al. [147] for example observed the formation of $(\text{La,Sr})_2\text{CoO}_4$ in flame-sprayed $\text{La}_{0.6}\text{Sr}_{0.4}\text{CoO}_{3-\delta}$. The related La_2CoO_4 phase is also known to be formed if the perovskite-type LaCoO_3 is reduced at high temperatures [148]. A preferential cation evaporation which was detected by Kubicek et al. [149] by time of flight secondary ion mass spectroscopy (ToF-SIMS) and ICP-AES was not observed. They analyzed annealed LSC thin films deposited by PLD and found a significant increase of the Sr/La- and Sr/Co-ratio in the topmost 2–5 nm, which contributes to a decrease in electrochemical activity.

The deposited LSC films analyzed in this work seem to be stoichiometric within the error limits of EDXS, because the average composition over the complete film thickness determined by EDXS and ICP-AES measurements of the precursor prior coating coincide. Small gradients of Co- and La-concentrations are suggested to originate from differential gelification, drying and pyrolysis reactions for the different elements. Furthermore, gas species (CO_2 and H_2O) leaving the cathode during pyrolysis may influence the resulting phase composition, too. However, no indications for differential cation evaporation exist, because the gradient in stoichiometry is most pronounced in LSC700 and the composition homogenates with temperature and time. The nominal stoichiometry is observed in LSC800-100 along the complete film thickness.

sample	film thickness l	grain size d	porosity ϕ	$ASR_{\text{chem}}^\dagger$
LSC700	(176 ± 15) nm	(17 ± 5) nm	(38 ± 10) %	22 mΩ cm ²
LSC700-10	(167 ± 13) nm	(27 ± 7) nm	(31 ± 7) %	48 mΩ cm ²
LSC700-100	(128 ± 12) nm	(28 ± 10) nm	(18 ± 5) %	69 mΩ cm ²
LSC800	(135 ± 26) nm	(29 ± 10) nm	(18 ± 5) %	27 mΩ cm ²
LSC800-10	(112 ± 13) nm	(49 ± 15) nm	5 % [‡]	106 mΩ cm ²
LSC800-100	(131 ± 25) nm	(90 ± 33) nm	5 % [‡]	165 mΩ cm ²

[†]Hayd et al. [122]

[‡]not measured, estimated value

Table 3.6.: Compilation of all measured microstructural (film thickness l , grain size d and porosity ϕ) and electrochemical parameters (area-specific resistance ASR_{chem} , measured in symmetric cells at 600 °C in stagnant air).

3.4.2. Correlation of microstructure with electrochemical cathode performance

The electrochemical performance of the samples was evaluated by determining the area-specific polarization resistance ASR_{pol} by means of electrochemical impedance spectroscopy using a symmetrical cell setup with an micro-crystalline $\text{La}_{0.6}\text{Sr}_{0.4}\text{CoO}_{3-\delta}$ current collector ($D_{50} = 1.8 \mu\text{m}$). It represents the sums of all cathodic losses resulting from the electrochemical reactions ASR_{chem} and gas diffusion ASR_{gas} . As the latter strongly depend on the testing setup and may be partially caused by the current collector layer (especially at low oxygen partial pressures). They are not related to the thin-film cathode and are therefore not considered here. Electrochemical impedance spectroscopy (EIS) was performed under stagnant air in temperature steps of 25 K from 400 °C to 600 °C by means of a Solartron 1260 frequency response analyzer in a frequency range of $10^{-1} \text{ Hz} < f < 10^6 \text{ Hz}$. A detailed description of electrochemical characterization is outlined by Hayd et al. [122, 150, 151].

An exceptionally low area-specific resistance resulting from electrochemical reaction losses as low as $ASR_{\text{chem}} = 22 \text{ m}\Omega \text{ cm}^2$ was measured for LSC700 at 600 °C in stagnant ambient air [150, 151]. An even lower value of $9 \text{ m}\Omega \text{ cm}^2$ was achieved if dry synthetic air (a mixture of N_2 and O_2 ($P_{\text{O}_2} = 0.20 \text{ atm}$)) is used [122]. Minor concentrations of impurities such as CO_2 or H_2O in ambient air are assumed to cause this significant difference. The results of all samples in comparison with microstructural data are summarized in **Table 3.6**. The ASR_{chem} values increase with annealing temperature and annealing time. This is expected from the reduction of the open porosity which reduces the available active surface area for the electrochemical reaction, resulting in an increase of the area-specific polarization losses. According to Adler [152], the ASR_{chem} is inverse proportional to the volume-specific surface area in the case of a surface-controlled cathodic reaction.

However, the excellent cathode performance cannot be fully understood by the increase of the inner surface area resulting from the downscaled microstructure if theoretical mod-

els like the one-dimensional model of Adler [152] or the three-dimensional finite element model of R uger et al. [153] are applied for ASR_{chem} calculation. An improved oxygen surface exchange must be invoked to explain the low values. This effect becomes more obvious, if LSC700-100 is compared to LSC800. Both samples exhibit about the same cathode-layer thickness, grain size and porosity. However, the ASR_{chem} value of LSC800 is about 2.5 times smaller. The most significant difference in both samples is the volume fraction and density of the Co_3O_4 precipitates, which is higher in LSC800. Hence, it is suggested that the catalytic activity of small Co_3O_4 precipitates in the upper part of the LSC layers leads to an enhanced oxygen surface exchange as already shown by Zhang and Yang [154]. Yamahara and co-workers [155] also demonstrated that infiltrating a $\text{La}_{0.85}\text{Sr}_{0.15}\text{MnO}_3$ cathode with cobalt nitrate solution results in a performance improvement of about a factor of two. AC measurements revealed that this effect results from a reduced non-ohmic cathode resistance and AC impedance response showed a decrease of the effective charge-transfer resistance. Recently Chen et al. [156] published comparable results for Co_3O_4 -dispersed $\text{Ba}_{0.5}\text{Sr}_{0.5}\text{Co}_{0.8}\text{Fe}_{0.2}\text{O}_{3-\delta}$ IT-SOFC cathodes. They found that the addition of Co_3O_4 results in an increase of the electrical conductivity, improvement of the electrode activity for oxygen reduction and in a decrease of the activation energy for oxygen reduction.

The contribution of Co_3O_4 is most pronounced directly after pyrolysis (LSC700 and LSC800) where the highest density of small Co_3O_4 precipitates is present. After 100 h annealing the density of precipitates is already strongly reduced by coarsening of the grain structure. The reduction of precipitate density is clearly observed in the Co-maps (**Figure 3.12**) correlating with a distinct increase of ASR_{chem} from values below $30\text{ m}\Omega\text{cm}^2$ for LSC700 and LSC800 to values of $69\text{ m}\Omega\text{cm}^2$ for LSC700-100 and $165\text{ m}\Omega\text{cm}^2$ for LSC800-100.

4. Microstructure of epitaxial LaCoO_3 thin films

4.1. Introduction

3d-transition metal oxides (TMOs), like manganites, cuprates or cobaltates, exhibit a wide range of properties based on a variety of structural, electronic and magnetic phases. Among these materials cobalt-based oxides have recently received intense interest, both experimentally and theoretically. This family of compounds with mixed-valency possess a rich variety of phases, many with unusual macroscopic properties based on different interactions in the electron system (like Hund's coupling, double exchange or crystal field) competing on a similar energy scale. Among these compounds, cobaltates exhibit an additional degree of freedom regarding the spin state of the transition metal ion compared to the structurally related manganites and cuprates. This additional degree of freedom makes them even more interesting because three different spin states of the cobalt ion are possible. The crossover between the different spin states arises from a delicate interplay between crystal-field splitting Δ_{cf} within the CoO_6 octahedron, i.e. between the t_{2g} and e_g energy levels, and the intra-atomic exchange interaction (Hund's rule coupling) Δ_{ex} .

Especially the perovskite-type rare-earth lanthanum cobalt oxide LaCoO_3 (LCO) has recently attracted much attention due to its unusual electronic and magnetic properties at ambient pressure [13,157] and the observation of ferromagnetism in epitaxially strained thin films [158,159]. At low temperatures ($T \leq 35$ K) unstrained LCO is a non-magnetic semiconductor, with a ground state of Co^{3+} ions in low-spin (LS) configuration ($t_{2g}^6 e_g^0$, $S = 0$). This changes to a primarily intermediate-spin (IS) ($t_{2g}^5 e_g^1$, $S = 1$) state in the temperature range $35 \text{ K} < T < 100 \text{ K}$ and further to a mixture of IS and high-spin (HS) ($t_{2g}^4 e_g^2$, $S = 2$) states in the interval $300 \text{ K} < T < 600 \text{ K}$ [13,160–163].

Various effects influence the population of the different spin states. The balance between Δ_{cf} and Δ_{ex} is affected by, e.g., hole or electron doping [164], and by chemical or external pressure [165,166]. Since the crystal-field splitting is very sensitive to changes of inter-atomic distances r , because $\Delta_{\text{ex}} \propto r^{-5}$ [167], and the Co–O–Co bond angle γ , structural changes with respect to bond length and angle easily change the spin state of the Co^{3+} ion. For instance, a population of higher spin states in LCO films can be enhanced by tensile strain, as shown by Fuchs et al. [158].

Goals and outline

Goal of the present work was the study of growth and relaxation processes of epitaxially strained LCO films on cubic lanthanum strontium aluminum tantalum oxide (LSAT) $(\text{LaAlO}_3)_{0.3}(\text{SrAl}_{0.5}\text{Ta}_{0.5}\text{O}_3)_{0.7}$ substrates. While investigation using X-ray diffractometry provides only integral information over a large sample area, transmission electron microscopy allows a more detailed and site specific investigation of the local microstructure. This directly interpretable microscopic information facilitates the interpretation of complex X-ray diffraction data.

The results will contribute to a better understanding on the microstructural origin of the suppression of the ferromagnetic state in LCO with increasing rhombohedral distortion. More details on the magnetic properties of the investigated samples can be found in [3].

4.2. Sample preparation

Sample fabrication was performed by Dirk Fuchs (*Institut für Festkörperphysik*, Karlsruhe Institute of Technology) using pulsed-laser deposition (PLD). This technique is highly suited for the precise growth of multi-component oxides, especially for TMO like LCO.

The LCO target used for PLD was fabricated by citric acid sol-gel method. For this purpose, baked out La_2O_3 and metallic cobalt were dissolved separately in 30% HNO_3 . After mixing both solutions and complete dissolution of the chelating agent citric acid monohydrate ($\text{HOC}(\text{COOH})(\text{CH}_2\text{COOH})_2 \cdot \text{H}_2\text{O}$), ethylene glycol ($\text{C}_2\text{H}_6\text{O}_2$) was added as cross-linker. The achieved reagent is decomposed on a hot plate, followed by complete incineration in an oven. The resulting LCO powder was pressed into tablets and sintered at 1250°C for about 35 h. The expected crystal structure was verified at room temperature by means of X-ray diffraction (XRD) (Cu source equipped with Ni β -filter). The material was single-phase LCO, XRD-cell refinement confirmed the space group $R\bar{3}c$ with lattice parameters $a = 0.544$ nm and $c = 1.310$ nm according to data in literature. For epitaxial deposition of LCO on LSAT, a pulsed KrF-excimer laser beam (wavelength $\lambda = 248$ nm, pulse energy $E = 350$ mJ, pulse frequency $f = 5$ Hz) is focused onto the polycrystalline LCO target. This short-wavelength laser is used due to the strong absorption of LCO in the ultraviolet (UV) spectral range. **Figure 4.1a** shows the KrF-excimer laser setup, beamline and the target chamber with flange for the rotatable sample holder and different gas supplies.

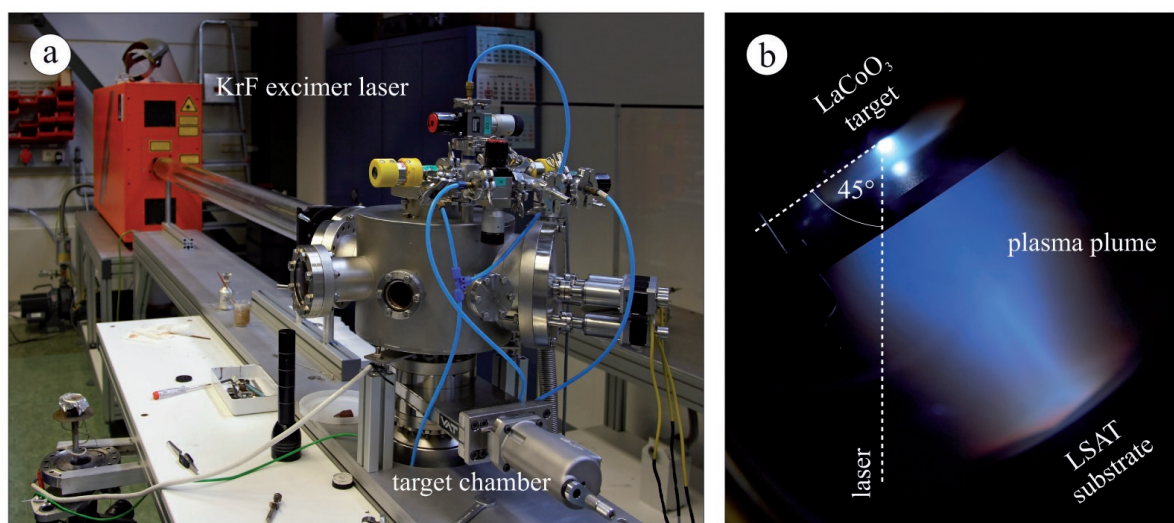


Figure 4.1.: a) Experimental setup for pulsed-laser deposition: KrF excimer laser, beamline and target chamber with supplies for different gases and b) originating plasma plume during laser ablation.

label	deposition parameters		
	$P_{\text{O}_2(\text{dep})}$	n_{ls}	$P_{\text{O}_2(\text{an})}$
LCO80	0.4 mbar	80	0.9 bar
LCO250	0.4 mbar	250	0.9 bar
LCO500	0.4 mbar	500	0.9 bar
LCO1000	0.4 mbar	1000	0.9 bar

Table 4.1.: LCO sample labeling and processing parameters

During deposition, the pulsed-laser beam strikes into the target and ablates an energetic plume of material, generally preserving cation stoichiometry, which precipitates on the substrate. The 5 mm x 5 mm single-crystalline LSAT substrates in [0 0 1] orientation are placed directly in the plasma plume during thin-film deposition to ensure a homogeneous film growth. **Figure 4.1b** shows the view into target chamber in top view during operation. The LSAT substrate is positioned opposite to the stoichiometric LCO target, which is struck by the laser under an angle of 45°. The originating plasma plume emerges perpendicular to the target surface.

While deposition, the LSAT substrates were heated to a temperature of $T_{\text{sub}} = 650^\circ\text{C}$ and the oxygen partial pressure was adjusted to $P_{\text{O}_2(\text{dep})} = 0.4\text{ mbar}$ to preserve the oxygen stoichiometry. The substrate temperature T_{sub} is a crucial parameter, because it provides the kinetic energy on the substrate surface, to ensure a perfect epitaxial growth. After deposition, the samples were cooled down to 500 °C, where they were kept for 30 min in $P_{\text{O}_2(\text{an})} = 0.9\text{ bar}$ oxygen atmosphere for a complete and homogeneous oxidation of the films.

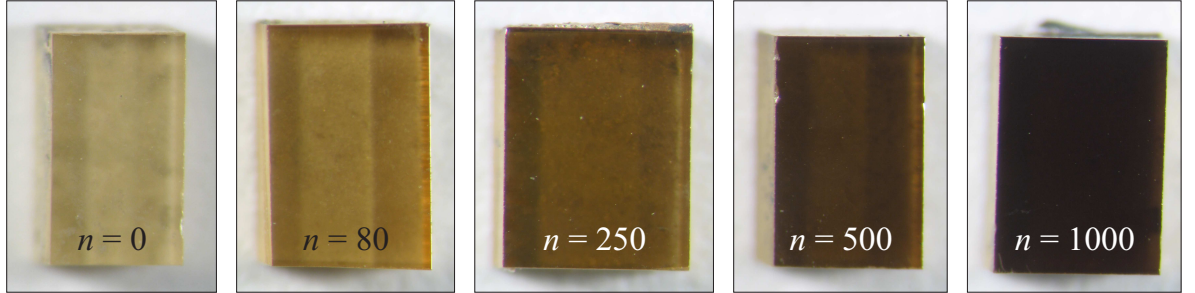


Figure 4.2.: LSAT substrate (as received, $n_{\text{ls}} = 0$) and coated with epitaxial grown LCO thin films using $n_{\text{ls}} = 80, 250, 500$ and 1000 laser shots on the LCO target for deposition.

Different film thicknesses were grown successively, using $n_{\text{ls}} = 80, 250, 500$ and 1000 laser shots on the LCO target. The samples are denoted as LCO80, LCO250, LCO500 and LCO1000 in the following. Processing parameters and sample labeling are summarized in **Table 4.1**. Small pieces (2 mm × 2.5 mm) of the prepared samples are depicted in

the photographs of **Figure 4.2** next to a piece of as-received LSAT substrate (left). The color changes with the number of used laser shots from yellow ochre ($n_{\text{ls}} = 80$) to nearly black/dark brown ($n_{\text{ls}} = 1000$) indicating the continuous increase of the LCO layer thickness.

4.3. Experimental results

The results of the microstructural characterization of epitaxial LCO films on LSAT substrates are presented in the following. The local investigation of microstructure was performed by means of TEM (Section 4.3.2), while structural properties such as out-of-plane c -axis lattice parameter and mosaic spread were analyzed by Dirk Fuchs employing X-ray diffraction (XRD) (Section 4.3.3). The film thickness was obtained from measurements with a Dektak profilometer, cross-section TEM bright-field images and X-ray diffraction if possible.

4.3.1. Geometric relation between deposited film and substrate

It is convenient to describe the rhombohedral perovskite structure of LCO in a pseudo-cubic representation. Especially in combination with a cubic substrate like LSAT it is advantageous to depict both structures in an analogous manner, because the relative orientation becomes more intuitive. The axes of the pseudo-cubic LCO unit cell correspond to those of the aristotype* perovskite, with lattice parameter a_{pc} and angle α_{pc} . The pseudo-cubic representation is marked with the index pc in the following. The rhombohedral lattice is formed by compressing the idealized cubic unit cell along one of the four body diagonals $\langle 111 \rangle$, i.e. $[111]$, $[\bar{1}\bar{1}1]$, $[\bar{1}1\bar{1}]$ and $[1\bar{1}\bar{1}]$, resulting in four different rhombohedral orientation variants, denoted by r_i ($i = 1 \dots 4$). The three rhombohedral basis vectors correspond to the $[110]_{\text{pc}}$, $[011]_{\text{pc}}$ and $[101]_{\text{pc}}$ direction in the pseudo-cubic representation. With the general dot product for non-rectangular coordinate systems the lattice parameter a_{pc} and angle α_{pc} can be calculated with the rhombohedral lattice parameter a_{rh} and angle α_{rh} :

$$\alpha_{\text{pc}} = \arccos \frac{1 - 2 \cos \alpha_{\text{rh}}}{2 \cos \alpha_{\text{rh}}} = 90.685^\circ$$
$$a_{\text{pc}} = \frac{1}{2} \sqrt{a_{\text{rh}}^2 (3 - 2 \cos \alpha_{\text{rh}})} = 3.826 \text{ \AA}$$

However, the experimental O–Co–O bond angle at room temperature is slightly larger $\alpha_{\text{pc,exp}} = 91.2^\circ$ [16,168]. The deviation is likely caused by the irregularity of the CoO_6 octahedra, i.e. different Co–O bonding lengths, caused by the Jahn-Teller distortion [169] and thus, related to the rhombohedral distortion. The geometric relation and the relative orientation between the rhombohedral LCO unit cell, its pseudo-cubic representation and the cubic LSAT substrate is depicted in **Figure 4.3**.

The LCO films were grown on (001)-oriented LSAT single-crystal substrates with a lattice constant of $a_{\text{sub}} = 3.865 \text{ \AA}$. Hence, the epitaxial LCO films experience an in-

* a high-symmetric structure, which can be viewed as an idealized version of a structure with lower symmetry. It was introduced by H. Megaw in relation to perovskites, where it is still mostly used. The cubic perovskite structure (adopted at most by half a dozen compounds) is regarded as the aristotype for the vast number of perovskites with lower symmetry, the so called hettotype structures.

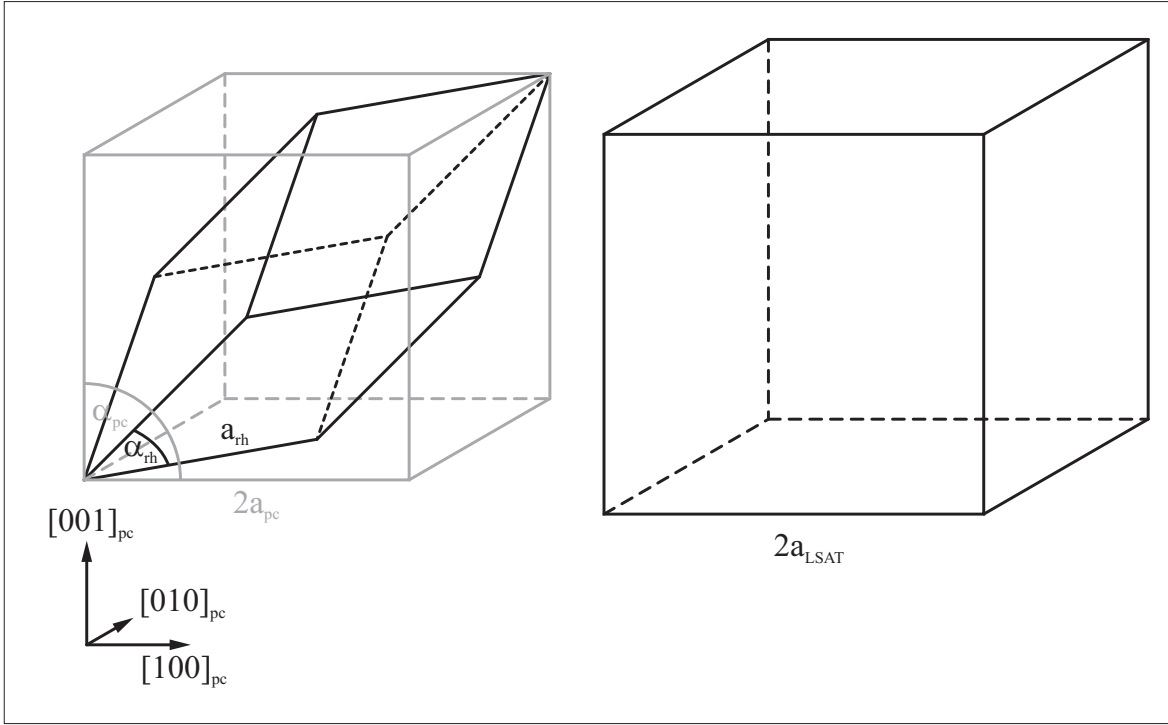


Figure 4.3.: Geometrical relation between rhombohedral LCO unit cell, its pseudo-cubic representation and the cubic LSAT substrate.

plane tensile lattice strain due to the lattice mismatch between LCO and LSAT. The mismatch ϵ between the substrate and the compound to be deposited is defined as

$$\epsilon = \frac{a_{pc} - a_{sub}}{a_{sub}} = -0.010.$$

where a_{pc} is the pseudo-cubic in-plane lattice parameter of LCO.

4.3.2. Microstructural characterization by electron microscopy

The ferromagnetic state of LCO can be changed by slight structural distortion. Since the crystal-field splitting Δ_{CF} is very sensitive to changes in the Co-O bond length and the Co-O-Co bond angle, structural changes modify the population of available spin states of the Co^{3+} -ion. Hence, the epitaxial LCO films were investigated by TEM to study the microstructure and the epitaxial quality of the LCO/LSAT interface in dependence of LCO film thickness. Based on the XRD results (presented in **Section 4.3.3**) two samples, LSC80 and LSC500, respectively, were chosen for detailed characterization.

The HRTEM cross-section micrograph (see **Figure 4.4a**) of LCO80 visualizes the abrupt and flat interface between epitaxial film and substrate. The image shows uniform contrast without formation of dislocations, anti-phase boundaries, domains or intermediate layers. The interface between LCO film and LSAT substrate is marked by red arrows.

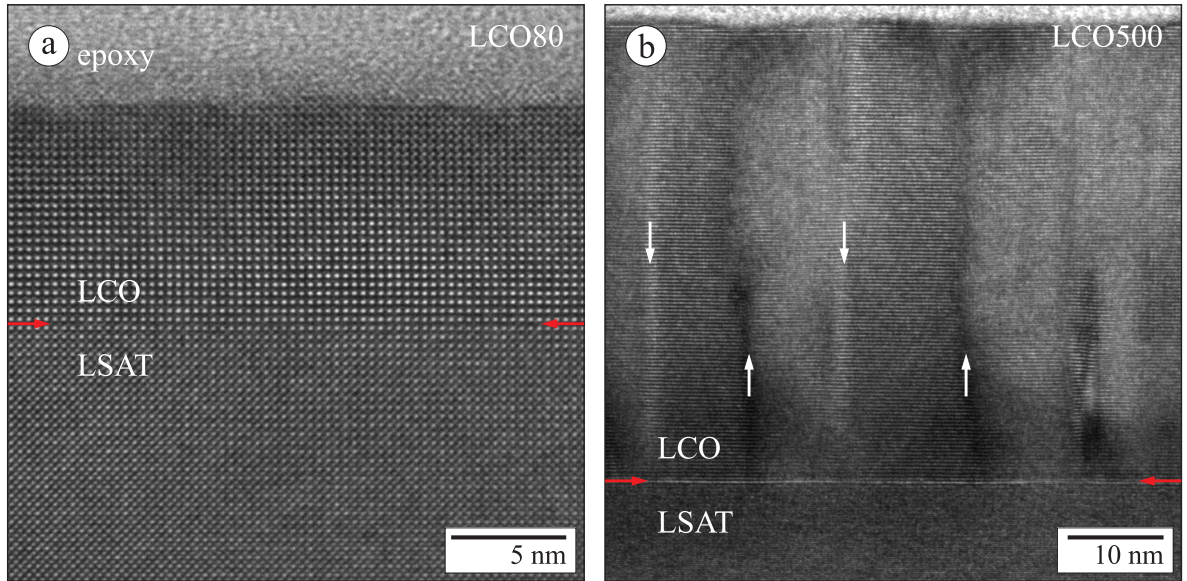


Figure 4.4.: a) High-resolution TEM image of LCO80 on (001) LSAT imaged along the [010] zone axis and b) lattice-fringe image of LCO500 imaged in $(002)_{pc}$ two-beam conditions along the [010] zone axis.

Figure 4.4b shows a $(002)_{pc}$ lattice-fringe image of LCO500 in a cross-section perspective obtained by the interference of the transmitted beam and the strongly excited $(002)_{pc}$. Due to the magnification of the image, only the brighter $(001)_{pc}$ fringes are visible. In contrast to LCO80, bright and dark bands (marked by white arrows) with diffuse contrast are observed perpendicular to the LCO/LSAT interface with an average periodicity of (19 ± 4) nm. Two different lattice inclinations (ascending and descending) are present within one period, changing at the bright or dark bands, respectively. The observed inclination is attributed to twin formation within the LCO film, while the bands represent the twin boundaries.

For further characterization of lattice plane inclination and modulation, $(001)_{pc}$ Bragg-filtered $(002)_{pc}$ lattice fringe images were evaluated by strain-state analysis using the digital analysis of lattice images (DALI) software package [170]. This facilitates the visualization of the local displacement of the $(001)_{pc}$ planes with respect to a reference lattice with the lattice parameter a_{sub} of the LSAT substrate. The evaluated local displacement is displayed in a color-coded map in fractional units of the LSAT (001) -plane distance a_{sub} . For better orientation, interfaces between epoxy/LCO and LCO/LSAT are marked by red arrows in the image. Lattice fringes observed in the amorphous epoxy layer are an artifact of digital image processing. No lattice modulation is detectable in the $(001)_{pc}$ lattice-fringe image of LCO80 (c.f. **Figure 4.5a**) by the naked eye.

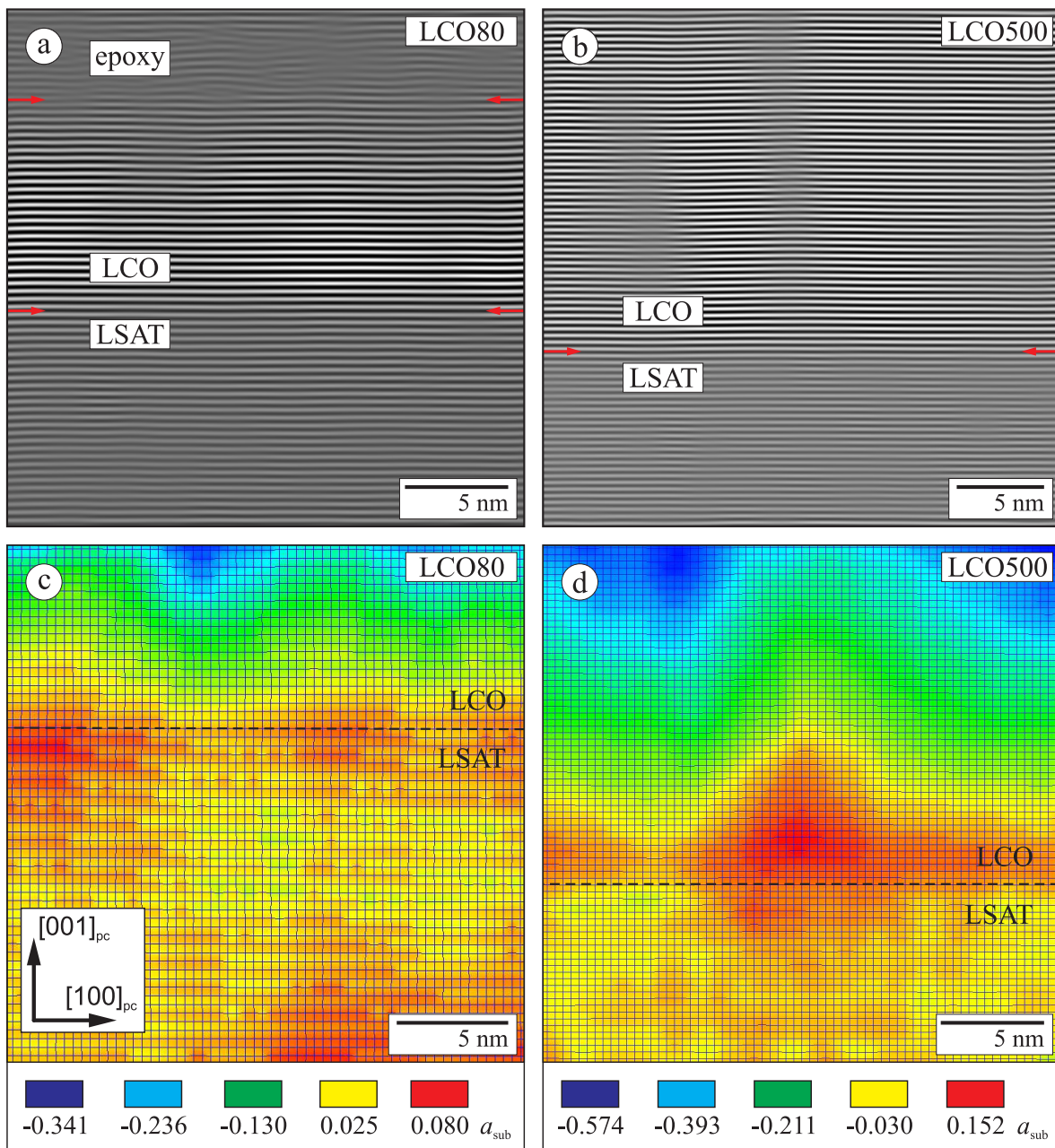


Figure 4.5.: High resolution Bragg filtered $(001)_{\text{pc}}$ lattice fringe of a) LCO80 and b) LCO500 and corresponding strain-state analysis of a) and b) showing the local displacement of the $(001)_{\text{pc}}$ planes with respect to a reference lattice with the lattice parameter a_{sub} of the LSAT substrate. The displacement is given in fractional units of a_{sub} .

However, the result of a strain-state analysis shown in **Figure 4.5c** reveals a sinusoidal lattice modulation perpendicular to the growth direction with a periodicity of (12 ± 2) nm, resulting in small rhombohedrally distorted regions merging fluently into another without formation of twins. This indicates that the epitaxial growth in the initial state is not pseudomorphic in a strict sense. In contrast, strain-state analysis of LCO500 (see **Figure 4.5d**) compared to LCO80 shows a more abrupt, zigzag-shaped inclination of the lattice planes, as expected for twin formation. For further characterization of the relative orientation of the lattice modulation with respect to the LSAT substrate, LCO80 was investigated in plan-view perspective. **Figure 4.6** shows TEM BF images of LCO80 as well as the corresponding diffraction patterns indicating the two-beam diffraction condition used for imaging close to the $[001]$ -zone axis. The bright-field micrograph **Figure 4.6a** was acquired in a $(110)_{pc}$ two-beam condition. Imaging conditions, respectively sample orientation relative to the incident electron beam, are depicted in **Figure 4.6b** (used aperture position for BF-imaging is marked by a dashed circle). The BF micrograph shows perpendicular oriented domains exhibiting a striped contrast. The domains/stripes are oriented along the pseudo-cubic $[100]_{pc}$ and $[010]_{pc}$ directions. The average stripe distance is about 15 nm. Beside domain boundaries between perpendicular oriented domains, boundaries between antiparallel domains are observed (marked in **Figure 4.6a** by red arrows), with lateral domain sizes between 50 nm and 200 nm. Furthermore, BF images in $(010)_{pc}$ and $(0\bar{1}0)_{pc}$ two-beam conditions and the corresponding diffraction patterns are displayed in **Figure 4.6c, d, e** and **f**, respectively. Within both BF micrographs only half of the domains are visible, indicating that the displacement vector \mathbf{R} of these lattice planes is perpendicular to the imaging vector as well as perpendicular to that of the invisible domains, according to the $\mathbf{g} \cdot \mathbf{R} = 0$ criterion [68]. **Figure 4.7a** shows the electron diffraction pattern of LCO and LSAT along the $[001]$ zone axis of the LSAT substrate using a $1 \mu\text{m}$ SAED aperture. Hence, different LCO domains contribute to the presented diffraction pattern due to the large size of the SAED aperture. Beside the major $\{h00\}$ and $\{hk0\}$ reflections of the LSAT substrate, weaker star-shaped satellite reflections are visible along the $[100]$ and $[010]$ direction in reciprocal space in the vicinity of the major reflections.

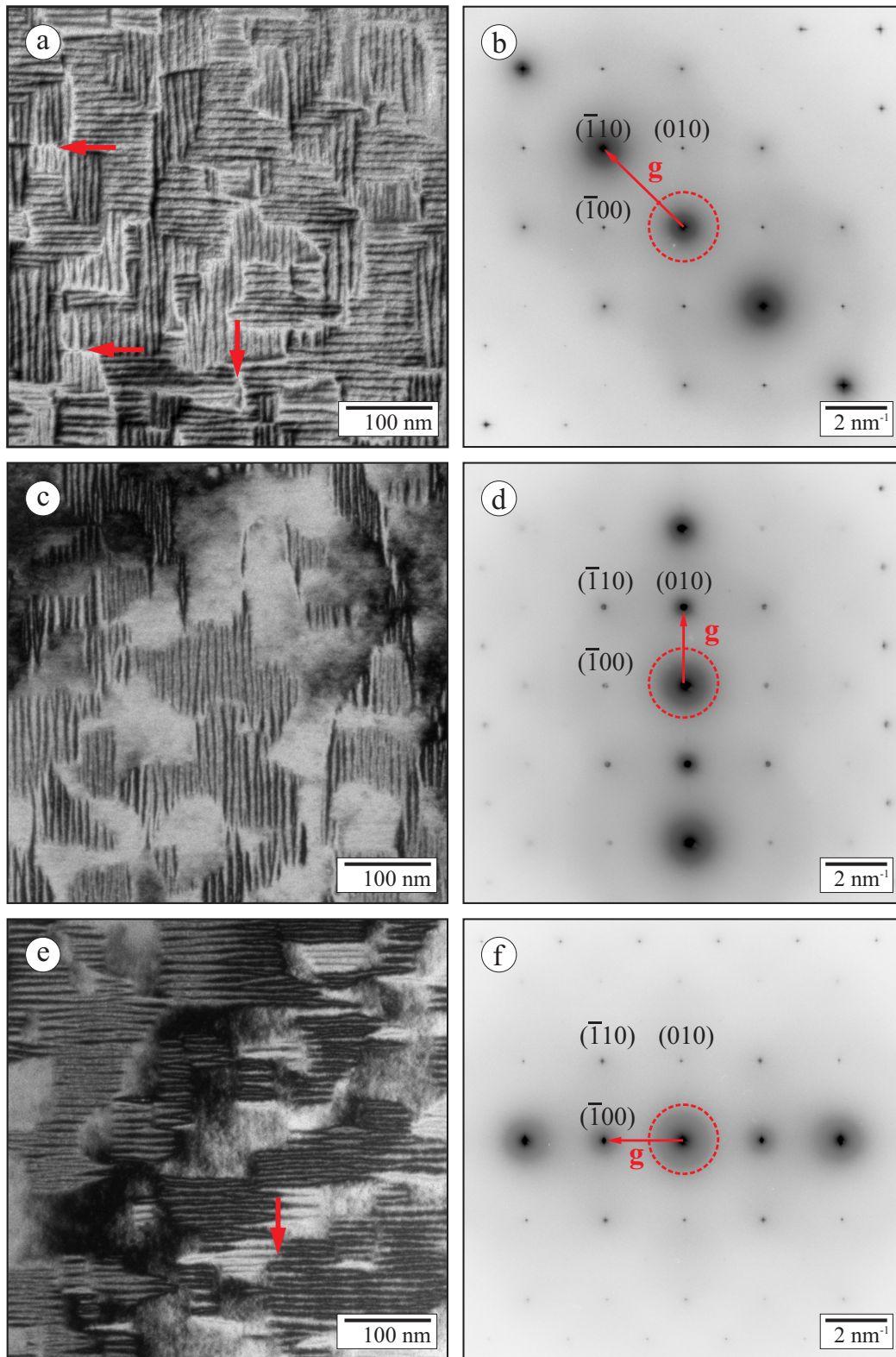


Figure 4.6.: TEM bright-field images (left column) and corresponding two-beam imaging conditions (left column) of LCO80.

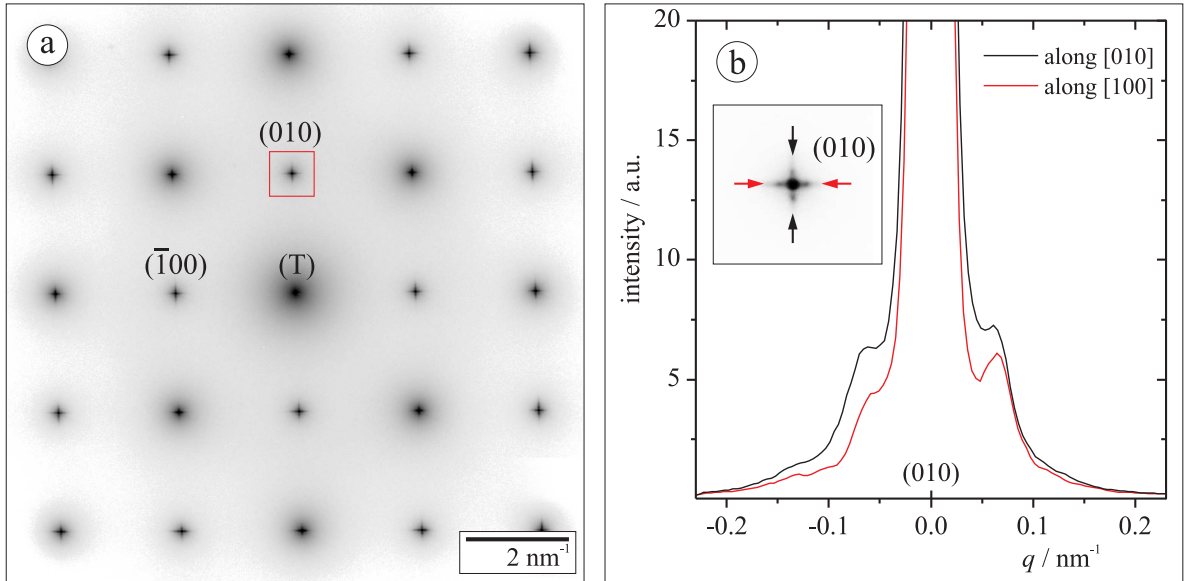


Figure 4.7.: a) Electron-diffraction pattern of LCO80 along the $[001]$ zone axis of the LSAT substrate and b) line-scan through the (010) reflection along $[100]$ and $[010]$.

The satellite reflections are more clearly seen in the inset of **Figure 4.7b**, which is an enlarged image of the area marked by a white box in **Figure 4.7a**. The periodicity of the structure was determined by analyzing the $(010)_{pc}$ -satellite reflections in more detail. **Figure 4.7b** shows two line scans through the $(010)_{pc}$ reflection along the $[100]_{pc}$ and $[010]_{pc}$ direction. Furthermore, an enlarged view, which corresponds to the area marked by a red square in **Figure 4.7a**, is given in the inset. Satellites were found to be present in both directions in a distance of $(0.069 \pm 0.003) \text{ nm}^{-1}$ from the substrate reflections. This indicates the presence of a long-periodic structure with a periodicity of $(14.4 \pm 0.5) \text{ nm}$ in real space. This value corresponds to the range of stripe periodicities observed for domains in **Figure 4.6a**. This slightly larger modulation periodicity compared to the periodicity derived from cross-section TEM images can be explained by stress relieve of LCO due to the small thickness or even complete loss of the LSAT substrate after plan-view TEM sample preparation. High strain and brittleness of thicker LCO films impedes the preparation of plan-view samples because fracture occurs during the preparation process.

4.3.3. Microstructural characterization by X-ray diffractometry

For determination of the structural properties of the epitaxial films such as the out-of-plane c-axis lattice parameter and the mosaic spread, $\theta/2\theta$ -scans and rocking curves were carried out by Dirk Fuchs using a two-circle x-ray diffractometer in Bragg-Brentano geometry. A four-circle x-ray diffractometer was used to determine the in-plane lattice parameters (see also [3]).

Due to the negative lattice mismatch between the pseudo-cubic LCO and cubic LSAT substrate, the films adopt a pseudo-tetragonal structure with $a_f \approx a_{\text{sub}} > c_f$ where c_f is the out-of plane lattice parameter of the LCO film [159]. The nearly perfect and defect-free pseudomorphic growth resulted in a mosaic spread of the LCO films, which is comparable to that of the single-crystal substrates. The mosaic spread was measured by full width at half maximum (FWHM) of the rocking curves of the $(00l)_{\text{pc}}$ film reflections. A non-elastic structural relaxation usually comprises structural lattice distortions, which lead to an increase in the mosaic spread $\Delta\omega$ of the film. **Figure 4.8a** shows rocking curves of the $(002)_{\text{pc}}$ reflection of the epitaxial LCO films for different film thicknesses (LCO80 to LCO1000). Besides the central peak at $\omega_0 \approx 23^\circ$ with a narrow line width of $\Delta\omega_0 = 0.2^\circ$, broad satellite peaks occur symmetrically with respect to the central peak. Rocking curves for different diffraction orders of LCO80 and LCO1000 are shown in **Figure 4.8b** and **Figure 4.8c**. For the thinner film (LCO80), only the first-order satellite peaks are visible symmetrically at both sides of the $(00l)_{\text{pc}}$ reflection indicating a rather short correlation length. Furthermore, the small LCO film thickness also contributes to the low intensity of the satellites and the absence of higher-order satellites. The angular difference between $(001)_{\text{pc}}$ central peak and the first-order satellites is l -times longer than for the higher order $(00l)_{\text{pc}}$ central peaks, indicating a periodic in-plane modulation. The modulation length as given by Gebhardt [171] is determined by

$$D = \frac{1}{\Delta q_x}$$

where Δq_x is the satellite spacing in reciprocal-lattice units. Since only first-order satellites are observed, Δq_x is approximated by the spacing between the central peak and the first-order satellite peak. Thus, the determined D values represent the modulation length to a limited extend. In **Figure 4.9a** the modulation length D is plotted as a function of the film thickness. For $t = 8$ nm, D is about 8 nm and increases with increasing t to roughly 22 nm for $t = 50$ nm, where it seems to saturate. Discrepancies with respect to the TEM data (open symbols in **Figure 4.9a**) can be explained by the small regions which are analyzed by TEM imaging.

In contrast, rocking curves of the thick film $t = 100$ nm show pronounced satellite peaks at 0.65° , independent of diffraction order. The peaks are attributed to macroscopic twin domains, caused by tilted $(001)_{\text{pc}}$ lattice planes with a twinning angle of 0.65° . Furthermore, faint satellite peaks arising from the periodic modulation are also present, which indicate a relationship between both structures. **Figure 4.9b** documents the twinning angle as a function of t . Only films with $t > 15$ nm displayed macroscopic twin domains with $\alpha \approx 0.65^\circ$. The observed twinning angle corresponds to the twinning angle of bulk LCO, $\beta = 90^\circ - \alpha_{\text{pc}}$, with the pseudo-cubic angle $\alpha_{\text{pc}} = 90.7^\circ$ and thus documents a relaxation toward the rhombohedral structure.

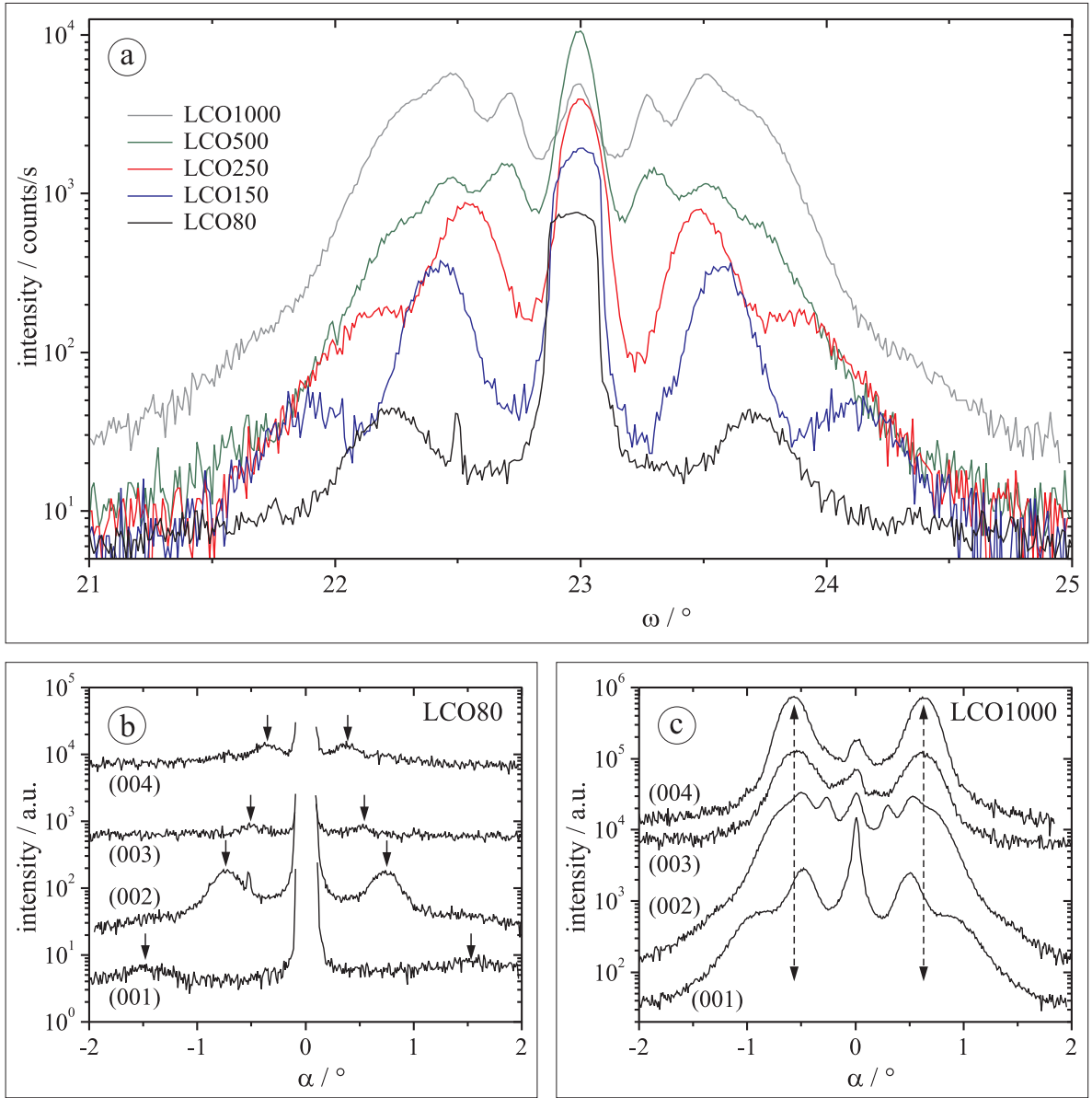


Figure 4.8.: Rocking curves a) at the $(002)_{pc}$ LCO reflection for different film thicknesses and for different orders of Bragg reflections for b) LCO80 and c) LCO1000 [3]. The intensity is plotted for b) and c) as a function of $\alpha = \omega - \omega_0$, where ω_0 corresponds to the position of the central peak. Satellite peaks caused by periodic twinning modulation and lattice-plane tilt are marked by arrows.

The c -axis lattice parameter determined from the $\{00l\}$ Bragg reflections of $\theta/2\theta$ scans does not change for films in the thickness range $15 \text{ nm} < t < 100 \text{ nm}$, i.e., $c_f = 3.78 \text{ \AA}$. For the in-plane lattice parameter a_f we observe only minor changes with respect to the substrate value $a_{\text{sub}/2} = 3.865 \text{ \AA}$. Therefore, the pseudo-tetragonal unit-cell volume $V = c_f \times a_f^2 \approx 56.5 \text{ \AA}^3$ is nearly constant for $t \leq 100 \text{ nm}$ (cf. **Figure 4.9c**). A noticeable increase to $c_f = 3.80 \text{ \AA}$ is only observed for films with $t > 120 \text{ nm}$. An investigation of the corresponding in-plane film lattice parameters reveals a strong relaxation of a_f as well. The films always show numerous macroscopic cracks, which are possibly caused by volume shrinkage, twinning, and corresponding local strain concentration. The cracking leads to some kind of exfoliation of the film from the substrate that strongly affects the mosaic spread. Hence, measurements on films with $t > 120 \text{ nm}$ were discarded for the following experiments. The volume fraction of the nearly homogeneously strained pseudomorphic part and the twinned (rhombohedrally distorted) part of the film is determined by integrating the rocking curves (see **Figure 4.8a**). The pseudomorphic part is proportional to the area of the central peak at ω_0 , whereas the twinned part is proportional to the area of the satellite peaks. For the central peak at ω_0 the $[001]_{\text{pc}}$ film direction is exactly parallel to the $[001]$ direction of the substrate. Hence, the narrow peak can be attributed to the pseudomorphic part of the film. The satellite peaks originate from a periodic-twinning modulation and nanotwinning and are thus caused by a partial relaxation of strain towards the rhombohedral structure of bulk LCO.

Figure 4.9d visualizes the decrease of the pseudomorphic (PM) volume fraction of the film as a function of t in comparison with the twinned (TW) volume fraction. The PM volume fraction decreases almost linearly up to a film thickness $t = 15 \text{ nm}$. For $t > 15 \text{ nm}$ the reduction of the PM volume fraction is less pronounced. The functional behavior indicates that the film does not grow completely pseudo-tetragonal up to a certain critical film thickness t_{crit} at which the pseudomorphic growth stops and above which the film starts to relax. For comparison, **Figure 4.9d** also shows the functional relation for a simple two-stage growth model (plotted as dashed line). In the first stage $t \leq t_{\text{crit}}$ a pure pseudomorphic and for $t > t_{\text{crit}}$ a fully relaxed growth with $t_{\text{crit}} = 15 \text{ nm}$ has been assumed. In the latter case, the PM volume fraction f_{PM} is calculated by

$$f_{\text{PM}}(t) = \frac{V_{\text{PM}}}{V_{\text{tot}}} = \frac{V_{\text{PM}}}{V_{\text{PM}} + V_{\text{relaxed}}} = \frac{t_{\text{crit}}}{t}$$

However, this model fits the observed behavior only to a limited extend. Moreover, it seems that nanotwinning occurs from the initial stage of growth, however, in an only moderate way, making the relaxation more gradual. This is obtained by periodic twinning modulation, whereas pseudomorphic regions in the films still grow well up to at least several tenths of nanometers.

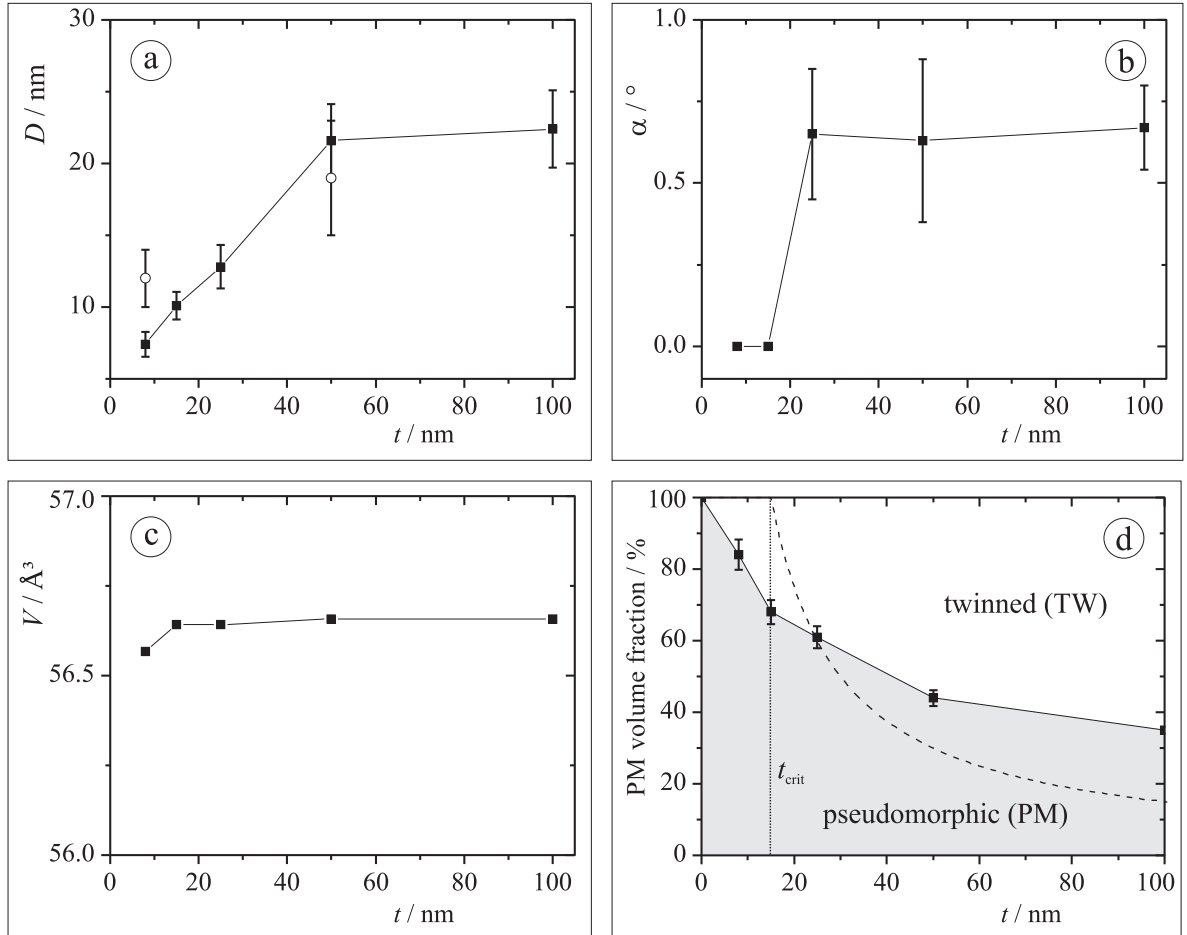


Figure 4.9.: a) The modulation length D of the periodic in-plane structure and b) the domain twinning angle α as determined from rocking curves versus the film thickness t . D values as extracted from TEM measurements are shown by open symbols. c) The pseudo-tetragonal unit-cell volume $V = c_f \times a_f^2$ of the LCO films versus t and d) the pseudomorphic (PM) volume fraction of the LCO film in dependence of the film thickness t . Courtesy of Dirk Fuchs [3].

4.4. Discussion

4.4.1. Microstructure

All films show single-phase $(001)_{\text{pc}}$ -oriented cube-on-cube growth, i.e., the in-plane directions of the film $[100]_{\text{pc}}$ and $[010]_{\text{pc}}$ are nearly parallel to $[100]$ and $[010]$ direction of the LSAT substrate. In the initial stage of growth the films usually show a pseudomorphic (PM) growth mode where the film adopts structural properties and symmetry of the substrate material within the growth plane with an in-plane film lattice parameter $a_f = a_s$. Perfect coherence of the lattice planes across the interface suggests that the misfit accommodation is purely elastic. Besides such an elastic accommodation of substrate-induced stress, perovskites also often show interfacial dislocations, the formation of antiphase domains or even phase transitions to relieve epitaxial strain. Most of these structural-phase transitions to lower symmetry are accompanied by twin formation. Symmetry breaking induced by phase transition gives rise to energetically equivalent domain states in the low-temperature phase which are mapped onto each other by the symmetry elements which are lost with respect to the prototype symmetry [172]. In particular, perovskites such as LaAlO_3 , $\text{La}_{1-x}\text{Sr}_x\text{MnO}_3$ or LCO, which undergo a displacive phase transition from a paraelastic cubic perovskite at high temperatures to a ferroelastic rhombohedral structure, usually show ferroelastic domains formed by deformation twinning [173, 174].

According to Streiffer et al. [175], the observed domain structure is explained by a combination r_i/r_j of two of the four structural variants r_1, r_2, r_3 and r_4 (c.f. **Section 4.3.1**) with respect to the orientation to the substrate. This results either in the formation of (100) or (110) -domain walls. In the actually investigated LCO thin films, (100) -domain walls are observed (see **Figure 4.6**). Possible r_i/r_j combinations and resulting domain patterns with $\{100\}_{\text{pc}}$ -twin planes are shown in a projection along the $[001]$ direction of the LSAT substrate in **Figure 4.10**. The different orientation variants of the pseudo-cubic $(111)_{\text{pc}}$ axis are represented by black arrows in the graph. The epitaxial growth of rhombohedral LCO on the cubic LSAT substrate results in a displacement of the LCO lattice sites along the $[100]$ and $[010]$ direction compared to the LSAT substrate when viewed along $[001]$. This slight displacement compared to the substrate explains the observed contrast behavior of the different domains. According to the invisibility criterion $\mathbf{g} \cdot \mathbf{R} = 0$ [68], where \mathbf{g} is the imaging vector and \mathbf{R} the displacement, r_1/r_2 and r_3/r_4 domains are invisible using a (100) -imaging vector (**Figure 4.6e, f**), while the r_2/r_3 and r_1/r_4 domains are observable. Vice versa, r_2/r_3 and r_1/r_4 domains are not observable using a (010) -imaging vector, while the r_1/r_2 and r_3/r_4 domains are visible (**Figure 4.6c, d**).

Rocking curves similar to those observed in this work were published for manganite films grown on (001) SrTiO_3 by Gebhardt et al. [171] recently. They were discussed in terms of periodic twinning modulation waves and twin domains. For thin films ($t = 26$ nm) the authors observed satellites with a constant in-plane momentum transfer implying a periodic height modulation with an in-plane periodicity of $D \approx 13$ nm. This was found also by Jin et al. [176] for $\text{La}_{0.7}\text{Sr}_{0.3}\text{MnO}_3$ on (001) LSAT. For thick films ($t = 88$ nm), the ω

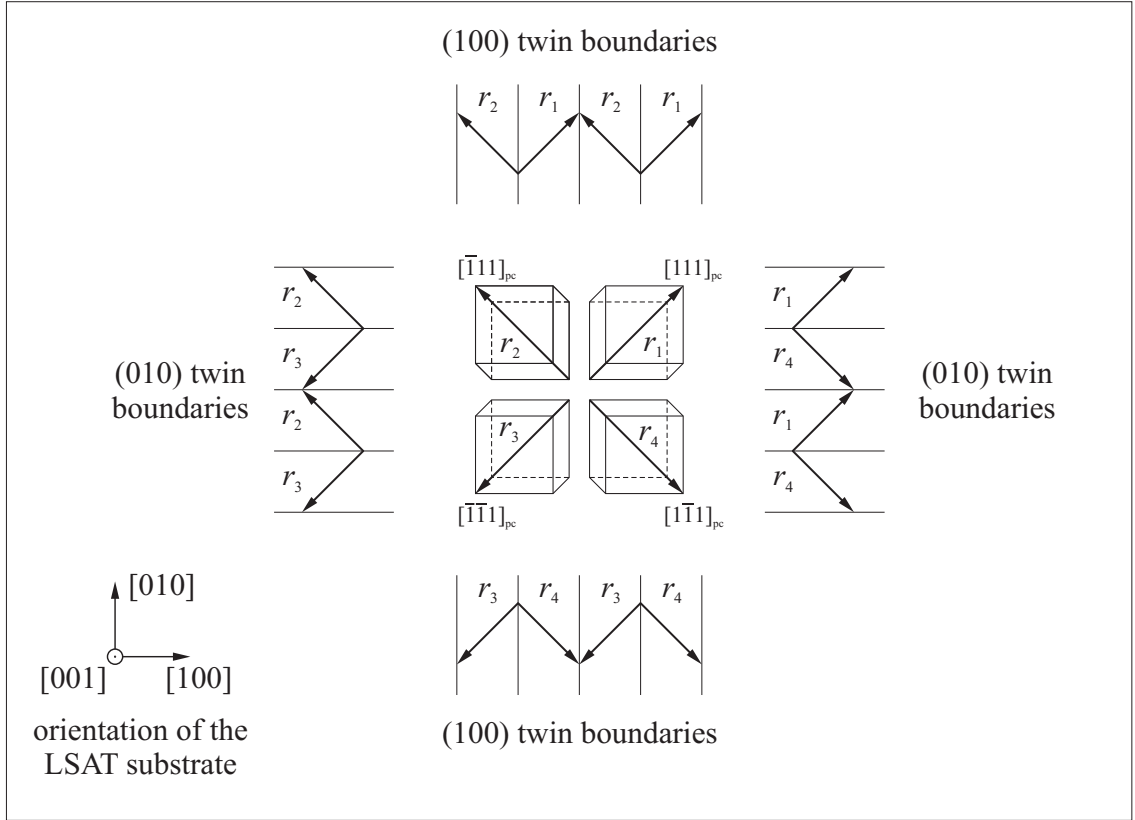


Figure 4.10.: $\{100\}$ - r_i/r_j twin patterns shown in projection along the $[001]$ direction of the LSAT substrate. The different orientation variants are shown in projection by the sense of arrows (based on [175]).

position of the satellites was found to be independent of the diffraction order, indicating individual twin domains with $(001)_{pc}$ lattice planes tilted by 0.5° with respect to the surface [171]. Beside the nanotwinning (LCO500), elastic lattice modulation is detected in LCO80. This is believed to be a prestage of the nanotwinning. This behavior is observed in many other systems. Vailionis et al. [177] for example investigated $\text{La}_{0.67}\text{Sr}_{0.33}\text{MnO}_3$ and SrRuO_3 on various single-crystalline substrates by XRD. They assume that the unit cells have a periodic displacement along the out-of-plane direction $[001]$. Using this as an input for their kinematical XRD model, they were able to reproduce all features of the XRD spectra: main Bragg peak, satellite peak positions, intensities and peak widths using the modulation amplitude and a slightly varying periodicity as parameters. However, simulations using a displacement along the $[110]$ direction did not reproduce the results satisfyingly, indicating that unit-cell displacements occur only along the out-of-plane direction. This is consistent with a coherent layer growth on a single-crystal substrate. Vailionis et al. [177] believe that the observed lattice response to epitaxial strain is of general nature and can be applied to other perovskite-type materials that possess orthorhombic or rhombohedral structures. Their structural model corresponds well with the results of strain-state analysis in this work.

4.4.2. Correlation with magnetic properties

The magnetic properties of the LCO films were studied using a superconducting quantum interference device (SQUID) system from Quantum Design. The measurements were performed by Dirk Fuchs. To determine T_C and m_{eff} , field-cooled (FC) magnetization measurements were carried out in the temperature range $4\text{ K} \leq T \leq 150\text{ K}$. The external field strength of $\mu_0 H = 20\text{ mT}$ was applied parallel to the film surface. To correct the diamagnetic contribution of the LSAT substrate, it was determined in separate experiments and subtracted from the magnetization data. To deduce the saturated moment m_s in the FM state, magnetization measurements as a function of external field were performed up to $\mu_0 H = 7\text{ T}$ at $T = 10\text{ K}$.

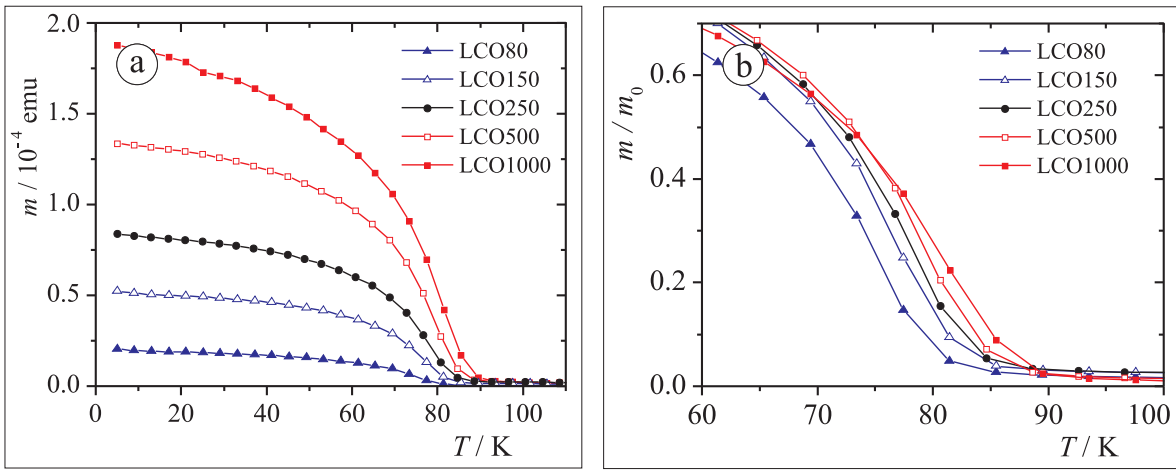


Figure 4.11.: a) Magnetic moment m and b) normalized magnetic moment m/m_0 as a function of the temperature T for LCO80, LCO150, LCO250, LCO500 and LCO1000, respectively. m_0 corresponds to the magnetic moment at $T = 5\text{ K}$. The field-cooled measurements were carried out using a field strength of $\mu_0 H = 20\text{ mT}$, applied parallel to the film surface [3].

Figure 4.11a displays field-cooled measurements of the magnetic moment m as a function of temperature for LCO80 to LCO1000. The magnetic moment increases with increasing film thickness due to increasing volume fraction of magnetic material, whereas the Curie temperature decreases with film thickness from $T_C \approx 87\text{ K}$ for LCO500 to $T_C \approx 80\text{ K}$ for LCO80. The Curie temperature T_C of the ferromagnetic (FM) phase transition was determined by extrapolating the magnetic moment to $m = 0$. There is a clear reduction in T_C with decreasing t . For clarification, **Figure 4.11b** shows the normalized magnetic moment m/m_0 versus T for films with different film thickness, where m_0 corresponds to the magnetic moment at $T = 5\text{ K}$. The Curie temperature decreases with film thickness from $T_C \approx 87\text{ K}$ for LCO500 to $T_C \approx 80\text{ K}$ for LCO80.

This decrease in T_C with decreasing film thickness is explained by the finite-size effect [178]. The rather broad FM transition may be also caused by this effect. A scaling analysis of T_C for the LCO films indeed results in the expected power-law scaling:

$$\frac{T_C(\infty) - T_C(t)}{T_C(\infty)} \propto t^{-\lambda}.$$

The critical shift exponent was determined to be $\lambda \approx 1$. Previous investigations by Fuchs et al. [164, 179] and Ziese et al. [180] on hole-doped cobaltates $\text{La}_{0.7}\text{A}_{0.3}\text{CoO}_3$ ($\text{A} = \text{Ca}, \text{Sr}, \text{Ba}$) as well as on $\text{La}_{0.7}\text{Ca}_{0.3}\text{MnO}_3$, respectively, revealed a power-law scaling with the same exponent. Hence, this behavior seems to be typical for FM cobaltate and manganite thin films. Besides the finite-size-effect epitaxial strain, structural phase transitions and microstructural deficiencies can also cause a reduced T_C . However, since the crystalline quality and epitaxial strain increases with decreasing t , these effects can be excluded. In addition, previous results have shown that an increase in tensile strain leads to an increase in T_C . The effective paramagnetic moment per Co-ion m_{eff} , deduced from the magnetic susceptibility above 100 K is $m_{\text{eff}} \approx 3.8 \mu_B$ and stays constant over the investigated thickness range.

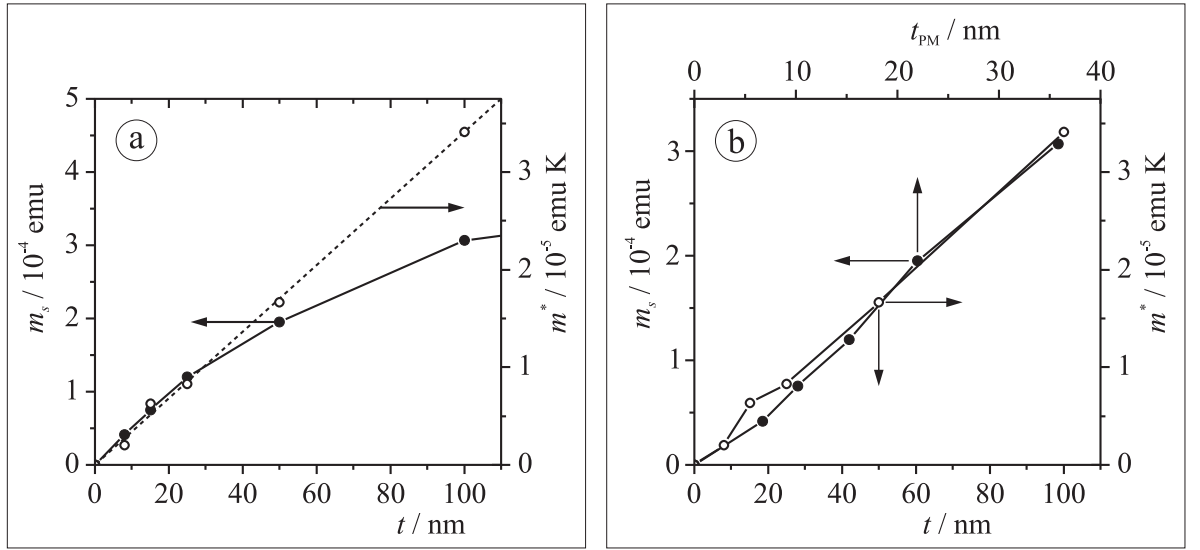


Figure 4.12.: a) Saturated ferromagnetic moment m_s at $T = 10$ K and $m^* = \partial m / \partial \frac{1}{T}$, which is proportional to the square of the effective paramagnetic moment above T_C and the film thickness, i.e. $m^* \propto t \times m_{\text{eff}}^2$, as a function of the film thickness t . b) Linear behavior of m and m_s in dependence of t and t_{PM} , respectively. $t_{\text{PM}} = t \times \text{PM}$ corresponds to an effective pseudomorphic thickness and PM is the pseudomorphic volume fraction of the LCO film [3].

In **Figure 4.12a** the slope $m^* = \partial m / \partial t$ for $T > 100$ K is plotted over the film thickness t . Assuming that the Curie-Weiss law is valid, m^* is determined by

$$m^* = \frac{n_{\text{Co}} H m_{\text{eff}}^2}{3k_{\text{B}}}$$

where n_{Co} is the number of Co-atoms and k_{B} the Boltzmann constant. Since n_{Co} is proportional to t , the slope of m versus t is proportional to m_{eff}^2 . The linear increase in m vs. t demonstrates the constant behavior of m_{eff} over the measured thickness range. The effective paramagnetic moment is determined by the angular momentum J , i.e. $m_{\text{eff}} \propto \sqrt{J(J+1)}$ and therefore strongly related to the spin state of the Co^{3+} -ion. Thus, the spin state above 100 K is constant over the investigated thickness range. In contrast, a cracked film with $t = 216$ nm, which contains a significant amount of fully-relaxed bulk-like material, shows a clear reduction of m by about 30 % with respect to the expected value from the linear increase in m vs. t . For bulk LCO m_{eff} amounts to about $2 \mu_{\text{B}}$ per Co-ion [181, 182]. Therefore, m_{eff} seems to depend more strongly on the unit-cell volume, which is nearly constant for $t \leq 120$ nm, than on the rhombohedral distortion which clearly proceeds with increasing t . The experimental findings are consistent with the generalized gradient-corrected density-functional calculations (GGA+U) by Knížek et al. [181], who calculated the dependence of the magnetic state of LCO on crystal structure parameters. Structures without a rhombohedral distortion $\alpha_{\text{pc}} = \eta = 90^\circ$ were compared to analogous structures with maximum observed rhombohedral deformation of $\eta = 91.5^\circ$, i.e. bulk LCO at $T = 4$ K. The calculations show that the effect of the rhombohedral distortion on the spin state is rather small. The authors found a rather abrupt transition from the LS to the IS state above $T \geq 100$ K ($\eta = 91.4^\circ$). The O–Co–O bond angle decreases only slightly to $\eta = 91^\circ$ at 700 K, indicating that the IS state is also stable in the presence of small rhombohedral distortions. A stabilization of the IS state of Co^{3+} was also found for an increasing unit-cell volume by Ravindran et al. [183]. The increased unit-cell volume of the LCO films, compared to that of bulk LCO, is nearly constant for $8 \text{ nm} \leq t \leq 100 \text{ nm}$. Therefore, m_{eff} does not change for $t < 100$ nm, even though a rhombohedral distortion is present in some part of the film. In contrast to the constant m_{eff} in the paramagnetic state above T_{C} , the magnetization in the FM state at 5 K and $\mu_0 H = 20$ mT decreases from about 0.6 to $0.3 \mu_{\text{B}}$ per Co with increasing t . The plot of m_{s} versus t (see **Figure 4.12a**) shows that the increase is sublinear above $t \approx 25$ nm, indicating that some parts of the film exhibit a reduced saturated moment or are even not in the FM state. **Figure 4.12b** shows m_{s} as a function of the "effective pseudomorphic thickness" t_{PM} , where $t_{\text{PM}} = t \times f_{\text{PM}}$. f_{PM} is the volume fraction of the pseudomorphic part of the LCO film (c.f. **Figure 4.9d**). Obviously, m_{s} shows a perfect linear dependence on f_{PM} as well as m^* on t . Hence, the FM state in epitaxially strained LCO films is confined to the pseudo-cubic (tetragonal) phase and instantly suppressed in case of emerging rhombohedral distortion of the unit-cell.

5. Summary

The physical properties of functional materials are determined to a large degree by their microstructure. Consequently, understanding the relationship between microstructure and physical properties can lead to fundamental physical insights and the development of materials with new or improved properties. Among the functional materials perovskite-based materials stand out due to their variety of physical properties. Within this work the microstructure of pure and Sr-substituted LaCoO_3 was studied by transmission electron microscopy (TEM). Sr-substituted LaCoO_3 provides outstanding electrocatalytic performance which makes it suited as cathode material for intermediate-temperature solid oxide fuel cells (IT-SOFCs). Moreover, the magnetic properties of LaCoO_3 are interesting from a fundamental point of view.

For TEM characterization, thin electron-transparent samples of high quality are indispensable. Since double-sector ion milling of multi-phase samples often fails, a single-sector Ar^+ -ion milling technique was developed, which allows the reliable preparation of TEM cross-section samples. This technique contributed significantly to the success of the microstructural characterization of $\text{La}_{0.6}\text{Sr}_{0.4}\text{CoO}_{3-\delta}$ thin-film cathodes and epitaxial LaCoO_3 films. Monte-Carlo simulations as well as ion-milling experiments on Si cross-section samples clearly showed that TEM cross-section samples with almost plane parallel surfaces and thus large electron-transparent regions with constant thickness can be prepared reproducibly by single-sector Ar^+ -ion milling. This plane parallelism is a feature, which is advantageous for most TEM techniques, especially for quantitative composition analyses in analytical TEM applications. In contrast, sample thinning by double-sector Ar^+ -ion milling results in wedge-shaped sample profiles where the thickness of the electron transparent area increases linearly with the distance to the sample edge. The wedge angle was found to be roughly two times the adjusted Ar^+ -ion sputtering angle. The proposed systematic ion-milling procedure is applicable for any commercial ion-milling system that allows separate milling of one of the two halves of a cross-section sample. The procedure is not restricted to the preparation of single-crystalline materials like silicon. It can be also applied for preparation of cross-sections of inhomogeneous materials with strongly differing sputtering yields, e.g., thin-films on polycrystalline substrates or epitaxial thin-films on single-crystalline substrates as shown by two examples in this work.

Another part of the presented work is concerned with nanocrystalline and nanoporous $\text{La}_{0.6}\text{Sr}_{0.4}\text{CoO}_{3-\delta}$ IT-SOFC thin-film cathodes, which were deposited on polycrystalline $\text{Ce}_{0.9}\text{Gd}_{0.1}\text{O}_{1.95}$ (CGO) electrolytes by low-temperature metal-organic deposition. After optimization of the annealing treatment, the cathodes exhibit an outstanding electrocat-

alytic performance with area-specific resistances as low as $9 \text{ m}\Omega \text{ cm}^2$ at $600 \text{ }^\circ\text{C}$ in synthetic air and $22 \text{ m}\Omega \text{ cm}^2$ in stagnant ambient air as observed by Hayd et al. [122,150,151]. The exceptional cathode performance cannot be fully understood by the increase of the inner-surface area resulting from the nm-scaled microstructure if theoretical models like the three-dimensional finite elements model of R uger et al. [153] are applied for calculating the area-specific resistance. To clarify the origin of the exceptional cathode performance, the microstructural changes in nanocrystalline and nanoporous $\text{La}_{0.6}\text{Sr}_{0.4}\text{CoO}_{3-\delta}$ (LSC) thin-film cathodes were studied by TEM as a function of annealing parameters. For quantification of the porosity, high-angle annular dark-field STEM tomography was applied to study quantitatively the coarsening and porosity of nm-scaled LSC cathodes for the first time.

Annealing at $T_{\text{max}} = 700 \text{ }^\circ\text{C}$ yields self-limited grain growth. The average grain size increases from 17 nm to 28 nm after annealing for 100 h. This increase in grain size is accompanied with a significantly decrease of porosity. As-prepared LSC cathodes exhibit a high volume fraction of open porosity of $(38 \pm 10) \%$ which results in a large electrochemically active surface area. Coarsening of the microstructure with annealing time leads to a decrease of the total porosity to $(18 \pm 5) \%$ after annealing at $700 \text{ }^\circ\text{C}$ for 100 h. An accelerated coarsening is observed at $T_{\text{max}} = 800 \text{ }^\circ\text{C}$. Here, the average grain size increases from 29 nm to 90 nm after annealing for 100 h. As-prepared LSC cathodes exhibits porosity values of $(18 \pm 5) \%$ with a marginal amount on open porosity. Additional annealing at $T_{\text{max}} = 800 \text{ }^\circ\text{C}$ leads to complete densification of the cathode films. This demonstrates that grain size and porosity of sol-gel derived LSC can be tailored by adequate annealing parameters to obtain high-performance cathodes for application in IT-SOFCs. However, the observed coarsening of the microstructure (increase of grain-size/decrease of porosity) limits the operating temperature of nanocrystalline and nanoporous LSC cathodes to temperatures of $\leq 600 \text{ }^\circ\text{C}$. Furthermore, chemical composition analyses revealed a high density of small Co_3O_4 precipitates close to the surface of the LSC thin films, which are formed as intermediate phase during pyrolysis. The particle number density of these precipitates decreases with the coarsening of the cathode microstructure. The local chemical composition after pyrolysis is not homogeneous due to the presence of the Co_3O_4 precipitates. However, quantitative energy-dispersive X-ray spectroscopy revealed that the intended composition of $\text{La}_{0.6}\text{Sr}_{0.4}\text{CoO}_{3-\delta}$ is achieved close to the CGO/LSC interface, whereas an enrichment of the Co-concentration and a slight La-depletion is observed close to the cathode surface. Nevertheless, the chemical composition homogenates with annealing time and temperature. It is reasonable suggest, that the Co_3O_4 precipitates contribute significantly to the outstanding electrochemical performance as shown by the correlation between microstructure, phase composition and electrochemical characterization. Hence, the application of Co_3O_4 -dispersed $\text{La}_{0.6}\text{Sr}_{0.4}\text{CoO}_{3-\delta}$ cathodes will be a promising approach to further enhance electrochemical performance of future IT-SOFCs cathodes.

The last major part of this work is concerned with the correlation of microstructure and magnetic properties of pure LaCoO_3 (LCO). For this purpose LCO was epitaxially deposited on single crystalline (001) -orientated $(\text{LaAlO}_3)_{0.3}(\text{SrAl}_{0.5}\text{Ta}_{0.5}\text{O}_3)_{0.7}$ (LSAT)

substrates by pulsed-laser deposition. LCO film with thicknesses between 8 nm and 100 nm were studied. In the initial state of film deposition the growth is nearly pseudomorphic which results in a pseudotetragonal LCO structure with increased unit-cell volume compared to bulk LCO. The strain is relieved elastically by nanotwinning along the $\langle 100 \rangle_{pc}$ directions in the investigated thickness range. This process already starts during the initial stage of growth by the formation of a periodic lattice modulation. Nevertheless, pseudomorphic regions in the films grow up to a thickness of at least several tenths of nanometers. The pseudomorphic volume fraction of the films decreases with increasing film thickness to about 35 %. The observed twinning of the LCO films is attributed to symmetry lowering of the epitaxially strained pseudotetragonal structure towards the fully relaxed rhombohedral structure of bulk LCO. Despite the different observed strain-relaxation mechanisms, the unit-cell volume was found to be nearly constant over the investigated thickness range. The Curie temperature of the LCO films is slightly reduced with decreasing layer thickness from $T_C = 87$ K for $t = 50$ nm to $T_C = 80$ K for $t = 8$ nm, which is likely to be caused by a finite-size effect. The effective paramagnetic moment m_{eff} and, thus, the spin state of the Co^{3+} -ion was found to be almost constant for $t \leq 100$ nm. However, the saturated ferromagnetic moment m_s is only proportional to the pseudotetragonal part of the film and decreases with increasing rhombohedral distortion. The experiments clearly demonstrate that the ferromagnetic state of LCO is strongly affected by the rhombohedral distortion. The increased unit-cell volume contributes to a lesser degree. It mainly controls the effective paramagnetic moment and, thus, the spin state of the Co^{3+} -ion. Hence, epitaxial strain is able to stabilize the pseudocubic tetragonal structure and thus the ferromagnetic state of LCO until strain relaxation via nanotwinning and emerging rhombohedral distortion takes place.

Appendix

A. MATLAB source code

Function used for calculating the sputtering yield

$$Y(\theta) = Y(0) \frac{1}{\cos(\theta)^f} \exp(-\Sigma(\frac{1}{\cos \theta} - 1))$$

using

$$\Sigma = f \cos(\theta_{\text{opt}})$$

```
1 function Y=sputteringYown(t,a)
2 %variables:
3 %a    sputtering angle
4 %t    local surface angle
5 t=abs(90+a-t);
6
7 %sputtering yield fitting parameters
8 a=4.91623;
9 b=3.30167;
10 S=0.06791;
11
12 %sputtering yield
13 Y=(1+a*(sin(t*pi/180))^(b))*exp(-S*(1/cos(t*pi/180)-1));
14
15 end
```

Function for building the cross-section sample matrix

```
1 function [mysample] = makeCSSamplewoGlue(samp,a,h)
2
3 %mysample sample matrix
4 %a         sputtering angle
5 %h         overall sample height
6
7 mysample=zeros(samp,5);
8 l=length(mysample);
9
10 % local coordinate x
11 for i=1:l
12     mysample(i,1)=i;
13 end
14
15 %local sample height
16 mysample(:,2)=h;
17
18 %change local sample material (epoxy)
19 mysample(:,3)=1;
20 for i=191:211
21     mysample(i,3)=2;
22 end
23
24 %local surface angle
25 mysample(1,4)=0;
26 for ind=2:l
27     mysample(ind,4)=-atan(mysample(ind-1,2)-mysample(ind,2))*180/pi;
28 end
29
30 %projected surface distance
31 for ind=1:l
32     n=((mysample(ind,2)-mysample(1,2))^2+ind^2)^0.5 *cos((90+a)*pi/180-
33         atan((mysample(ind,2)-mysample(1,2))/ind));
34     if n<0
35         mysample(ind,5)=0
36     else
37         mysample(ind,5)=n;
38     end
39 end
```

Main program

```
1 function sputtering()
2
3 clear mysample
4 %=====
5 %variable parameters
6 %angle incident Ar ions
7 a=-4; %-10:
8
9 %sample height
10 h=100;
11
12 %sampling points of sample should be an odd number
13 samp=401;
14
15 %number of iteration
16 iterations=1500;%500
17
18 %interactions per iteration
19 interactions=3000;%300000
20
21 %sputter parameter
22 sputterparameter=0.001;%0.00001
23
24 %factor for epoxy sputtering
25 f=1.5;
26
27 %sample matrix
28 %column 1 - x
29 %column 2 - height
30 %column 3 - material
31 %column 4 - surface angle
32 %column 5 - projected surface length
33
34 %initialize arrays
35 %surface topography
36 timeevolution=zeros(samp,iterations+1);
37 %surface angle
38 timeevolutionangle=zeros(samp,iterations+1);
39
40 for i=1:samp
41     %initialize x-coordinate in first column in both arrays
42     timeevolution(i,1)=i*10-1010;
43     timeevolutionangle(i,1)=i*10-1010;
44 end
45
46 %make CSsample
47 sample=makeCSsampleGlue(samp,a,h)
48
49 %initial surface and angles
50 timeevolution(:,2)=sample(:,2)*10;
```

```

51 timeevolutionangle(:,2)=sample(:,4);
52
53 %=====start ion bombardment=====
54 for k=1:iterations
55
56     for j=1:interactions
57
58         %generate Ar ion at random position x
59         arx=rand*max(sample(:,5));
60
61         %find first projected surface length bigger than arx
62         ind=find(sample(:,5)>arx,1);
63
64         %reduce height
65         %be carefull, reduction in sputtered height <= shadowed area
66         if sample(ind,3)==2
67             yield=f*sputteringYown(sample(ind,4),a);
68         else
69             yield=sputteringYown(sample(ind,4),a);
70         end
71
72         %scale sputtering yield
73         sputtered=sputterparameter*yield;
74
75         %new local sample height
76         sample(ind,2)=sample(ind,2)-sputtered/cos(sample(ind,4)*pi/180);
77
78         %new local surface angle
79         if ind > 1
80             sample(ind,4)=-atan(sample(ind-1,2)-sample(ind,2))*180/pi;
81         end
82         if ind < samp
83             sample(ind+1,4)=+atan(sample(ind+1,2)-sample(ind,2))*180/pi;
84         end
85         %new integrated projected surface length
86         sample(ind,5)=((sample(ind,2)-sample(1,2))^2+ind^2)^0.5 *cos((90+a)
            *pi/180-atan((sample(ind,2)-sample(1,2))/ind));
87
88     end
89     %save surfacetopography and angles for iteration step
90     timeevolution(:,k+1)=sample(:,2)*10;
91     timeevolutionangle(:,k+1)=sample(:,4);
92
93     %if k==rot
94         sample=RotateSample(sample,a);
95     %end
96 end
97 save timeevolution;
98
99 end

```

Function for rotating the cross-section sample matrix

```
1 function RS=RotateSample(sample,a)
2 %length of sample matrix
3 [l,w]=size(sample);
4 %initialize rotated sample matrix with length l and 5 columns
5 RS=zeros(l,5);
6 %boundary condition - surface angle for index1=0 -> prevent edge
  effects
7 RS(1,4)=0;
8
9 RS(:,1)=sample(:,1);
10
11 for i=1:l
12     RS(i,2:3)=sample(1-i+1,2:3);
13     RS(i,5)=((RS(i,2)-RS(1,2))^2+i^2)^0.5 *cos((90+a)*pi/180-atan((RS(i
      ,2)-RS(1,2))/i));
14 end
15
16 for i=2:l
17     RS(i,4)=-atan(RS(i-1,2)-RS(i,2))*180/pi;
18 end
19
20 end
```


Bibliography

- [1] L. Dieterle, B. Butz, and E. Müller. Optimized Ar⁺-ion milling procedure for TEM cross-section sample preparation. *Ultramicroscopy*, 111(11):1636–1644, 2011.
- [2] L. Dieterle, P. Bockstaller, D. Gerthsen, J. Hayd, E. Ivers-Tiffée, and U. Guntow. Microstructure of nanoscaled La_{0.6}Sr_{0.4}CoO_{3-δ} cathodes for intermediate-temperature solid oxide fuel cells. *Advanced Energy Materials*, 1(2):249–258, 2011.
- [3] D. Fuchs, L. Dieterle, E. Arac, R. Eder, P. Adelman, V. Eyert, T. Kopp, R. Schneider, D. Gerthsen, and H. v. Löhneysen. Suppression of the ferromagnetic state in LaCoO₃ films by rhombohedral distortion. *Physical Review B*, 79(2):024424, 2009.
- [4] M. Descloizeaux. Note sur les formes cristallines de la pérowskite. *Annales de Chimie et de Physique*, 13(3):338, 1845.
- [5] K. Nash. <http://www.mindat.org/photo-170962.html>, November 2011.
- [6] V. M. Goldschmidt. Die Gesetze der Krystallochemie. *Naturwissenschaften*, 14(21):477–485, 1926.
- [7] G. Thornton, B. C. Tofield, and A. W. Hewat. A neutron diffraction study of LaCoO₃ in the temperature range 4.2 < T < 1248 K. *Journal of Solid State Chemistry*, 61(3):301–307, 1986.
- [8] R. P. Haggerty and R. Seshadri. Oxygen stoichiometry, crystal structure, and magnetism of La_{0.5}Sr_{0.5}CoO_{3-δ}. *Journal of Physics: Condensed Matter*, 16:6477–6484, 2004.
- [9] R. D. Shannon. Revised effective ionic radii and systematic studies of interatomic distances in halides and chalcogenides. *Acta Crystallographica Section A*, 32(5):751–767, 1976.
- [10] F. Askham, I. Fankuchen, and R. Ward. The preparation and structure of lanthanum cobaltic oxide. *Journal of the American Chemical Society*, 72(8):3799–3800, 1950.
- [11] G. H. Jonker and J. H. Van Santen. Magnetic compounds with perovskite structure III. ferromagnetic compounds of cobalt. *Physica*, 19(1–12):120–130, 1953.
- [12] A. Wold, B. Post, and E. Banks. Lanthanum, rhodium and lanthanum cobalt oxides. *Journal of the American Chemical Society*, 79(24):6365–6366, 1957.

- [13] P. M. Raccach and J. B. Goodenough. First-order localized-electron \rightleftharpoons collective-electron transition in LaCoO_3 . *Physical Review*, 155(3):932–943, 1967.
- [14] A. N. Petrov, O. F. Kononchuk, A. V. Andreev, V. A. Cherepanov, and P. Kofstad. Crystal structure, electrical and magnetic properties of $\text{La}_{1-x}\text{Sr}_x\text{CoO}_{3-y}$. *Solid State Ionics*, 80(3–4):189–199, 1995.
- [15] V. G. Sathe, A. V. Pimpale, V. Siruguri, and S. K. Karanjpe. Neutron diffraction studies of perovskite-type compounds $\text{La}_{1-x}\text{Sr}_x\text{CoO}_3$ ($x = 0.1, 0.2, 0.3, 0.4, 0.5$). *Journal of Physics: Condensed Matter*, 8:3889–3896, 1996.
- [16] H. D. Megaw and C. N. W. Darlington. Geometrical and structural relations in the rhombohedral perovskites. *Acta Crystallographica Section A*, 31(2):161–173, 1975.
- [17] J. Mastin, M.-A. Einarsrud, and T. Grande. Structural and thermal properties of $\text{La}_{1-x}\text{Sr}_x\text{CoO}_{3-\delta}$. *Chemistry of Materials*, 18(25):6047–6053, 2006.
- [18] V. V. Kharton, E. N. Naumovich, A. A. Vecher, and A. V. Nikolaev. Oxide Ion Conduction in Solid Solutions $\text{Ln}_{1-x}\text{Sr}_x\text{CoO}_{3-\delta}$ ($\text{Ln} = \text{La}, \text{Pr}, \text{Nd}$). *Journal of Solid State Chemistry*, 120(1):128–136, 1995.
- [19] R. H. E. van Doorn and A. J. Burggraaf. Structural aspects of the ionic conductivity of $\text{La}_{1-x}\text{Sr}_x\text{CoO}_{3-\delta}$. *Solid State Ionics*, 128(1–4):65–78, 2000.
- [20] A. Mineshige, M. Inaba, T. Yao, Z. Ogumi, K. Kikuchi, and M. Kawase. Crystal structure and metal-insulator transition of $\text{La}_{1-x}\text{Sr}_x\text{CoO}_3$. *Journal of Solid State Chemistry*, 121(2):423–429, 1996.
- [21] V. A. Cherepanov, E. A. Filonova, V. I. Voronin, I. F. Berger, and L. Yu. Barkhatova. Phase equilibria in the $\text{LaCoO}_3 - \text{LaMnO}_3 - \text{SrCoO}_{2.5} - \text{SrMnO}_3$ system. *Materials Research Bulletin*, 34(9):1481–1489, 1999.
- [22] M. T. Anderson, J. T. Vaughey, and K. R. Poeppelmeier. Structural similarities among oxygen-deficient perovskites. *Chemistry of Materials*, 5(2):151–165, 1993.
- [23] O. H. Hansteen and H. Fjellvåg. Synthesis, crystal structure, and magnetic properties of $\text{La}_4\text{Co}_3\text{O}_{10+\delta}$ ($0.00 \leq \delta \leq 0.30$). *Journal of Solid State Chemistry*, 141(1):212–220, 1998.
- [24] O. H. Hansteen, H. Fjellvåg, and B. C. Hauback. Crystal structure, thermal and magnetic properties of $\text{La}_3\text{Co}_3\text{O}_8$. Phase relations for $\text{LaCoO}_{3-\delta}$ ($0.00 \leq \delta \leq 0.50$) at 673 K. *Journal of Materials Chemistry*, 8(9):2081–2088, 1998.
- [25] O. H. Hansteen, H. Fjellvåg, and B. C. Hauback. Crystal structure and magnetic properties of $\text{La}_2\text{Co}_2\text{O}_5$. *Journal of Solid State Chemistry*, 141(2):411–417, 1998.

- [26] R. F. Klie, Y. Ito, S. Stemmer, and N. D. Browning. Observation of oxygen vacancy ordering and segregation in perovskite oxides. *Ultramicroscopy*, 86(3–4):289–302, 2001.
- [27] S. Stemmer, A. J. Jacobson, X. Chen, and A. Ignatiev. Oxygen vacancy ordering in epitaxial $\text{La}_{0.5}\text{Sr}_{0.5}\text{CoO}_{3-\delta}$ thin films on (001) LaAlO_3 . *Journal of Applied Physics*, 90(7):3319–3324, 2001.
- [28] S. Stemmer, A. Sane, N. D. Browning, and T. J. Mazanec. Characterization of oxygen-deficient $\text{SrCoO}_{3-\delta}$ by electron energy-loss spectroscopy and Z-contrast imaging. *Solid State Ionics*, 130(1–2):71–80, 2000.
- [29] M. A. Alario-Franco, J. M. Gonzalez-Calbet, M. Vallet-Regi, and J. C. Grenier. Brownmillerite-type microdomains in the calcium lanthanum ferrites: $\text{Ca}_x\text{La}_{1-x}\text{FeO}_{3-y}$. *Journal of Solid State Chemistry*, 49(2):219–231, 1983.
- [30] N. Nakayama, M. Takano, S. Inamura, N. Nakanishi, and K. Kosuge. Electron microscopy study of the "cubic" perovskite phase $\text{SrFe}_{1-x}\text{V}_x\text{O}_{2.5+x}$ ($0.05 \leq x \leq 0.1$). *Journal of Solid State Chemistry*, 71(2):403–417, 1987.
- [31] C. Gspan, W. Grogger, B. Bitschnau, E. Bucher, W. Sitte, and F. Hofer. Crystal structure of $\text{La}_{0.4}\text{Sr}_{0.6}\text{CoO}_{2.71}$ investigated by TEM and XRD. *Journal of Solid State Chemistry*, 181(11):2976–2982, 2008.
- [32] S. B. Adler, S. Russek, J. Reimer, M. Fendorf, A. Stacy, Q. Huang, A. Santoro, J. Lynn, J. Baltisberger, and U. Werner. Local structure and oxide-ion motion in defective perovskites. *Solid State Ionics*, 68(3–4):193–211, 1994.
- [33] L. Barbey, N. Nguyen, V. Caignaert, M. Hervieu, and B. Raveau. Mixed oxides of cobalt and copper with a double pyramidal layer structure. *Materials Research Bulletin*, 27(3):295–301, 1992.
- [34] T. Aksenova, M. Anan'ev, L. Gavrilova, and V. Cherepanov. Phase equilibria and crystal structures of solid solutions in the system $\text{LaCoO}_{3-\delta}$ – $\text{SrCoO}_{2.5\pm\delta}$ – $\text{SrFeO}_{3-\delta}$ – $\text{LaFeO}_{3-\delta}$. *Inorganic Materials*, 43:296–300, 2007.
- [35] V. Cherepanov, L. Gavrilova, L. Barkhatova, V. Voronin, M. Trifonova, and O. Bukhner. Phase equilibria in the La–Me–Co–O (Me = Ca, Sr, Ba) systems. *Ionics*, 4(3):309–315, 1998.
- [36] F. Morin, G. Trudel, and Y. Denos. The phase stability of $\text{La}_{0.5}\text{Sr}_{0.5}\text{CoO}_{3-\delta}$. *Solid State Ionics*, 96(3–4):129–139, 1997.
- [37] J. Ovenstone, J. S. White, and S. T. Misture. Phase transitions and phase decomposition of $\text{La}_{1-x}\text{Sr}_x\text{CoO}_{3-\delta}$ in low oxygen partial pressures. *Journal of Power Sources*, 181(1):56–61, 2008.

- [38] J. Mizusaki, J. Tabuchi, T. Matsuura, S. Yamauchi, and K. Fueki. Electrical conductivity and seebeck coefficient of nonstoichiometric $\text{La}_{1-x}\text{Sr}_x\text{CoO}_{3-\delta}$. *Journal of the Electrochemical Society*, 136(7):2082–2088, 1989.
- [39] F. A. Kröger and H. J. Vink. Relations between the concentrations of imperfections in crystalline solids. In F. Seitz and D. Turnbull, editors, *Advances in Research and Applications*, volume 3, pages 307–435. Academic Press, 1956.
- [40] A. Petric, P. Huang, and F. Tietz. Evaluation of La–Sr–Co–Fe–O perovskites for solid oxide fuel cells and gas separation membranes. *Solid State Ionics*, 135(1–4):719–725, 2000.
- [41] E. Bucher. *Defect chemistry, transport properties and microstructure of (La,Sr)(Fe,Co)O₃*. PhD thesis, Montanuniversität Leoben, 2003.
- [42] H. Ullmann, N. Trofimenko, F. Tietz, D. Stöver, and A. Ahmad-Khanlou. Correlation between thermal expansion and oxide ion transport in mixed conducting perovskite-type oxides for SOFC cathodes. *Solid State Ionics*, 138(1-2):79–90, 2000.
- [43] Y. Teraoka, H. M. Zhang, K. Okamoto, and N. Yamazoe. Mixed ionic-electronic conductivity of $\text{La}_{1-x}\text{Sr}_x\text{Co}_{1-y}\text{Fe}_y\text{O}_{3-\delta}$ perovskite-type oxides. *Materials Research Bulletin*, 23(1):51–58, 1988.
- [44] W. Sitte, E. Bucher, W. Preis, I. Papst, W. Grogger, and F. Hofer. Microstructural aspects of the ionic transport properties of strontium-substituted lanthanum cobaltites. In *MRS Proceedings*, volume 756, 2002.
- [45] Y. Ohno, S. Nagata, and H. Sato. Properties of oxides for high temperature solid electrolyte fuel cell. *Solid State Ionics*, 9–10(2):1001–1007, 1983.
- [46] S. B. Adler. Chemical expansivity of electrochemical ceramics. *Journal of the American Ceramic Society*, 84(9):2117–2119, 2001.
- [47] Y. Chen and S. B. Adler. Thermal and chemical expansion of Sr-doped lanthanum cobalt oxide $\text{La}_{1-x}\text{Sr}_x\text{CoO}_{3-\delta}$. *Chemistry of Materials*, 17(17):4537–4546, 2005.
- [48] H. Hayashi, T. Saitou, N. Maruyama, H. Inaba, K. Kawamura, and M. Mori. Thermal expansion coefficient of yttria stabilized zirconia for various yttria contents. *Solid State Ionics*, 176(5–6):613–619, 2005.
- [49] H. Hayashi, M. Kanoh, C. J. Quan, H. Inaba, S. Wang, M. Dokiya, and H. Tagawa. Thermal expansion of Gd-doped ceria and reduced ceria. *Solid State Ionics*, 132(3–4):227–233, 2000.
- [50] C. Peters. *Grain-Size Effects in Nanoscaled Electrolyte and Cathode Thin Films for Solid Oxide Fuel Cells (SOFC)*. Universitätsverlag Karlsruhe, 2009.

- [51] Orbital Viewer - visualization software for electron orbitals.
<http://www.orbitals.com/orb/>.
- [52] M. Wojdyr. Fityk: a general-purpose peak fitting program. *Journal of Applied Crystallography*, 43:1126–1128, 2010.
- [53] P. Stadelmann. Image analysis and simulation software in transmission electron microscopy. *Microscopy and Microanalysis*, 9(3):60–61, 2003.
- [54] B. Bruckschen, H. Seitz, T. M. Buzug, C. Tille, B. Leukers, and S. Irsen. Comparing different porosity measurement methods for characterisation of 3D printed bone replacement scaffolds. *Biomedizinische Technik*, 1:1609–1610, 2005.
- [55] J. Joos, B. Rüger, T. Carraro, A. Weber, and E. Ivers-Tiffée. Electrode reconstruction by FIB/SEM and microstructure modeling. In *ECS Transactions Vancouver*, 2010.
- [56] J. R. Wilson, J. S. Cronin, S. A. Barnett, and S. J. Harris. Measurement of three-dimensional microstructure in a LiCoO₂ positive electrode. *Journal of Power Sources*, 196(7):3443–3447, 2011.
- [57] D. Gostovic, J. R. Smith, D. P. Kundinger, K. S. Jones, and E. D. Wachsman. Three-dimensional reconstruction of porous LSCF cathodes. *Electrochemical and Solid-State Letters*, 10(12):B214–B217, 2007.
- [58] K. N. Grew, Y. S. Chu, J. Yi, A. A. Peracchio, Jr. John R. I., Y. Hwu, F. de Carlo, and W. K. S. Chiu. Nondestructive nanoscale 3D elemental mapping and analysis of a solid oxide fuel cell anode. *Journal of The Electrochemical Society*, 157(6):B783–B792, 2010.
- [59] P. R. Shearing, J. Gelb, and N. P. Brandon. X-ray nano computerised tomography of SOFC electrodes using a focused ion beam sample-preparation technique. *Journal of the European Ceramic Society*, 30(8):1809–1814, 2010.
- [60] J. R. Izzo, Jr., A. A. Peracchio, and W. K. S. Chiu. Modeling of gas transport through a tubular solid oxide fuel cell and the porous anode layer. *Journal of Power Sources*, 176(1):200–206, 2008.
- [61] D. Marrero-López, J. C. Ruiz-Morales, J. Peña-Martínez, J. Canales-Vázquez, and P. Núñez. Preparation of thin layer materials with macroporous microstructure for SOFC applications. *Journal of Solid State Chemistry*, 181(4):685–692, 2008.
- [62] Y.-B. P. Kwan and J. R. Alcock. The impact of water impregnation method on the accuracy of open porosity measurements. *Journal of Materials Science*, 37(12):2557–2561, 2002.

- [63] J. Frank, editor. *Electron Tomography. Three-Dimensional Imaging with the Transmission Electron Microscope (Mathematical Concepts and Methods in Science and Engineering)*. Kluwer Academic / Plenum Publishers, 1st edition, 1992.
- [64] P. Hartel, H. Rose, and C. Dinges. Conditions and reasons for incoherent imaging in STEM. *Ultramicroscopy*, 63(2):93–114, 1996.
- [65] H. Cramér and H. Wold. Some theorems on distribution functions. *Journal of the London Mathematical Society*, s1-11(4):290–294, 1936.
- [66] P. Gilbert. Iterative methods for the three-dimensional reconstruction of an object from projections. *Journal of Theoretical Biology*, 36(1):105–117, 1972.
- [67] P. A. Midgley, E. P. W. Ward, A. B. Hungria, and J. Meurig Thomas. Nanotomography in the chemical, biological and materials sciences. *Chemical Society Reviews*, 36(9):1477–1494, 2007.
- [68] D. B. Williams and C. B. Carter. *Transmission Electron Microscopy - A Textbook for Materials Science*. Springer, 2nd edition, August 2009.
- [69] R. Jenkins, R. Manne, R. Robin, and C. Senemaud. IUPAC nomenclature system for X-ray spectroscopy. *X-Ray Spectrometry*, 20(3):149–155, 1991.
- [70] G. Cliff and G. W. Lorimer. The quantitative analysis of thin specimens. *Journal of Microscopy*, 103:203–207, 1975.
- [71] C. T. Chantler, K. Olsen, R. A. Dragoset, J. Chang, A. R. Kishore, S. A. Kotochigova, and D. S. Zucker. Detailed tabulation of atomic form factors, photoelectric absorption and scattering cross section, and mass attenuation coefficients for $Z = 1-92$ from $E = 1-10$ eV to $E = 0.4-1$ MeV. <http://www.nist.gov/physlab/data/ffast/index.cfm>, August 2005.
- [72] Z. Horita, T. Sano, and M. Nemoto. Simplification of X-ray absorption correction in thin-sample quantitative microanalysis. *Ultramicroscopy*, 21(3):271–276, 1987.
- [73] J. Ayache, L. Beaunier, J. Boumendil, G. Ehret, and D. Laub. *Sample Preparation Handbook for Transmission Electron Microscopy - Techniques*. Springer, 2010.
- [74] J. Ayache, L. Beaunier, J. Boumendil, G. Ehret, and D. Laub. *Sample Preparation Handbook for Transmission Electron Microscopy - Methodology*. Springer, 2010.
- [75] S. Suder, C. A. Faunce, and S. E. Donnelly. Thin solid film sample preparation by a small-angle cleavage for transmission electron microscopy. *Thin Solid Films*, 304(1-2):157–159, 1997.
- [76] J. P. McCaffrey. Small-angle cleavage of semiconductors for transmission electron microscopy. *Ultramicroscopy*, 38(2):149–157, 1991.

- [77] V. S. Teodorescu and M.-G. Blanchin. Fast and simple specimen preparation for TEM studies of oxide films deposited on silicon wafers. *Microscopy and Microanalysis*, 15(1):15–19, 2009.
- [78] M. Kawasaki, T. Yoshioka, and M. Shiojiri. A new specimen preparation method for cross-section TEM using diamond powders. *Journal of Electron Microscopy*, 48(2):131–137, 1999.
- [79] J. Ayache and P. H. Albarède. Application of the ionless tripod polisher to the preparation of YBCO superconducting multilayer and bulk ceramics thin films. *Ultramicroscopy*, 60(2):195–206, 1995.
- [80] E. Eberg, A. F. Monsen, T. Tybell, A. T. J. van Helvoort, and R. Holmestad. Comparison of TEM specimen preparation of perovskite thin films by tripod polishing and conventional ion milling. *Journal of Electron Microscopy*, 57(6):175–179, 2008.
- [81] A. Strecker, U. Baeder, M. Kelsch, U. Salzberger, M. Sycha, M. Gao, G. Richter, and K. V. Benthem. Progress in the preparation of cross-sectional TEM specimens by ion-beam thinning. *Zeitschrift für Metallkunde*, 94(3):290–297, 2003.
- [82] A. C. Dürr, F. Schreiber, M. Kelsch, and H. Dosch. Optimized preparation of cross-sectional TEM specimens of organic thin films. *Ultramicroscopy*, 98(1):51–55, 2003.
- [83] U. Helmersson and J.-E. Sundgren. Cross-Section preparation for TEM of film-substrate combinations with a large difference in sputtering yields. *Journal of Electron Microscopy Technique*, 4(4):361–369, 1986.
- [84] Y. Liu, R. Wang, X. Guo, and J. Dai. A cross-sectional TEM sample preparation method for films deposited on metallic substrates. *Materials Characterization*, 58(7):666–669, 2007.
- [85] S. J. Zinkle, C. P. Haltom, L. C. Jenkins, and C. K. H. DuBose. Technique for preparing cross-section transmission electron microscope specimens from ion-irradiated ceramics. *Journal of Electron Microscopy Technique*, 19(4):452–460, 1991.
- [86] A. Barna. Topographic kinetics and practice of low angle ion beam thinning. In Anderson, Tracy, and Bravman, editors, *Specimen preparation for transmission electron microscopy of materials*, volume 254, pages 3–22. Materials Research Society, 1992.
- [87] R. Alani and P. R. Swann. Precision ion polishing system - A new instrument for TEM specimen preparation of materials. *Materials Research Society Symposium Proceedings*, 254:43–63, 1992.
- [88] U. Nitschke. Low angle ion milling for transmission electron microscopy. *Praktische Metallographie*, 31(8):422–425, 1994.

- [89] The MathWorks Inc. <http://www.mathworks.com/>.
- [90] H. Sommerfeldt, E. S. Mashkova, and V. A. Molchanov. Sputtering of silicon and germanium by middle-energy heavy ions. *Physics Letters A*, 38(4):237–238, 1972.
- [91] R. P. Webb, C. Jeynes, and I. H. Wilson. The effect of angle of incidence on interface broadening. *Nuclear Instruments and Methods in Physics Research Section B: Beam Interactions with Materials and Atoms*, 13(1-3):449–452, 1986.
- [92] R. Wedell and J.-P. Kuska. Theoretical description of sputtering at grazing incidence. *Nuclear Instruments and Methods in Physics Research Section B: Beam Interactions with Materials and Atoms*, 78(1-4):204–211, 1993.
- [93] A. E. Morgan, H. A. M. de Grefte, N. Warmoltz, H. W. Werner, and H. J. Tolle. The influence of bombardment conditions upon the sputtering and secondary ion yields of silicon. *Applications of Surface Science*, 7(4):372–392, 1981.
- [94] R. Cong-Xin, C. Guo-Ming, F. Xtn-Ding, Y. Jie, F. Hong-Li, and T. Shih-Chang. Topographical changes induced by low energy ion beam sputtering at oblique incidence. *Radiation Effects*, 77(3):177–193, 1983.
- [95] V. I. Bachurin, P. A. Lepshin, and V. K. Smirnov. Angular dependences of surface composition, sputtering and ripple formation on silicon under N^{2+} ion bombardment. *Vacuum*, 56(4):241–245, 2000.
- [96] S. T. Kang, R. Shimizu, and T. Okutani. Sputtering of Si with keV Ar^+ Ions. I. Measurement and Monte Carlo calculations of sputtering yield. *Japanese Journal of Applied Physics*, 18(9):1717–1725, 1979.
- [97] Y. Yamamura, Y. Itekawa, and N. Itoh. Angular dependence of sputtering yields of monoatomic solids. Technical report, IPPJ-AM-26, Institute of Plasma Physics, Nagoya University, 1983.
- [98] J. P. McCaffrey and J. Hulse. Transmitted color and interference fringes for TEM sample preparation of silicon. *Micron*, 29(2–3):139–144, 1998.
- [99] P. Stadelmann. EMS online. <http://cecm.insa-lyon.fr/CIOLS/crystal1.pl>.
- [100] M. P. Seah, C. A. Clifford, F. M. Green, and I. S. Gilmore. An accurate semi-empirical equation for sputtering yields I: for argon ions. *Surface and Interface Analysis*, 37(5):444–458, 2005.
- [101] A. Keller and S. Facsko. Ion-induced nanoscale ripple patterns on Si surfaces: theory and experiment. *Materials*, 3(10):4811–4841, 2010.
- [102] J. L. Nagy. The energy spectrum of ion beam emitted by a penning-type ion source. *Nuclear Instruments and Methods*, 32(2):229–234, 1965.

- [103] N. Q. Minh. Ceramic fuel cells. *Journal of the American Ceramic Society*, 76(3):563–588, 1993.
- [104] S. C. Singhal and K. Kendall, editors. *High Temperature Solid Oxide Fuel Cells: Fundamentals, Design and Applications*. Elsevier Advanced Technology, 2003.
- [105] Wikipedia. <http://en.wikipedia.org/wiki/SOFC>, July 2011.
- [106] B. C. H. Steele. Appraisal of $\text{Ce}_{1-y}\text{Gd}_y\text{O}_{2-\frac{y}{2}}$ electrolytes for IT-SOFC operation at 500 °C. *Solid State Ionics*, 129(1-4):95–110, 2000.
- [107] N. Sammes and Y. Du. Intermediate-temperature SOFC electrolytes. In N. Sammes, A. Smirnova, and O. Vasylyev, editors, *NATO Science Series*, volume 202, pages 19–34. Springer Netherlands, 2005.
- [108] L. Dieterle, D. Bach, R. Schneider, H. Störmer, D. Gerthsen, U. Guntow, E. Ivers-Tiffée, A. Weber, C. Peters, and H. Yokokawa. Structural and chemical properties of nanocrystalline $\text{La}_{0.5}\text{Sr}_{0.5}\text{CoO}_{3-\delta}$ layers on yttria-stabilized zirconia analyzed by transmission electron microscopy. *Journal of Materials Science*, 43(9):3135–3143, 2008.
- [109] M. Kornely, A. Neumann, N. H. Menzler, A. Leonide, A. Weber, and E. Ivers-Tiffée. Degradation of anode supported cell (ASC) performance by Cr-poisoning. *Journal of Power Sources*, 196(17):7203–7208, 2011.
- [110] S. C. Singhal. Solid oxide fuel cells for stationary, mobile, and military applications. *Solid State Ionics*, 152-153:405–410, 2002.
- [111] P. Lamp, J. Tachtler, O. Finkenwirth, S. Mukerjee, and S. Shaffer. Development of an auxiliary power unit with solid oxide fuel cells for automotive applications. *Fuel Cells*, 3(3):146–152, 2003.
- [112] C.-C. Chao, C.-M. Hsu, Y. Cui, and F. B. Prinz. Improved solid oxide fuel cell performance with nanostructured electrolytes. *ACS Nano*, pages 5692–5696, 2011.
- [113] H. L. Tuller. Solid state electrochemical systems—opportunities for nanofabricated or nanostructured materials. *Journal of Electroceramics*, 1(3):211–218, 1997.
- [114] H. L. Tuller. Ionic conduction in nanocrystalline materials. *Solid State Ionics*, 131(1–2):143–157, 2000.
- [115] J. Maier. Thermodynamic aspects and morphology of nano-structured ion conductors: Aspects of nano-ionics Part I. *Solid State Ionics*, 154–155(0):291–301, 2002.
- [116] J. Maier. Nano-sized mixed conductors (Aspects of nano-ionics. Part III). *Solid State Ionics*, 148(3-4):367–374, 2002.

- [117] J. Maier. Defect chemistry and ion transport in nanostructured materials: Part II. Aspects of nanoionics. *Solid State Ionics*, 157(1-4):327–334, 2003.
- [118] J. Maier. Nano-ionics: Trivial and non-trivial size effects on ion conduction in solids. *Zeitschrift für Physikalische Chemie*, 217(4-2003):415–436, 2003.
- [119] J. Maier. Ionic transport in nano-sized systems. *Solid State Ionics*, 175(1-4):7–12, 2004.
- [120] J. Maier. Transport in electroceramics: micro- and nano-structural aspects. *Journal of the European Ceramic Society*, 24(6):1251–1257, 2004.
- [121] J. Maier. Nanoionics: ion transport and electrochemical storage in confined systems. *Nature Materials*, 4(11):805–815, 2005.
- [122] J. Hayd, U. Guntow, and E. Ivers-Tiffée. Detailed electrochemical analysis of high-performance nanoscaled $\text{La}_{0.6}\text{Sr}_{0.4}\text{CoO}_{3-\delta}$ thin film cathodes. *ECS Transactions*, 35(1):2261–2273, 2011.
- [123] C. J. Brinker, G. C. Frye, A. J. Hurd, and C. S. Ashley. Fundamentals of sol-gel dip coating. *Thin Solid Films*, 201(1):97–108, 1991.
- [124] L. D. Landau and B. G. Levich. Dragging of a liquid by a moving plate. *Acta Physicochimica U.R.S.S.*, 17:42–54, 1942.
- [125] S. R. Gallagher. *Digital Image Processing and Analysis with ImageJ*. John Wiley & Sons, Inc., 2008.
- [126] N. Kawase, M. Kato, H. Nishioka, and H. Jinnai. Transmission electron microtomography without the "missing wedge" for quantitative structural analysis. *Ultramicroscopy*, 107(1):8–15, 2007.
- [127] P. Baggethun. Radial profile plot, ImageJ plugin. <http://rsbweb.nih.gov/ij/plugins/radial-profile.html>, May 2009.
- [128] W. L. Roth. The magnetic structure of Co_3O_4 . *Journal of Physics and Chemistry of Solids*, 25(1):1–10, 1964.
- [129] Z. Horita, T. Sano, and M. Nemoto. Determination of the absorption-free k_{ANI} factors for quantitative microanalysis of nickel base alloys. *Journal of Electron Microscopy*, 35(4):324–334, 1986.
- [130] V. D. Scott, G. Love, and S. J. B. Reed. *Quantitative electron-probe microanalysis*. Ellis Horwood Limited, 1995.
- [131] C. V. Thompson. Grain-growth in thin-films. *Annual Review of Materials Science*, 20:245–268, 1990.
- [132] M. N. Rahaman. *Sintering of ceramics*. CRC Press, 2007.

- [133] M. F. Yan. Microstructural control in the processing of electronic ceramics. *Materials Science and Engineering*, 48(1):53–72, 1981.
- [134] C. V. Thompson and R. Carel. Stress and grain growth in thin films. *Journal of the Mechanics and Physics of Solids*, 44(5):657–673, 1996.
- [135] C. S. Smith. Grains, phases, and interfaces: An interpretation of microstructure. In *Metals Technology 1948 – Volume XV*, number 15 in Transactions of the Metallurgical Society. AIME, 1948.
- [136] N. Moelans, B. Blanpain, and P. Wollants. A phase field model for the simulation of grain growth in materials containing finely dispersed incoherent second-phase particles. *Acta Materialia*, 53(6):1771–1781, 2005.
- [137] T. Akashi, C. Muraoka, H. Kiyono, and S. Shimada. Grain growth of LaCoO_3 film dispersed with a second phase prepared by a sol-gel technique. *Transaction of the Materials Research Society of Japan*, 32:127, 2007.
- [138] T. Sawada and T. Akashi. Grain growth behavior of $\text{La}_{0.6}\text{Sr}_{0.4}\text{CoO}_{3-\delta}$ film dispersed with a second phase. *ECS Transactions*, 16(44):199–204, 2009.
- [139] G. Westin, M. Ottoson, and A. Pohl. Alkoxide route to $\text{La}_{0.5}\text{Sr}_{0.5}\text{CoO}_3$ epitaxial thin films on SrTiO_3 . *Thin Solid Films*, 516(15):4673–4678, 2008.
- [140] N. P. Bansal and Z. Zhong. Combustion synthesis of $\text{Sm}_{0.5}\text{Sr}_{0.5}\text{CoO}_{3-x}$ and $\text{La}_{0.6}\text{Sr}_{0.4}\text{CoO}_{3-x}$ nanopowders for solid oxide fuel cell cathodes. *Journal of Power Sources*, 158(1):148–153, 2006.
- [141] M. Radermacher. Three-dimensional reconstruction of single particles from random and nonrandom tilt series. *Journal of Electron Microscopy Technique*, 9(4):359–394, 1988.
- [142] M. Radermacher. Weighted back-projection methods. In J. Frank, editor, *Electron Tomography: Three-Dimensional Imaging with the Transmission Electron Microscope*. Springer, 1992.
- [143] S. S. van Bavel and J. Loos. Volume organization of polymer and hybrid solar cells as revealed by electron tomography. *Advanced Functional Materials*, 20(19):3217–3234, 2010.
- [144] A. Pohl and G. Westin. Alkoxide route to $\text{La}_{0.5}\text{Sr}_{0.5}\text{CoO}_3$ films and powders. *Journal of the American Ceramic Society*, 88(8):2099–2105, 2005.
- [145] S. Cizauskaite and A. Kareiva. Sol-gel preparation and characterization of non-substituted and Sr-substituted lanthanum cobaltates. *Central European Journal of Chemistry*, 6(3):456–464, 2008.

- [146] M. Palcut, K. Wiik, and T. Grande. Cation self-diffusion in LaCoO_3 and La_2CoO_4 studied by diffusion couple experiments. *The Journal of Physical Chemistry B*, 111(9):2299–2308, 2007.
- [147] A. Heel, P. Holtappels, and T. Graule. On the synthesis and performance of flame-made nanoscale $\text{La}_{0.6}\text{Sr}_{0.4}\text{CoO}_{3-\delta}$ and its influence on the application as an intermediate temperature solid oxide fuel cell cathode. *Journal of Power Sources*, 195(19):6709–6718, 2010.
- [148] A. Petrov, V. Cherepanov, and A. Zuev. Thermodynamics, defect structure, and charge transfer in doped lanthanum cobaltites: An overview. *Journal of Solid State Electrochemistry*, 10(8):517–537, 2006.
- [149] M. Kubicek, A. Limbeck, T. Fromling, H. Hutter, and J. Fleig. Relationship between cation segregation and the electrochemical oxygen reduction kinetics of $\text{La}_{0.6}\text{Sr}_{0.4}\text{CoO}_{3-\delta}$ thin film electrodes. *Journal of The Electrochemical Society*, 158(6):B727–B734, 2011.
- [150] J. Hayd, U. Guntow, and E. Ivers-Tiffée. Electrochemical performance of nanoscaled $\text{La}_{0.6}\text{Sr}_{0.4}\text{CoO}_{3-\delta}$ as intermediate temperature soft cathode. In M. Mogenssen, T. Armstrong, T. Gur, and H. Yokokawa, editors, *ECS Transactions*, volume 28, pages 3–15. ECS, 2010.
- [151] J. Hayd, L. Dieterle, U. Guntow, D. Gerthsen, and E. Ivers-Tiffée. Nanoscaled $\text{La}_{0.6}\text{Sr}_{0.4}\text{CoO}_{3-\delta}$ as intermediate temperature solid oxide fuel cell cathode: Microstructure and electrochemical performance. *Journal of Power Sources*, 196(17):7263–7270, 2011.
- [152] S. B. Adler. Mechanism and kinetics of oxygen reduction on porous $\text{La}_{1-x}\text{Sr}_x\text{CoO}_{3-\delta}$ electrodes. *Solid State Ionics*, 111(1–2):125–134, 1998.
- [153] B. Rüger, A. Weber, and E. Ivers-Tiffée. 3D-modelling and performance evaluation of mixed conducting (MIEC) vathodes. *ECS Transaction*, 7(1):2065–2074, 2007.
- [154] H. Zhang and W. Yang. Highly efficient electrocatalysts for oxygen reduction reaction. *Chemical Communication*, 41(41):4215–4217, 2007.
- [155] K. Yamahara, C. P. Jacobson, S. J. Visco, X.-F. Zhang, and L. C. De Jonghe. Thin film SOFCs with cobalt-infiltrated cathodes. *Solid State Ionics*, 176(3–4):275–279, 2005.
- [156] D. Chen, C. Huang, R. Ran, H. J. Park, C. Kwak, and Z. Shao. New $\text{Ba}_{0.5}\text{Sr}_{0.5}\text{Co}_{0.8}\text{Fe}_{0.2}\text{O}_{3-\delta} + \text{Co}_3\text{O}_4$ composite electrode for IT-SOFCs with improved electrical conductivity and catalytic activity. *Electrochemistry Communications*, 13(2):197–199, 2011.
- [157] G. H. Jonker. Magnetic and semiconducting properties of perovskites containing manganese and cobalt. *Journal of Applied Physics*, 37(3):1424–1430, 1966.

- [158] D. Fuchs, C. Pinta, T. Schwarz, P. Schweiss, P. Nagel, S. Schuppler, R. Schneider, M. Merz, G. Roth, and H. v. Löhneysen. Ferromagnetic order in epitaxially strained LaCoO_3 thin films. *Physical Review B*, 75(14):144402, 2007.
- [159] D. Fuchs, E. Arac, C. Pinta, S. Schuppler, R. Schneider, and H. v. Löhneysen. Tuning the magnetic properties of LaCoO_3 thin films by epitaxial strain. *Physical Review B*, 77(1):014434, 2008.
- [160] K. Asai, A. Yoneda, O. Yokokura, J. M. Tranquada, G. Shirane, and K. Kohn. Two spin-state transitions in LaCoO_3 . *Journal of the Physical Society of Japan*, 67(1):290–296, 1998.
- [161] J.-Q. Yan, J.-S. Zhou, and J. B. Goodenough. Bond-length fluctuations and the spin-state transition in LCoO_3 (L=La, Pr, and Nd). *Physical Review B*, 69(13):134409, 2004.
- [162] M. A. Korotin, S. Y. Ezhov, I. V. Solovyev, V. I. Anisimov, D. I. Khomskii, and G. A. Sawatzky. Intermediate-spin state and properties of LaCoO_3 . *Physical Review B*, 54(8):5309–5316, 1996.
- [163] R. H. Potze, G. A. Sawatzky, and M. Abbate. Possibility for an intermediate-spin ground state in the charge-transfer material SrCoO_3 . *Physical Review B*, 51(17):11501–11506, 1995.
- [164] D. Fuchs, P. Schweiss, P. Adelman, T. Schwarz, and R. Schneider. Ferromagnetic order in the electron-doped system $\text{La}_{1-x}\text{Ce}_x\text{CoO}_3$. *Physical Review B*, 72(1):014466, 2005.
- [165] K. Asai, O. Yokokura, M. Suzuki, T. Naka, T. Matsumoto, H. Takahashi, N. Môri, and K. Kohn. Pressure dependence of the 100 K spin-state transition in LaCoO_3 . *Journal of the Physical Society of Japan*, 66(4):967–970, 1997.
- [166] J.-S. Zhou, J.-Q. Yan, and J. B. Goodenough. Bulk modulus anomaly in RCoO_3 (R=La, Pr, and Nd). *Physical Review B*, 71(22):220103, 2005.
- [167] D. M. Sherman. Structural and magnetic phase transitions in minerals, advances in physical geochemistry. Springer, New York, 1988.
- [168] P. G. Radaelli and S.-W. Cheong. Structural phenomena associated with the spin-state transition in LaCoO_3 . *Physical Review B*, 66(9):094408, 2002.
- [169] G. Maris, Y. Ren, V. Volotchaev, C. Zobel, T. Lorenz, and T. T. M. Palstra. Evidence for orbital ordering in LaCoO_3 . *Physical Review B*, 67(22):224423, June 2003.
- [170] A. Rosenauer, S. Kaiser, T. Reisinger, J. Zweck, W. Gebhardt, and D. Gerthsen. Digital analysis of HRTEM lattice images. *Optik*, 102:63–69, 1996.

- [171] U. M. Gebhardt. *Strukturelle Relaxation von epitaktischen, dünnen La/Sr-Manganitfilmen in Abhängigkeit von der Schichtdicke*. PhD thesis, Universitätsbibliothek der Universität Stuttgart, 2007.
- [172] K. Aizu. Possible species of ferromagnetic, ferroelectric, and ferroelastic crystals. *Physical Review B*, 2(3):754–772, 1970.
- [173] S. Bueble, K. Knorr, E. Brecht, and W. W. Schmahl. Influence of the ferroelastic twin domain structure on the $\{100\}$ surface morphology of LaAlO_3 HTSC substrates. *Surface Science*, 400(1-3):345–355, 1998.
- [174] O. I. Lebedev, G. Van Tendeloo, S. Amelinckx, F. Razavi, and H.-U. Habermeier. Periodic microtwinning as a possible mechanism for the accommodation of the epitaxial film-substrate mismatch in the $\text{La}_{1-x}\text{Sr}_x\text{MnO}_3 / \text{SrTiO}_3$ system. *Philosophical Magazine A*, 81(4):797–824, 2001.
- [175] S. K. Streiffer, C. B. Parker, A. E. Romanov, M. J. Lefevre, L. Zhao, J. S. Speck, W. Pompe, C. M. Foster, and G. R. Bai. Domain patterns in epitaxial rhombohedral ferroelectric films. I. Geometry and experiments. *Journal of Applied Physics*, 83(5):2742–2753, 1998.
- [176] S. W. Jin, G. Y. Gao, Z. Huang, Z. Z. Yin, X. Zheng, and Wenbin Wu. Shear-strain-induced low symmetry phase and domain ordering in epitaxial $\text{La}_{0.7}\text{Sr}_{0.3}\text{MnO}_3$ thin films. *Applied Physics Letters*, 92(26):261901, 2008.
- [177] A. Vailionis, H. Boschker, W. Siemons, E. P. Houwman, D. H. A. Blank, G. Rijnders, and G. Koster. Misfit strain accommodation in epitaxial ABO_3 perovskites: Lattice rotations and lattice modulations. *Physical Review B*, 83(6):064101, 2011.
- [178] M. E. Fisher and M. N. Barber. Scaling theory for finite-size effects in the critical region. *Physical Review Letters*, 28(23):1516–1519, 1972.
- [179] D. Fuchs, O. Morán, P. Adelman, and R. Schneider. Finite size effect in epitaxial $\text{La}_{0.7}\text{A}_{0.3}\text{CoO}_3$ ($\text{A} = \text{Ca}, \text{Sr}, \text{Ba}$) thin films. *Physica B: Condensed Matter*, 349(1-4):337–341, 2004.
- [180] M. Ziese, H. C. Semmelhack, K. H. Han, S. P. Sena, and H. J. Blythe. Thickness dependent magnetic and magnetotransport properties of strain-relaxed $\text{La}_{0.7}\text{Ca}_{0.3}\text{MnO}_3$ films. *Journal of Applied Physics*, 91(12):9930–9936, 2002.
- [181] K. Knížek, P. Novák, and Z. Jirák. Spin state of LaCoO_3 : Dependence on CoO_6 octahedra geometry. *Physical Review B*, 71(5):054420, 2005.
- [182] D. P. Kozlenko, N. O. Golosova, Z. Jirák, L. S. Dubrovinsky, B. N. Savenko, M. G. Tucker, Y. Le Godec, and V. P. Glazkov. Temperature- and pressure-driven spin-state transitions in LaCoO_3 . *Physical Review B*, 75(6):064422, 2007.

- [183] P. Ravindran, P. A. Korzhavyi, H. Fjellvåg, and A. Kjekshus. Electronic structure, phase stability, and magnetic properties of $\text{La}_{1-x}\text{Sr}_x\text{CoO}_3$ from first-principles full-potential calculations. *Physical Review B*, 60(24):16423–16434, 1999.
- [184] L. Dieterle, P. Bockstaller, D. Gerthsen, J. Hayd, E. Ivers-Tiffée, and U. Guntow. Solid oxide fuel cells: Microstructure of nanoscaled $\text{La}_{0.6}\text{Sr}_{0.4}\text{CoO}_{3-\delta}$ cathodes for intermediate-temperature solid oxide fuel cells (Adv. Energy Mater. 2/2011). *Advanced Energy Materials*, 1(2):138–138, 2011.

Own publications and contributions to conferences

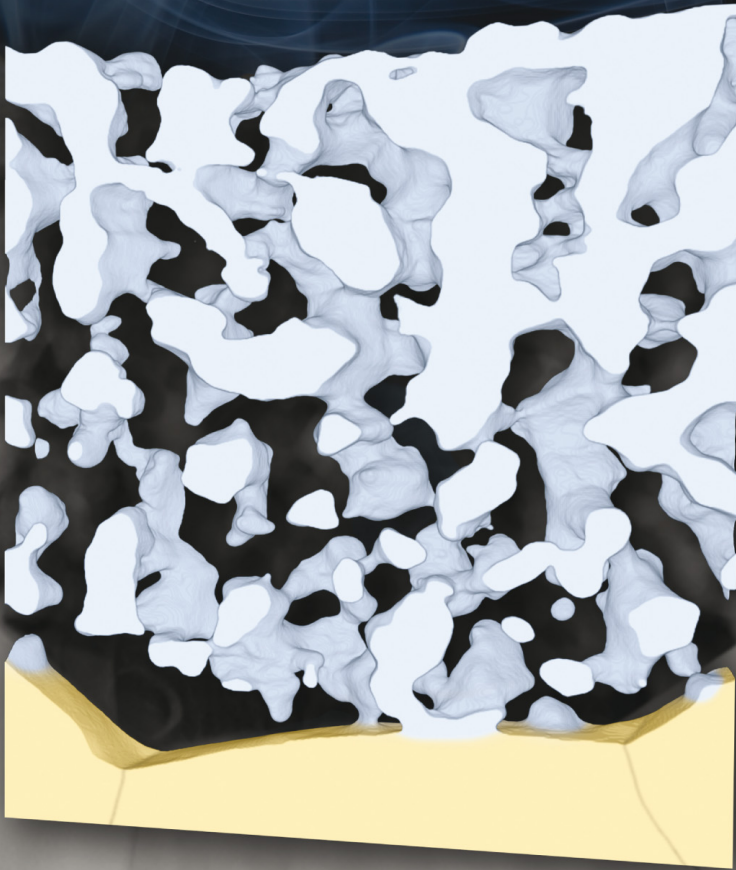
Related publications (reviewed)

- L. Dieterle, D. Bach, R. Schneider, H. Störmer, D. Gerthsen, U. Guntow, E. Ivers-Tiffée, A. Weber, C. Peters, and H. Yokokawa. Structural and chemical properties of nanocrystalline $\text{La}_{0.5}\text{Sr}_{0.5}\text{CoO}_{3-\delta}$ layers on yttria-stabilized zirconia analyzed by transmission electron microscopy. *Journal of Materials Science*, 43(9):3135–3143, 2008.
- D. Fuchs, L. Dieterle, E. Arac, R. Eder, P. Adelman, V. Eyert, T. Kopp, R. Schneider, D. Gerthsen, and H. v. Löhneysen. Suppression of the ferromagnetic state in LaCoO_3 films by rhombohedral distortion. *Physical Review B*, 79:024424/1-9, 2009.
- J. Hayd, L. Dieterle, U. Guntow, D. Gerthsen, and E. Ivers-Tiffée. Nanoscaled $\text{La}_{0.6}\text{Sr}_{0.4}\text{CoO}_{3-\delta}$ as intermediate temperature solid oxide fuel cell cathode: Microstructure and electrochemical performance. *Journal of Power Sources*, 196(17):7263–7270, 2011.
- L. Dieterle, P. Bockstaller, D. Gerthsen, J. Hayd, E. Ivers-Tiffée, and U. Guntow. Microstructure of nanoscaled $\text{La}_{0.6}\text{Sr}_{0.4}\text{CoO}_{3-\delta}$ cathodes for intermediate-temperature solid oxide fuel cells. *Advanced Energy Materials*, 1(2):249–258, 2011.
- L. Dieterle, P. Bockstaller, D. Gerthsen, J. Hayd, E. Ivers-Tiffée, U. Guntow, and C. Kübel. Microstructure of sol-gel derived nanoscaled $\text{La}_{0.6}\text{Sr}_{0.4}\text{CoO}_{3-\delta}$ cathodes for intermediate-temperature SOFCs, 219th ECS Meeting Montreal, QC, Canada, Solid Oxide Fuel Cells 12 (SOFC-XII) eds.: S. Singhal and K. Eguchi, *ECS Transactions*, 35(1):1909-1918, 2011.
- L. Dieterle, B. Butz, and E. Müller. Optimized Ar^+ -ion milling procedure for TEM cross-section sample preparation. *Ultramicroscopy*, 111(11):1636–1644, 2011.

Vol. 1 • No. 2 • March 18 • 2011

www.advenergymat.de

ADVANCED ENERGY MATERIALS



 WILEY-VCH

Solid Oxide Fuel Cell Cathodes

Figure 5.1.: Inside cover, Advanced Energy Materials, Vol. 1(2), 2011 [184]

Further Publications (reviewed)

- P. Müller, L. Dieterle, E. Müller, H. Störmer, D. Gerthsen, C. Niedrig, S. Taufall, S. F. Wagner, and E. Ivers-Tiffée. $\text{Ba}_{0.5}\text{Sr}_{0.5}\text{Co}_{0.8}\text{Fe}_{0.2}\text{O}_{3-\delta}$ for oxygen separation membranes, *ECS Transactions*, 28:309-314, 2010.
- I. Tischer, M. Feneberg, M. Schirra, H. Yacoub, R. Sauer, K. Thonke, T. Wunderer, F. Scholz, L. Dieterle, E. Müller, and D. Gerthsen. Stacking fault-related luminescence features in semi-polar GaN, *Physica Status Solidi B*, 248(3):611–615, 2011.
- I. Tischer, M. Feneberg, M. Schirra, H. Yacoub, R. Sauer, K. Thonke, T. Wunderer, F. Scholz, L. Dieterle, E. Müller, and D. Gerthsen. I_2 basal plane stacking fault in GaN: Origin of the 3.32 eV luminescence band, *Physical Review B*, 83:035314, 2011.
- M. Wissinger, D. Fuchs, L. Dieterle, H. Leiste, R. Schneider, D. Gerthsen, and H. v. Löhneysen. Anisotropic lattice changes and ferromagnetic order in $\text{Sr}_{1-x}\text{Ca}_x\text{RuO}_3$, *Physical Review B* 83:144430, 2011.
- P. Müller, H. Störmer, L. Dieterle, C. Niedrig, E. Ivers-Tiffée, and D. Gerthsen. Decomposition pathway of cubic $\text{Ba}_{0.5}\text{Sr}_{0.5}\text{Co}_{0.8}\text{Fe}_{0.2}\text{O}_{3-\delta}$ between 700 °C and 1000 °C analyzed by electron microscopic techniques, *Solid State Ionics* 206(1):57-66, 2012.

Contributions to conferences (presenting author underlined)

- C. Peters, A. Weber, E. Ivers-Tiffée, U. Guntow, L. Dieterle, and D. Gerthsen. Nanoscale MIEC cathode for solid oxide fuel cells (poster), European Materials Research Society (EMRS), Spring Meeting 2006, Nice, France, May 29–June 2, 2006.
- L. Dieterle, D. Gerthsen, C. Peters, A. Weber, and U. Guntow, (B. Butz). Structural Characterization and chemical stability of nanoscale $\text{La}_{0.5}\text{Sr}_{0.5}\text{CoO}_{3-\delta}$ cathodes on YSZ (poster), MRS Fall Meeting 2006, Boston, USA, November 27–December 1, 2006.
- C. Peters, L. Dieterle, D. Gerthsen, A. Weber, and E. Ivers-Tiffée. Nanoskalige $\text{La}_{0.5}\text{Sr}_{0.5}\text{CoO}_3$ -Dünnschichtkathoden für Hochtemperaturbrennstoffzellen (poster), DGM-Tag der Deutschen Gesellschaft der Materialkunde e.V., Karlsruhe, Germany, June 21–22, 2007.
- L. Dieterle, D. Gerthsen, E. Ivers-Tiffée, C. Peters, A. Weber, U. Guntow, and H. Yokokawa. Structural characterization and chemical stability of nanocrystalline $\text{La}_{0.5}\text{Sr}_{0.5}\text{CoO}_{3-\delta}$ cathode layers on YSZ obtained by sol-gel processing (poster). International Conference on Electroceramics 2007 (Arusha, Tanzania), July 31–August 3, 2007.
- L. Dieterle, D. Bach, R. Schneider, H. Störmer, D. Gerthsen, C. Peters, A. Weber, E. Ivers-Tiffée, and U. Guntow. Microstructure of sol-gel deposited $\text{La}_{1-x}\text{Sr}_x\text{CoO}_{3-\delta}$ thin films (poster), Microscopy Conference, Saarbrücken, Germany, September 2–7, 2007.
- L. Dieterle, D. Bach, R. Schneider, H. Störmer, D. Gerthsen, C. Peters, A. Weber, E. Ivers-Tiffée, and U. Guntow. Chemical stability and structural properties of nanocrystalline $\text{La}_{0.5}\text{Sr}_{0.5}\text{CoO}_{3-\delta}$ layers on yttria-stabilized zirconia (poster), Euromat (Nurnberg, Germany), September 10–13, 2007.
- L. Dieterle, D. Gerthsen, and D. Fuchs. Microstructure of epitaxially strained LaCoO_3 thin films (talk). 14th European Microscopy Congress - EMC 2008, Aachen, September 1–5, 2008.
- D. Fuchs, L. Dieterle, E. Arac, P. Adelman, R. Schneider, D. Gerthsen, and H. von Löhneysen. Relaxation of epitaxial strain in LaCoO_3 films by nano-twinning (talk). Villa Conference on Complex Oxide Heterostructures, Orlando (Florida), USA, November 2–6, 2008.
- L. Dieterle, D. Gerthsen, J. Hayd, and E. Ivers-Tiffée. Microstructural and electrochemical characterization of nanoscaled $\text{La}_{0.6}\text{Sr}_{0.4}\text{CoO}_{3-\delta}$ films as cathode material for solid oxide fuel cells (poster). 11th International Fischer Symposium on Microscopy in Electrochemistry, Benediktbeuern, Germany, July 26–31, 2009.

- D. Fuchs, L. Dieterle, E. Arac, R. Schneider, V. Eyert, T. Kopp, D. Gerthsen, and H. von Löhneysen. Suppression of the strain-induced ferromagnetic state in LaCoO_3 thin films by rhombohedral distortion (talk). The International Conference on Magnetism - ICM 2009, Karlsruhe, Germany, July 26–31, 2009.
- L. Dieterle, B. Butz, and D. Fuchs. Optimized Ar^+ -ion etching for TEM cross-section sample preparation (poster, **best poster award**), Microscopy Conference–MC2009, Graz, Austria, August 30–September 4, 2009.
- L. Dieterle, D. Fuchs, and D. Gerthsen. Structural features of epitaxially strained LaCoO_3 thin films (poster). 452th WE-Heraeus-Seminar: Strain in transition metal oxides – tuning magnetic and electric functionalities, Bad Honnef, Germany, March 15–17, 2010.
- P. Müller, L. Dieterle, E. Müller, H. Störmer, D. Gerthsen, C. Niedrig, S. Taufall, S.F. Wagner, and E. Ivers-Tiffée. $\text{Ba}_{0.5}\text{Sr}_{0.5}\text{Co}_{0.8}\text{Fe}_{0.2}\text{O}_{3-\delta}$ for Oxygen Separation Membranes (talk). 217th ECS Meeting, Vancouver, Canada, April 25–30, 2010.
- I. Tischer, H. Yacoub, M. Schirra, M. Feneberg, T. Wunderer, F. Scholz, L. Dieterle, E. Müller, D. Gerthsen, and Klaus Thonke. Detailed investigation of the defect-related emissions around 3.3 eV in GaN ELOG structures (talk). DPG Frühjahrstagung – Semiconductor Physics Division, Fachverband Halbleiterphysik (HL), Regensburg, Germany, March 21–26, 2010.
- L. Dieterle, P. Bockstaller, J. Hayd, E. Ivers-Tiffée, U. Guntow, and D. Gerthsen. Characterization of nanoscaled $\text{La}_{0.6}\text{Sr}_{0.4}\text{CoO}_{3-\delta}$ as cathode material for solid oxide fuel cells by transmission electron microscopy (poster). First International Conference on Materials for Energy, Karlsruhe, Germany, July 4–8, 2010.
- P. Müller, L. Dieterle, H. Störmer, and D. Gerthsen. Determination of the crystal structure of $\text{Ba}_{0.5}\text{Sr}_{0.5}\text{Co}_{0.8}\text{Fe}_{0.2}\text{O}_{3-\delta}$ by electron diffraction (poster). Facets of Electron Crystallography, Berlin, July 7–9, 2010.
- P. Müller, L. Dieterle, H. Störmer, D. Gerthsen, and D. Fuchs. Determination of phase composition of $\text{Ba}_{0.5}\text{Sr}_{0.5}\text{Co}_{0.8}\text{Fe}_{0.2}\text{O}_{3-\delta}$ under application-relevant conditions using advanced electron microscopy (poster). Summer School–Ceramic Membranes for Green Chemical Production and Clean Power Generation, Valencia, Espania, September 8–10, 2010.
- D. Fuchs, M. Merz, L. Dieterle, S. Uebe, M. Wissinger, A. Asmman, P. Nagel, S. Schuppler, D. Gerthsen, and H. von Löhneysen. Tuning the spin blockade in layered cobaltates by chemical and epitaxial pressure (poster). Materials Research Society Fall Meeting, Boston, Massachusetts, USA, November 29–December 3, 2010.

- M. Wissinger, D. Fuchs, L. Dieterle, H. Leiste, R. Schneider, D. Gerthsen, and H. von Löhneysen. Effect of anisotropic lattice changes on ferromagnetic order in $\text{Sr}_{1-x}\text{Ca}_x\text{RuO}_3$ (talk). DPG Frühjahrstagung – Magnetism Division, Fachverband Magnetismus (MA), Dresden, Germany, March 13–18, 2011.
- D. Fuchs, M. Merz, L. Dieterle, S. Uebe, M. Wissinger, A. Assmann, P. Nagel, R. Schneider, S. Schuppler, D. Gerthsen, and H. von Löhneysen. Spin-states in the single-layered cobaltates (talk). DPG Frühjahrstagung – Magnetism Division, Fachverband Magnetismus (MA), Dresden, Germany, March 13–18, 2011.
- L. Dieterle, P. Bockstaller, D. Gerthsen, J. Hayd, E. Ivers-Tiffée, and U. Guntow. Microstructure of sol-gel derived nanoscaled $\text{La}_{0.6}\text{Sr}_{0.4}\text{CoO}_{3-\delta}$ cathodes for intermediate-temperature SOFCs (talk). 219th Electrochemical Society Meeting – Solid Oxide Fuel Cells XII, Montreal, Canada, May 1–6, 2011.
- P. Müller, H. Stormer, L. Dieterle, N. Firman, and D. Gerthsen. Investigation of the decomposition pathway of cubic $\text{Ba}_{0.5}\text{Sr}_{0.5}\text{Co}_{0.8}\text{Fe}_{0.2}\text{O}_{3-\delta}$ (BSCF) by electron microscopy (poster). Microscopy Conference 2011, Kiel, Germany, August 28—September 02, 2011.
- L. Dieterle, P. Bockstaller, R. Schneider, D. Gerthsen, J. Hayd, and C. Kübel. Nanoscaled sol-gel derived $\text{La}_{0.6}\text{Sr}_{0.4}\text{CoO}_{3-\delta}$ cathodes for intermediate-temperature solid oxide fuel cells (SOFCs) (poster, **best poster award**). Microscopy Conference 2011, Kiel, Germany, August 28—September 02, 2011.

Danksagung

An dieser Stelle möchte ich mich bei allen Personen bedanken, die mich bei der Erstellung dieser Arbeit unterstützt und maßgeblich zu ihrem Gelingen beigetragen haben.

Prof. Dr. Dagmar Gerthsen danke ich für die wissenschaftliche Freiheit, die sie mir während meiner gesamten Forschungszeit gewährte. Dies ermöglichte die Einbindung weiterer wissenschaftlicher Fragestellungen, welche sich im Verlauf der Arbeit ergaben. Dies trug somit maßgeblich zum Gelingen dieser Arbeit bei. Ihr kompetenter Rat und umfangreiches Fachwissen war immer sehr hilfreich, wann immer es Probleme gab. Die exzellente Labor- und Mikroskopausstattung des Laboratoriums für Elektronenmikroskopie erleichterte mir dabei die Arbeit erheblich.

Desweiteren möchte ich Prof. Dr.-Ing. Ellen Ivers-Tiffée danken. Zum Einen für ihr Engagement und guten Ideen die sie zu dieser Arbeit besteuerte, zum Anderen für die Übernahme des Korreferats.

Dr.-Ing. Christoph Peters und Dipl.-Wi.-Ing. Jan Hayd danke ich für die vielen fruchtbaren Diskussionen rund um das Thema SOFC Kathodenmaterialien sowie die elektrochemische Charakterisierung der Kathodenschichten. Dr. Dirk Fuchs danke ich für die gute Zusammenarbeit sowie die magnetische und strukturelle Charakterisierung (mittels XRD) epitaktischer LCO Schichten.

PD Dr. habil. Reinhard Schneider und Dr. Benjamin Butz danke ich für die vielen fachlichen Diskussionen rund um das Thema Elektronenmikroskopie, sowie Dr.-Ing. Heike Störmer für ihre Hilfe bei materialwissenschaftlichen Problemen.

Ein besonderer Dank geht an alle meine Kollegen am Laboratorium für Elektronenmikroskopie für die tolle Zeit, die ich mit ihnen verbringen durfte, sowie das außerordentlich gute Arbeitsklima, welches ich sehr vermissen werde. Hierzu trugen nicht zuletzt meine Bürokollegen Heike Störmer, Philipp Müller, Christian Rockenhäuser sowie Benjamin Butz bei.

Meinen Eltern danke ich dafür, dass sie mir das Studium der Physik ermöglicht haben, liebevoll zur Seite standen und mich während der Anfertigung der Doktorarbeit stets unterstützt haben.

Letztendlich gebührt ein besonderer Dank meiner großen Liebe Katrin, die mich immer wieder antrieb, motivierte und nach misslungenen Experimenten wieder aufbaute.